Dissertation zur Erlangung des Doktorgrades
der Fakultät für Chemie und Pharmazie
der Ludwig-Maximilians-Universität München

Structural and biochemical characterization of the interaction between focal adhesion receptor integrin α5β1 and fibronectin

Stephanie Schumacher

aus

Wiesbaden, Deutschland

2020

Erklärung

Diese Dissertation wurde im Sinne von § 7 der Promotionsordnung vom 28. November 2011 von Frau Prof. Dr. Elena Conti betreut.

Eidesstattliche Versicherung

Diese Dissertation wurde eigenständig und ohne unerlaubte Hilfe erarbeitet.

München, den 14.10.2020

_____

Stephanie Schumacher

Dissertation eingereicht am: 14.10.2020

Erstgutachter: Prof. Dr. Elena Conti

Zweitgutachter: Prof. Dr. Karl-Peter Hopfner

Mündliche Prüfung am: 2.12.2020

Index

List of Figures

Summary

Integrins are the key receptors of focal adhesions and crucial for basic cellular processes such as adhesion and migration. On a molecular level, integrins consist of two subunits, α and β, which are both comprised of an N-terminal ectodomain, transmembrane and C-terminal cytoplasmic tail domains. Integrins bind to the extracellular matrix with their ectodomain, to the actin cytoskeleton machinery via their cytoplasmic tails and are involved in bidirectional signaling across the plasma membrane. 18 α and 8 β subunits form 24 integrin heterodimer combinations which exhibit diverse expression patterns. Based on structural studies of the last two decades, integrins are thought to undergo conformational changes upon ligand binding, i.e. switch between an acutely bent, low affinity and an open-extended, ligand-bound state. However, as only a couple of integrins out of the 24 existing isoforms have been studied structurally, it is unclear whether the proposed canonical activation mechanism applies to all isoforms.

Integrin α5β1 is the ubiquitously expressed major fibronectin receptor. Altered expression or function of either α5β1 or fibronectin can have detrimental consequences for the body and result in multiple diseases, such as neoangiogenesis during cancer formation. To fully understand the integrin α5β1-fibronectin activation mechanism in atomic detail, physiological α5β1 was purified from human placenta and subjected to cryo-electron microscopy analysis. The two structures of resting, low affinity as well as fibronectin ('FN')-bound integrin α5β1 were obtained at resolutions of 4.6 Å and 3.1 Å, respectively. The interface between fibronectin fragment FN7-10 and integrin α5β1 revealed three major interactions sites: (1.) the well-studied RGD motif on FN10, bound to both α5 and β1 subunits, (2.) the synergy site on FN9, engaged in α5 subunit binding, and (3.) novel residues on FN10 interacting with a metal ion binding site on the integrin β1 subunit. Together with these interaction sites, an N-glycan on the α5 subunit seems to contribute to stabilizing the interaction between integrin and fibronectin. Resting integrin α5β1 revealed a novel, incompletely bent conformation, which does not exhibit the acute bending observed for previous integrin structures. Furthermore, via biochemical and negative-stain electron microscopy studies, an uncoupling of affinity and conformational states for integrin α5β1 was observed, which stands in contrast to other studied integrins.

Taken together, the presented study describes how integrin α5β1 activation is regulated and how the crosstalk between α5β1 and fibronectin is conducted on a molecular level. The results obtained in this study contribute to deciphering a mechanism of how integrin α5β1 fine-tuned its regulation and activity.

Preface

Integrins are the major receptors of focal adhesions, and thus crucial for many basic cellular processes such as adhesion, migration and tissue homeostasis. Aberrant function can have detrimental effects on the body and is linked to several pathologies. Thus, it is crucial to understand how cells manage to properly function during adhesion and how they connect to their surrounding tissue. The studies presented here aim to provide a glimpse into the vast field of integrin biology and may hopefully contribute to a better understanding of integrin function.

The work summarized in this dissertation was conducted in the group of Naoko Mizuno at the Max Planck Institute of Biochemistry in Martinsried, Germany, and resulted in one publication and a recently submitted manuscript, which are presented in a cumulative manner.

In chapter 1, an introduction into focal adhesion biology is presented. The chapter summarizes the current knowledge of the field and gives an overview of the most important concepts. This includes how focal adhesions are generally assembled, what their molecular architecture looks like and how they function under force exposure. Next, the main focus is shifted to integrin, the key receptor of focal adhesions. Structural knowledge as well as the integrin activation mechanism, which includes conformational changes, are described in detail. Lastly, available knowledge on the intracellular integrin activators talin and kindlin is reviewed.

In chapter 2, the aim and scope of the presented thesis is described.

The results section in chapter 3 comprises two sub-chapters: in chapter 3.1, a recently submitted manuscript on the integrin α5β1-fibronectin interaction, titled 'Structural insights into the integrin α5β1 crosstalk with fibronectin ligand' is presented, which represents the main body of work during my PhD. Chapter 3.2 comprises a structural study of the intracellular integrin activator talin 1 to which I contributed. This article was published in 2019, titled 'The architecture of talin1 reveals an autoinhibition mechanism', and I am listed as one of the co-authors.

After a detailed discussion of the described work in chapter 4, focusing on my main project of the integrin-fibronectin interaction, an outlook in chapter 5 gives an overview of some future perspectives in the field.

List of publications

1. Schumacher, S., Dedden, D., Matoba, K., Takagi, J., Biertümpfel, C., and Mizuno, N. Structural insights into the integrin α5β1 crosstalk with fibronectin ligand.
(Manuscript submitted)

2. Dedden, D., **Schumacher, S.**, Kelley, C.F., Zacharias, M., Biertümpfel, C., Fässler, R., and Mizuno, N. (2019). The Architecture of Talin1 Reveals an Autoinhibition Mechanism. Cell 179, 120-131 e113

Abbreviations

ABS	Actin binding site
ADMIDAS	Adjacent to MIDAS
Arp	Actin-related proteins
CT	Cytoplasmic tail
DD	Dimerization domain
ECM	Extracellular matrix
EGF	Epidermal growth factor-like
EM	Electron microscopy
FA	Focal adhesion
FAK	Focal adhesion kinase
FERM	4.1-ezrin-radixin-moesin
FIB	Focused ion beam
FLIM	Fluorescence lifetime imaging microscopy
FN	Fibronectin
FRAP	fluorescence recovery after photobleaching
FRET	Förster resonance energy tranfer
IBS	Integrin binding site
ICAM	Intercellular adhesion molecule 1
ICAP1	integrin cytoplasmic domain-associated protein 1
ILK	Integrin-linked kinase
IMC	Inner membrane clasp
iPALM	Interferometric photo-activated localization microscopy
IPP	ILK-PINCH-parvin
MD	Molecular dynamics
MIDAS	Metal ion-dependent adhesion site
NA	Nascent adhesion
NMR	Nuclear magnetic resonance
OMC	Outer membrane clasp
PINCH	Particularly interesting new cysteine-histidine-rich protein
PIP_2	Phosphatidylinositol 4,5-biphosphate
PSI	Plexin-semaphorin-integrin

PTB	Phosphotyrosine binding
RIAM	Rap1-GTP-interacting adaptor molecule
Salipro	Saposin-lipoprotein
SMALP	Styrene maleic-acid lipid particles
SyMBS	Synergistic metal ion-binding site
TGF-β	Transforming growth factor β
TM	Transmembrane
αI	Integrin α inserted domain
βI	Integrin β inserted-like domain

1. Introduction

1.1 Focal adhesions

1.1.1 Overview

Cellular adhesions are of crucial importance for the development of multicellular organisms as well as tissue morphogenesis, as they enable cells to connect to other cells and to their environment. So-called focal adhesions (FAs) are large protein complexes located at the plasma membrane. They fulfill two major purposes; first, they are involved in mechanically linking the cytoskeleton of a cell to the extracellular matrix (ECM), and second, they sense their environment and bidirectionally transmit signals across the plasma membrane (Geiger et al., 2001; Winograd-Katz et al., 2014; Wozniak et al., 2004). FAs are specific types of adhesions that are integrin-based, i.e. have the transmembrane protein integrin as core receptor recognizing parts of the ECM and other cells (Hynes, 2002). Integrins are heterodimeric transmembrane proteins consisting of a single α and β subunit and have the ability to switch between an active and inactive state. This switch can be triggered either by an extracellular ligand binding to integrin (outside-in signaling) or by intracellular proteins connecting to the cytoplasmic part of integrin (inside-out signaling) (Hynes, 2002). During outside-in signaling, binding to the ECM results in integrin activation. Subsequent conformational changes expose intracellular motifs to which key FA proteins talin and kindlin bind. Integrin's interaction with talin and kindlin then triggers further recruitment of proteins and maturation into vast complexes containing ~150-200 different proteins that extensively connect to the actin cytoskeleton (Winograd-Katz et al., 2014; Zaidel-Bar and Geiger, 2010; Zaidel-Bar et al., 2007). Apart from providing a structural connection, adhesions also play a role in transmitting signals that affect cell survival or differentiation by altering gene expression (reviewed in (Legate et al., 2009)).

Despite the plethora of proteins associated with mature FAs, only a couple of proteins, such as kindlin, talin and vinculin, are essential for initial FA assembly, i.e. for the formation of so-called nascent adhesions (NA) (Bachir et al., 2014). The precise spatiotemporal organization of these key proteins with integrin, actin fibers as well as other FA proteins has been the focus of studies for many decades, employing numerous techniques such as biophysical methods, force measurements, mass spectrometry, super-

resolution as well as electron microscopy (EM) (reviewed in (Schiller and Fassler, 2013)). Elucidating basic molecular mechanisms such as migration and adhesion can lead to a deeper understanding of how cells function and react to their surroundings, which is the first step in comprehending how aberrations in these processes result in diseases such as cancer (Winograd-Katz et al., 2014).

1.1.2 Molecular architecture of focal adhesions

To study FA organization at a molecular level has been a major goal in the field for decades; however, studies have been hampered by different behavior of individual cell types, protein isoforms, the high number of proteins involved as well as assembly dynamics. Still, some general conclusions have been drawn, especially by employing super-resolution microscopy techniques (Case et al., 2015; Kanchanawong et al., 2010; Paszek et al., 2012) and cryo-electron tomography (Patla et al., 2010). Via super-resolution techniques, the following organizational properties of adhesions, both in vertical (perpendicular to plasma membrane) as well as lateral (parallel to membrane) direction have been found to be conserved:

The vertical architecture of FAs has been studied by interferometric photo-activated localization microscopy (iPALM), where several key components of FAs have been fluorescently labelled in cells (Kanchanawong et al., 2010). 3D imaging revealed that a ~40 nm wide region lies between integrins and the actin cytoskeleton, which consists of three layers: the integrin signaling, the force transduction and the actin regulatory layer (**Figure 1**). Each layer contains distinct sets of proteins, except for talin, the major connector between integrin and actin, which spans over all three layers (Liu et al., 2015).

Laterally, it has been observed that when FAs mature, they elongate in the direction of the actin retrograde flow, and that proteins such as talin and vinculin align in the same direction (Choi et al., 2008; Margadant et al., 2011; Zaidel-Bar et al., 2003). Furthermore, it has been shown that nanoclusters form within adhesions, which consist of integrin islands (Spiess et al., 2018). This organization has been compared to an 'archipelago architecture', where integrin islands can diffuse rapidly in and out of FAs (Shibata et al., 2012), while the overall architecture of the FA itself appears relatively stable. This concept allows for fast turnover of proteins and thus flexible adjustment of FA formation and has been directly observed by fluorescence recovery after

photobleaching (FRAP) studies for talin, vinculin, kindlin and others (Lavelin et al., 2013; Lele et al., 2008; Wolfenson et al., 2009).

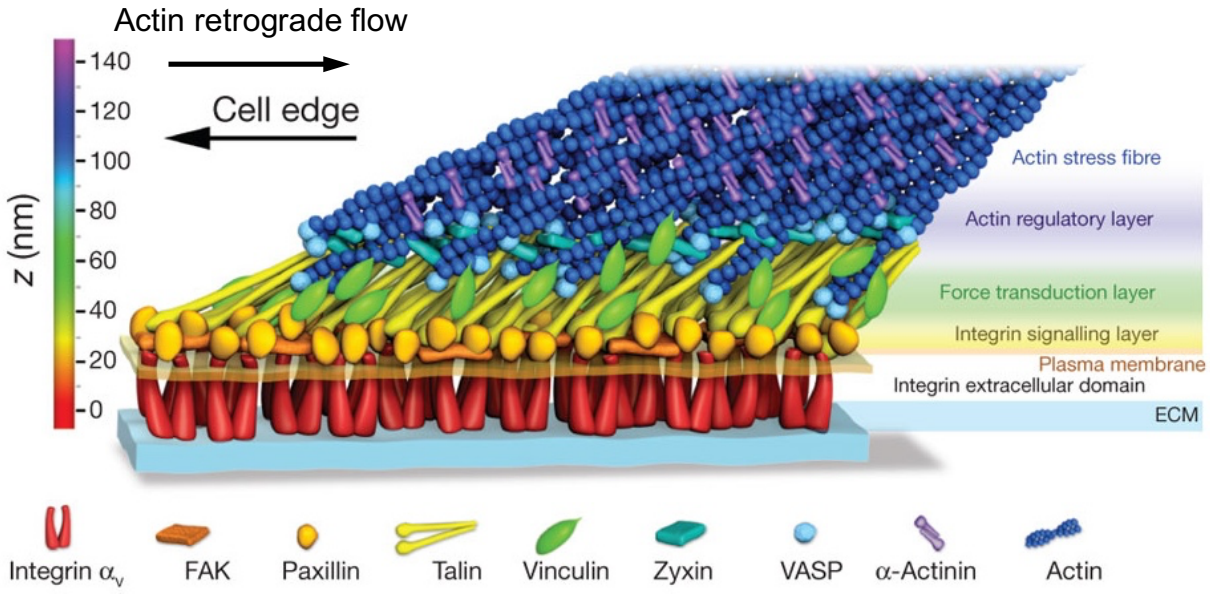

Figure 1: Nanoscale organization of FAs.
Focal adhesions share a similar architecture. The distance between integrins and actin fibers is ~40 nm and is organized in three layers, as determined by iPALM: the integrin signaling, force transduction and actin regulatory layers. The position of key proteins of FAs (e.g. integrin, talin, vinculin; see legend) are depicted in the different layers. Notably, talin (yellow) spans over all three layers. The actin retrograde flow (generated by actin polymerization towards the cell's edge and myosin-dependent contraction) goes from left to right in this depiction.
[Figure adapted from (Kanchanawong et al., 2010)]

1.1.3 Maturation and disassembly of focal adhesions

The assembly process of FA complexes seems to generally occur in a progressive and coordinated manner (Bachir et al., 2014; Geiger and Yamada, 2011). At the earliest stage, NAs form at membrane protrusions at the leading edge of cells, i.e. at lamellipodia and filopodia. These NAs are rather small (~100 nm in diameter), highly transient and short-lived (1 min life time), as has been determined via fluorescence fluctuation methods (Bachir et al., 2014; Geiger and Yamada, 2011). Only a couple of proteins are involved in these first assembly steps, such as the integrin binding (and activating) proteins kindlin and talin.

NAs periodically fluctuate between assembly and disassembly until they eventually mature into full FAs which are larger (up to several μm) and longer-lived (~20 min). FAs might further mature into even larger and longer-lived fibrillar adhesions, which are associated with fibronectin fibrillogenesis (Geiger and Yamada, 2011). Generally, maturation from NA to FA seems to occur upon generation of a positive feedback loop which is highly linked to mechanical force; i.e. ECM stiffness and myosin II contractility (Schiller and Fassler, 2013; Wehrle-Haller, 2012). Thus, it has been found that by inhibiting myosin II, NA formation remains unchanged but further FA maturation is inhibited (Choi et al., 2008).

Interestingly, although it is generally accepted that FAs have a well-organized architecture, the exact hierarchical steps of the assembly process are still unclear. A study using fluorescence fluctuation microscopy found that integrin-kindlin complexes are present first in NAs and form initial clusters (Bachir et al., 2014). Then, α-actinin and talin-vinculin complexes start assembling until finally, the FA is stabilized by connections to actin and by pulling forces generated by myosin II. However, the role different proteins play in the assembly of FAs might be integrin- and cell type-specific (Sun et al., 2014).

At the rear end of the cell, adhesions have to disassemble in order to allow for cell detachment and movement. The exact spatiotemporal mechanisms are still unclear; however, it has been suggested that altered local plasma membrane composition as well as mechanical tension play a role (Wehrle-Haller, 2012). Furthermore, increased calpain 2 recruitment, which cleaves and deactivates the major FA component talin, has been observed to play a major role in FA disassembly (Franco et al., 2004).

1.1.4 Mechanotransduction, molecular clutch and mechanosensitivity

As adhesions are involved in attachment and migration of cells, they provide a link between the ECM and the actin cytoskeleton. Thus, the molecules within adhesions are constantly exposed to mechanical forces, generated by both constant actin polymerization toward the membrane as well as actomyosin contraction of the cytoskeleton. Both factors lead to a phenomenon known as actin retrograde flow, where actin fibers are continuously shifted from the leading edge to the cell core (Lin et al., 1997; Ponti et al., 2004) (indicated in **Figure 1**). A model to describe how force generated by the cell's cytoskeleton is transmitted to the ECM is called the 'molecular clutch' (Mitchison and Kirschner, 1988). The molecular clutch system consists of adaptor proteins and integrins, which link the force-generating cytoskeleton to the ECM (Elosegui-Artola et al., 2018). When engaged in binding to the ECM, the molecular clutch transmits the retrograde flow of actin into forward movement of a cell. The interplay between all components of the molecular clutch as well as their individual behavior under force affects cell migration as well as mechanosensitivity. Mechanosensitivity (or rigidity sensing) describes the ability of a cell to transduce force into biochemical signals in response to varying mechanical stimuli, e.g. substrate stiffness or patterning, which affects adhesion maturation, the cell's behavior, and ultimately cell fate (Chan and Odde, 2008; Engler et al., 2006; Oria et al., 2017). In this regard, the molecular clutch contains several proteins that are affected differently by mechanical stress, such as integrin and talin. The strength of an integrin-ECM bond is increasing with applied force, which marks it as a so-called 'catch-bond' (Kong et al., 2009). In contrast, talin's conformation is altered upon force, as it unfolds, which marks it as a 'slip-bond' (Elosegui-Artola et al., 2018). This unfolding leads to exposure of cryptic binding sites on talin for proteins like vinculin and thus promotes further FA growth (del Rio et al., 2009; Gingras et al., 2005). The different behavior of only two FA protein examples hints at the complexity of the whole molecular clutch network, and how the interplay of the whole FA adhesome might affect the precise fine-tuning of mechanosensitivity.

1.2 Integrins

1.2.1 Overview

The main receptors of FAs are integrins. This type I transmembrane receptor family functions as link between the extracellular environment and the cytoskeleton of a cell and is thus important for basic processes such as cellular adhesion and migration.

Integrins are heterodimers, consisting of a non-covalently linked α and β subunit. In vertebrates, 18 α and 8 β isoforms form 24 different integrins, recognizing different ligands and exhibiting diverse expression profiles (Hynes, 2002). Both α and β subunits consist of a large extracellular domain (~800 amino acids), followed by a single transmembrane helix (~20 amino acids) and a short cytoplasmic tail domain (~13-70 amino acids) (Moser et al., 2009b). Integrins can be divided into four subclasses, depending on their ligand recognition profile, i.e. by binding to RGD, collagen, laminin or leucocyte-specific receptors (**Figure 2**).

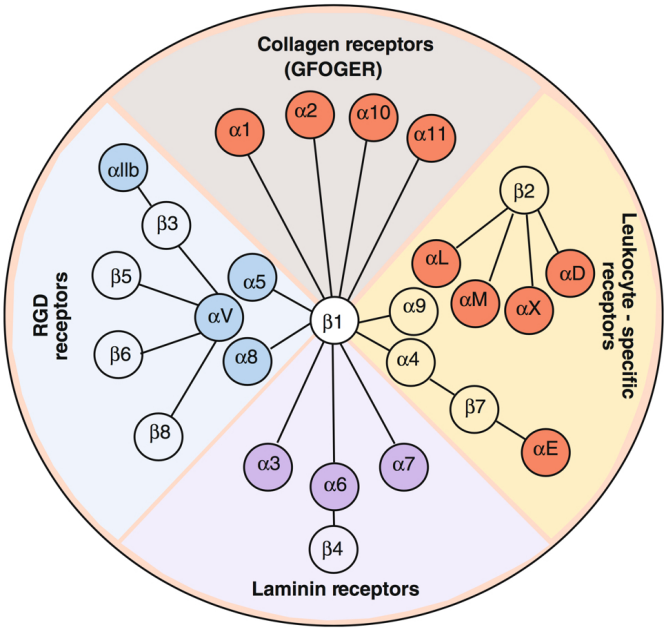

Figure 2: Integrin family divided into subclasses by ligand specificity.
18 α and 8 β subunits form 24 different integrins. These can be divided into four classes, depending on their ligand specificity. 8 integrins recognize RGD (blue), 4 integrins recognize collagen (beige), 8 integrins are leucocyte-specific receptors (yellow) and 4 integrins recognize laminin (purple). The 9 α subunits containing αI domains are labelled orange.
[Figure adapted from (Barczyk et al., 2010)]

While mechanically linking the ECM to the cytoskeleton, integrins are also involved in bidirectional signaling across the plasma membrane (Hynes, 2002). On the one hand, they are able to mediate stimuli from the outside to the inside of the cell. Here, upon ligand binding, integrins undergo conformational changes which enable intracellular proteins to bind, connect to actin and transduce chemical and mechanical signals further into the cell (outside-in signaling)(Legate et al., 2009). On the other hand, their ligand binding affinity can also be regulated by binding of intracellular proteins (inside-out signaling). By changing their structural conformation from a bent-closed to an extended-open state (Hynes, 2002), integrins can integrate and transduce stimuli across the plasma membrane which affects downstream signaling and cell fate (Legate et al., 2009). These conformational states of integrins are highly linked to their ligand binding affinity and will be described in more detail in the chapter below.

Integrins are involved in a variety of processes, ranging from tissue development, maintenance and angiogenesis to leucocyte functions such as leucocyte rolling and platelet activation (Hynes, 2002; Winograd-Katz et al., 2014). Some integrins are also involved in direct intercellular communication between leucocytes and in transforming growth factor β (TGF-β) signaling, as in the case of αvβ6 and αvβ8.

Integrins bind to parts of the extracellular matrix, e.g. fibronectin, vitronectin or collagen, via their extracellular domains. They are partially promiscuous in their behavior, since some integrins are able to bind to more than one ligand (Humphries et al., 2006). Vice versa, some ligands can bind to multiple integrins as well (Humphries et al., 2006; Humphries, 1990; Plow et al., 2000; van der Flier and Sonnenberg, 2001). Interestingly, although integrins can share a set of ligands, they are non-redundant. This was shown by knockout experiments, in which each isoform knockout in mice resulted in severe phenotypes, ranging from early embryonic lethality to defects in angiogenesis, inflammation or leucocyte function (Hynes, 2002).

Inside the cell, integrins form the connection between the cytoskeleton and the ECM via linker proteins such as talin and kindlin (Hynes, 2002). Except for integrin β4, the cytoplasmic tails of all β subunits can interact with talin and kindlin by two recognition motifs, NPxY and NxxY (where 'x' stands for any amino acid) (Moser et al. (2009b). Talin is the major link between integrin and the actin cytoskeleton and recognizes the membrane-proximal NPxY motif of β integrins (Calderwood et al., 2002). After activation, talin binds to both integrin as well as actin and thus acts as a molecular

adaptor. The role of kindlin is still not well understood; however, after binding to the membrane-distal NxxY motif, it has been suggested to play a role in initial activation and clustering of integrins (Ye et al., 2013). The exact sequential order of these binding steps is still under investigation.

1.2.2 Structure and activation mechanism

Structural studies of integrin in the last two decades have provided deep insights into integrin function on a molecular level. A revolutionary step was the first crystal structure of the full ectodomain of αvβ3, published in 2001 (Xiong et al., 2001). It showed how the extracellular parts of the two subunits are arranged and contact each other with unprecedented clarity, which led to a new way of thinking about integrin function. In the following years, numerous structural studies followed, all revolving around the highly debated question: how are conformation and activity of integrin linked?

In this part, an overview about structural knowledge will be presented, followed by the description of the currently most accepted model of integrin's activation mechanism.

1.2.2.1 Domain organization

Integrin α and β subunits are comprised of three main parts: the N-terminal ectodomain, the transmembrane (TM) and the C-terminal cytoplasmic tail (CT) domains. The ectodomains themselves can be divided into headpiece and tailpiece or, alternatively, into head, upper leg and lower leg regions (Luo et al., 2007) (**Figure 3 A, B**).

Ectodomain

The α subunit's ectodomain consists of an N-terminal β-propeller, followed by thigh, genu, calf-1 and -2 domains (Luo et al., 2007) (**Figure 3 A, B**). 9 of the 18 α subunits are α inserted domain (αI)-containing integrins, as they consist of an additional domain which is responsible for ligand binding. This αI domain is inserted between blades 2 and 3 of the β-propeller of the α subunit (Shimaoka et al., 2002) (**Figure 3 A**) and adapts a so-

called Rossmann fold, which is characterized by repeating β strands and α helices (Luo et al., 2007).

The β subunit's ectodomain is comprised of 8 domains: the β inserted-like (βI) domain, which is homologous to the αI domain, is followed by a hybrid, a plexin-semaphorin-integrin (PSI), four integrin epidermal growth factor-like (EGF 1-4) and the β-tail domains (**Figure 3 A, B**). Interestingly, this arrangement of the domains is seen in the folded protein structure; however, in the amino acid sequence, the first three N-terminal domains are nested. The hybrid domain is inserted into the PSI domain, and the βI domain is inserted into the hybrid domain. Sequence-wise, the N-C terminal order of the first three domains is: PSI-part 1, hybrid part 1, βI domain, hybrid part 2, PSI part 2 (Luo et al., 2007) (**Figure 3 A, B**). Both α and β subunits range from 80-150 kDa in size and vary among isoforms.

Notably, integrin's structure and function depends on divalent metal ions, such as Ca^{2+} and Mg^{2+} (Zhang and Chen, 2012). Structurally, 3-4 Ca^{2+} ions contribute to the stability of the β-propeller by being coordinated by hairpin loops within the propeller blades (Luo et al., 2007; Xiong et al., 2001; Zhang and Chen, 2012). Another Ca^{2+} ion is present in the genu domain of the α subunit. The exact role of this metal binding site is unclear; however, it has been suggested to stabilize an extended conformation of integrin (Xiong et al., 2001; Zhang and Chen, 2012).

Functionally, both Ca^{2+} and Mg^{2+} ions are involved in ligand binding and conformational changes (Luo et al., 2007; Zhang and Chen, 2012). There are three metal ion binding sites in the βI domain, that are crucial for ligand binding: the metal ion-dependent adhesion site (MIDAS), the adjacent to MIDAS (ADMIDAS) and the synergistic metal ion-binding site (SyMBS) (Zhang and Chen, 2012) (**Figure 4**). The MIDAS has a coordinated Mg^{2+} ion that is directly involved in binding negatively charged ligand residues (described in more detail below). The MIDAS contains the common motif Asp-X-Ser-X-Ser (Xiong et al., 2001). Similarly, in αI-containing integrins, the αI domain contains a MIDAS which is used for ligand recognition instead of the MIDAS located in the βI domain. In the βI domain, two other metal ion binding sites flank the MIDAS. Next to the MIDAS sits the ADMIDAS, which binds to Ca^{2+} and has a negative regulatory effect on ligand binding (Chen et al., 2003; Mould et al., 2003). In contrast, the SyMBS also binds Ca^{2+} and has a positive effect on ligand binding (Chen et al., 2003; Mould et al., 2003; Zhu

et al., 2008). It should be noted, however, that the roles of the two flanking metal binding sites might differ among integrin types as mutations have different effects on the regulation of conformational states (Zhang and Chen, 2012).

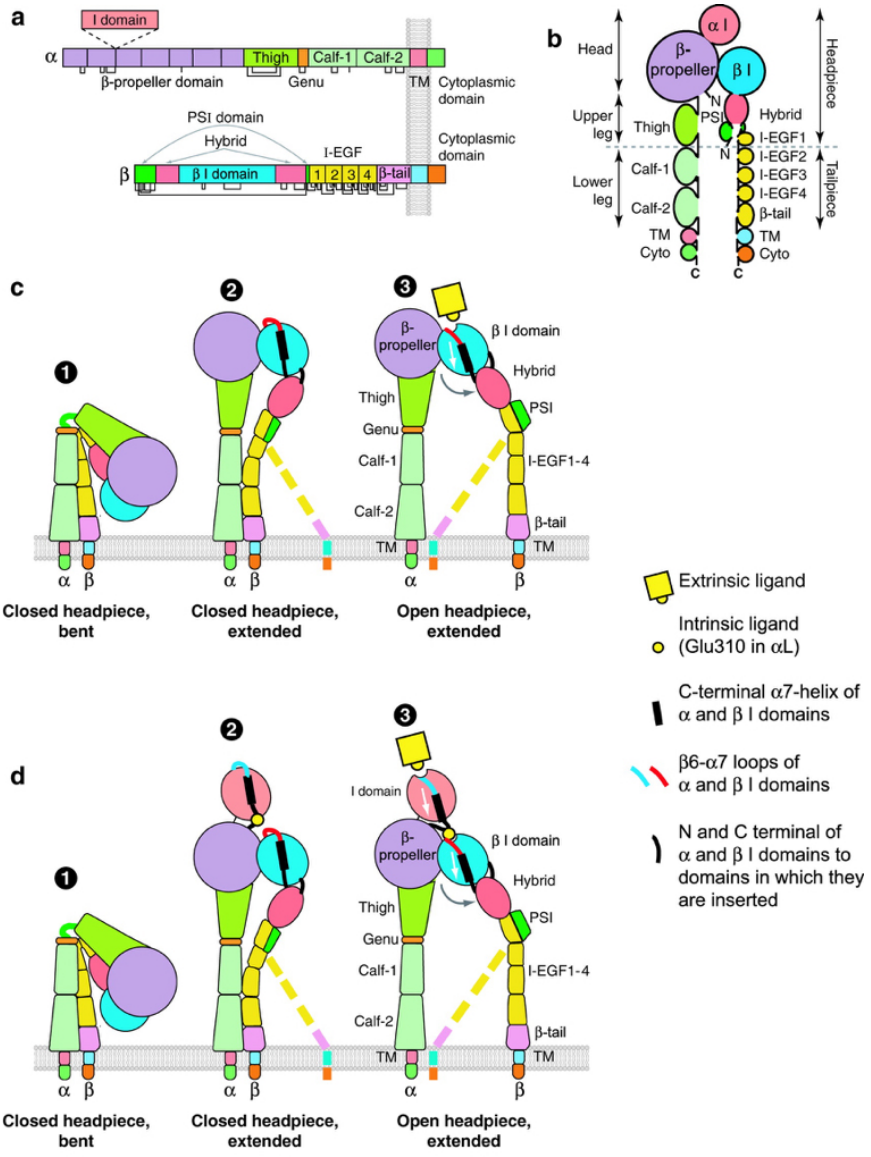

Figure 3: Integrin domain organization and conformational states.
A: Domain organization of integrin subunits α and β. Some integrin α subunits have an inserted αI domain (orange). The black lines indicate cysteines and disulfide bridges.
B: Peptide chain trace of integrin domains and nomenclature of extracellular domain parts, i.e. headpiece and tailpiece; or head, upper and lower legs are indicated.
C: Three activation states of αI-less integrins: (1.) bent, (2.) extended-closed and (3.) extended-open. Upon ligand binding, displacement of the α7 helix (black bar in state 2 and 3) leads to a swing-out of the hybrid domain, which results in headpiece opening.
D: Three activation states of αI-containing integrins: (1.) bent, (2.) extended-closed and (3.) extended-open. Upon ligand binding to the αI domain, the helix displacement of αI-α7 in αI is transferred to the βI domain, where displacement of the βI-α7 helix occurs (black bars in state 2 and 3). This results in a swing-out of the hybrid domain and subsequent headpiece opening.
[Figure adapted from (Luo et al., 2007)]

In *in vitro* studies, it was found that the use of Mn^{2+} activates integrin, which has been used to mimic inside-out activation (Takagi et al., 2002; Takagi et al., 2003). Most likely, Mn^{2+} replaces the Mg^{2+} ion in the MIDAS, and potentially the Ca^{2+} ions in the other metal ion binding sites (Valdramidou et al., 2008; Xiong et al., 2002; Zhu et al., 2013).

Since most of the data are based on *in vitro* observations, the role of divalent cations on integrin function *in vivo* is not entirely clear. There are some indications that cations could have an integrin-dependent effect on cell migration behavior during injury. While the concentration of Ca^{2+} and Mg^{2+} is roughly 1 mM in body fluids (Luo et al., 2007), it was found to be altered upon injury. Increased Mg^{2+} concentrations were found in wound fluids, thus possibly leading to increased migrations of cells (Grzesiak and Pierschbacher, 1995; Zhang and Chen, 2012).

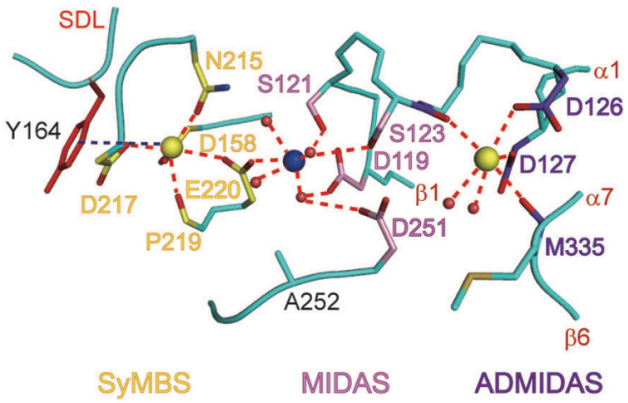

Figure 4: The three βI metal ion binding sites are directly or indirectly involved in ligand binding.
The MIDAS (middle, coordinating amino acids labelled in pink) coordinates Mg^{2+} which is directly binding to negatively charged ligand residues. It is flanked by SyMBS (left, coordinating amino acids labelled in yellow) and ADMIDAS (right, coordinating amino acids labelled in blue) which both bind Ca^{2+} and either positively or negatively regulate binding affinity, respectively. Amino acid residues numberings are according to β3.
[Figure adapted from (Zhang and Chen, 2012)]

Integrins bind to their respective ligands via their ectodomains. In integrins without αI domains, such as RGD-recognizing integrins, the binding pocket is located in a cleft between the β-propeller of the α subunit and the βI domain of the β subunit. The RGD motif, present on many proteins of the extracellular matrix, such as fibronectin or

fibrinogen, is bound by both subunits (Nagae et al., 2012; Xiao et al., 2004; Xiong et al., 2002). Arginine (R) of RGD is bound by 1-2 negatively charged residues of the α subunit (e.g. Q221 and D227 in α5). The aspartic acid (D) of the ligand is coordinated by the metal ion of the MIDAS within the βI subunit. For αI-containing integrins, ligand binding is achieved by the αI domain alone and conformational changes are transmitted to the interface between β-propeller and βI domain (Luo et al., 2007) (**Figure 3 C, D** and see below for detailed molecular mechanism).

Transmembrane and cytoplasmic tail domains

Both α and β subunit contain a single transmembrane (TM) helix. These TM segments comprise between 23 and 29 amino acids and have been, despite their small size, the focus of extensive studies in the recent years (Armulik et al., 1999; Lau et al., 2008a; Lau et al., 2009; Lau et al., 2008b; Stefansson et al., 2004; Ulmer, 2010) (**Figure 5**). It has to be noted that most studies have been performed using the TM segments of αIIb and β3, although major parts have been found to be conserved among isoforms. For αIIb integrin, 23 hydrophobic residues form a helix (I966-K989), followed by four hydrophobic residues which are still embedded into the lipid bilayer (Ulmer, 2010) (**Figure 5 A**). For β3, a longer helix is formed by 29 amino acids (I693-I721), which, interestingly, has been found to be tilted by ~25° inside the lipid bilayer (Lau et al., 2009; Lau et al., 2008b; Zhu et al., 2009). Together, they form a right-handed coiled-coil helix pair, in which the α-TM helix is oriented straight with regard to the lipid bilayer, while the β-TM helix is tilted (**Figure 5 B**).

The elaborate interaction between the two TM segments has been suggested to contribute to integrin stabilization as well as activation (Wegener and Campbell, 2008). By disulfide bond scanning analysis (Luo et al., 2004), mutational studies (Partridge et al., 2005) and nuclear magnetic resonance (NMR) studies (Lau et al., 2009), it has been shown that the interface between the two subunits is specific and consists of several modules. The N-terminal outer membrane clasp (OMC) is formed by alipathic amino acids and three glycines (G972(α), G976(α) and G708(β)). The inner membrane clasp (IMC) is comprised of F992(α), F993(α), L712(β), W715(β), K716(β), I719(β), R995(α), as part of a conserved GFFKR motif, and D723(β) (Ulmer, 2010) (**Figure 5 B**). Furthermore, it has been suggested that the tilt of the β-TM segment poses the positive lysine residue K716

close to the negatively charged phospholipid head groups. This residue, termed 'snorkeling' lysine, has been denoted as one of the main components stabilizing both the helix tilt as well as the interaction between the two segments, especially for αIIbβ3 integrin (Kim et al., 2011). However, in a study testing the effect of mutations of this lysine in different integrins, it has been observed that the mechanism derived from platelet integrin αIIbβ3 might not apply to all integrins (Lu et al., 2016).

The cytoplasmic tails (CT) of integrins are relatively short, ranging from 10-70 amino acids in length, except for the β4 tail, which contains ~1000 amino acids. Integrin CT domains were reported to interact via a salt bridge formed by R995(αIIb) and D723(β3), an extended part of the IMC that is outside of the lipid bilayer (Hughes et al., 1996; Ulmer, 2010). These two residues forming the salt bridge are conserved among integrins (Vinogradova et al., 2002) and their interaction was determined to be rather weak, with a measured K_d of roughly 7-50 μM for αIIbβ3 tails (Vallar et al., 1999). When the salt bridge is disrupted, either by mutations (Vinogradova et al., 2002) or by adaptor proteins such as talin head (Kim et al., 2003), integrins were found to be active. Generally, separation of the two CTs (as well as TM helices) is associated with integrin activation from the inside-out (Hughes et al., 1996; Kim et al., 2003; O'Toole et al., 1994; O'Toole et al., 1991). However, in an *in vivo* study, where the salt bridge of β1 integrins has been mutated in mice, no obvious differences in phenotype could be observed, reinforcing the notion that not all integrins might follow the same molecular mechanisms (Czuchra et al., 2006)

The CT domains are mostly disordered, but contain recognition motifs that are important for intracellular signaling pathways. Despite their small size, integrin CT domains are considered as 'interaction hubs' for proteins of the intracellular signaling network (Legate and Fassler, 2009; Wegener and Campbell, 2008). Especially the β CT domain is of major importance, as it contains several conserved recognition motifs, such as the HDRK, NPxY and NxxY motifs (Legate and Fassler, 2009) (**Figure 5 C**).

The first motif HDRK (HDRR for β1 and β5) is part of the recognition sequence for proteins such as focal adhesion kinase (FAK), paxillin and skelemin (Reddy et al., 1998; Schaller et al., 1995). The aspartate (D) in this motif is part of the salt bridge that forms between α and β CT and contributes to the stabilization of inactive integrin (Vinogradova et al., 2002). The second motif, the membrane-proximal NPxY motif, is part of the

recognition motif for phosphotyrosine binding (PTB)-containing proteins, such as talin and dok1 (Calderwood et al., 2002; Yamanashi and Baltimore, 1997). While some intracellular PTB-containing proteins bind to one specific integrin, some others can bind to multiple integrin tails (Calderwood et al., 2003). Talin is one of the most studied intracellular adaptor protein that links integrin to the actin cytoskeleton. It has been shown that binding of the talin head domain separates the CT and TM domains and thus activates integrins *in vitro* (Anthis et al., 2010; Anthis et al., 2009; Bouaouina et al., 2008; Calderwood et al., 2002; Garcia-Alvarez et al., 2003; Kim et al., 2012; Wegener et al., 2007; Ye et al., 2010). The exact function and activation mechanism of talin itself will be discussed in more detail below. The last motif, membrane-distal motif NxxY, can be bound by proteins such as integrin cytoplasmic domain-associated protein 1 (ICAP1), CD98 and kindlin (Legate and Fassler, 2009; Montanez et al., 2008; Moser et al., 2009a; Moser et al., 2009b; Moser et al., 2008; Ussar et al., 2008; Wegener and Campbell, 2008). Kindlin will be discussed in more detail below.

Since multiple proteins can bind to partially overlapping regions on the β integrin CT domains and likely compete with each other, it has been suggested that some kind of regulation exists (Legate and Fassler, 2009). Phosphorylation mechanisms could be employed to 'switch' between adaptor protein binding, as in the case of talin or dok1 (Oxley et al., 2008). Similarly, the roles of lipids in the recruitment of adaptor proteins have been discussed. Several adaptor proteins contain domains that are known for lipid binding (e.g. Ph domain in kindlin) (Legate and Fassler, 2009). In this regard, it has been observed that increased lipid synthesis can take place in FAs due to phosphatidylinositide phosphate kinase activity, which likely supports and regulates the recruitment of FA proteins (Di Paolo et al., 2002; Ling et al., 2002).

Although the β CT domain is considered as the main binding hub, some proteins also bind to the α CT domain. One example is paxillin which binds to the α4 CT segment (Liu et al., 1999).

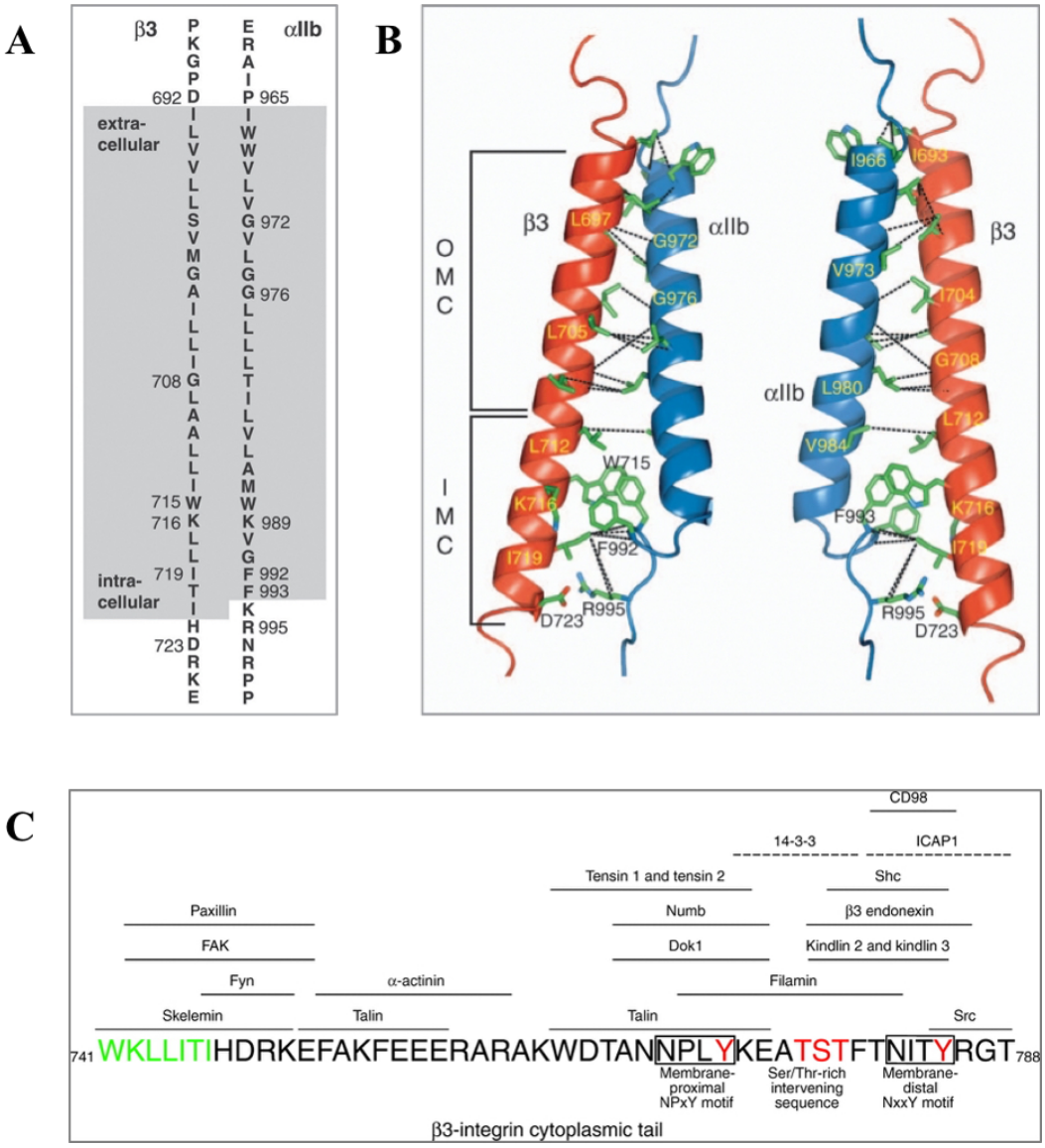

Figure 5: Transmembrane (TM) segments and cytoplasmic tail (CT) domains of integrin αIIbβ3.

A: The amino acid sequence of TM domains of αIIbβ3 is displayed. Residues embedded into the lipid bilayer are highlighted in grey.

B: The structure of the TM domains, as determined by NMR (2k9j), is shown. The residues involved in TM stabilization are depicted. OMC=outer membrane clasp, IMC=inner membrane clasp.

C: The sequence of β3 CT domain is shown, with indicated recognition motifs of different intracellular proteins.

[Figure A and B adapted from (Ulmer, 2010), Figure C adapted from (Legate and Fassler, 2009)]

1.2.2.2 Link between conformation and activation mechanism

Studies of the last two decades, employing various techniques, such as X-ray crystallography, electron microscopy, NMR as well as light microscopy approaches (Förster resonance energy transfer (FRET)/ fluorescence lifetime imaging microscopy (FLIM)) have revealed a link between integrin conformation and its ligand binding affinity (Kim et al., 2003; Takagi et al., 2002; Takagi et al., 2003; Xiao et al., 2004).

Integrins are thought to exist in three main conformations: bent, extended-closed and extended-open (Campbell and Humphries, 2011; Hynes, 2002; Luo et al., 2007) (**Figure 3 C, D**). In the bent state, the structure has a 'folded' appearance, where the head is in close proximity to the legs and the legs are closely contacting each other. In this conformation, integrin displays low ligand binding affinity (Luo et al., 2007). Upon activation, integrin extends and its N-terminal head is pushed about 200 Å away from the plasma membrane (Luo et al., 2007); however, the legs are still closely contacting each other (extended-closed). Further strengthening of ligand binding then leads to an opening of the headpiece and separation of the legs (extended-open). Ligand binding affinity of integrin α5β1 has been estimated to be ~5000 times higher after opening of the headpiece (Li et al., 2017b). It has been assumed that integrins are constantly shifting between the different conformational states, which can be described as a conformational equilibrium (Hynes, 2002; Luo et al., 2007). The equilibrium can be shifted to either side by different factors, e.g. by binding of intracellular activators or ligands (Luo et al., 2007) (**Figure 3 C, D)**.

Evidence for the ability of integrins to switch between conformational states that are closely related to their affinity has been accumulating during the last two decades. The first crystal structure of αvβ3 (Xiong et al., 2001) as well as αIIbβ3 (Zhu et al., 2008) or αXβ2 (Xie et al., 2010) revealed acutely bent structures in absence of ligand. Initially via negative-stain EM (Eng et al., 2011; Nishida et al., 2006; Su et al., 2016; Takagi et al., 2001; Takagi et al., 2002; Takagi et al., 2003) but also later on via X-ray crystallography (Xiao et al., 2004; Zhu et al., 2013), SAXS (Eng et al., 2011) and tomography (Iwasaki et al., 2005), active integrins have been investigated and their conformations analyzed. In most of these studies, the general conformational change with headpiece opening upon ligand binding has been clearly observed.

The molecular mechanism underlying these conformational changes has been thoroughly investigated. Initially, a lot has been learned from the truncated αI domains that have been expressed and crystallized (Luo et al., 2007). Later on, via structural studies, mostly by X-ray crystallography but also negative-stain EM, the detailed outside-in activation mechanism has been investigated for larger parts of ectodomains, especially with regard to αI-less and RGD-binding integrins, such as αIIbβ3 (Eng et al., 2011; Xiao et al., 2004; Zhu et al., 2008; Zhu et al., 2013). The following molecular activation mechanism has been proposed (Luo et al., 2007; Zhu et al., 2013) (**Figure 6**):

Upon RGD ligand binding, the arginine (R) is bound to the α subunit (residue D224 in αIIb; or Q221/D227 in α5) while the aspartate (D) is interacting with the MIDAS cation in the βI domain (Nagae et al., 2012; Xia and Springer, 2014; Xiao et al., 2004; Zhu et al., 2013) (**Figure 6 A, B**). Subsequently, rearrangements in the βI domain occur, while the α subunit stays relatively fixed. First, the amino acids coordinating the metal ion of MIDAS

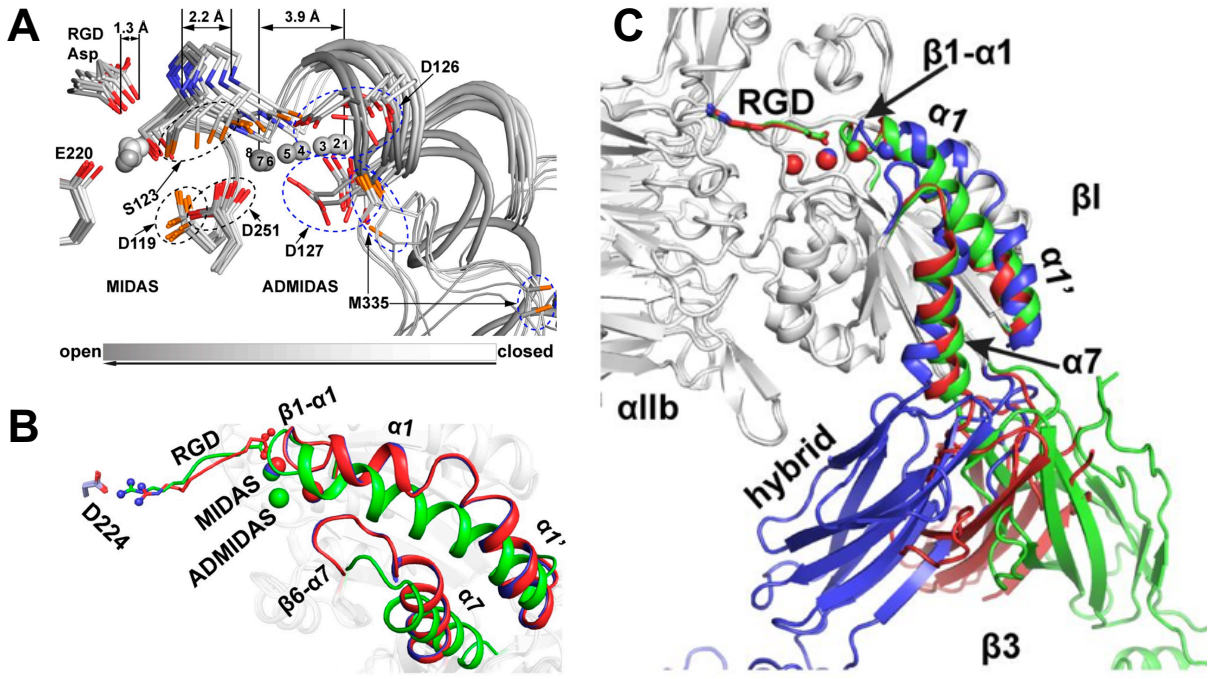

Figure 6: Molecular mechanism of αIIbβ3 headpiece opening can be explained by changes in the βI and hybrid domain upon ligand binding.
A: Close-up of changes in the MIDAS and ADMIDAS region upon ligand (RGD) binding, focusing on the amino acids in close proximity of the metal binding regions. Gradient from light to dark color indicates changes in 8 steps from closed to open conformation.
B: Close-up of βI domain changes upon ligand binding, with special regard to the helix displacements of α1 and α7. Red=closed/unbound state; green=open/ligand-bound state.
C: The structural changes in the βI domain upon RGD binding are translated into a swing-out motion of the hybrid domain. Blue: closed/unbound state; red: intermediate, green: open/ligand-bound state.
[Figure adapted from (Zhu et al., 2013)]

move ~2 Å toward the ligand, and thus closer to the α subunit (**Figure 6 A**). Through this movement, the backbone chain, which includes the α1 helix and ADMIDAS, is pulled closer to the α subunit as well (**Figure 6 B**). The ADMIDAS cation is coordinated by residues in the α1 helix (D126 and D127) and in the β6-α7 loop (M335). As the ADMIDAS is shifted by ~4 Å towards the binding site, the coordinating ADMIDAS residues in both α1 helix and β6-α7 loop are remodeled as a result (**Figure 6 A, B**). The following translocations of both α1 helix and β6-α7 loop then displace the α7 helix, which is further connected to the hybrid domain (**Figure 6 B, C**). As the α7 helix undergoes a piston-like downward movement, the hybrid domain swings out by ~60° (Takagi et al., 2002; Xiao et al., 2004; Zhu et al., 2008) (**Figure 6 C**).

In this opening mechanism, the hybrid domain seems to be the major translator of global conformations (Luo et al., 2007). Hybrid domain swing-out leads to headpiece opening, the extension of the whole integrin molecule and to separation of the legs by ~70 Å (Campbell and Humphries, 2011; Luo et al., 2007; Xiao et al., 2004) (**Figure 3 C, D**). This further results in TM and CT domain separation since the interaction between these domains is relatively weak (Kim et al., 2003; Lau et al., 2008a; Lau et al., 2009; Lau et al., 2008b; Luo et al., 2004). The described activation mechanism enables the step-wise transmission of the signal across the whole molecule, from N- to C-terminus.

Inside-out activation, i.e. the modulation of ligand binding affinity by intracellular protein binding, may follow a similar mechanism, in reverse order (Luo et al., 2007). Binding of intracellular components (such as talin or kindlin) would lead to the separation of CT and TM domains, followed by the separation of the lower legs, detachment of the headpiece and extension. This movement would aid the hybrid domain to swing out and shift the integrin equilibrium to the high affinity state (Luo et al., 2007). In a study by (Ye et al., 2010), it has been shown by negative-stain EM and biochemical assays, that integrin is active and extended upon binding of its intracellular activator talin *in vitro*.

For αI-containing integrins, the molecular activation mechanism follows a very similar process (**Figure 3 D**). However, the αI domain with its own MIDAS is the domain that directly contacts the ligand, such as collagen or intercellular adhesion molecules (ICAMs) (Luo et al., 2007). Upon binding, displacements of helices α1 and α7 occur in the αI domain, which are similar to the βI domain changes described above. Then, a glutamic acid (e.g. E310 in αL) is moved downward together with the α7 helix, and interacts with

the MIDAS cation in the βI domain, which triggers the subsequent molecular events described above.

Relevance of conformational change

The importance of a tight control on ligand binding affinity and the linked conformation is best displayed by integrins found on migrating cells, such as leucocytes (e.g. αXβ2) and platelets (αIIbβ3). Platelets need to be completely inactive until they are needed during injury. Thus, platelet integrin αIIbβ3 should undergo quickly a severe conformational change that renders it inactive (acutely bent form) or active (completely extended). Otherwise, severe bleeding disorder or thrombosis could occur (Hynes, 2002; Kato, 1997). Similarly, leucocytes might not be able to function properly in immune responses, if integrin function is impaired (Hynes, 2002; Rosenkranz and Mayadas, 1999). However, other integrin types, especially those involved in cellular adhesion and migration of basal cells, such as α5β1, might require different fine-tuning of their activity (Miyazaki et al., 2018).

Stabilization of bent state

It has been assumed that the bent, low affinity state of integrin is stabilized by several interfaces (Luo et al., 2007). Bent integrin seems to be stabilized by the contacts between TM and CT domains, e.g. by the salt bridge between the two helices (R995/D723 for αIIbβ3, see paragraph above). The importance of the interaction between the TM/CT domains for bent/inactive integrin has been shown by generating and studying a 'clasped' version of integrin, where TM/CT were exchanged to a coiled-coil ACID/BASE pair (clasp) (Takagi et al., 2001). Upon cleaving the clasp ('unclasping'), headpiece opening occurred and integrin bound more readily to ligands. In addition, there are several interfaces in the ectodomain which play a role in stabilizing the bent state; i.e. between the headpiece and the legs as well as in between the lower legs of the α and β subunits (Luo et al., 2007). However, by themselves, these interactions are most likely rather weak and integrin might easily be shifted to its active/extended conformation (Luo et al., 2007).

Do all integrins undergo conformational changes?

Interestingly, there is evidence that not all integrins function in a similar manner, i.e. that some integrins might not undergo the described changes from bent to extended-

open upon ligand binding (Arnaout et al., 2005; Campbell et al., 2020; Cormier et al., 2018; Miyazaki et al., 2018).

The concept that integrin's conformational changes are linked to its affinity, escpecially that active integrin functions in its extended state, has been termed the 'switchblade model' (Luo et al., 2007; Takagi et al., 2002). In some studies, it has also been proposed that integrin might function in its bent state only; a concept which has been summarized as the 'deadbolt model' (Adair et al., 2005; Arnaout et al., 2005; Xiong et al., 2009; Xiong et al., 2003; Xiong et al., 2002). However, it has been extensively debated whether these observations are due to artefacts of the individual experimental setups (e.g. buffer conditions) (Luo and Springer, 2006). Overall, a majority of negative-stain EM studies rather suggest that a conformational change takes place (Eng et al., 2011; Luo et al., 2007; Nishida et al., 2006; Su et al., 2016; Takagi et al., 2001; Takagi et al., 2002; Takagi et al., 2003).

Recently, however, newer studies have suggested that different integrin isoforms exhibit diverse activation behaviors. It has been observed that integrin αvβ8 is always extended and functions without the major changes between bent and extended conformations (Campbell et al., 2020; Cormier et al., 2018). Integrin αvβ8 is thought to 'search' for ligands by rotation of its headpiece in a 'sunflower-like' motion (Campbell et al., 2020; Cormier et al., 2018). Furthermore, an extensive negative-stain EM study showed that the extent to which integrins are bent in their low-affinity or in their primed state (after addition of Mn^{2+}) varies strongly between different isoforms (Miyazaki et al., 2018).

One possible explanation for the diverse behavior of integrins could be that the different parts on both subunits might contribute in opposite ways to maintaining the bent or open conformational state. It has been suggested that in αvβ8, the αv hinge (between thigh and calf-1 in αv) stabilizes its extended form, as determined by the cryo-EM structure of a recent study by (Campbell et al., 2020; Cormier et al., 2018). In another study, it has been observed that the β knee acts as an entropic spring, that readily leads to extension of integrin once the contact to α subunit is lost after hybrid domain swing-out (Smagghe et al., 2010).

Overall, all of these different observations are difficult to explain by only one activation model. Since several portions of both subunits could contribute in different ways to the bending or extension of integrin, and there are 24 different combinations, one

can easily imagine that the outcome of how bent or extended an integrin is might be unique. Furthermore, in a cellular context, additional factors are present that contribute to integrin conformation and function, such as mechanical force and integrin clustering.

Mechanical force and integrin activation

Integrins are the receptors at the center of FAs, which are complex cellular protein assemblies mediating adhesion to the ECM as well as migration of cells. They connect to the actin cytoskeleton and are thus exposed to mechanical force during adhesion maturation (Kuo et al., 2011; Wehrle-Haller, 2012) and rigidity sensing (Ross et al., 2013). This force is translated through several components, including integrins themselves, once they are engaged in binding to ligands and to intracellular components such as talin and actin. Several studies have shown that integrins are affected by force (Alon and Dustin, 2007; Astrof et al., 2006; Evans and Calderwood, 2007; Zhu et al., 2008). Pulling on integrins might stabilize their extended-open conformation and ligand binding affinity. This feature marks the integrin-ligand connection as a catch-bond, i.e. a bond that is strengthened by applied force (Kong et al., 2009). This has been observed via several techniques, such as pulling on cells via force probes (Chen et al., 2012), stretching of cells by a device that applies strain to the substrate they grow on (Katsumi et al., 2005) and atomic force microscopy to pull on single integrin-ligand bonds (Kong et al., 2009). The force that integrin-ECM bonds can withstand until the bond breaks has been measured to be relatively high, i.e. 50-100 pN (Roca-Cusachs et al., 2012). However, the catch-bond behavior has not been observed for all integrins. In a study comparing fibronectin-bound $\alpha5\beta1$ and $\alpha v\beta3$, it has been shown that $\alpha5\beta1$ has a much higher resistance to mechanical forces than $\alpha v\beta3$ (Roca-Cusachs et al., 2009).

Furthermore, molecular dynamics (MD) studies have suggested that pulling on the $\alpha1$ helix in βI results in hybrid domain swing-out (Puklin-Faucher et al., 2006). There is also indication derived from simulations where the integrin legs can be pulled apart by lateral force, which results in integrin activation and stabilization of ligand binding (Zhu et al., 2008). The force needed to maintain the open conformation of integrin was estimated to be around 1-3 pN *in vitro* (Li and Springer, 2017). In cells, similar forces of around 1-7 pN have been measured to affect a single integrin-ligand bond (Chang et al., 2016).

Interestingly, it has been observed that all bound αLβ2 integrins align in the direction of the actin flow, due to the FA adhesome which transmits force over the β subunit leg and then pulls the integrin legs apart (Nordenfelt et al., 2017).

Clustering of integrins on the membrane surface

Integrins have been visualized via light microscopy techniques to appear as clusters on the cell surfaces, where they act in concert to function properly and transiently fluctuate into and out of FAs (Iwamoto and Calderwood, 2015; Shibata et al., 2012; Shroff et al., 2007; Spiess et al., 2018). There is a strong link between integrin clustering and force transduction (Sun et al., 2019; Sun et al., 2016a). Via integrin clustering, more integrin molecules are concentrated at a single point and can divide the growing mechanical force among them (Moore et al., 2010). Furthermore, as integrins are continuously switching between conformational states, the probability of a single dissociated integrin to reattach to the ECM is greatly increased if it is still part of a cluster that is overall ECM-bound and interacting with intracellular proteins (Schoen et al., 2013; Sun et al., 2016a). Interestingly, there is also evidence that different types of integrins with diverse mechanical features can work together within the same adhesion; i.e. α5β1 integrins can form stronger bonds to fibronectin, while αvβ3 manages intracellular protein recruitment (Roca-Cusachs et al., 2009).

Although there have been some studies which reported homodimerization between TM domains of integrins by NMR (Li et al., 2001), these have been seen as controversial by the field and could be due to limitations of the experimental setup (Luo et al., 2007). Most likely, the clustering effect cannot be explained by structural studies of integrin alone, as the whole FA adhesome possibly contributes via complex multiprotein linkages. Clustering is likely achieved by intracellular proteins such as kindlin (Ye et al., 2013) and talin (Ellis et al., 2014), or possibly by the ECM network that contains several ligand binding sites. Interestingly, as some of these proteins have also been suggested to play a role in changing the conformational state of integrin, such as talin, it is likely that there is a connection between clustering and activation (Iwamoto and Calderwood, 2015). In addition, it has also been suggested that the glycocalyx, the cell's glycoprotein layer of 80 nm in length, is able to trap integrins and promote clustering (Paszek et al., 2009; Paszek et al., 2014).

Studies on full-length integrin

Most studies on the structure and activation mechanism of integrins have been performed using truncated integrins (e.g. ectodomains or TM/CT segments). To decipher the complete mechanism, studies on full-length are required. Indeed, there are some structural studies on full-length integrin, embedded in either nanodiscs (Choi et al., 2013; Dai et al., 2015; Xu et al., 2016; Ye et al., 2010), liposomes (Ye et al., 2010) or solubilized in detergent micelles (Adair and Yeager, 2002; Eng et al., 2011) by employing either negative-stain or cryo-electron microscopy (EM). However, so far, most of these studies has been focused on platelet integrin αIIbβ3. Furthermore, no high-resolution structural information of full-length integrin has been obtained yet.

In general, EM is a powerful tool for studying membrane proteins in a more physiological context, as it does not require protein crystallization. Especially in the recent years, with the help of new advances such as the development of direct detectors, it has become possible to gain high-resolution structural information on vitrified protein samples ('resolution revolution' (Kuhlbrandt, 2014)). This is potentially interesting for studying membrane proteins such as integrin.

1.2.2.3 N-glycosylation of integrin

Another interesting aspect of integrin function is its connection to post-translational modifications, in particular N-glycosylations. Many studies have revealed the importance of N-glycosylation for the proper biological function of integrin and how N-glycan patterns can be altered during tumorigenesis (Gu and Taniguchi, 2004). In α5β1, 14 potential N-glycosylation sites exist on α5, and 12 on β1 (Isaji et al., 2009; Isaji et al., 2006). Another layer of complexity is added by analyzing the types of oligosaccharides present on integrins: on α5β1 purified from human placenta, 35 different types have been found (Nakagawa et al., 1996).

How much integrins depend on N-glycosylation has been demonstrated in a number of studies. When purified integrin α5β1 was deglycosylated by PNGase-F, loss of binding activity to its ligand fibronectin and dissociation of the integrin subunits was observed (Zheng et al., 1994). Similarly, mutations of potential N-glycosylation sites in both subunits α5 and β1 led to decreased expression and cell spreading (Isaji et al., 2009; Isaji et al., 2006). Furthermore, alteration of N-glycosylation patterns of α5β1 have been

linked to decreased cellular adhesion *in vitro* (Akiyama et al., 1989) and of α3β1 to enhanced tumor development and metastasis (Pochec et al., 2003). Conversely, elevated levels of N-acetylglucosaminyltransferase V, a well-characterized and cancer-associated glycosyltransferase, resulted in increased cell migration (Guo et al., 2002; Nagae et al., 2018).

In summary, these observations underline the significance of N-glycosylation for integrin function.

1.2.3 Integrin α5β1

One of the most-studied integrins is the major fibronectin ('FN') receptor α5β1 which is ubiquitously expressed (Sechler et al., 1997).

FN itself is a key component of the ECM, present in blood as well as in connective tissues throughout the body. It is usually present as soluble dimer in blood or as fibrillary polymers as part of the ECM (Schwarzbauer and Sechler, 1999). Although the exact mechanism of polymerization is not completely understood so far, it seems to occur upon binding to activated integrin α5β1 on cell surfaces. The subsequent stretching, i.e. mechanical stress transmitted from the cytoskeleton, leads to conformational changes within FN resulting in exposure of sites which promote self-association (Johansson et al., 1997; Mao and Schwarzbauer, 2005; Schwarzbauer and Sechler, 1999; Sechler et al., 1996; Singh et al., 2010). A single FN molecule is about ~250 kDa in size and contains several, repetitive modules (Pankov and Yamada, 2002). The third module (FN III) contains the integrin RGD recognition motif in a flexible loop in domain FN10; as well as a so-called 'synergy site' on FN9 (Leahy et al., 1996). The single domains are relatively flexible in respect to each other, and their organization has been described as 'pearls-on-a-string' (Engel et al., 1981; Erickson et al., 1981; Mezzenga and Mitsi, 2019).

In addition to recognizing the common RGD motif, integrin α5β1 also interacts with a secondary interaction motif in FN, the synergy site (Mould et al., 1997; Nagae et al., 2012; Obara et al., 1988). While the RGD motif is engaged with both subunits through the binding pocket formed by α5 and β1, the synergy site only interacts with the α5 subunit (Mould et al., 1997). The synergy site is comprised of the 8 amino acid long sequence DRVPHSRN on FN9 (Aota et al., 1991; Redick et al., 2000). Mutational studies have determined the two arginines R1374 and R1379 within this sequence as key residues for

a stable α5β1-fibronectin interaction (Redick et al., 2000). The exact function of the synergy site has long been the focus of extensive studies. It has been proposed that, although the main interaction occurs via the RGD motif, the synergy site helps to guide the rather big FN molecule to align it properly with integrin. This would support a stable orientation and binding of the otherwise flexible RGD loop within the binding pocket of integrin (Main et al., 1992; Takagi et al., 2003). Kinetic analyses via surface plasmon resonance showed that mutations in the synergy site led to a decrease in both affinity as well as association rate, which suggests that the synergy site promotes the initial encounter between the two molecules FN and α5β1 (Takagi et al., 2003). Mutational and modelling studies have shown that the interaction between R1379 in the synergy site and D154 on α5 is crucial for the binding between FN and α5β1 (Nagae et al., 2012). Furthermore, the synergy site has been suggested to play a key role in force transduction, when the integrin-FN 'catch-bond' (Kong et al., 2009) is subjected to mechanical forces during cell adhesion. In a force measurement study via a spinning disc device, it has been found that synergy site mutations led to weaker FN-α5β1 bonds (Friedland et al., 2009; Garcia-Alvarez et al., 2003). Moreover, mutations in the synergy site resulted in decreased cell spreading (Aota et al., 1991) as well as bleeding defects in mice (Benito-Jardon et al., 2017), underlining the importance of this secondary interaction site for integrin binding to the ECM.

So far, only the structure of the α5β1 headpiece has been solved by X-ray crystallography (Nagae et al., 2012; Xia and Springer, 2014), and shows a similar subunit arrangement to previous structures of integrins αvβ3 and αIIbβ3 (Xiao et al., 2004; Xiong et al., 2001; Zhu et al., 2008). RGD-bound headpiece structures have also been crystallized and show how RGD is bound by residues Q221 and D227 in the α5 subunit as well as the MIDAS cation in the β1 subunit (Nagae et al., 2012; Xia and Springer, 2014). However, no headpiece opening upon hybrid domain swing-out has been observed in these structures, which could be attributed to the use of an inhibitory antibody SG/19 in the first study (Nagae et al., 2012) or general limitations due to crystal packing (Nagae et al., 2012; Xia and Springer, 2014). Nonetheless, extensive negative-stain EM studies on truncated ectodomain fragments have suggested that inactive α5β1 is bent and active α5β1 displays an open headpiece with hybrid domain swing-out (Miyazaki et al., 2018; Su et al., 2016; Takagi et al., 2003). The presence of bent and open integrin α5β1 has also been indicated by FRET studies, suggesting that integrin α5β1 undergoes similar conformational

changes in cells (Askari et al., 2010). However, as high-resolution structural information on whole integrin α5β1 in a more physiological surrounding and in context of a larger ligand is lacking, the exact mechanism of how the conformational change in integrin α5β1 is regulated remains to be elucidated.

1.2.4 Clinical relevance

Mutations in the FA adhesome correlate highly to human genetic diseases. In a study from 2014, it was shown that roughly 60% of the FA-associated proteins are linked to cardiovascular, musculoskeletal, hematopoietic, dermatological or developmental disorders, as well as cancerogenesis (Winograd-Katz et al., 2014).

Especially integrins are of high interest for pharmaceutical research regarding treatment of cancer, inflammation and fibrosis, due to their diverse roles in cell migration and adhesion. New approaches are developed constantly, partially by employing structural knowledge of integrins for design of antagonists and agonists (Zheng and Leftheris, 2020). Since integrins are cell surface receptors, clinical antibodies are a common approach to target integrins. Integrin antibodies can be divided into three groups: they either (1.) act as inhibitors, i.e. occupy the binding pocket without activating integrin, or (2.) as stimulators, i.e. recognize and lock integrins in their active state or (3.) are non-functional (Byron et al., 2009). Furthermore, small molecule inhibitors have been developed, such as peptides mimicking the RGD motif (Zheng and Leftheris, 2020).

In addition to its role in general processes related to cellular adhesion and migration, the α5β1 receptor is also relevant for angiogenesis (Schaffner et al., 2013). Knockout of β1 in mice resulted in pre-implantation lethality of embryos (Hynes, 2002) and knockout of α5 resulted in death at E10-11, defects in mesoderm and in vascular development as well as neural crest apoptosis (Goh et al., 1997; Taverna et al., 1998; Yang et al., 1993). The exact role of integrin α5β1 in cancer and its therapeutic relevance is still under investigation. Overexpression and upregulation of α5β1 seems to be a potential diagnostic marker for some solid tumors and is indicated to play a role in tumor neoangiogenesis (Schaffner et al., 2013). Integrin α5β1 has been the subject of extensive studies that connect it to malignant melanomas and liver-specific metastasis (Huang and Rofstad, 2018). A clinical antibody called Volociximab, that specifically binds to α5β1,

showed promising results in initial tests. However, its development was stopped during clinical trials due to lack of efficiency (Raab-Westphal et al., 2017). The small peptide ATN-161, a peptide mimicking the synergy site, has recently shown some promising results in clinical trials as it seems to decrease tumor angiogenesis (Huang and Rofstad, 2018).

Other integrins of therapeutic interest are αvβ6 and αvβ8 (Raab-Westphal et al., 2017). These integrins recognize TGF-β in its latent form and can activate it; the molecular mechanism of how this is achieved has been shown for αvβ8 by cryo-EM (Campbell et al., 2020). TGF-β is involved in signaling pathways that are broadly linked to immune functions and inflammation, and thus is connected to diseases such as cancer and fibrosis (Raab-Westphal et al., 2017). Antibodies targeting the binding site of integrins αvβ6 and αvβ8 could help to decrease the amounts of active TGF-β and thus lead to more specific TGF-β inhibition in therapeutic treatments.

Conclusively, the FA adhesome, with special regard to integrins, is a 'hot spot' for genetic disorders as well as cancer development and thus of great significance for drug research (Winograd-Katz et al., 2014). Elucidating the molecular mechanisms underlying FA formation, especially integrin function, has great potential in enabling the design of more specific and effective drugs. However, because of their roles in various cellular functions, such as adhesion, migration, platelet aggregation and leucocyte function, targeting integrins in the body remains tricky. The effect of inhibiting the function of a certain integrin might vary among patients, depending on the context of the disease and the individual patient (Raab-Westphal et al., 2017). This is most likely due to the fact that to this day, not all factors involved in integrin and FA function are completely understood. Thus, elucidating the roles of integrins in a larger context is necessary. Most likely, targeting one specific integrin is not sufficient to inhibit their function in disease; however, targeting multiple integrins might lead to toxicity. Therefore, fine-tuning seems to be of importance for drug design.

1.3 Intracellular focal adhesion adaptor proteins

Out of the over 200 proteins-containing integrin adhesome, only a variety of intracellular proteins are involved in the initial integrin activation and adhesion assembly steps. Two major FA components are talin and kindlin, which are both able to activate integrins by inside-out activation and further trigger FA assembly. They are 4.1-ezrin-radixin-moesin (FERM) domain-containing proteins and both bind to the CT domain of the β subunit of integrin. The CT domain contains two NxxY motifs: the membrane-proximal NPxY motif, which is recognized by talin, and the membrane-distal NxxY motif, which is recognized by kindlin (Moser et al., 2009b). Neither talin nor kindlin alone are thought to activate integrins by themselves, and are thus considered as co-dependent activators (Moser et al., 2009b). The binding mode, however, still remains to be elucidated (Calderwood et al., 2013; Moser et al., 2009b). It is unclear whether talin and kindlin interact directly on the same β-tail, which would be possible since they bind to different motifs. Other possibilities include that they bind sequentially to the same tail or simultaneously to different tails within the same adhesion. In the following chapter, current knowledge on talin and kindlin will be presented, as they are the major integrin activators and critical for adhesion assembly.

1.3.1 Talin

Talin is the one of the main integrin activators and, as the major link between integrins and the actin cytoskeleton, one of first proteins present in NAs (Bachir et al., 2014; Calderwood et al., 2013). Furthermore, it is important for mechanotransduction, as it is able to sense mechanical force and to transduce force to biochemical signals (Klapholz and Brown, 2017).

In mammals, two isoforms of talin exist: talin 1 and 2, which have 76% identical sequences and share overlapping functions (Gough and Goult, 2018). While talin 1 is abundantly expressed throughout the body, talin 2 is mostly expressed in heart, brain and kidney (Gough and Goult, 2018). The significance of this 270 kDa protein for proper cell adherence and function has been demonstrated by a plethora of studies. Double knockout mice of talin 1 display embryonic lethality (at E 8.5)(Monkley et al., 2000) or severe defects when targeted to specific tissues (summarized in (Calderwood et al., 2013)). On a

cellular level, depleted talin can lead to decreased integrin activation and impaired cell spreading (Nieswandt et al., 2007; Tadokoro et al., 2003; Zhang et al., 2008). For the most part, talin 1 can compensate for talin 2 knockout in mice. However, these mice still show mild defects, which hints at the fact that they might not be completely redundant (Debrand et al., 2012).

Talin consists of an N-terminal head and a C-terminal rod domain, which are connected by a long unstructured linker region (**Figure 7 A**). The head domain of talin is an atypical FERM domain, as next to FERM domains F1, F2 and F3, it possesses an additional F0 domain. The head domain has been suggested to adopt an elongated form (Elliott et al., 2010). The rod domain is comprised of 62 α helices arranged into 13 helical bundles (R1-R13), consisting of 4-5 helices per bundle. A dimerization domain (DD) is located at the C-terminus (Calderwood et al., 2013; Gingras et al., 2008), which, in combination with some early EM studies, has suggested that talin might undergo homodimerization (Goult et al., 2013).

As it is present in most integrin-based adhesions and crucial for inside-out activation of integrin, talin has been denoted the 'core' (Gough and Goult, 2018) or 'master' of FAs (Klapholz and Brown, 2017). The F3 domain of the talin head domain binds to NPxY on the integrin β CT and thus inhibits the salt bridge interaction between the CT domains of the α and β subunits (Anthis et al., 2009; Calderwood et al., 2002; Calderwood et al., 1999; Garcia-Alvarez et al., 2003; Tadokoro et al., 2003; Vinogradova et al., 2002; Wegener et al., 2007). By separating the two CT domains, integrin is activated and adopts its extended-open conformation with increased ligand binding activity (Ye et al., 2010).

The role of talin for integrin activation has been studied for many years. Although it has been found in *in vitro* studies that purified talin head is sufficient to activate integrin αIIbβ3 embedded in nanodiscs (Ye et al., 2010), there is also evidence that in a cellular context, other proteins such as kindlin are needed for cooperation (Moser et al., 2009b). Talin also contains a secondary integrin binding site in its rod domain (**Figure 7 A**); however, its relevance and specific function are still not fully understood (Klapholz and Brown, 2017).

Since talin is significant for many cellular processes regarding FAs, as it links integrins to the actin cytoskeleton, several control and recruitment mechanisms tightly regulate its activation. Talin can be switched on and off by undergoing conformational changes. It has been observed by early EM studies that talin can exist in both globular and

extended conformations (Winkler et al., 1997). Biochemical and structural analyses have suggested an autoinhibited state of talin, in which several interfaces within the compact molecule are shielded from interaction with other FA proteins (Klapholz and Brown, 2017). Mainly the interaction between F3 and R9 is of importance, as it protects the main integrin binding site 1 (IBS1) in the talin head domain (**Figure 7 A**).

It was suggested by different studies that phosphatidylinositol 4,5-biphosphate (PIP_2) helps to resolve the autoinhibiting interaction between F3-R9 and thus might open up the molecule (Anthis et al., 2009; Goksoy et al., 2008; Goult et al., 2009; Song et al., 2012). Analysis of the talin head structure shows many basic patches on the surface, which could facilitate orientation to the plasma membrane as well as binding to the integrin β CT (Elliott et al., 2010).

Upon opening of the molecule, talin connects to the actin cytoskeleton. As it contains three actin binding sites (ABS1-3), located in both head and rod domains (Calderwood et al., 2013) (**Figure 7 A**), the exact sequential steps of actin binding have been unclear for some time. A recent study has found that ABS3 might be the initial connection point to the actin cytoskeleton (Atherton et al., 2015). Upon binding to integrin and actin, talin extends to a 60-100 nm long fibrous strand (Liu et al., 2015; Molony et al., 1987; Winkler et al., 1997). This elongation enables talin to span the distance between integrins and actin fibers (Kanchanawong et al., 2010) and to act as a cytoskeletal linker and mechanosensor (Klapholz and Brown, 2017).

Upon actin polymerization and myosin contraction, force is generated which adds another layer of control. On average, force in the range of ~7-10 pN can be transduced along one talin molecule, which has been measured via specific calibrated FRET-based biosensors (Austen et al., 2015). This leads to further stretching of extended talin and the exposure of up to 11 cryptic binding sites for vinculin. Vinculin binding then results in further actin crosslinking and talin stabilization (del Rio et al., 2009; Gingras et al., 2005).

Post-translational mechanisms can control talin function as well. The phosphorylation of the tyrosine in the NxPY motif by the Src family kinase has been shown to switch off talin binding to integrin (Anthis et al., 2009; Oxley et al., 2008).

Other proteins involved in talin regulation are Rap1-GTP-interacting adaptor molecule (RIAM), which helps in recruiting talin to the membrane, where it is displaced by vinculin (Goult et al., 2013; Lee et al., 2013); talin-activator Kank (Sun et al., 2016b), filamin (Calderwood et al., 2001), integrin cytoplasmic domain-associated protein 1

(ICAP1) (Chang et al., 2002) and α-actinin (Roca-Cusachs et al., 2013).

Furthermore, the protease calpain 2 mediates FA turnover by cleaving two sites in talin, thus inactivating it (Bate et al., 2012; Franco et al., 2004) (**Figure 7 B**).

Due to its function as a linker between integrins and actin in FAs, talin is a flexible protein. Initially, several structures of truncated domain fragments have been solved by NMR or X-ray crystallography (reviewed in (Calderwood et al., 2013)). For a long time, a structural model of full-length talin has been hypothesized based on these individual domain structures (**Figure 7 B**). In our recent study, we have determined the structure of full-length talin 1 by employing cryo-EM (Dedden et al., 2019). This structure depicts how the rod domains are arranged in autoinhibited talin, which shows a compact conformation in which most major interaction sites (e.g. for vinculin and integrin) are shielded by the entangled architecture of talin itself. The full-length structure confirms interactions predicted by NMR and X-ray crystallography studies of truncated domains, but also reveals new interactions, such as an interaction between the FERM domain and R12, that shields the basic residues of the F2/F3 domains. Interestingly, although it has been hypothesized for years that homodimerization through the C-terminal DD domain is necessary for talin's autoinhibition (Gingras et al., 2008; Goult et al., 2013), our structure and biochemical data suggest that talin behaves mostly as a monomer (Dedden et al., 2019).

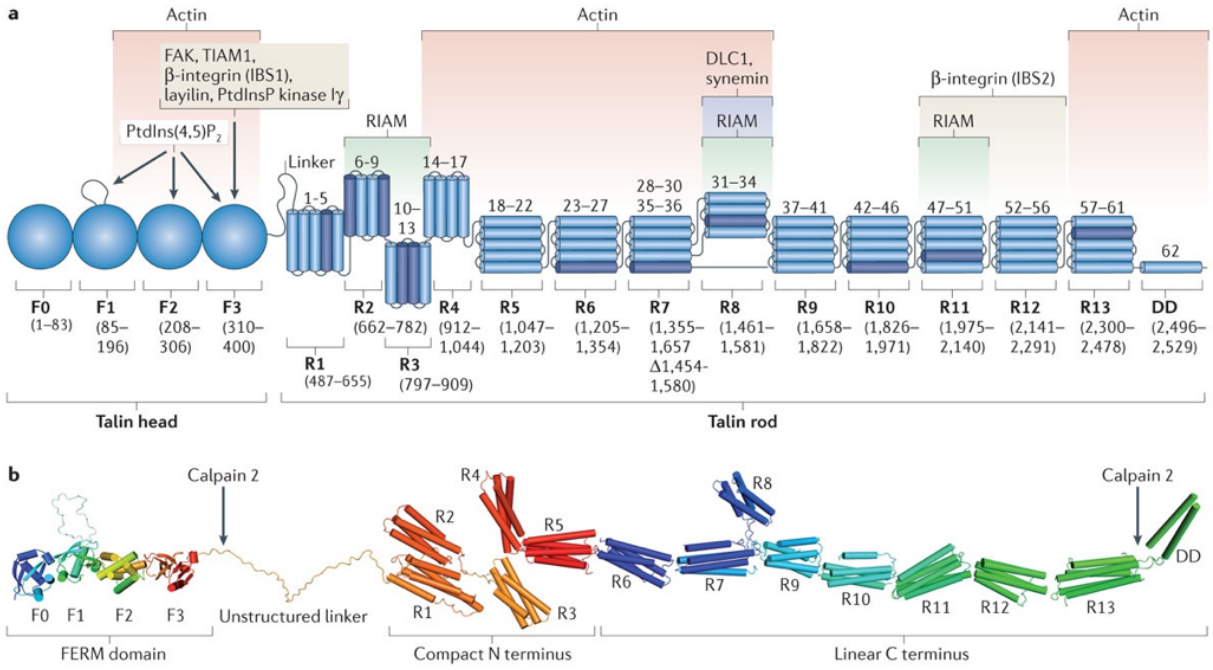

Figure 7: Talin 1 domain organization
A: Talin domain organization, showing the head and rod domains. The head is a FERM domain and contains the main integrin binding site 1 (IBS1). It also binds to negatively charged PIP_2. The rod domain consists of 13 helical bundles (R1-R13) and a dimerization domain (DD). Between head and rod is a long, unstructured linker region. Binding sites for diverse protein interactions are indicated, e.g. two integrin, 11 potential vinculin (dark blue helices) and three actin binding sites.
B: Hypothetical structural model of talin, combining the previously known NMR and crystal structures of single domains and helical bundles. Calpain 2 cleavage sites are indicated.
[Figure adapted from (Calderwood et al., 2013)]

1.3.2 Kindlin

The second major integrin activator is kindlin, another atypical FERM domain containing protein. It is ~75 kDa in size and resembles talin head, as it consists of F0-F3 domains; but also has an additional inserted pleckstrin homology domain with affinity for PIP_2 (Moser et al., 2009b; Qu et al., 2011). In mammals, three isoforms exist: kindlin 1, 2 and 3, which exhibit varying expression patterns. Kindlin 1 is mainly expressed in epithelial cells, kindlin 3 in hematopoietic cells while kindlin 2 is expressed ubiquitously, except for hematopoietic cells (Moser et al., 2009b; Rognoni et al., 2016). Consistent with these expression profiles, knockout experiments in mice have shown that kindlin 1 deletion leads to severe defects in epithelial tissues, such as skin blistering (Ussar et al., 2008); kindlin 2 deletion leads to embryonic death (Montanez et al., 2008) and deletion of kindlin 3 leads to severe bleeding disorders (Moser et al., 2008). On a cellular level,

kindlin depletion leads to impaired inside-out integrin activation, FA formation and cell spreading, even when talin is present (Ma et al., 2008; Montanez et al., 2008; Moser et al., 2008; Ussar et al., 2008). Furthermore, it has been shown that kindlin is present very early in NA formation (Bachir et al., 2014).

Kindlins bind to the membrane-distal NxxY motif of integrin β CT domains (Moser et al., 2009b). A crystal structure of kindlin 2 in complex with integrin β1 CT also revealed that an additional binding motif on the β tail, TTV, is necessary for binding and proper recruitment of kindlin to FA in cells (Li et al., 2017a).

Studies have generally shown that a cooperation of talins and kindlin takes place and that both components are needed to fully activate integrins during the course of inside-out integrin activation (reviewed in (Calderwood et al., 2013; Moser et al., 2009b)). The details of how this is achieved specifically, however, are still poorly understood. Some studies indicate that instead of breaking the interaction of integrin α and β CT domains like talin (Bledzka et al., 2012), kindlin might be necessary to cluster integrins; and that clustering is necessary for the full activation of integrins on cellular surfaces (Ye et al., 2013). This notion is supported by a recent crystal structure of kindlin 2, which indicates its ability to homodimerize (Li et al., 2017a). Furthermore, in a cellular context, proteins such as kindlin might help to outcompete other integrin β CT binding proteins such as filamin or ICAP1 and thus counter their inhibitory effect (Calderwood et al., 2013).

Kindlin also very likely plays a role in transducing signaling cascades within FAs. It has been shown to interact with both migfilin and integrin-linked kinase (ILK) (Fukuda et al., 2014). In addition, ILK was shown to form a complex with particularly interesting new cysteine-histidine-rich protein (PINCH) and parvin, forming the so-called ILK-PINCH-parvin ('IPP') complex. The IPP complex helps to connect integrin further to the actin cytoskeleton (Mackinnon et al., 2002; Tu et al., 2003). Kindlin can also recruit several other FA proteins such as actin-related proteins 2/3 (Arp2/3) to FAs (Bottcher et al., 2017) and thus act as a signaling hub for actin cytoskeleton-linked proteins (Sun et al., 2019). Furthermore, it can also interact with paxillin, which binds to FAK and triggers signaling pathways including Rho and Src signaling that ultimately affect cell fate (Huveneers and Danen, 2009; Theodosiou et al., 2016).

Taken together, all these findings underline the importance the intracellular adaptor proteins talin and kindlin have for integrin activation in a cellular context and for FA function in general.

2. Thesis objective

The objective of the presented cumulative study is to characterize the focal adhesion proteins integrin α5β1 as well as the intracellular integrin activator talin 1 using structural and biochemical methods.

Integrin α5β1 is the major fibronectin binding receptor in the human body and relevant for basic cellular processes such as adhesion, migration and development.

Although the activation mechanism of integrins has been studied extensively in the last decades, the molecular properties of all 24 integrins have been deduced and extrapolated mostly from studying a few specific integrins, i.e. αIIbβ3 and αvβ3. Thus, the exact mechanism of how integrin α5β1 and fibronectin interact with each other has not been fully understood yet. This study addresses the question of how integrin α5β1 is activated and how headpiece opening is achieved in molecular detail. To accomplish this, physiological integrin α5β1 from human placenta is studied and cryo-EM employed to analyze two conformational states: the inactive, resting as well as the active, fibronectin-bound conformations. The presented manuscript addresses the newly gained insights; in particular, how exactly the interface between fibronectin and α5β1 looks like, and whether additional interactions are present next to RGD and synergy sites. In addition, the role of physiological N-glycosylation patterns and how they contribute to integrin function is also analyzed. Furthermore, the inactive state of integrin, which revealed a novel half-bent conformation that differs from other integrins is discussed. The findings presented in this study might help to elucidate the functional mechanism of integrin α5β1.

In the second part of this cumulative thesis, I contributed to the structural and biochemical characterization of the integrin activator talin 1. In this study, talin 1 was purified and subjected to biochemical studies as well as structural analysis by cryo-EM. The findings shed light on how autoinhibition is achieved in full-length talin 1. Mainly, it is analyzed how the integrin, membrane-binding, actin and vinculin binding sites are shielded in the entangled structural organization. The results suggest how talin is kept inactive until it is needed and may contribute to a better understanding of the spatiotemporal order of how adhesion assembly is regulated.

3. Results

3.1 Structural insights into the integrin α5β1 crosstalk with fibronectin ligand

Authors:

Stephanie Schumacher, Dirk Dedden, Kyoko Matoba, Junichi Takagi, Christian Biertümpfel, Naoko Mizuno

(Manuscript submitted)

In this work, the molecular mechanism of integrin α5β1 activation upon fibronectin binding is characterized. The interface between fibronectin and integrin α5β1 revealed, next to the well-known interaction motif RGD and the synergy site, additional residues of fibronectin that are interacting with the ADMIDAS of integrin. In addition, the role of N-glycosylation in integrin activation is elucidated. Interestingly, the inactive conformation of integrin α5β1 shows a novel, incompletely bent arrangement, which has not been observed previously for other integrins. Overall, this study provides new insights into integrin α5β1 function and shows that α5β1 adopted an activation mechanisms that is different from other well-studied integrins such as αIIbβ3 or αvβ3.

The study was conducted under the supervision of Naoko Mizuno at the Max Planck Institute of Biochemistry in Martinsried, Germany. I performed purification of integrin α5β1 and biochemical assays, including insertion of integrin into nanodiscs, analytical size exclusion experiments and solid-phase equilibrium assays. Furthermore, I performed negative-stain as well as cryo-EM sample preparation, data acquisition and analysis.

Structural insights into the integrin α5β1 crosstalk with fibronectin ligand

Authors: Stephanie Schumacher[1], Dirk Dedden[1], Kyoko Matoba[2], Junichi Takagi[2]*, Christian Biertümpfel[3]*, Naoko Mizuno[1,3,4*#]

Affiliations:

1 Department of Structural Cell Biology, Max Planck Institute of Biochemistry, Am Klopferspitz 18, D-82152 Martinsried, Germany

2 Osaka University Institute for Protein Research, Osaka University, 3-2 Yamadaoka, Suita, Osaka 565-0871, Japan.

3 Laboratory of Structural Cell Biology, National Heart, Lung, and Blood Institute, National Institutes of Health, 50 South Dr. Bethesda, MD, 20814, USA

4 National Institute of Arthritis and Musculoskeletal and Skin Diseases, National Institutes of Health, 50 South Dr. Bethesda, MD, 20814, USA

*Correspondence

#lead contact: naoko.mizuno@nih.gov

Summary

Integrin α5β1 is a major fibronectin receptor critical for cell migration. Upon complex formation, fibronectin and α5β1 undergoes a compelling conformational change for their engagement. Here, we report cryo-EM structures of native human integrin α5β1 in its open conformation with fibronectin and TS2/16 antibody to 3.1Å, and in its resting state to 4.6Å resolution. The α5β1-fibronectin revealed synergistic interactions at the RGD loop, the synergy site and juxta-RGD, proximal to the integrin metal ion binding site ADMIDAS. In its resting state, α5β1 employs a half-closed conformation, challenging the traditional model of bent/open conformations tightly coupled to ligand affinity. Our biochemical and structural analyses revealed that Mn^{2+} increases the affinity of α5β1 for fibronectin while still in its half-bent conformation and only as a result of ligand-binding, the large opening is stabilized. Our study demonstrates a novel mechanism of integrin conformational change, showing integrins use a variety of regulatory modes.

Introduction

Integrin α5β1 is the primary fibronectin (FN) receptor (Sechler et al., 1997), responsible for cell migration and adhesion. Integrin α5β1-FN interactions are of particular interest as both proteins are ubiquitously expressed in various cell and tissue types to maintain the communication between cells and extracellular matrix (ECM). Furthermore, α5β1 represents an integrin prototype that is fundamental to cellular processes, yet its crosstalk with FN, the major component of the extracellular matrix (ECM), is not well understood.

Serving as a direct bidirectional link between the cell and its environment, integrin α5β1 functions as control hub for the intracellular focal adhesion machinery consisting of hundreds of signaling and mechano-sensing factors, transmitting extracellular signals to downstream players, including the actin cytoskeleton (Hynes, 2002; Kechagia et al., 2019; Zaidel-Bar et al., 2007). The resulting remodeling and changes in the dynamic behavior of the actin cytoskeleton direct cell shape formation and cell motility, hence dictating cell fate (Hynes, 2002). Integrin α5β1 connects to the ligand FN, a major component of the ECM, through its extracellular domains and to the actin cytoskeleton through its cytoplasmic tail domain (Campbell and Humphries, 2011). Failure of integrin function and corresponding impairment of the focal adhesion machinery is related to numerous diseases (Winograd-Katz et al., 2014), including aggressive cancer formation due to uncoordinated migration. Integrin α5β1 is particularly related to cancer metastasis, reflected by its upregulation in invasive cancer cells (Huang and Rofstad, 2018; Schaffner et al., 2013).

FN, the binding partner of integrin α5β1, is a fibrous dimer acting as a core component of the meshwork formation of the ECM. FN comprises repetitive modules of type I, II, and III domains, which show a 'beads on a string' morphology (Engel et al., 1981; Erickson et al., 1981). FN is recognized by the N-terminal large extracellular domain of integrin α5β1, termed ectodomain, via the common integrin ligand motif 'Arginine-Glycine-Aspartate' (RGD) in the FN10 domain. During cell movement, as bound integrin is exposed to mechanical force, it grips FN through its so-called synergy site with a sequence of DRVPHSRN in FN9 domain (Leahy et al., 1996; Wierzbicka-Patynowski and Schwarzbauer, 2003) and anchors cells with unknown mechanism. How FN engages integrin α5β1 and activates cells remains enigmatic.

Despite being a major class of integrin, interestingly, α5β1 has been proposed not to follow the classical integrin open-close paradigm, which has been derived mostly from αIIbβ3 and αvβ3 integrins (Eng et al., 2011; Luo et al., 2007; Takagi et al., 2002; Xiao et al., 2004; Zhu et al., 2008; 2013). In this classical β3-based model, integrins on resting cells exhibit an acutely bent conformation, in which the heads of the ectodomains point towards the plasma membrane and the legs and transmembrane domains of α- and β-subunits are in close contact with each other (Campbell and Humphries, 2011; Eng et al., 2011; Takagi et al., 2002; Xie et al., 2010; Xiong et al., 2001; Zhu et al., 2008). In this unprimed state, integrins show low affinity for their ligands with their heads occluding access to the ligand binding stie by facing to the plasma membrane (Campbell and Humphries, 2011; Luo et al., 2007). In the presence of Mn^{2+}, mimicking intracellular signals, classical integrins become 'primed', and show an increased affinity for their ligands (Campbell and Humphries, 2011; Takagi et al., 2002; 2003). The upright conformation releases the ligand-binding integrin heads from the steric hindrance and therefore renders them more potent to capture ligands. Structural studies of the integrin headpieces indicated that the binding of the RGD peptide to the groove at the tip of the integrin heads (Xiao et al., 2004; Xiong et al., 2002; Zhu et al., 2013) translates conformational changes from the metal-ion-dependent adhesion site (MIDAS) to the allosteric swing-out motion of the β hybrid domain (Luo et al., 2007), leading to the opening of the legs. However, this mode of action does not apply to integrin α5β1. Majority of truncated integrin α5β1 does not undergo the large conformational change in the presence of RGD peptide alone (Takagi et al., 2003); moreover, negative-stain EM observations of its resting state hinted at incomplete bending of the α5β1 ectodomain (Miyazaki et al., 2018), which challenges the view that bending secures the inhibition of ligand attachments. These observations raised the question whether integrin α5β1 employs a unique mechanism with only weak coupling between its global conformational change and its ligand binding affinity. Considering its critical biological roles in cell attachment and metastatic detachment, it is imperative to uncover how the activation of α5β1 differs from the canonical model, and how FN crosstalks with α5β1.

Here, we report the cryo-EM structures of native human integrin α5β1 purified from human placenta in 1) its fully extended open conformation in complex with FN and the stabilizing antibody TS2/16 and 2) in its resting state employing only a half-bent conformation. Using non-recombinant full-length native integrin ensures the

physiological relevance of the novel half-bent structure. The complex of integrin α5β1 with FN7-10 revealed three interacting sites critical for their functions including the stabilization of integrin opening and the cell-tissue tethering, namely, (1) at the RGD of FN10, (2) at the adjacent to metal-ion-dependent adhesion site (ADMIDAS) of the integrin β1 βI domain, and (3) at the synergy site of FN9; all of which were aligned in a single plane. The dual binding of FN9 and FN10 synchronously oriented FN10 to stabilize the large opening of α5β1. Particularly, key interactions centered at R1445 and Y1446 of FN and the ADMIDAS of β1 βI domain secures the integrin opening by pulling α1 helix of the βI domain closer to FN. In the resting state, integrin α5β1 employed a unique, incomplete bent conformation. In this state, the engagement of the FN to integrin is more challenging as the FN binding surface on integrin head was no longer aligned in a single plane; however interestingly, the incomplete bending would not occlude the integrin head from FN. Indeed, side-by-side structural and biochemical comparison indicated that integrin α5β1 changes its affinity for FN while still in its half-bent conformation and the integrin opening is only the result of the FN binding, instead of the FN binding as the consequence of the integrin opening. Our study thus reveals a mechanism of integrin recognition by FN, and demonstrates that integrins have a wide variety of regulating mechanisms.

Results

Ligand-bound native integrin α5β1 displays an extended conformation

To gain mechanistic insights into the regulation of integrin α5β1 on a molecular level, full-length native integrin α5β1 (Fig. 1 and S1A) was purified from human placenta (Pytela et al., 1987) and embedded into membrane-scaffolding nanodiscs (Fig. S1B and S1C) (Denisov et al., 2004). To understand the integrin opening and ligand engagement, we determined the structure of integrin α5β1 in complex with its ligand FN fragment III containing domains 7-10 (FN7-10) in the presence of $MnCl_2$ (Fig. 1A and 1C, Fig. S2 and S3) and the stabilizing antibody fragment TS2/16 Fv-clasp (Arimori et al., 2017) by cryo-electron microscopy (cryo-EM) at an overall resolution of 3.5 Å, with the head resolved up to 3.1 Å (Fig. S2 and S3). Although the C-terminal portion including the lower legs, the transmembrane helices, and the cytoplasmic tails was not visible from the cryo-EM map due to its flexibility, the corresponding negative-staining analysis showed the full integrin complex embedded into the nanodiscs (Fig. S1C) in an overall arrangement similar to that observed in negative-stain EM images of the recombinant ectodomain fragment of unliganded α5β1 (Miyazaki et al., 2018). These results assured a successful reconstitution of native integrin into the membrane scaffold.

The structure revealed an arrangement of the integrin, where the globular head domains of α and β subunits were in close contact with each other (Fig. 1A and 1C). FN formed a dual contact with FN9 contacting the α5 head and FN10 contacting both the α5 head and the β1 head. The α5β1 domains were in a wide open, extended conformation, with the upper legs about 95 Å apart from each other (Fig. 1A and C). That opening of the headpiece largely agrees with the arrangement seen in the crystal structures of truncated headpieces of other integrin isoforms, namely αIIbβ3 in complex with the ligand-mimetic compounds (Springer et al., 2008; Xiao et al., 2004). The integrin βI domain contains three functional metal ion pockets exhibiting clear densities, namely, MIDAS, ADMIDAS and the synergistic metal ion-binding site SyMBS (Fig. 1D). Consistent with previous assignments (Zhu et al., 2013), we assigned the densities as Mn^{2+} ions, which were used in excess during sample preparation. The structures of the integrin heads, the bound FN9-10, and TS2/16 were well resolved, reaching a resolution of 3.1 Å, however, the leg portions and FN7-8 resolved at 4-7 Å (Fig. S2C), indicating the higher flexibility of the lower legs, the downstream domains and the parts of FN distant from the integrin heads.

Integrin was purified from a natural source, allowing us to evaluate the physiological relevance of post-translational modifications, particularly glycosylation (Fig. 2). The identified N-glycosylation sites (Fig. 2A) validated the previous structural visualizations of recombinantly prepared samples (Nagae et al., 2012; Xia and Springer, 2014), and agreed well with previous biophysical analyses (α: (Isaji et al., 2006) , β: (Isaji et al., 2009)). Of the 14 and 12 predicted potential N-glycosylation sites in the α- and β-subunits, 6 and 4 were found in our cryo-EM density map, respectively (Fig. 2A). Interestingly, the glycan attached to N275 (in the α5 head) reached out to the interface between FN9 and FN10 (Fig. 2B and 2C). The glycan was surrounded by a positively charged surface and sandwiched between residues R220 and Y226 of integrin α5, which contacted a mannose and an N-acetylglucosamine moiety, respectively. S223 (α5) further restricted the flexibility of the glycan chain (Fig. 2B). Integrin αv also contains an N-glycan at the corresponding location (N266 of the αv head) (Fig. 2D), however, the previously reported structure showed a different FN contact surface ((Xiong et al., 2009)). The αvβ3-FN10 structure lacks FN9, and therefore the recognition of the glycan by FN was likely not fully engaged. Our structure offers a direct structural explanation of why glycosylation is essential for integrin's interaction with FN and demonstrates the relevance of the glycosylation in cells and *in vivo* (Gu et al., 2009; Zheng et al., 1994).

Fibronectin FN9-10 locks the integrin α5β1 opening by a gear-like mechanism

The arrangement of the integrin α5β1 heads with respect to FN7-10 revealed that both the RGD motif (residues 1493-1495) in FN10 and the synergy site (residues 1373-1380, DRVPHSRN) in FN9, face towards the integrin heads and interact simultaneously (Fig. 3A-3D). The RGD motif located within a loop of FN10 interlocks deeply into the pocket between the α and β integrin -subunits with a stable conformation (Fig. 3A, 3B and 3C). This loop was previously shown to be flexible in an isolated FN10 domain by NMR (Main et al., 1992). The arrangement of the loop in the complex structure resembles that of single RGD peptides bound to the headpiece of α5β1 (Fig. 3E, (Xia and Springer, 2014)). While the well characterized interactions of the RGD motif with various integrin headpieces were present, we also observed that the succeeding P1497 in FN10 made a prominent van-der-Waals contact with the backbone of helix α1, adjacent to S134 and packed against Y133 in the β1- βI domain. Interestingly, S134 was also part of the MIDAS metal coordination sphere (Fig. 3B and 3C).

Analyses of various integrin structures collectively led to the hypothesis that engagement of MIDAS induces the translocation of the α1 and α7 helices in the βI domain, triggering a piston-like movement, which leads to the swing-out motion of the hybrid domain and the separation of the α- and β- legs (Campbell and Humphries, 2011; Luo et al., 2007; Takagi et al., 2002; 2003; Zhu et al., 2008; 2013). Our structure also showed engagement of the ligand RGD motif with MIDAS (Fig. 3B), and the resulting open-leg conformation (Fig. 1). This reinforces the notion that various integrin isotypes share a common molecular movement in which the interaction with ligands or ligand-mimetics at MIDAS triggers a switch in the βI domain that translates to a large conformational change. However, to date, none of the tested RGD motif-containing peptides were able to induce the large conformational opening of integrin α5β1 (Nagae et al., 2012; Xia and Springer, 2014). The structural differences between the head domains bound to cyclic RGD peptide (Fig. 3E, PDB: 4wk4 (Xia and Springer, 2014)) and the head domains in our FN-bound integrin are significant, giving an overall root mean square difference (R.M.S.D.) of 1.4 (over 687 Cα atoms). That indicates that FN has an extra element to optimally induces and stabilizes the opening of integrin. A closer look at the interaction surfaces between FN and integrin allowed us to identify additional interactions contributing to stabilization of the head domains in the open conformation (Fig. 3C). Adjacent to the RGD loop, we found that R1445 in FN10 formed a salt bridge with E320 in integrin β1, and that Y1446 in FN10 was in hydrogen bonding distance to D137 in integrin β1. D137 is also part of ADMIDAS, which coordinates the metal ion. Interestingly, the hydroxyl oxygen of Y1446 was located close to Mn^{2+} (at a distance of 3.8 Å). The close approach of R1445 and Y1446 towards the ADMIDAS coordinating residues (juxta-ADMIDAS) would move helix α1 and its upstream portion closer to FN (Fig. 3F), facilitating a large tilt of the β- head. The importance of that interaction is supported by a previous report that an R1445A mutant displayed drastic reduced cellular adhesion (Redick et al., 2000). Together, the observed arrangement of FN10 R1445 and Y1446 at ADMIDAS, together with the RGD loop and P1497 at MIDAS is part of the critical pivoting point for induction of the large conformational change of integrin in coordination with the concomitant insertion of the RGD motif into the interaction pocket at the integrin head.

Comparison of our structure of protein ligand-attached integrin α5β1 to the structures of other ligand-bound integrin isotypes offers further insights into the ligand-induced opening of integrin. Interestingly, each integrin structure reveals its own distinct mode of

ligand recognition and the opening of the headpiece. For αvβ6-proTGF-β1, an additional helix is formed immediately after the proTGF-β1 RGD motif. The helix then forms hydrophobic interactions with integrin, which appears to be the key interactions to move the specificity-determining loop 1 (SDL1), which is the loop upstream of the α1 helix (Dong et al., 2017). Furthermore, proTGF- β1 recognizes integrin β6 SDL2 as a secondary interaction surface (Dong et al., 2017). In contrast, the SDL2 (residues 176-195) of integrin β1 did not exhibit interaction with FN (Fig. S4). In the case of α6β1-laminin, the multiple contacts of each laminin subunit stabilized the formation of the open groove of the α6β1 heads (Arimori et al., co-submitted with this manuscript). In both cases and unlike FN-α5β1, ADMIDAS was not directly contacted by the ligand. Despite the differences, however, the various ligand interactions all result in the same open topology of the head domains.

The synergy site is located in FN9 (Fig. 3A) and interacts with integrin α5 by a salt bridge (R1379-D154) as well as hydrophobic contacts made by I1382 and P1376 in FN9 with Y208 in α5 (Fig. 3D). Particularly, the R1379-D154 interaction agrees with previous biochemical identifications of D154 as a key residue for interaction with the synergy site (Nagae et al., 2012), and of R1379 in FN9 as a residue involved in the force-induced reinforcement of integrin-FN binding called catch-bond formation (Friedland et al., 2009; Kong et al., 2009). Our structure explains the molecular basis of the dramatically reduced cell adhesion activity of the triple mutant R1374A/P1376A/R1379A (Redick et al., 2000), although in this conformation, we saw no apparent interaction of FN R1374 with the integrin surface.

The FN molecule covered the top of the α- and β- integrin heads (Fig. 3A). The structure of FN9-10 was rigid reaching a local resolution of 3.1 Å, while the upstream F7-F8 was less resolved (local resolution of 4-7 Å), indicating its flexibility (Fig. S2C). The domain architecture of FN9-10 showed an interdomain tilt angle between FN9 and FN10 of 28°, which is more tilted than 12° angle observed in the crystal structure of FN7-10 (PDB 1fnf, (Leahy et al., 1996)) (R.M.S.D of 1.59 Å for the FN9-10 portion). This tilt accommodates the docking of the RGD motif into the groove of the integrin heads, which is noteworthy as our integrin-bound FN7-9 and the FN7-9 alone in the crystal structure had a similar topological arrangement with an R.M.S.D of 1.04 Å, while FN10 was tilted away. That also suggests that the rather flexible FN9-10 connection (Copié et al., 1998) functions as a critical factor to scaffold the open conformation of integrin. Our structure agrees well with

a previous observation that fixing the interdomain tilt angle of FN9-FN10 to 28° increases the affinity for integrin as well as cellular adhesion (Altroff et al., 2004).

TS2/16 recognizes integrin α5β1 without interfering with key residues for conformational change

TS2/16 is a stimulatory antibody that recognizes the head domain of the β1 subunit (reviewed in (Byron et al., 2009)). It is reported to reduce the off-rate of integrin-ligand interactions, thus promoting the integrin-ligand association. In our cryo-EM 3D reconstruction, TS2/16 contacted the side of the βI domain with a buried surface area of 114.9 $Å^2$ (Fig. 1A, pink, Fig. 3G) and centered around the reported epitope of residues 207-218 in the β1-head (Takada and Puzon, 1993). Residue K208 of the βI domain made a prominent contact by reaching into a hydrophobic pocket on the surface of TS2/16 and formed a cation-π interaction with Y100a of TS2/16 CDR-H3 (Fig. 3H). In addition, D93 of TS2/16 CDR-L3 formed a salt bridge to R161 in the βI domain. We note that the recognition surface in β1 was distant from the sites where the movements occur during the large conformational change, which explains why TS2/16 also recognizes the closed conformation of integrin α5β1 (Su et al., 2016).

Integrin α5β1 in its resting state shows incomplete bending

To understand the conformational change of integrin α5β1 and its consequence to FN binding, we obtained the cryo-EM structure of integrin α5β1 in its resting conformation (Fig. 4, S5-S7) in the presence of Ca^{2+} and Mg^{2+}, but without Mn^{2+}. The resting conformation revealed the density of the whole ectodomain (Fig. 4). Unlike the known resting structures of β3-containing integrins such as αvβ3 or αIIbβ3 (Xiong et al., 2001; Zhu et al., 2008), which show acutely bent structures, α5β1 exhibited only a half-bent conformation (Fig. 4A-F) with an angle of ~90° at the knee between the lower legs and the headpiece. This conformation was hinted at by previous negative-stain EM studies using a recombinant obligate dimeric form of α5β1, raising an important open question (Miyazaki et al., 2018; Su et al., 2016). Compared with the ligand-bound open conformation of integrin α5β1, the lower legs of both the α- and β-subunits in resting integrin were less flexible, enough to be clearly visible. That is likely because of parallel closure of the α - and β - legs (Fig. 4G), while in the open conformation the contact points of the legs are lost as a result of the opening of the upper legs. That shows that ligand

binding to the head domains and the subsequent swing-out of the hybrid domain destabilizes the half-bent conformation (Fig. 5A).

The upper part of the ectodomain was the most stable portion of the whole structure, with a resolution reaching 4.6 Å in the core of the integrin head (Fig. S5B and S5C, S6), partially resolving the side chains (Fig. S5D). The integrin heads were tilted in the closed conformation, making the three FN binding sites uncoordinated. In particular, the ADMIDAS area was moved away from FN10 Y1446 (Fig. 5B) so that ADMIDAS was not readily engaged for the binding. Furthermore, interestingly, we found that the N-glycan at N343 of the βI domain presented a steric hindrance to the docking of FN10 when the head was closed (Fig. 5C), while it moved away from the FN binding site when integrin α5β1 employed an open conformation (Fig. 5C). That motion suggests that N343 has a critical inhibitive function in ligand binding.

In contrast, the resolution of the lower legs was insufficient for model building. Therefore rigid-body molecular fitting of individual domains was performed using available α5β1 structures and homology models of calf1 and calf2 for the α- subunit and PSI, EGF1-4 and β-tail domains for the β- subunit. The main contacting surface between the lower legs of α5 and β1 was the interface between the α- thigh/calf 1 domain and β- EGF2/3 (Fig. 4G), which were aligned in parallel similarly to the available structures of acutely bent integrins (Xiong et al., 2001; Zhu et al., 2008). Subsequent multibody analysis, implemented in the processing software Relion3 (Nakane et al., 2018; Zivanov et al., 2018), of the lower legs and the headpiece revealed fluctuation at the knee with variation of the angle between the upper and lower legs ranging between 71° and 93° (Fig. 4H and Fig. S7, movie 1), suggesting that integrin is not rigidly fixed in this resting conformation but bears a certain degree of flexibility. It should be noted, however, that our analysis did not indicate any sub-population of molecules in the acutely bent conformation observed for the β3-integrins. In contrast to the acutely bent conformation, no interaction between the hybrid domain and the lower legs of the β- subunit was evident in our structure. Nevertheless, the interaction of the hinge-like interface at the knees, between calf1 and EGF2/3, was robust enough to hold the half-bent conformation.

Mn^{2+} is necessary for integrin α5β1 ligand binding but does not induce large conformational change

To closely follow the key steps leading from the resting to the fully open conformation of integrin α5β1, we investigated the conformations of integrin in the presence of buffer containing various concentrations of Mn^{2+}. Cryo-EM analysis showed that integrin α5β1 employed the half-bent resting conformation even at the extreme concentration of 100 mM Mn^{2+} (Fig. 6A). Together with previous results showing that the integrin α5β1 headpiece does not change its conformation when it binds with RGD peptide (Nagae et al., 2012; Xia and Springer, 2014), it demonstrates that neither the addition of Mn^{2+} nor that of RGD containing peptide is enough to induce a large conformational change of the β-subunit. That is in stark contrast to αIIbβ3, for which either Mn^{2+} or ligand-mimicking peptide was sufficient to induce full opening (Eng et al., 2011).

Those findings led us to hypothesize that the large conformational change of integrin α5β1 is only stabilized as a result of FN binding, rather being the cause of FN binding. To test that, we performed solid-phase equilibrium binding assays (Fig. 6B). For that ELISA-like assay, wells were coated with full-length FN, and the binding of α5β1 to FN was measured in the presence or absence of Mn^{2+}. When Mn^{2+} was added, we observed a drastic increase of the binding of α5β1 to FN compared with that in control conditions without Mn^{2+}, indicating that the affinity of integrin α5β1 for FN was increased. However, our cryo-EM analysis showed that integrin α5β1 in the presence of Mn^{2+} employed a half-bent conformation (Fig. 6A). Those results demonstrate that the affinity of integrin α5β1 for FN was increased, with the integrin still mostly employing a half-bent conformation. Combined with the observation that RGD motif was not sufficient to cause opening of the integrin α- and β- subunits, we concluded that the opening of integrin α5β1 is stabilized only by the binding of the structural domain of FN.

Furthermore, to systematically survey the global conformations of integrin α5β1, we performed reconstitution assays using size-exclusion chromatography (SEC) followed by surveillance of the conformations using negative-stain EM (Fig. 7). While vitrified integrin samples for cryo-EM are instrumental in structural analyses of robustly folded populations, negative-stain EM allows the visualization of flexible entities that do not align well because of the low signal-to-noise ratio of cryo-EM images, and would therefore be discarded during the image analysis. First, the effect of Mn^{2+} on ligand binding was examined. Integrin α5β1 was mixed with FN7-10 and TS2/16 in the presence and absence

of Mn^{2+} and subjected the mixtures to analytical SEC (Fig. 7A and 7B). The elution profiles revealed no observable shift in integrin α5β1 with or without Mn^{2+}, indicating no large structural change, which was further confirmed by negative-stain observations (Fig. 7A, green line/middle SDS-PAGE and Fig. 7C). Those results were in agreement with our cryo-EM observations (Fig. 6A) showing the half-bent conformation. On the other hand, α5β1 co-eluted with FN7-10 in the presence of Mn^{2+}, indicating their interaction (7A, right side, blue lines, peak marked with *), whereas no binding took place without Mn^{2+} (7A, left side). Subsequent negative-stain EM observation and conformational assessment revealed an increase in the proportion of molecules in the open conformation (41 %), compared with that in the same condition without Mn^{2+} (0 %) or without FN7-10 but with Mn^{2+} (7 %) (Fig. 7C), although the FN density was only partially visible because of dissociation during the negative-stain preparation. Altogether, our results demonstrated that the large extension and opening of integrin is not coupled to the affinity of integrin for FN, but is instead stabilized as a result of FN binding.

Discussion

Integrin is the master adhesion receptor, controlling numerous signaling pathways and determining cell fates, such as migration and polarization (Hynes, 2002). There is a strong incentive to understand the molecular mechanism of conformational changes in integrin because of their biological and medical relevance. In this study, we successfully purified human integrin α5β1 from a natural source (human placenta) and reconstituted the complex with FN in a membrane scaffold to facilitate a comprehensive biochemical and structural analysis. Our strategy has two important advantages: 1) Our results were obtained with native proteins in a biologically relevant context and 2) We were able to perform a direct and straightforward analysis without adjusting the conditions or impairing the complex integrity.

Our study provides the first reconstitution and structural analysis of the open, elongated conformation of integrin α5β1. Remarkably, we found that three binding sites of the FN ligand at FN9 and FN10 were engaged (Fig. 3), which explains the conundrum why the strong binding of RGD peptides was not sufficient for integrin opening in previous studies of α5β1 (Nagae et al., 2012; Xia and Springer, 2014). We also identified that R1445 and Y1446 in FN10 approach close to the ADMIDAS region, which caused the translocation of ADMIDAS and downward helix α1, leading to the stabilization of the open conformation of the β1 βI domain. That movement further allosterically triggered the swing-out motion to extend and open the α5β1 legs (Fig. 1 and 5A). To date, two examples of truncated integrins bound to their protein ligands have been reported, namely αVβ6-proTGF-β1 and αVβ8-proTGF-β1. While αVβ6 opens its α- and β- subunits in complex with proTGF-β1 (Dong et al., 2017), αVβ8 does not open its legs even upon ligand binding, and its ADMIDAS does not contain any metal ion (Campbell et al., 2020). Together, those observations implicate the importance of ADMIDAS for the opening of integrins. On the other hand, the synergy site is reported to be responsible for the force-induced reinforcement of the integrin-FN interaction (Friedland et al., 2009). Indeed, our structural analysis provides a clue as to how the synergy site in FN9 is required to position FN10 and the RGD region for full engagement of FN with integrin.

Uncoupling of the integrin α5β1 conformation and the affinity of α5β1 for FN

The toolbox prepared for this study, including physiologically relevant full-length integrin together with our cryo-EM pipeline, allowed us to investigate the stepwise molecular

response during integrin α5β1 ligand engagement. Our analysis revealed that the behavior of α5β1 is surprisingly distinct from that of the well-studied β3-containing integrins, which show a tightly coupled conformational change upon addition of either ligand-mimetic peptides or specific ions. For the FN receptor α5β1, the extended, open conformation was observed only when both Mn^{2+} and FN were present (Fig. 7C). That means that FN-binding does not require prior opening, but instead, the open conformation of α5β1 becomes dominant as a result of the FN-binding. We further showed that binding of Mn^{2+} is key to facilitate the interaction between FN and α5β1 without altering the conformational dynamics. We surmise that Mn^{2+}-coordination at ADMIDAS might play a critical role in increasing the affinity for FN. Once the juxta-ADMIDAS FN-binding site is primed, FN may engage the three binding sites on the integrin surface. That binding fosters the translocation of ADMIDAS, which then, together with the synergy site, facilitates the RGD driven allosteric conformational change leading to the downstream opening of the legs (Fig. 8). On the other hand, without Mn^{2+}, integrin is not competent to stably capture FN, as the interaction is transient and short-lived without Mn^{2+} *in vitro* (Fig. 7A and 7B).

In addition, our conformational analysis together with previous studies (Miyazaki et al., 2018; Su et al., 2016), showed that the closure of α5β1 is not tightly fixed but is rather a dynamic shift within the equilibrium of different states, showing 51 % of extended conformation in the presence of resting buffer without Mn^{2+} (Fig 7C). Even within the half-bent structure, our multibody analysis hints at flexibility between the legs and the heads (Fig. 4H and S7). That concept, termed molecular breathing has been discussed previously with regard to integrins (Takagi et al., 2002; Zhu et al., 2008). We speculate that the half-bent conformation of α5β1 is still physically accessible to FN, but a breathing motion towards extension might increase the probability of docking of the three interaction sites to FN. Finally, when FN binds, integrin α5β1 is globally extended with its legs open, which is facilitated by the movement of the helix α7 along with local rearrangements near ADMIDAS, and further by the molecular constraint of the beads-on-string arrangement of FN9-10. Overall, it is intriguing that the ligand recognition mechanisms of integrin isoforms appear to be optimized and fine-tuned for their specific ligands, presumably, depending on how robust an interaction has to be for their biological functions.

Various conformations of resting Integrin

The resting conformation has been shown to employ a sharply bent arrangement (~45˚) in integrin isoforms such as αvβ3 and αIIbβ3 (Xiong et al., 2001; Zhu et al., 2008), which makes the ligand binding surface inaccessible because of its proximity to the plasma membrane. However, in the case of β1 integrin, the most prominent integrin subunit dimerizing with 12 different α subunits (Hynes, 2002), it was hinted by negative-stain EM that the conventional open-bent model deduced from the behavior of β3 integrin might not be applicable (Miyazaki et al., 2018). We directly showed that the resting conformation of integrin α5β1 is only half-bent with a 90˚ angle between the headpiece and the legs (Fig. 4 and S7). A higher-resolution structures of the lower leg is needed to elucidate the precise molecular mechanism of that angular arrangement. Interestingly, αVβ8 integrin has been reported to employ an extended but closed conformation regardless of its ligand binding state (Campbell et al., 2020; Cormier et al., 2018), whereas αVβ6 integrin follows the canonical open-close conformational change (Dong et al., 2017). The αvβ8 integrin is mostly expressed in immune cells, and it is plausible that the closed-extended conformation is advantageous for searching and binding to its ligands and subsequent cellular activation (Campbell et al., 2020; Cormier et al., 2018). In contrast, αIIbβ3 is enriched on the surface of platelets, and there is a clear distinction between its closed-inaccessible and open-extended conformations, because the aggregation of platelets has to be tightly regulated to avoid detrimental effects on blood circulation. On the other hand, α5β1 is ubiquitously expressed throughout various tissues and is generally involved in cellular responses that are slower than those of the immune system. Therefore, the loose closure of α5β1 might reflect that functional aspect and thus provide a less acute response to extracellular cues. Altogether, the differences among integrin isoforms likely provide important regulatory features and might be related to the different functions of the isoforms within specific cell types.

Integrin-mediated focal adhesion in a cellular context

We demonstrated a stepwise mechanism of large conformational change in α5β1 (summarized in Fig. 8). However, in a cellular context, different intracellular factors, such as the integrin activators talin, kindlin and the downstream contractile actomyosin network, contribute to full engagement of integrin with the ECM. It will be particularly important to elucidate which intracellular factors and mechanisms trigger integrin α5β1

to assume the primed state mimicked by the presence of Mn^{2+}, in which the integrin can readily associate with FN at the ECM. Moreover, once integrin α5β1 is engaged with FN, force is applied through the intracellular focal adhesion machinery bound to the integrin tail (Kechagia et al., 2019). It has been proposed that the FN synergy site is involved in the reinforcement of the interaction with integrin (Friedland et al., 2009). Although a partial synergy site mutation (R1374A/R1379A) did not affect the viability of mice, it caused a bleeding disorder and accompanying cellular biological experiments indicated that the site is not essential for the formation of focal adhesion but is critical for focal adhesion maturation (Benito-Jardón et al., 2017). Those findings support the hypothesis that the key function of the FN synergy site-integrin interaction is to provide a site for catch-bond formation when force is applied (Friedland et al., 2009; Kong et al., 2009; Redick et al., 2000). In that context, we note that FN R1374, which has been reported as a key residue for force-transduction function (Friedland et al., 2009; Redick et al., 2000), was not engaged in the interaction with integrin in our structure. That suggests the possibility that the interaction surface might change to engage FN R1374 in the presence of applied force. We nevertheless observed a comprehensive picture of the molecular interaction of FN and integrin α5β1 in the absence of force, which can be used as a basis for further analyses.

FN acts as a dimer in its full-length context and polymerizes into a fibrous form when integrated in the ECM network. The polymerization is induced by interaction with integrin α5β1 (Sechler et al., 1997). In turn, the FN within the ECM might also act as a platform to induce integrin clustering, which contributes to stabilize the large intracellular multi-layered focal adhesion machinery consisting of hundreds of proteins (Zaidel-Bar et al., 2007). Furthermore, the phenomenon of molecular breathing has been observed for the intracellular focal adhesion proteins talin (Dedden et al., 2019) and vinculin (Kelley et al., 2020), which together with integrin, may play an important role in the dynamic behaviors of focal adhesions. Molecular breathing might be advantageous in the cellular context of focal adhesion formation that requires associated molecules to react quickly to diverse stimuli. Molecular breathing allows a degree of flexibility in the recruitment and disassociation of various factors from focal adhesions, thus enabling fast assembly and disassembly during cell migration.

Acknowledgements

We thank Dr. Christoph Hübener (LMU Klinikum Munich, Klinik und Poliklinik für Frauenheilkunde und Geburtshilfe, Campus Großhadern), for providing de-identified human placentas. We are grateful to Ryota Izawa for his work in the early stages of establishing the purification protocol of integrin α5β1 from human placenta. We thank Sven Schkölziger for technical support. We acknowledge Elena Conti and the Max Planck Institute of Biochemistry cryo-electron microscopy (Daniel Bollschweiler and Tilman Schäfer) and biochemistry core facilities for support and infrastructure. We also thank members of the Mizuno and Takagi labs for helpful discussions. NM acknowledges the Max Planck Society, Boehringer Ingelheim Foundation Plus 3 Program, and the European Research Council (ERC-CoG, 724209) for funding. NM is a recipient of the EMBO Young Investigator award. NM is further supported by the Intramural Research Program of the National Heart Lung and Blood Institute, and by the National Institute of Arthritis and Musculoskeletal and Skin Diseases of National Institutes of Health. This work was performed under the International Collaborative Research Program of the Institute for Protein Research, Osaka University (ICR-18-05).

STAR Methods

Integrin α5β1 purification

Human endogenous integrin α5β1 was purified from placenta by adapting a previously published protocol (Pytela et al., 1987). De-identified human placentas were obtained from LMU Klinikum Munich, Klinik und Poliklinik für Frauenheilkunde und Geburtshilfe, Campus Großhadern. Amnion and umbilical cords were first removed from the human placentas. The remaining placenta tissue was then cut into small pieces, mixed with Tris-buffered saline (TBS: 50 mM Tris, 150 mM NaCl, pH 7.5), 1 mM $MgCl_2$, 1 mM $CaCl_2$, and protease inhibitor cocktail (Roche cOmplete) and homogenized. Debris was removed by centrifugation at 12,000*g* for 15 min at 4 °C (Beckmann centrifuge, J14 rotor). The supernatant was then sonicated (Vs70T, Bandelin) and centrifuged again at 10,000*g* for 10 min at 4 °C (Beckmann Avanti J-26 centrifuge, JA-14 rotor). Next, the membrane fraction was pelleted by ultracentrifugation (150,000*g*, 4 °C; Beckmann, Ti 45 rotor), and the pellet was washed five times in a 50 mL mixture of 50 mM Tris (pH 7.5), 1 M NaCl, 1 mM $MgCl_2$, 1 mM $CaCl_2$, and protease inhibitor cocktail. The membrane fraction was then solubilized by incubation with detergent (1% Triton-X100 in TBS (pH 7.5), 1 mM $MgCl_2$, 1 mM $CaCl_2$, and protease inhibitor cocktail) overnight at 4 °C. After ultracentrifugation (150,000*g*, 4 °C; Beckmann, Ti70), the supernatant was incubated with 2 mL KH72 monoclonal antibody-coupled sepharose beads overnight at 4 °C. The beads with bound protein were then washed five times with 10 mL TBS (pH 7.5), 1 mM $MgCl_2$, 1 mM $CaCl_2$, and 0.1% Triton X-100 in a gravity flow column. Protein was eluted using a 20 mL mixture of 20 mM PIPES (pH 7.0), 150 mM NaCl, 1 mM $CaCl_2$, 3 M $MgCl_2$, and 0.1% Triton X-100. After determination that protein was present by SDS-PAGE, fractions containing protein were pooled and dialyzed overnight at 4 °C against TBS (pH 7.5), 1 mM $MgCl_2$, 1 mM $CaCl_2$, and 0.1% Triton X-100. The dialyzed samples were concentrated by ultrafiltration (Amicon) at a maximum speed of 2,500*g* in 5 min steps. The protein was then flash frozen and stored at -80 °C.

Preparation of KH72 monoclonal antibody

Hybridomas expressing the KH72 monoclonal antibody were kindly gifted by Dr. K. Miyake (University of Tokyo). Cells were cultured in RPMI 1640 medium (Gibco, with 25 mM HEPES and L-glutamine) supplemented with 10% fetal bovine serum, 0.1 mg/mL kanamycin, 2 mM L-glutamine, and 10 μM β-mercaptoethanol. The cells were grown at 37

°C with 5% CO_2 in T125 flasks and were split at confluency every 2–3 days by gently shaking the cells off and transferring ~30% of the volume to a new flask with fresh medium. Supernatant medium containing the expressed KH72 monoclonal antibody was collected, frozen, and stored at -20 °C.

For purification of KH72 from the collected hybridoma medium, 1 L culture supernatant was thawed in a water bath at 37 °C. Dead cells were removed by centrifugation at 4,000*g* for 10 min at 4 °C (Beckmann, JLA-8.1000 rotor). The supernatant was filtered using a 0.22 µm pore PES membrane filter (Corning). The pH was then adjusted with NaOH to pH 8.2, and the sample was loaded onto 2 mL Protein A Agarose (Pierce, ThermoFisher) in a gravity column. The resin was then washed five times with a 20 mL mixture of 20 mM Tris (pH 8.8) and 150 mM NaCl. Bound protein was eluted with low-pH IgG elution buffer (Pierce, ThermoFisher) and collected in 1 mL fractions, which were immediately neutralized by addition of Tris (pH 8.8) to a final concentration of 150 mM. Fractions containing purified KH72, as determined by SDS-PAGE, were pooled and concentrated using an Amicon ultrafiltration device to a concentration of ~1 mg/mL. Coupling to NHS-sepharose (GE) was performed in coupling buffer containing 200 mM $NaHCO_3$ and 500 mM NaCl (pH 8.3). KH72 was dialyzed against coupling buffer for 4 h at room temperature using 7K MWCO Slide-A-Lyzer dialysis tubes with one exchange of the buffer. Then, ~1 mg KH72 was added to 250 µL activated NHS-sepharose and incubated overnight at 4 °C. The next day, 150 mM Tris (pH 8.8) was added to stop the reaction, and the KH72-bound sepharose was stored in a solution of 50 mM Tris and 150 mM NaCl (pH 7.5) containing 0.05% NaN_3.

Preparation of membrane scaffold protein (MSP)

MSP was purified using a previously published protocol (Denisov et al., 2004) with the following details. MSPE3D1 or MSP ΔH5 (Hagn et al., 2018) with an N-terminal 6×His tag was expressed in Bl21 gold DE3 cells grown in TB medium containing kanamycin (50 µg/mL). The cells were grown until the OD_{600} reached 2 at 37 °C. Then, expression was induced by incubation with 1 mM IPTG overnight at 18 °C. The cells were then harvested and lysed by sonication in phosphate buffered saline (PBS, Sigma), 1% Triton X-100, and phenylmethylsulfonyl fluoride (PMSF). After removal of debris by centrifugation at 20,000*g* for 30 min at 4 °C (Beckmann centrifuge, JA 25.50 rotor), the supernatant was filtered with a 0.22 µm pore PES membrane filter (Corning), incubated on an Ni-NTA

column (5 mL, Protino, Macherey-Nagel), and washed with 50 mL of each of the following buffers: first with 40 mM Tris (pH 8), 300 mM NaCl, and 1% Triton X-100; then with 40 mM Tris (pH 8), 300 mM NaCl, and 50 mM sodium cholate; and finally with 40 mM Tris (pH 8), 300 mM NaCl, and 5 mM imidazole. Protein was then eluted with 40 mM Tris (pH 8), 300 mM NaCl, and 500 mM imidazole. Fractions containing protein, as determined by SDS-PAGE, were pooled and concentrated using an Amicon ultrafiltration device (10K MWCO), and the buffer was exchanged through SEC to 20 mM Tris (pH 7.4), 100 mM NaCl, and 0.5 mM EDTA using a Superdex200 column on an ÄKTA pure (GE) machine. The protein peak was then pooled, concentrated using an Amicon ultrafiltration device (10K MWCO) to a concentration of ~4 mg/mL, flash frozen, and stored at -80 °C.

Purification of FN 7-10

FN7-10 was purified as previously (Leahy et al., 1996) with the following adaptations. Fn7-10 was expressed in Bl21 gold DE3 cells in LB medium containing ampicillin (100 µg/mL). The cells were grown until the OD_{600} reached ~0.8–1 at 37 °C. Expression was induced by incubation with 0.4 mM IPTG for 3–4 h at 37 °C. The cells were then harvested, pelleted, re-suspended in lysis buffer (50 mM Tris, 100 mM NaCl, and 1 mM EDTA (pH 8)) with 0.2 mg/mL lysozyme, and stirred for 30 min at room temperature. Then, 1% Triton X-100 and 0.1 mM PMSF were added, and the mixture was stirred further for 30 min at room temperature. The solution was then freeze-thawed and continuously stirred for 1 h at room temperature in the presence of additional 0.1 mM PMSF, 10 mM $MgCl_2$, and 10 µg/mL DNAse I. The lysate was cleared by centrifugation at 76,000*g* for 30 min at 4 °C (Beckmann centrifuge, JA 25.50), and the supernatant was subjected to precipitation by 40% $(NH_4)_2SO_4$. The resulting pellet was re-suspended in 20 mM Tris and 0.02% NaN_3 at pH 7.9 and subjected to MonoQ chromatography. Protein was eluted in a gradient from 100 mM to 300 mM NaCl. If the protein peak (as determined by SDS-PAGE) was not clean enough after elution, an additional MonoS step was included. For that, the MonoQ peak was pooled, dialyzed against 20 mM formic acid, adjusted to pH 4.2 with NaOH, and subjected to MonoS chromatography in a linear gradient of NaCl, where it was eluted at 400 mM NaCl. The protein peak (after either MonoQ or MonoS) was pooled, concentrated using an Amicon centrifugation device (10K MWCO), flash frozen, and stored at -80 °C.

TS2/16 Fv-clasp purification

TS2/16 Fv-clasp protein was purified as described previously (Arimori et al., 2017). V_H-SARAH and V_L-SARAH fragments were individually expressed in Bl21 gold DE3 cells grown in LB medium. The cells were grown until the OD_{600} reached ~0.6 at 37 °C. Expression was then induced by incubation with 0.4 mM IPTG for 4 h at 37 °C. The TS2/16 Fv-clasp protein was expressed in inclusion bodies. After the cells were lysed by sonication, the inclusion bodies were isolated by centrifugation and solubilized in 50 mM Tris, 150 mM NaCl, 6 M guanidine-HCl, and 375 μM β-mercaptoethanol (pH 8). VH-SARAH and VL-SARAH were then mixed at a 1:1 molar ratio in a total volume of 12 mL. To induce protein refolding, 50 mM Tris, 4 M urea, 0.4 M L-arginine, 375 μM GSSG, and 150 mM NaCl (pH 8) were added, bringing the total volume up to 300 mL (25× dilution), and the mixture was incubated for 4 h at 4 °C. Then, a 300 mL mixture of 50 mM Tris, 0.4 M L-arginine, 375 μM GSSG, and 150 mM NaCl (pH 8) was added (2× dilution) and incubated for 16 h at 4 °C. After precipitation by 80% $(NH_4)_2SO_4$, the protein was dissolved and dialyzed in TBS. The protein was then subjected to SEC on a HiLoad 16/600 Superdex 200 pg column (GE) in 20 mM Tris and 150 mM NaCl (pH 8). The peak containing TS2/16 Fv-clasp, as determined by SDS-PAGE, was then pooled, concentrated, diluted in 20 mM Tris and 50 mM NaCl (pH 7.5), and further subjected to MonoQ chromatography. Elution was carried out in a linear gradient from 100 mM to 500 mM NaCl. The major eluting peak contained fully folded TS2/16 Fv-clasp and was pooled, concentrated using an Amicon ultrafiltration device (10K MWCO), flash frozen, and stored at -80 °C.

Assembly of integrin α5β1 into nanodiscs

Nanodiscs containing integrin α5β1 were assembled according to a previously published protocol (Denisov et al., 2004) with the following adaptations. Isoform MSPE3D1 was used for all experiments, except that we used MSPΔH5 to test the effects of different Mn^{2+} concentrations on the integrin conformation in cryo-EM (Fig. 6A). Lipid stock (from Folch fraction I, bovine brain, Sigma) was stored in chloroform:methanol:H_2O (20:9:1) at a concentration of 25 mg/mL at -20 °C. Before use, the required amount of lipid was dried in a stream of nitrogen and further vacuum dried for 2 h. The resulting lipid film was solubilized in 20 mM HEPES (pH 7), 150 mM NaCl, and 1% DDM on a thermoshaker for 1 h at 37 °C, resulting in a final concentration of 25 mg/mL. MSPE3D1 or MSPΔH5, α5β1,

and lipids were mixed in a ratio of ~29:1:3460 for MSPE3D1 or ~45:1:110 for MSPΔH5 and then incubated for 1 h at room temperature. SM-2 Biobeads (BioRad) were added to the mix to remove detergent overnight at 4 °C. The mixture was then subjected to SEC (Superose 6i GL10/300 on an ÄKTA pure (GE)) in TBS (pH 7.5), 1 mM $MgCl_2$, and 1 mM $CaCl_2$. The peak containing ND with inserted α5β1 (ND–α5β1; as determined by SDS-PAGE and negative-stain EM) was then pooled, concentrated (Amicon, 50K MWCO) at a maximum speed of 4,000*g* until an A_{280} ~1.2–1.6 mg/mL (~5 μM) was reached, flash frozen, and stored at -80 °C.

Solid-phase integrin-FN binding assay

To test the affinity of integrin for FN in the presence of different additives, we conducted solid-phase binding assays based on a previously published protocol (Nagae et al., 2012) with some adaptations. 96-well microtiter plates were coated with 50 μL/well of either 0.01 mg/mL full-length FN (Sigma) in TBS (pH 7.5) or 5% (w/v) bovine serum albumin (BSA, Sigma) in TBS (pH 7.5) and incubated overnight at 4 °C. The wells were then blocked with 200 μL/well 5% BSA in TBS (pH 7.5) for 1 h at room temperature. Then, ND-α5β1 was added in various concentrations in either TBS (pH 7.5), 1 mM $MgCl_2$, and 1 mM $CaCl_2$ or TBS (pH 7.5) and 1 mM $MnCl_2$. The mixture (total volume 50 μL/well) was then incubated for 3 h at room temperature. The wells were then washed three times with 200 μL/well of the respective buffers (containing either $MgCl_2$/$CaCl_2$ or $MnCl_2$), and 50 μL/well antibody (TS2/16-biotin, 0.005 mg/mL) in the respective buffers containing additional 0.1% BSA was added. After incubation for 2h at room temperature, the wells were washed three times with 200 μL/well of the respective buffers, and SA-HRP (1.25 μg/mL, Life Technologies) in the respective buffers containing additional 0.1% BSA was added to bring the total volume to 50 μL/well. After incubation for 1 h at room temperature, the wells were washed four times with 200 μL/well of the respective buffers, and 100 μL/well ABTS/H_2O_2 solution (Sigma, ready-to-use) was added. Absorption at 420 nm was measured 6 min after the addition of ABTS/H_2O_2 using a plate reader (Tecan, Infinite M1000 PRO). Graphs were generated and assessed using GraphPad Prism software.

Analytical SEC

To assess the binding between ND-α5β1 and FN7–10 in the presence or absence of TS2/16 Fv-clasp, the reaction components were mixed, incubated, and injected into a Superose 6i column (S6i, 3.2/300 on ÄKTAmicro system (GE)), either in TBS (pH 7.5), 1 mM $MgCl_2$, and 1 mM $CaCl_2$ or in TBS (pH 7.5) and 1 mM $MnCl_2$. When the effect of manganese was tested, ND-α5β1 was first incubated with $MnCl_2$ at a final concentration of 10 mM for 30 min at 4 °C.

For the ND-α5β1/FN7–10 runs, 0.08 nmol of each component were mixed, incubated for 30 min at 4 °C, and loaded onto the S6i column. For the TS2/16 Fv-clasp runs, ND-α5β1 and FN7–10 were first mixed and incubated for 30 min at 4 °C. Then, TS2/16 Fv-clasp was added to a final ND-α5β1:FN7–10:TS2/16 Fv-clasp molar ratio of 1:2:2, and the mixture was incubated for 10 min at 4 °C. If a component was left out for a control run, it was replaced with a corresponding amount of buffer.

Electron microscopy (EM)

Negative-stain EM

For negative-stain EM, 5 µl sample (protein concentration ranging from ~4 µg/mL to 12 µg/mL) was incubated on glow-discharged carbon-coated copper grids (homemade carbon layer) for 1 min at room temperature and then washed twice in 100 µl drops of H_2O. Excess H_2O was removed by touching the rim of the grids with blotting paper. The grids were then stained with 5 µl 2% uranyl acetate solution for 1 min at room temperature, and excess uranyl acetate solution was removed by touching the rim of the grids with blotting paper. Datasets were collected using a Titan Halo (FEI) equipped with a Falcon 2 detector in nano-probe mode at an operating voltage of 300 kV. Micrographs were recorded with EPU software at 58,000× magnification (1.847 Å/pixel) with varying defoci from -1.5 µm to -2.5 in 0.5 µm steps at an exposure of 4 s with 10 frames/micrograph and a total dose of 105 e/$Å^2$. Recorded, gain-normalized frames were aligned, motion corrected, and dose-weighted using MotionCor2 software (Zheng et al., 2017). Defocus values were assessed using either GCTF (Zhang, 2016) or CTFFIND4 software (Rohou and Grigorieff, 2015). Using RELION3 (Zivanov et al., 2018), ~300 particles were manually picked and boxed out with a box size of 240 pixels. 2D alignment and classification was then performed. The resulting 5 initial 2D class averages were used

as templates for automated picking with Gautomatch software (https://www2.mrc-lmb.cam.ac.uk/research/locally-developed-software/zhang-software/). For all quantifications, 20,000 particles (with a box size of 340 pixels) were aligned and 2D classified in RELION3. After the first round of 2D classification, ~10,000 particles with clear signals were selected for the second round, which was used for quantification of the particles into the bent, intermediate, and extended conformational states (related to Fig. 7C).

For the representative 2D classes displayed in Fig. S1C, the whole dataset of resting ND-α5β1 (81249 particles in total) were boxed out (with a box size of 240 pixels) and submitted to alignment and 2D classification in RELION3.

Cryo-EM

Cryo-EM sample preparation

FN-bound and resting α5β1 were used at concentrations of 0.15 mg/mL and 0.3 mg/mL, respectively. For the samples testing the effect of different Mn^{2+} concentrations (Fig. 6A), a concentration of 0.2 mg/mL was used for ND-α5β1 (MSPΔH5). 3 μL of ND-α5β1 supplemented with 0 mM, 10 mM, or 100 mM $MnCl_2$ (final concentrations) was incubated for 1 h at 4 °C. Then, the sample was placed on a glow-discharged (GloQube, 30 s, 20 mA) R 1.2/1.3 Cu200 mesh grid (Quantifoil), blotted for 3.5 s, and plunge-frozen immediately in liquid ethane-propane using a Vitrobot Mark IV (FEI) at 4 °C and 100% humidity.

Cryo-EM data collection for screening and initial reconstruction

The assessment of the large conformational change by cryo-EM (Fig. 6A), as well as the initial screening and reconstruction necessary for the final structural analysis, were performed as follows. A screening dataset for FN-bound α5β1 was collected using EPU software (ThermoFisher) and a Talos Arctica (ThermoFisher) equipped with a Falcon 3 direct detector in nano-probe mode with the following parameters: operating voltage 200 kV, 92,000× magnification (1.61 Å/pix), varying defoci from -2 μm to -3 μm, 0.5 μm steps, exposure of 3 s, 40 frames/micrograph, and total dose 67 e/$Å^2$. The recorded, gain-normalized frames were aligned, motion corrected, and dose-weighted using MotionCor2. Defocus values were assessed by GCTF. Using RELION 3, 754 particles were manually picked and boxed out (with a box size of 300 pixels). Then 2D alignment and classification were performed. Out of 4 generated 2D averaged classes, the 3 classes with distinct

patterns were used as a template for automated picking with Gautomatch. Of 105,351 particles that were initially picked, 4 of 2D classes containing 10,949 particles (with a box size of 340 pixels) were selected. Those 4 classes were also used as a template for automated picking with Gautomatch of the dataset used for the high-resolution structural analysis of FN-bound α5β1 described below. The 10,949 particles of the 4 classes were further used to reconstruct an initial model using the initial model option in RELION 3. After a 3D classification run using the initial model as a reference, out of 8 generated classes, the reconstruction with the most prominent features (16,765 particles) was selected as an initial reference for 3D reconstruction of the dataset of FN-bound integrin α5β1 for high-resolution analysis, as described below.

For resting integrin α5β1, 2600 micrographs were recorded using SerialEM software (Mastronarde, 2005) and a K2 Summit direct detector with a quantum energy filter (20 eV and 40 eV slit width) (Gatan) with the following parameters: counting mode, 130,000× magnification (1.06 Å/pixel), varying defoci from -1.5 μm to -3.5 μm, 0.2 μm steps, and total dose 51 e/Å^2 (6 s exposure, 30 frames, 1.7 e/Å^2 frame dose). The micrograph frames were gain-normalized, motion corrected, aligned, and dose-weighted using MotionCor2. Defocus and image resolution values were assessed using GCTF. Then, 502 particles were manually picked and boxed out with a box size of 220 pixels, then 2D alignment and classification were performed using RELION3. Six selected 2D class averages were used as a template for automated picking with Gautomatch. A total of 103,534 automatically picked particles were boxed out with a box size of 300 pixels, binned to 150 pixels, and used to generate an initial 3D map using the *ab-initio* reconstruction option in cryoSPARC (Punjani et al., 2017). After the model was imported from cryoSPARC into RELION3 and further sorting by 3D classification, 23,332 remaining particles were refined. The refined 3D map was used as a reference for the main dataset of resting integrin α5β1 used for high-resolution analysis as described below.

For testing the effect of various Mn^{2+} concentrations on integrin α5β1 conformation, 3 datasets were obtained using a Talos Arctica and a Glacios (ThermoFisher). The datasets for α5β1 at final concentrations of 10 mM and 100 mM Mn^{2+} were collected using EPU software and a Talos Arctica with a Falcon 3 direct detector with the following parameters: nano-probe mode, operating voltage 200 kV, 92,000× magnification (1.61 Å/pix), varying defoci from -2 μm to -3 μm, 0.5 μm steps, exposure of 3 s, 40 frames/micrograph, and total dose 67 e/Å^2. The recorded, gain-normalized frames were

aligned, motion corrected, and dose-weighted using MotionCor2. Defocus values were assessed using CTFFIND4. A total of 965 and 88 micrographs were acquired for 10 mM Mn^{2+} and 100 mM Mn^{2+}, respectively. Automated picking with Gautomatch was performed, and 202,156 and 18,822 particles were picked for 10 mM Mn^{2+} and 100 mM Mn^{2+}, respectively. Those particles were boxed out with a box size of 200 pixels, 2D alignment and classification were performed using RELION. Representative images and classes are displayed in Fig. 6A. The dataset for the control sample with 0 mM $MnCl_2$ was collected using SerialEM software (Mastronarde, 2005) and a Glacios electron microscope equipped with a K2 Summit direct detector with the following parameters: nano-probe mode, operating voltage 200 kV, 22,000× magnification (1.885 Å/pix), varying defoci from -1.5 μm to -3 μm, 0.5 μm steps, exposure of 15 s, 50 frames/micrograph, and total dose 58.5 e/Å^2. The recorded frames were gain-normalized, aligned, motion corrected, and dose-weighted using MotionCor2 software (Zheng et al., 2017). Defocus values were assessed using CTFFIND4 software. A total of 1935 micrographs were acquired with automated picking by Gautomatch. The particles were boxed out with a box size of 174 pixels. Then 2D alignment and classification were performed in RELION3. Representative images and classes are displayed in Fig. 6A. After particle alignment and 2D classification, only densities for the ectodomains of α5β1 were visible in both conditions. Despite extensive efforts to optimize the cryo grid preparation, we were not able to visualize the membrane density. However, SEC, corresponding negative-staining, peptide sequencing, and mass spectrometry showed full coverage of the sequence. Therefore, we concluded that the lack of membrane density was due to the specific characteristics of the cryo-EM sample preparation, such as the interaction of the membrane scaffolding with the air–water interface. That interaction in particular is known to cause local instability on embedded proteins during cryo-EM sample preparation, which might cause the integrin to become separated from the membrane scaffold. Therefore, the remaining transmembrane helices and cytoplasmic domains would be too flexible to appear as shown in the 2D and 3D classes, a notion supported by the progressive decrease in local resolution at the lower leg and the further downstream portion of the 3D reconstruction.

Cryo-EM data collection for high-resolution structural analysis

Datasets for high-resolution image analyses of FN-bound (Fig. 1) and resting (Fig. 4) integrin α5β1 were collected using SerialEM software (Mastronarde, 2005) and a Titan

Krios (ThermoFisher) equipped with a K3 Summit direct detector and a quantum energy filter (20 eV slit width) (Gatan) in nano-probe mode at an operating voltage of 300 kV.
For the resting integrin α5β1 dataset (Fig. 4), 2818 micrographs were recorded at 105,000× magnification (0.85 Å/pixel) in counting mode with varying defoci from -0.5 μm to -3.2 μm in 0.3 μm steps at a total dose of either 65.8 e/Å^2 (2 s exposure, 20 frames, 3.13 e/Å^2 frame dose) or 82.3 e/Å^2 (2.5 s exposure, 50 frames, 1.65 e/Å^2 frame dose). The frames of the combined micrographs were gain-normalized, motion corrected, aligned, and dose-weighted using MotionCor2. Defocus and image resolution values were assessed using either GCTF or CTFFIND4. A total of 1424 particles were manually picked and boxed out with a box size of 300 pixels. Then 2D alignment and classification were performed using RELION3. 6 of 2D class averages with distinct features were used as a template for automated picking with Gautomatch. A total of 496,356 automatically picked particles were boxed out with a box size of 300 pixels, downscaled to 150 pixels, aligned, and 2D classified in RELION3. After initial sorting, 255,514 particles remained and were further sorted into 8 classes by 3D classification. The reference for the 3D classification was the reconstruction obtained from the screening dataset, which was then low-pass filtered to 30 Å. The 98,750 particles with the most prominent features were selected from the reconstruction for further processing. Those particles were rescaled to the original box size of 300 and further refined in the RELION3 processing pipeline, resulting in the final density map of the whole molecule with 6.2 Å total resolution, as determined by the gold-standard Fourier shell correlation criterion (FSC=0.143) in the RELION3 postprocessing option. Using Chimera (Pettersen et al., 2004) and the implemented Segger plugin (Pintilie et al., 2010; 2009), the map of the whole molecule was divided into the headpiece and the lower legs (see Fig. S6) and then low-pass filtered to 15 Å. The envelopes were then used to generate masks, which were subsequently used for the Multibody refinement option in RELION3 (Nakane et al., 2018). The Multibody refinement displayed movement between the two parts. Next, partial signal subtraction of either the headpiece or the lower leg signal was performed within RELION3, taking their different orientations as determined by Multibody refinement into account. With focused 3D refinement after subtraction, the headpiece resolution was improved to 4.6 Å, as determined by the FSC=0.143 criterion using the RELION3 postprocessing option. The resolution of the lower leg part was more flexible and determined to be 8 Å according to the local resolution analysis.

For the FN7-10-bound and TS2/16 Fv-clasp–bound α5β1 dataset (Fig. 1), 9,431 micrographs were recorded at 64,000× magnification (1.38 Å/pixel) in counting mode with varying defoci from -0.8 μm to -2.6 μm in 0.3 μm steps at a total dose of 59.7 e/Å^2 (7.39 s exposure, 37 frames, 1.61 e/Å^2 frame dose). Initial image processing steps were automatically performed on a GPU workstation running the modular Focus software (Biyani et al., 2017). Those steps included gain normalization, motion correction, and dose-weighting by MotionCor2; CTF estimation by GCTF; and particle picking by Gautomatch, using a template obtained from a the screening dataset of the same sample (see above). A total of 4,218,951 particles were boxed out with a box size of 360 pixels, initially downscaled to 90 pixels, aligned, and 2D classified in RELION3. After initial sorting, 1,492,856 particles remained and were further sorted by 3D classification using a 30 Å low-pass filtered map obtained from a previous dataset created on the same sample grid (see the paragraph below for details on how 3D reference was initially obtained). From the 6 initially generated 3D classes, the two with the clearest signal were selected, which resulted in 680,610 particles. Those particles were rescaled to their original size (360 pixels) and further refined in the RELION3 processing pipeline, resulting in the final density map of the whole molecule with 3.5 Å total resolution, as determined by the FSC=0.143 criterion in the RELION3 postprocessing option. Using Chimera (Pettersen et al., 2004) and the implemented Segger plugin (Pintilie et al., 2010; 2009), the map was divided into 2 parts: the stable core, comprising the β-propeller, βI and hybrid domains, and the FN 9-10 and TS2/16 Fv-clasp; and the flexible, protruding densities, combining FN7-8 as well as the remaining integrin leg densities (thigh domain and PSI) (see Fig. 1 and S3). Both maps were imported into RELION3, low-pass filtered to 15 Å, and used to generate masks. Within RELION3, the signal of the flexible, protruding parts was partially subtracted, and the remaining density was subjected to focused 3D refinement, using the whole molecule as a reference and applying the mask of the 'core'. That procedure improved the resolution of the core part to 3.1 Å, as determined by the FSC=0.143 criterion in the RELION3 postprocessing option.

Model building

To prepare an initial model of the FN-bound and TS2/16-bound integrin α5β1, the available crystal structures 4wk0 (α5β1 headpiece (Xia and Springer, 2014)), 3vi3 (α5β1 headpiece with upper legs (Nagae et al., 2012), 5xcx (TS2/16 Fv-clasp (Arimori et al.,

2017)), and 1fnf (FN 7-10 (Leahy et al., 1996)) were fit as rigid bodies into the EM density maps using CHIMERA (Pettersen et al., 2004)). The model was further refined by manual building and real-space refinement in COOT (Emsley et al., 2010), using maps of the core density of integrin (integrin α5β1, FN 9-10, and TS2/16 Fv-clasp) at a resolution of 3.1 Å and that of the whole molecule at a resolution of 3.5 Å as references. B factors were then added, and the structure was validated using PHENIX (Afonine et al., 2018). The final structure fitted well to the cryo-EM density, with a correlation coefficient around the model (CC_{mask}) of 0.77 (Table S1). Note that the B-factors of the periphery of the model (FN7 and integrin legs) are high because of the flexibilities of the corresponding portions. For the resting integrin α5β1, the crystal structures 4wjk (Xia and Springer, 2014) and 3vi3 (Nagae et al., 2012) showing the headpiece and headpiece with upper legs, respectively, were used for initial fitting in CHIMERA. The missing parts of the lower legs (calf 1 and 2, PSI, EGF 1-4, and β-tail domains) were prepared by homology modeling based on the crystal structure 3fcs (ectodomain of integrin αIIbβ3 (Zhu et al., 2008)) using MODELLER (Webb and Sali, 2014). The initial model was manually adjusted, and domains were linked using COOT. B factors were added, and the structure was validated using PHENIX (Afonine et al., 2018). The final structure fit well to the cryo-EM density, with a correlation coefficient around the model (CC_{mask}) of 0.61 (Table S1). Note that the B-factors of the periphery of the model (integrin lower legs) are high because of the flexibilities of the corresponding portions.

Figure 1: Cryo-EM analysis of FN-bound integrin α5β1 reveals an open conformation.

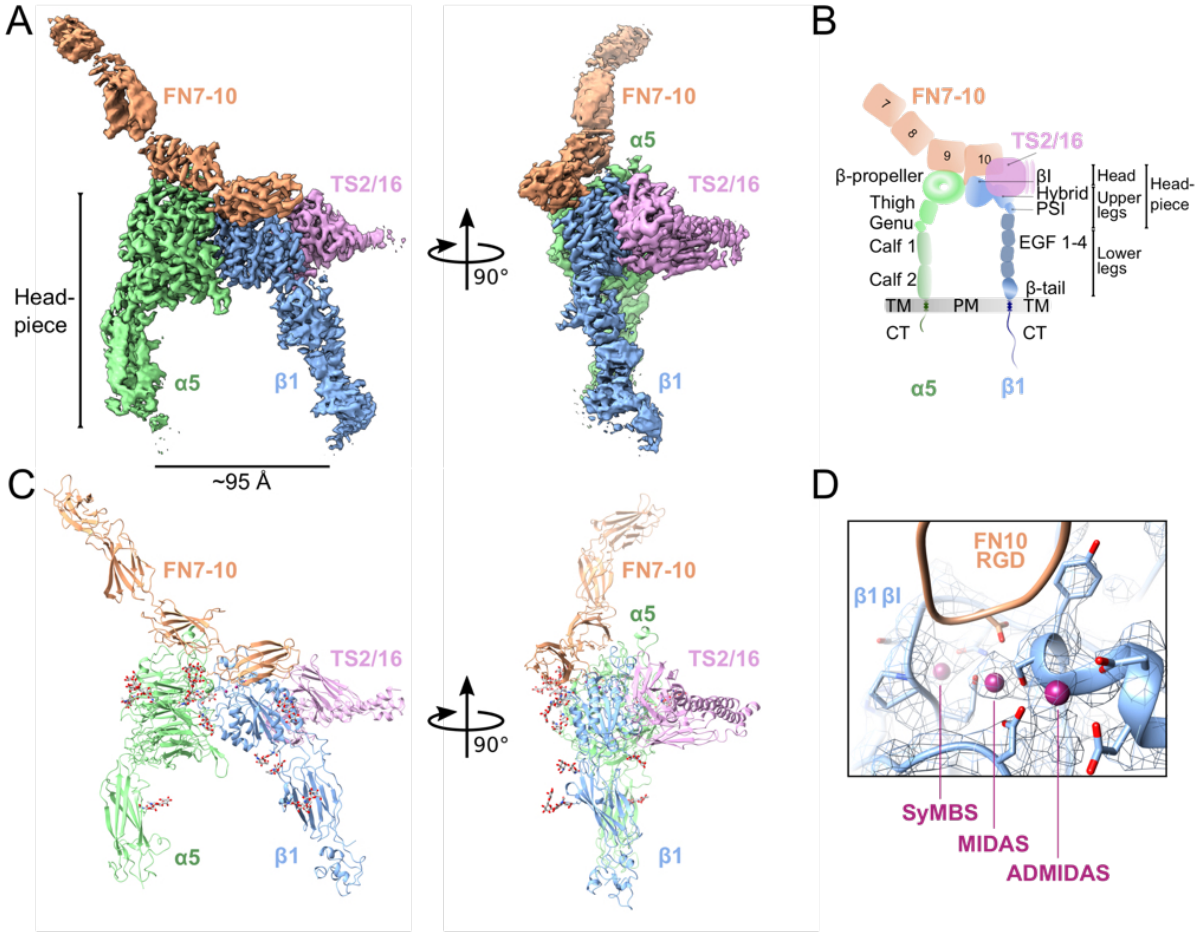

Figure 1: Cryo-EM analysis of FN-bound integrin α5β1 reveals an open conformation.

A: Two views of the FN7-10 (orange) -bound α5β1 (green - α subunit, blue - β subunit) cryo-EM structure, stabilized by TS2/16 (pink). The headpiece reveals an open conformation.

B: Schematic of integrin α5β1 domain architecture and nomenclature of different parts (headpiece, head, upper legs and lower legs), including FN7-10 and TS2/16.

C: Molecular model based on the cryo-EM density, showing the same two views as A.

D: Close-up and overlay of cryo-EM density with the modeled metal ion binding sites SyMBS, MIDAS and ADMIDAS within the βI domain.

Figure 2: N-glycosylation of integrin α5β1 bridges interface to FN.

A

Integrin	Residue	Domain	Visible Tree
α_5	N43	β-propeller	
α_5	N141	β-propeller	
α_5	N256	β-propeller	
α_5	N266	β-propeller	
α_5	N275	β-propeller	
α_5	N568	Linker region	
β_1	N249	βI	
β_1	N343	βI	
β_1	N386	Hybrid	
β_1	N397	Hybrid	

● D-Mannose ■ N-Acetyl-D-Glucosamine

B

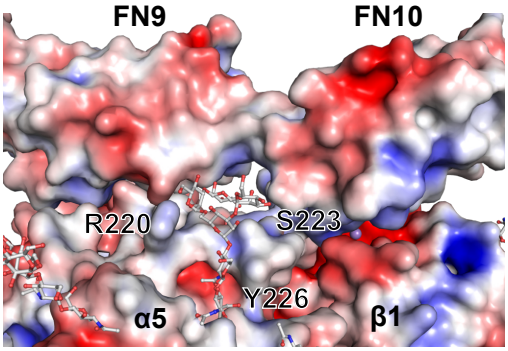

C

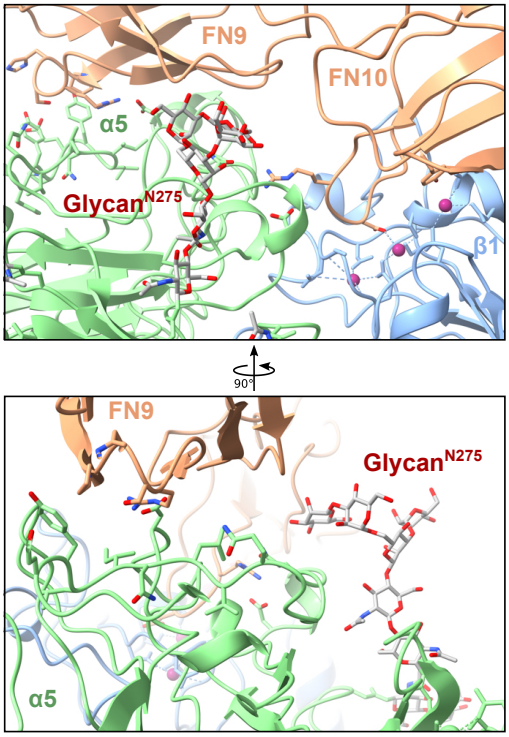

D

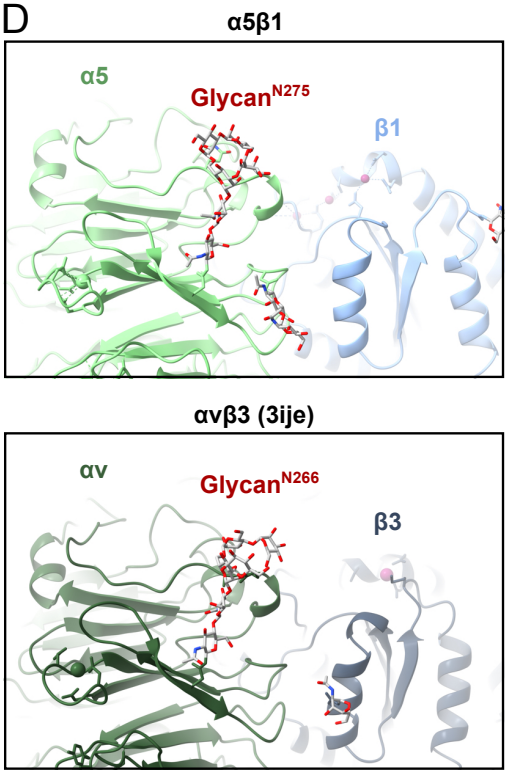

Figure 2: N-glycosylation of integrin α5β1 bridges interface to FN.

A: Table listing the N-glycosylation sites and the types of glycan trees as determined in our structure.

B: Electrostatic potential map of the FN-integrin interface and the N275-glycan.

C: Two views of the N275-glycan on α5, which is part of the extensive α5β1-FN interface. The N275-glycan contacts with FN9.

D: Comparison of glycan position between integrin α5β1 and integrin αvβ3 (3ije (*32*)). The N275-glycan (α5β1) is a conserved glycosylation site among FN-recognizing integrins such as αvβ3.

Figure 3: Binding of integrin α5β1 to FN7-10 occurs through an extensive interface, including RGD, synergy site and an additional juxta-ADMIDAS area.

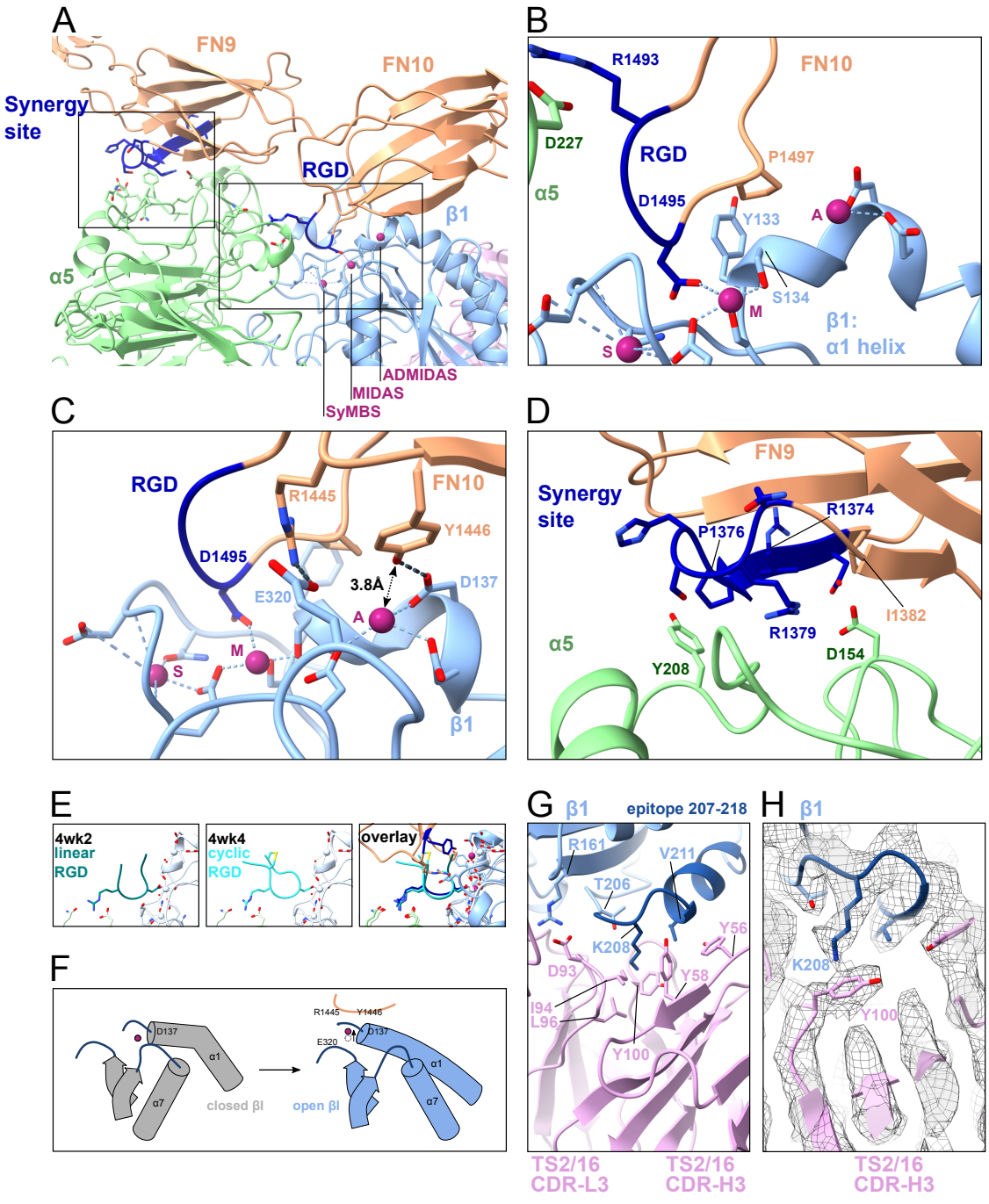

Figure 3: Binding of integrin α5β1 to FN7-10 occurs through an extensive interface, including RGD, the FN synergy site and the additional juxta-ADMIDAS area.

A. Overview of the extensive α5β1-FN interface. The main sites, RGD-MIDAS, ADMIDAS and the synergy site, are expanded in panels (B-D).

B: The RGD loop of FN10 is inserted into the binding pocket between the α5- and β1-subunits, and binds to the amino acids of α5 (Q221 and D227) and the MIDAS cation located in β1. New interactions are identified between P1497(FN10) and -Y133(β1) and between P1497(FN10) and -S134(β1).

C: Key interactions around ADMIDAS identified in this study, between R1445 (FN10) and E320 (β1), forming a salt bridge, and between Y1446 (FN10) and D137 (β1).

D. The synergy site of FN9 contacts the α5-subunit, through the key salt bridge between R1379 (FN9) and D154 (α5), and the interaction of P1376(FN9) and Y208(α5). R1374 is not visibly engaged.

E: Comparison of our FN-bound structure with two structures of RGD peptide-bound α5β1 (4wk2 and 4wk4, paler colors (Xia and Springer, 2014)) reveals that the comparable interactions among those structures; however RGD peptide is not enough to translocate the ADMIDAS and thus the opening of the headpiece.

F: Schematics of the different arrangement of the secondary elements around ADMIDAS and FN.

G: Interaction between the antibody TS2/16 and integrin β1 centered with K208 in βI domain surrounded by hydrophobic interactions.

(Abbreviations: A=ADMIDAS, M=MIDAS, S=SyMBS)

H: Close-up of the cation-π interaction between K208 (β1) and Y100 (TS2/16 CDR-H3) and overlay with cryo-EM density (grey).

Figure 4: Resting integrin α5β1 reveals an incompletely bent conformation.

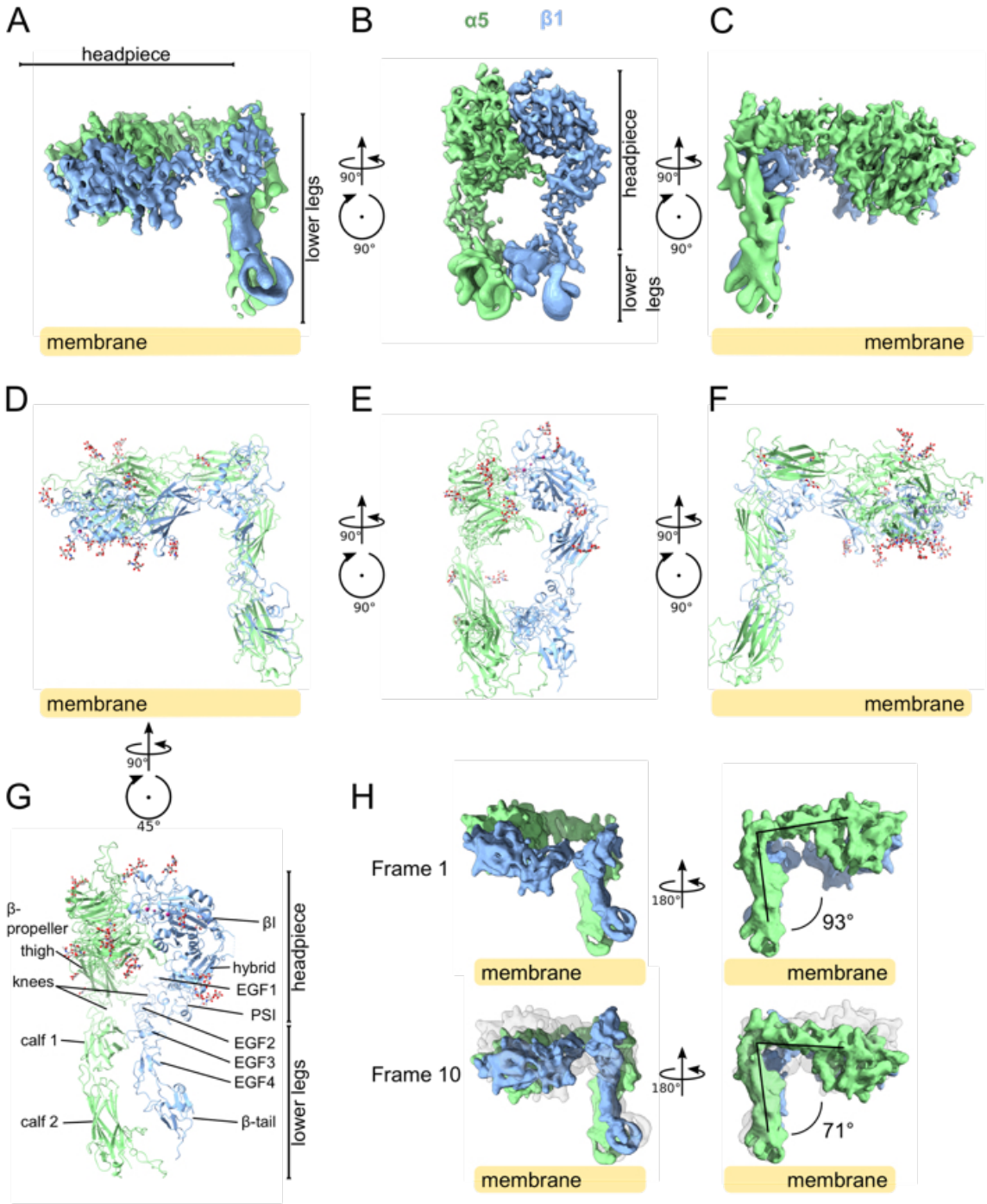

Figure 4: Resting integrin α5β1 reveals an incompletely bent conformation.

A-C: Three views of the resting integrin α5β1 cryo-EM structure. The position of the membrane is indicated in yellow.

D-F: The structure of the headpieces and modeled structure using homology models of PDB: 3fcs for the lower legs. The headpiece reveals a closed conformation, with an orthogonal angle between the headpiece and legs.

G: The lower legs of integrin α5β1 are parallelly contacting each other, between EGF1/2 (β1) and calf 1 (α5).

H: Multibody analysis revealed flexibility between the headpiece and lower legs, with an angle varying from 71° to 93° between the first analyzed state ('frame 1') and the last state ('frame 10'). See Fig. S7 for all the frames.

Figure 5: Resting integrin α5β1 is disadvantageous for FN binding.

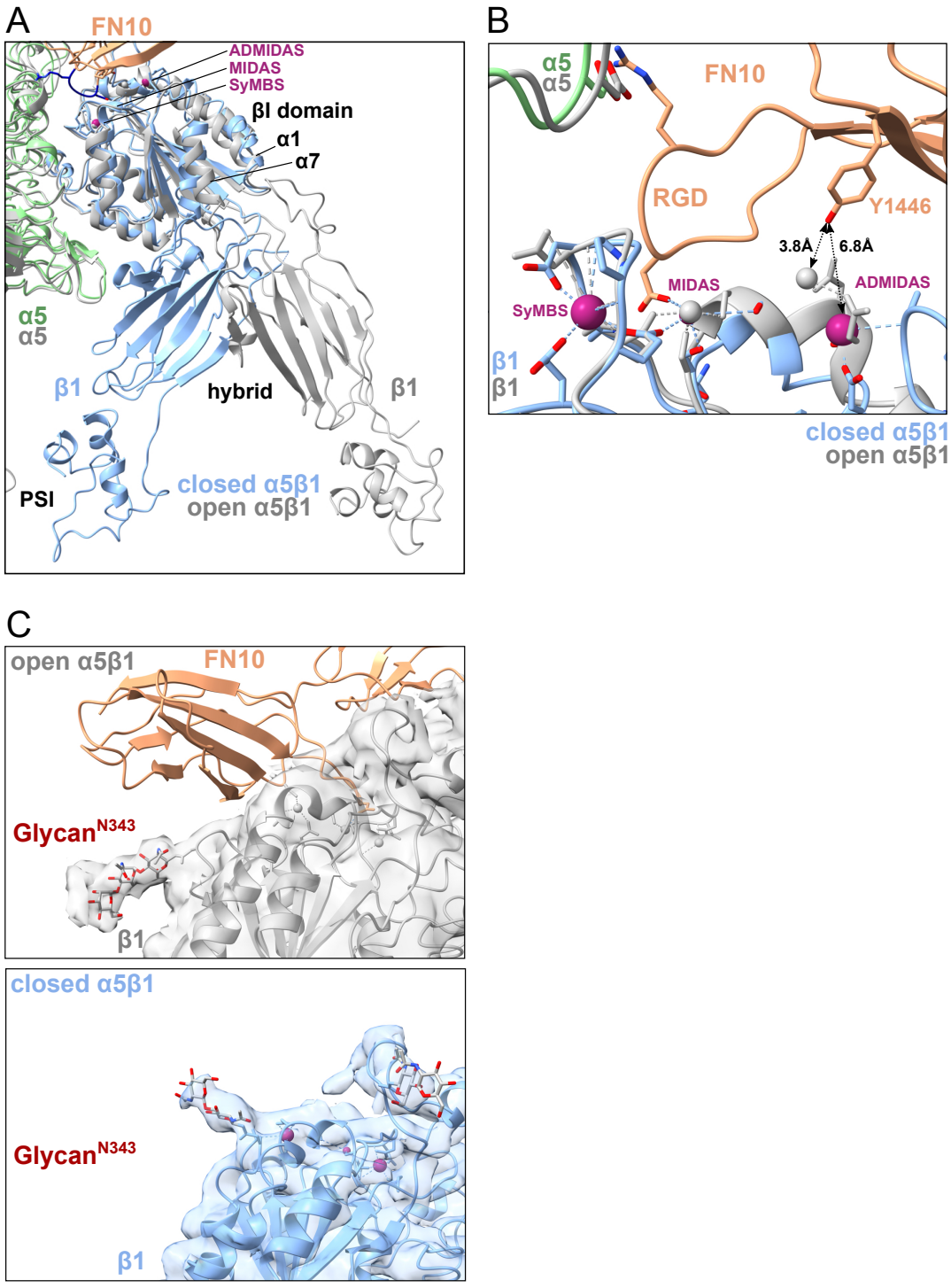

Figure 5: Resting integrin α5β1 is disadvantageous for FN binding

A: An overlay of the βI, hybrid, and PSI domains of resting (blue) and FN-bound integrin (grey) show the movement of the α1 and α7 helices in the βI domain and the subsequent swing-out motion of the hybrid domain.

B: ADMIDAS is farther from FN10 (Y1446) in the resting βI domain (blue) than in the open βI domain (grey).

C: Comparison of the position of N343-glycan on β1 with (top) and without (bottom) ligand binding. The N343-glycan hinders the FN binding in the resting structure.

Figure 6: FN binding of nanodisc containing α5β1 is enhanced by Mn^{2+}.

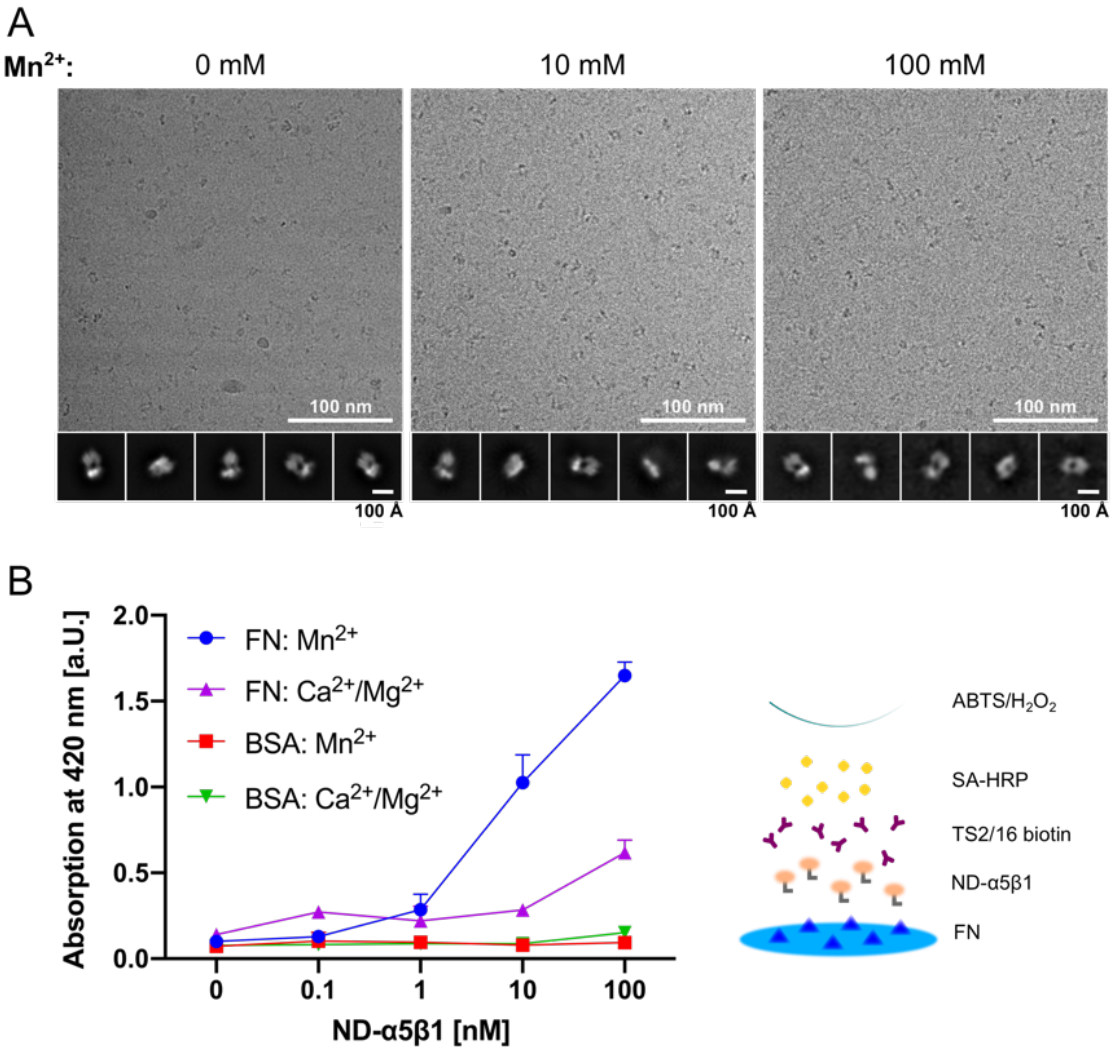

Figure 6: FN-binding of nanodiscs containing α5β1 is enhanced by Mn^{2+}.

A: Cryo-EM image of α5β1 with various concentrations of Mn^{2+}. 2D class averages are shown, revealing no integrin opening.

B: Solid-phase binding assays to measure integrin binding to full-length FN in the presence of activating (Mn^{2+}) or resting (Ca^{2+}/Mg^{2+}) buffer conditions and varying integrin α5β1 concentration. The principle of the assay is shown on the right. ND: nanodisc. Three individual experiments were conducted and all conditions were measured and averaged. Control measurements of α5β1 on BSA are shown.

Figure 7: Integrin α5β1 exists in an equilibrium of conformational states that can be altered by a combination of the ligands and stabilizing factors Mn^{2+}, FN7-10 and TS2/16.

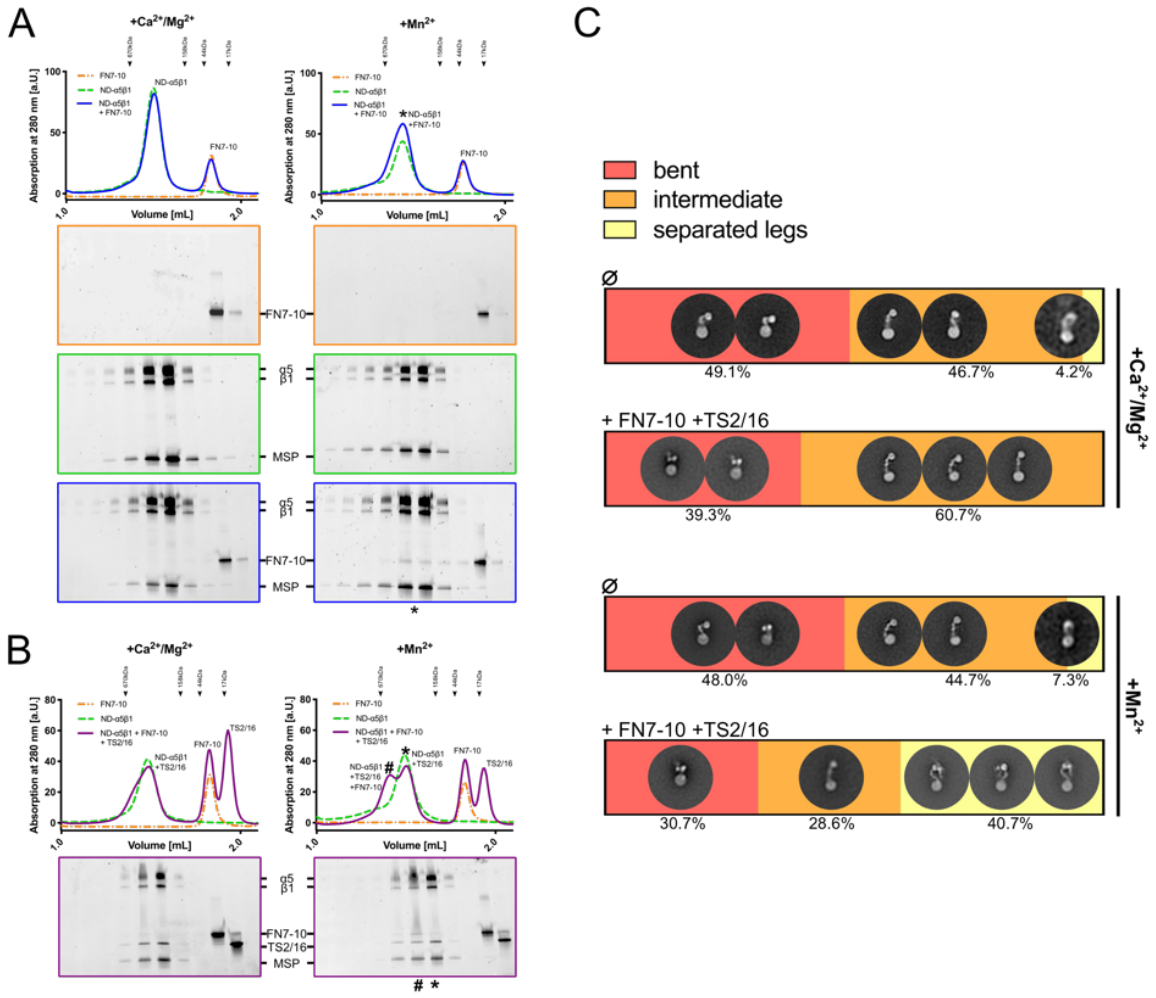

Figure 7: Integrin α5β1 exists in an equilibrium of conformational states that can be altered by a combination of ligands and stabilizing factors Mn^{2+}, FN7-10 and TS2/16.

A. FN7-10 binding to α5β1 was tested by SEC in resting (Ca^{2+}/Mg^{2+}) and activating (Mn^{2+}) buffer conditions. In the presence of Mn^{2+}, FN7-10 binding could be detected by SDS-PAGE. The peak containing ND-α5β1 and FN7-10 is marked with *. MSP: Membrane Scaffolding Protein used to form nanodiscs. The positions of molecular weight standards for gel filtration are marked with arrows on top of the chromatograms.

B. The effect of the antibody fragment TS2/16 Fv-clasp on α5β1 binding to FN7-10 was tested in the presence or absence of $MnCl_2$. When Mn^{2+}, FN7-10 and TS2/16 are mixed together with ND-α5β1, a peak shift can be observed (#). The positions of molecular weight standards for gel filtration are marked with arrows on top of the chromatograms.

C. Summary of the negative staining quantification of ND-α5β1 alone or mixed with Fn7-10 and TS2/16 Fv-clasp in resting (Ca^{2+}/Mg^{2+}) and activating (Mn^{2+}) buffer conditions. Particles were sorted into three states: 'bent', 'intermediate', and 'separated legs'. For each condition, ~20000 particles were initially picked, and those displaying a clear signal (i.e. ~5000-8000) were selected for the final quantification. Examples of 2D classes assigned to one of the states are shown.

Figure 8: Hypothetical model for integrin α5β1 opening.

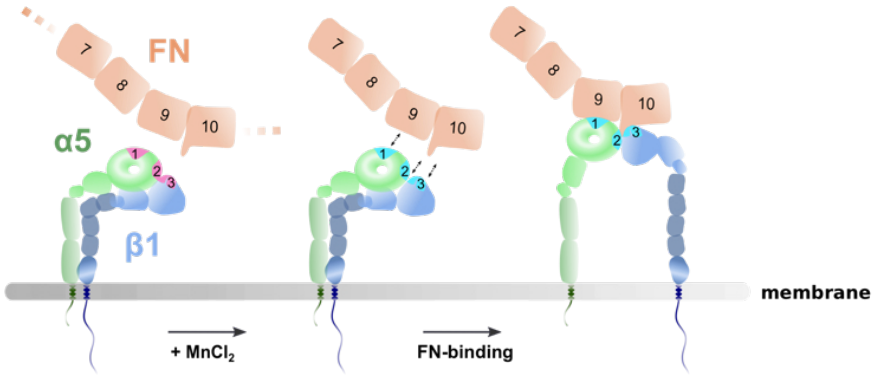

Figure 8: Model of integrin α5β1 opening.

Integrin α5β1 exists in an equilibrium of conformational states, fluctuating between bending and extension. FN binding secures the extended and open conformation of integrin α5β1 through three binding sites (marked as 1, 2 and 3) at the integrin heads. Mn^{2+} primes binding sites, SyMBS, ADMIDAS, and MIDAS and bring integrin to a ready state in which it is ready to bind to FN. Full engagement of FN takes place, resulting in the integrin α5β1 opening.

Supplementary:

S1: Purification of integrin α5β1 from human placenta and insertion into nanodiscs (ND).

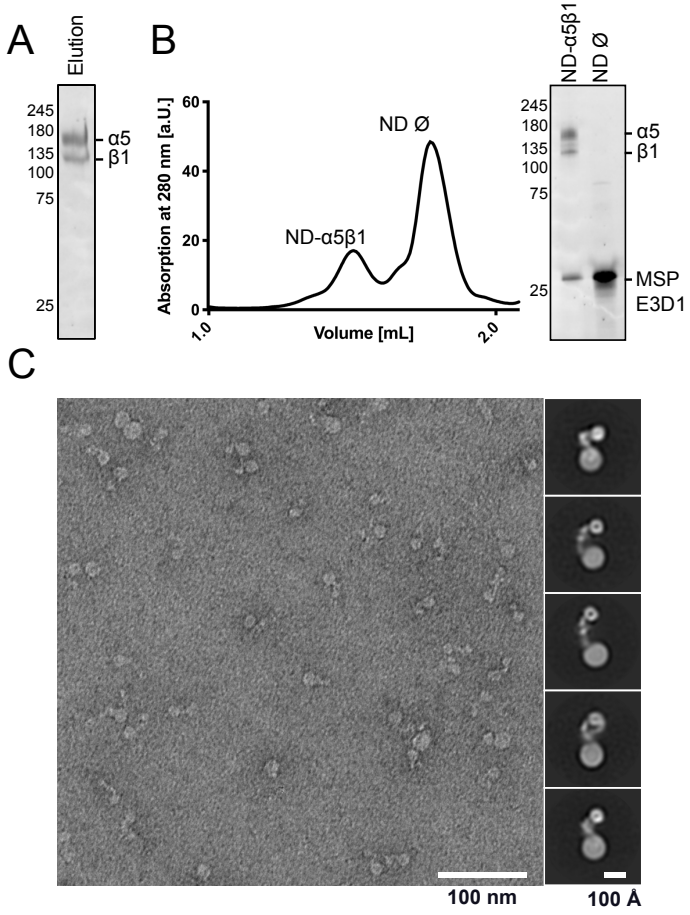

Figure S1: Purification of integrin α5β1 from human placenta and insertion into nanodiscs (Lele et al.).

A: Purified integrin α5β1 from placenta tissue.

B Left: Insertion of α5β1 into NDs (membrane scaffolding protein MSPE3D1) and lipid. NDs that contain α5β1 can be separated from empty NDs by size-exclusion chromatography (SEC). **Right:** SDS-PAGE analysis of the peak fractions showing that the first eluting peak contains α5β1 in complex with NDs, and the second peak contains only empty NDs (labelled with ∅).

C: Negative-stain analysis of the ND-α5β1 in B showing that α5β1 is properly inserted into the ND. Representative class averages are shown on the right side.

S2: Single-particle cryo-EM analysis of FN7-10, TS2/16-bound integrin α5β1.

A

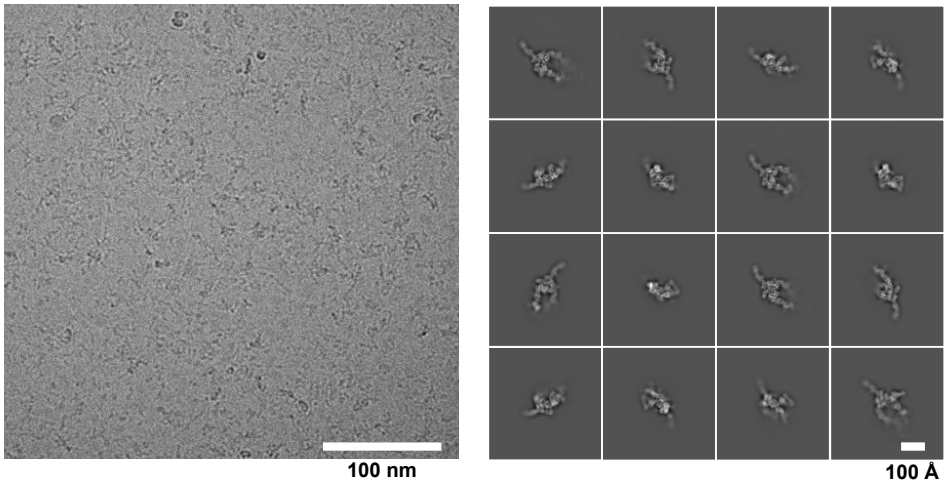

B

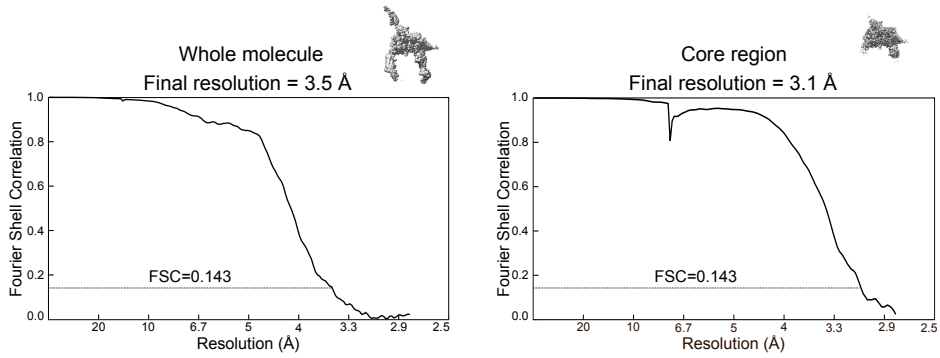

C

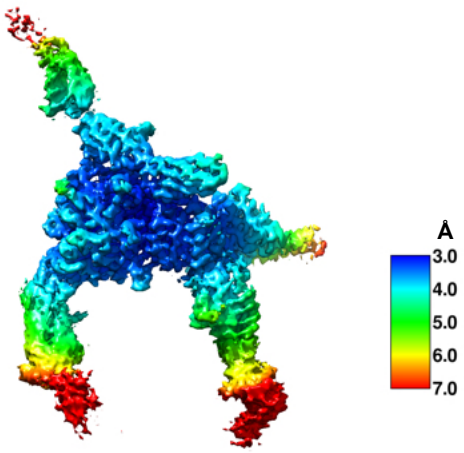

Figure S2: Single-particle cryo-EM analysis of FN7-10, TS2/16-bound integrin α5β1.
A Left: Representative cryo-EM image of the complex of FN7-10, TS2/16-bound integrin α5β1 and **right:** 2D class averages.
B: The FSC curve of the whole molecule revealing the α5β1 headpiece, FN7-10, and TS2/16, **left:** shows a global resolution of 3.5 Å. The FSC curve of the core (α5β1 head, FN9-10, TS2/16), **right**: after focused refinement shows a global resolution of 3.1 Å.
C: Local resolution analysis displays the resolution range within the cryo-EM density between 3-7 Å.

S3: Details of the data processing scheme that resulted in the final cryo-EM density maps of FN7-10 and TS2/16-bound integrin α5β1.

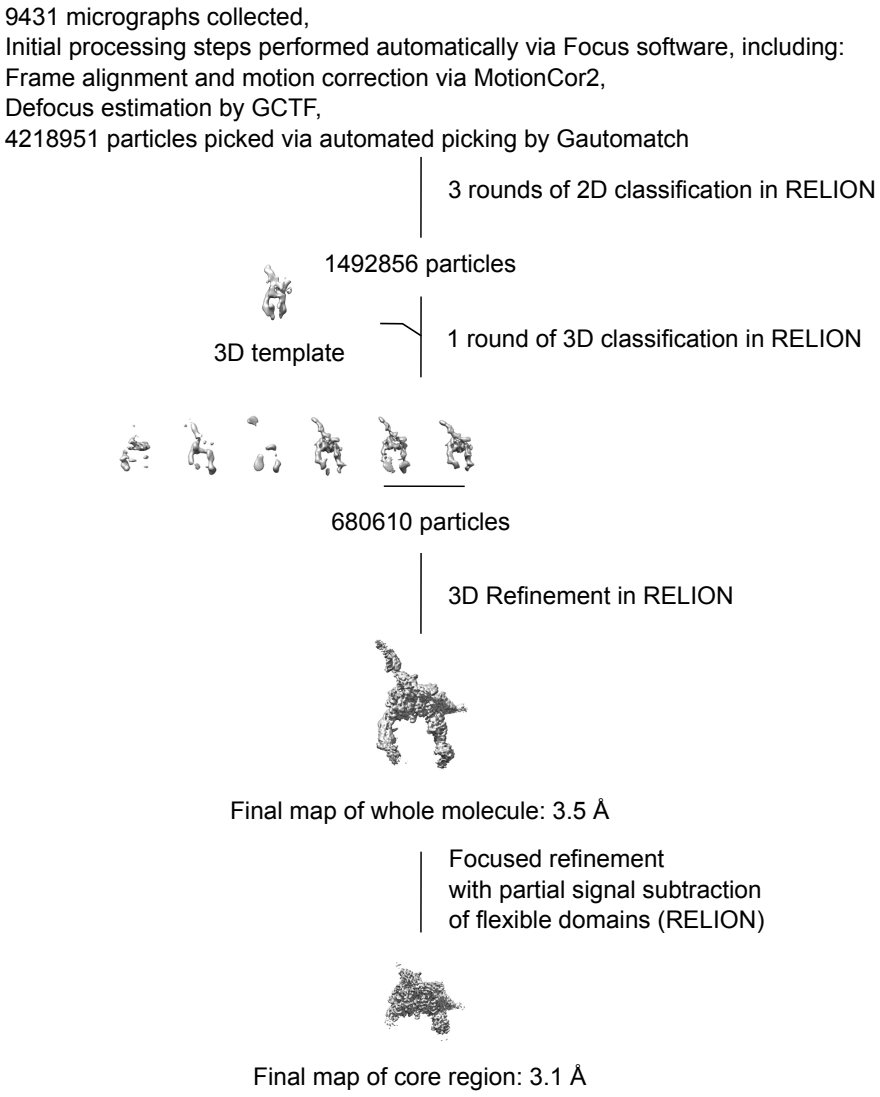

Figure S3: Details of the data processing scheme that resulted in the final cryo-EM density maps of FN7-10 and TS2/16-bound integrin α5β1.

Graphical summary of the data processing scheme for Fn7-10-bound and TS2/16-bound α5β1. Out of 4,218,951 automatically picked particles, 680,610 particles were selected after 2D and 3D classification in RELION3. Those particles resulted in the map of the whole molecule with a global resolution of 3.5 Å. After subtracting the flexible densities at the protruding parts of the molecule and performing focused refinement, the resolution of the core density was improved to 3.1 Å. The initial 3D template for 3D classification was obtained from a screening dataset.

S4: Integrin α5β1 and αvβ6 recognize their ligands in different ways.

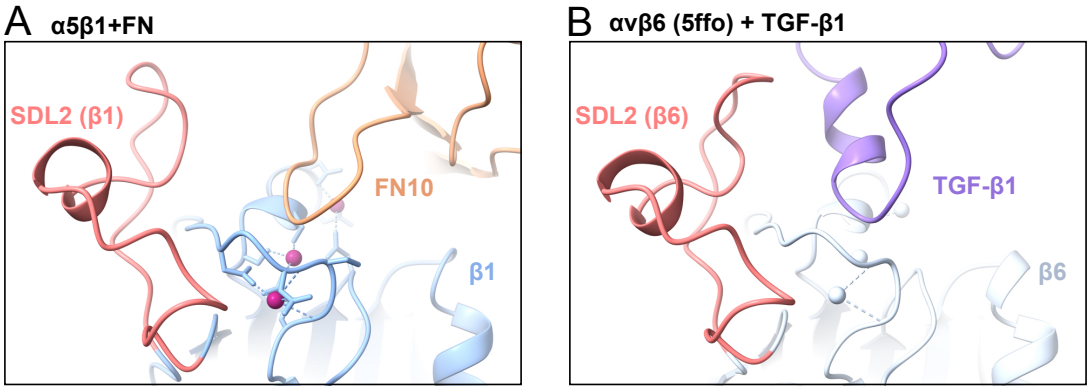

Figure S4: Integrin α5β1 and αvβ6 recognize their ligands in different ways.

A: SDL2 of α5β1 is unoccupied by the ligand FN.

B: In the structure of proTGF-b1-bound αvβ6, SDL2 is part of the ligand recognition site.

S5: Single-particle cryo-EM analysis of resting integrin α5β1.

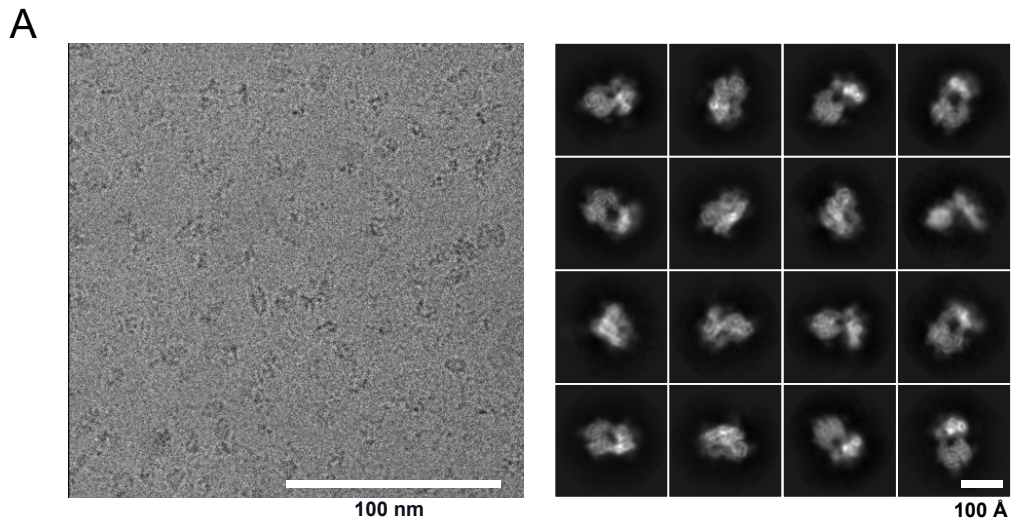

Figure S5: Single-particle cryo-EM analysis of resting integrin α5β1.

A Left: Representative cryo-EM image of resting integrin α5β1 and **Right:** 2D class averages.

B: The FSC curve of the whole molecule (α5β1 ectodomain, left) shows a global resolution of 6.2 Å. The FSC curve of the α5β1 headpiece (right) after Multibody and focused refinement shows a global resolution of 4.6 Å.

C: Local resolution analysis displays the resolution range within the cryo-EM density between 4.5-8.5 Å.

D: Example close-up view of the β1 headpiece overlay with cryo-EM density; the density for the side chain of K326 is clearly visible.

S6: Details of the data processing scheme that resulted in the final cryo-EM density maps of resting integrin α5β1.

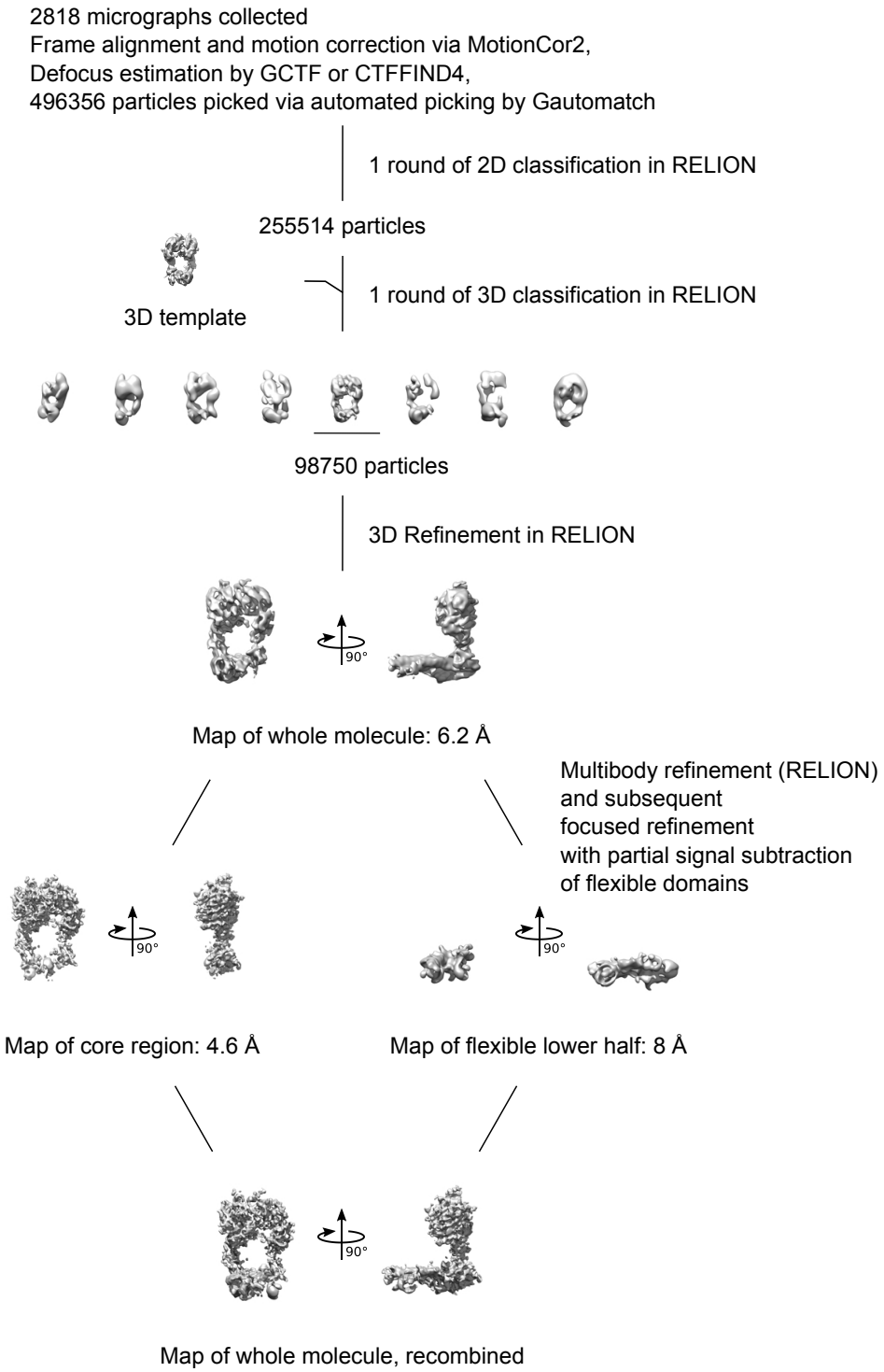

Figure S6: Details of the data processing scheme that resulted in the final cryo-EM density maps of resting integrin α5β1.

Graphical summary of the data processing scheme for resting α5β1. Out of 496,356 automatically picked particles, 98,750 particles were selected after 2D and 3D classification in RELION3. Those particles resulted in the map of the whole molecule with a global resolution of 6.2 Å. After performing multibody refinement and subsequent focused refinement with partial signal subtraction of the flexible leg parts, the resolution of the core density was improved to 4.6 Å. The initial 3D template for 3D classification was obtained from a separately obtained smaller dataset.

S7: Bent integrin α5β1 exhibits flexibility between headpiece and lower legs.

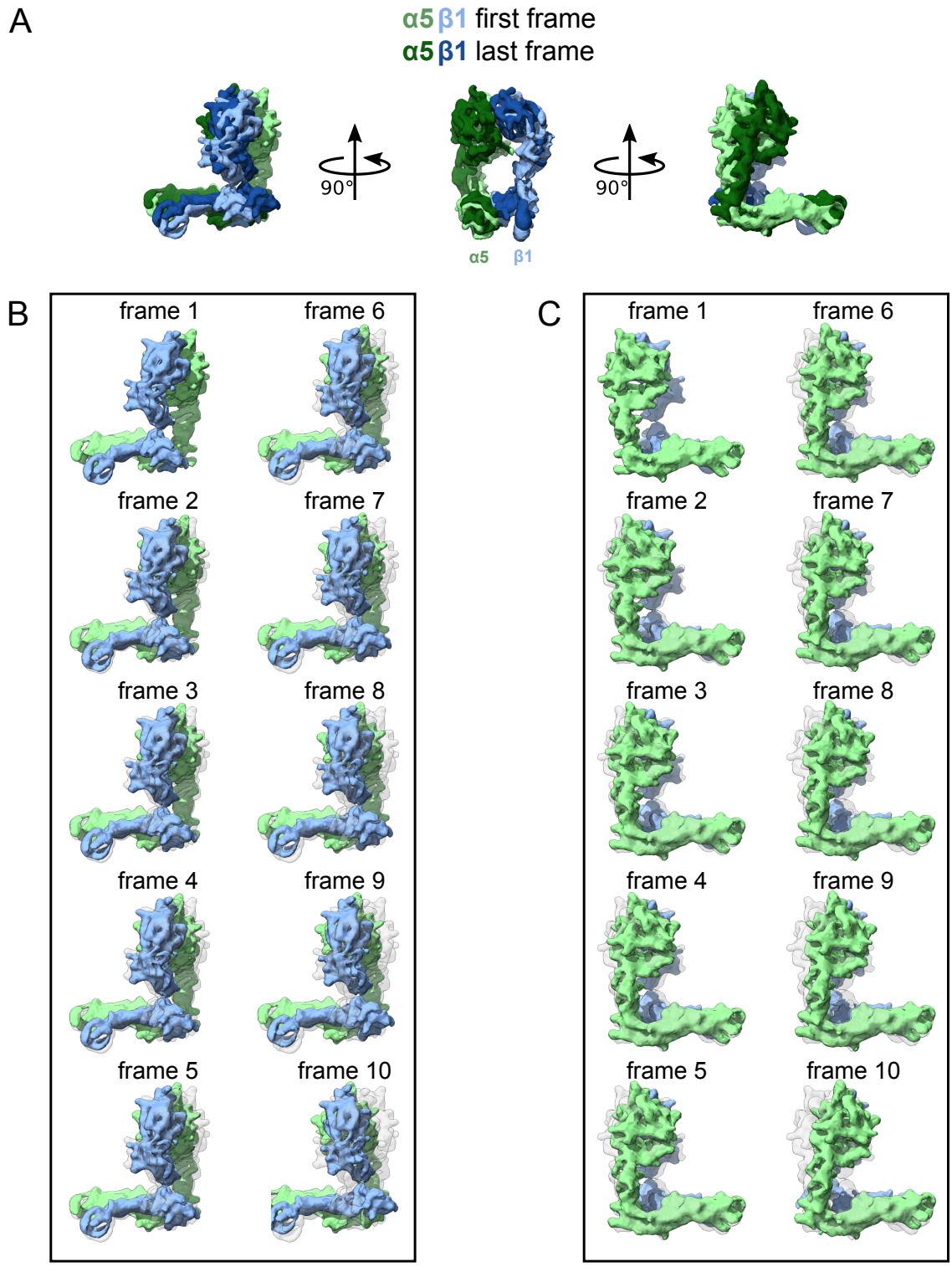

Figure S7: Bent integrin α5β1 exhibits flexibility between the headpiece and lower legs.

Multibody analysis (implemented in RELION3) between the headpiece and lower legs was performed to assess the flexibility.

A: Three views of bent integrin with the frame 1 shown in light colors and frame 10 displayed in dark colors.

B: All 10 frames of the two side views are overlaid with state 1 (frame 1) which is colored in light grey.

References

Afonine, P.V., Poon, B.K., Read, R.J., Sobolev, O.V., Terwilliger, T.C., Urzhumtsev, A., and Adams, P.D. (2018). Real-space refinement in PHENIX for cryo-EM and crystallography. Acta Crystallogr D Struct Biol *74*, 531–544.

Altroff, H., Schlinkert, R., van der Walle, C.F., Bernini, A., Campbell, I.D., Werner, J.M., and Mardon, H.J. (2004). Interdomain tilt angle determines integrin-dependent function of the ninth and tenth FIII domains of human fibronectin. J. Biol. Chem. *279*, 55995–56003.

Arimori, T., Kitago, Y., Umitsu, M., Fujii, Y., Asaki, R., Tamura-Kawakami, K., and Takagi, J. (2017). Fv-clasp: An Artificially Designed Small Antibody Fragment with Improved Production Compatibility, Stability, and Crystallizability. Structure *25*, 1611–1622.e1614.

Benito-Jardón, M., Klapproth, S., Gimeno-LLuch, I., Petzold, T., Bharadwaj, M., Müller, D.J., Zuchtriegel, G., Reichel, C.A., and Costell, M. (2017). The fibronectin synergy site re-enforces cell adhesion and mediates a crosstalk between integrin classes. Elife *6*, 562.

Biyani, N., Righetto, R.D., McLeod, R., Caujolle-Bert, D., Castano-Diez, D., Goldie, K.N., and Stahlberg, H. (2017). Focus: The interface between data collection and data processing in cryo-EM. J. Struct. Biol. *198*, 124–133.

Byron, A., Humphries, J.D., Askari, J.A., Craig, S.E., Mould, A.P., and Humphries, M.J. (2009). Anti-integrin monoclonal antibodies. J. Cell. Sci. *122*, 4009–4011.

Campbell, I.D., and Humphries, M.J. (2011). Integrin structure, activation, and interactions. Cold Spring Harb Perspect Biol *3*, a004994–a004994.

Campbell, M.G., Cormier, A., Ito, S., Seed, R.I., Bondesson, A.J., Lou, J., Marks, J.D., Baron, J.L., Cheng, Y., and Nishimura, S.L. (2020). Cryo-EM Reveals Integrin-Mediated TGF-β Activation without Release from Latent TGF-β. Cell *180*, 490–501.e16.

Copié, V., Tomita, Y., Akiyama, S.K., Aota, S., Yamada, K.M., Venable, R.M., Pastor, R.W., Krueger, S., and Torchia, D.A. (1998). Solution structure and dynamics of linked cell attachment modules of mouse fibronectin containing the RGD and synergy regions: comparison with the human fibronectin crystal structure. J. Mol. Biol. *277*, 663–682.

Cormier, A., Campbell, M.G., Ito, S., Wu, S., Lou, J., Marks, J., Baron, J.L., Nishimura, S.L., and Cheng, Y. (2018). Cryo-EM structure of the αvβ8 integrin reveals a mechanism for stabilizing integrin extension. Nat. Struct. Mol. Biol. *25*, 698–704.

Dedden, D., Schumacher, S., Kelley, C.F., Zacharias, M., Biertümpfel, C., Fässler, R., and Mizuno, N. (2019). The Architecture of Talin1 Reveals an Autoinhibition Mechanism. Cell *179*, 120–131.e13.

Denisov, I.G., Grinkova, Y.V., Lazarides, A.A., and Sligar, S.G. (2004). Directed self-assembly of monodisperse phospholipid bilayer Nanodiscs with controlled size. J. Am. Chem. Soc. *126*, 3477–3487.

Dong, X., Zhao, B., Iacob, R.E., Zhu, J., Koksal, A.C., Lu, C., Engen, J.R., and Springer, T.A. (2017). Force interacts with macromolecular structure in activation of TGF-β. Nature

542, 55–59.

Emsley, P., Lohkamp, B., Scott, W.G., and Cowtan, K. (2010). Features and development of Coot. Acta Crystallogr. D Biol. Crystallogr. *66*, 486–501.

Eng, E.T., Smagghe, B.J., Walz, T., and Springer, T.A. (2011). Intact alphaIIbbeta3 integrin is extended after activation as measured by solution X-ray scattering and electron microscopy. J. Biol. Chem. *286*, 35218–35226.

Engel, J., Odermatt, E., Engel, A., Madri, J.A., Furthmayr, H., Rohde, H., and Timpl, R. (1981). Shapes, domain organizations and flexibility of laminin and fibronectin, two multifunctional proteins of the extracellular matrix. J. Mol. Biol. *150*, 97–120.

Erickson, H.P., Carrell, N., and McDonagh, J. (1981). Fibronectin molecule visualized in electron microscopy: a long, thin, flexible strand. J. Cell Biol. *91*, 673–678.

Friedland, J.C., Lee, M.H., and Boettiger, D. (2009). Mechanically activated integrin switch controls alpha5beta1 function. Science *323*, 642–644.

Gu, J., Isaji, T., Sato, Y., Kariya, Y., and Fukuda, T. (2009). Importance of N-glycosylation on alpha5beta1 integrin for its biological functions. Biol. Pharm. Bull. *32*, 780–785.

Hagn, F., Nasr, M.L., and Wagner, G. (2018). Assembly of phospholipid nanodiscs of controlled size for structural studies of membrane proteins by NMR. Nat Protoc *13*, 79–98.

Huang, R., and Rofstad, E.K. (2018). Integrins as therapeutic targets in the organ-specific metastasis of human malignant melanoma. J. Exp. Clin. Cancer Res. *37*, 92–14.

Humphries, J.D., Byron, A., and Humphries, M.J. (2006). Integrin ligands at a glance. J. Cell. Sci. *119*, 3901–3903.

Hynes, R.O. (2002). Integrins: bidirectional, allosteric signaling machines. Cell *110*, 673–687.

Isaji, T., Sato, Y., Fukuda, T., and Gu, J. (2009). N-glycosylation of the I-like domain of beta1 integrin is essential for beta1 integrin expression and biological function: identification of the minimal N-glycosylation requirement for alpha5beta1. J. Biol. Chem. *284*, 12207–12216.

Isaji, T., Sato, Y., Zhao, Y., Miyoshi, E., Wada, Y., Taniguchi, N., and Gu, J. (2006). N-glycosylation of the beta-propeller domain of the integrin alpha5 subunit is essential for alpha5beta1 heterodimerization, expression on the cell surface, and its biological function. J. Biol. Chem. *281*, 33258–33267.

Kechagia, J.Z., Ivaska, J., and Roca-Cusachs, P. (2019). Integrins as biomechanical sensors of the microenvironment. Nat. Rev. Mol. Cell Biol. *20*, 457–473.

Kelley, C.F., Litschel, T., Schumacher, S., Dedden, D., Schwille, P., and Mizuno, N. (2020). Phosphoinositides regulate force-independent interactions between talin, vinculin, and actin. Elife *9*.

Kong, F., García, A.J., Mould, A.P., Humphries, M.J., and Zhu, C. (2009). Demonstration of catch bonds between an integrin and its ligand. J. Cell Biol. *185*, 1275–1284.

Leahy, D.J., Aukhil, I., and Erickson, H.P. (1996). 2.0 A crystal structure of a four-domain segment of human fibronectin encompassing the RGD loop and synergy region. Cell *84*, 155–164.

Luo, B.-H., Carman, C.V., and Springer, T.A. (2007). Structural basis of integrin regulation and signaling. Annu. Rev. Immunol. *25*, 619–647.

Main, A.L., Harvey, T.S., Baron, M., Boyd, J., and Campbell, I.D. (1992). The three-dimensional structure of the tenth type III module of fibronectin: an insight into RGD-mediated interactions. Cell *71*, 671–678.

Mastronarde, D.N. (2005). Automated electron microscope tomography using robust prediction of specimen movements. J. Struct. Biol. *152*, 36–51.

Miyazaki, N., Iwasaki, K., and Takagi, J. (2018). A systematic survey of conformational states in β1 and β4 integrins using negative-stain electron microscopy. J. Cell. Sci. *131*, jcs216754.

Nagae, M., Re, S., Mihara, E., Nogi, T., Sugita, Y., and Takagi, J. (2012). Crystal structure of α5β1 integrin ectodomain: atomic details of the fibronectin receptor. J. Cell Biol. *197*, 131–140.

Nakane, T., Kimanius, D., Lindahl, E., and Scheres, S.H. (2018). Characterisation of molecular motions in cryo-EM single-particle data by multi-body refinement in RELION. Elife *7*, 1485.

Pettersen, E.F., Goddard, T.D., Huang, C.C., Couch, G.S., Greenblatt, D.M., Meng, E.C., and Ferrin, T.E. (2004). UCSF Chimera--a visualization system for exploratory research and analysis. J Comput Chem *25*, 1605–1612.

Pintilie, G.D., Zhang, J., Goddard, T.D., Chiu, W., and Gossard, D.C. (2010). Quantitative analysis of cryo-EM density map segmentation by watershed and scale-space filtering, and fitting of structures by alignment to regions. J. Struct. Biol. *170*, 427–438.

Pintilie, G., Zhang, J., Chiu, W., and Gossard, D. (2009). Identifying Components in 3D Density Maps of Protein Nanomachines by Multi-scale Segmentation. IEEE NIH Life Sci Syst Appl Workshop *2009*, 44–47.

Punjani, A., Rubinstein, J.L., Fleet, D.J., and Brubaker, M.A. (2017). cryoSPARC: algorithms for rapid unsupervised cryo-EM structure determination. Nat. Methods *14*, 290–296.

Pytela, R., Pierschbacher, M.D., Argraves, S., Suzuki, S., and Ruoslahti, E. (1987). Arginine-glycine-aspartic acid adhesion receptors. Meth. Enzymol. *144*, 475–489.

Redick, S.D., Settles, D.L., Briscoe, G., and Erickson, H.P. (2000). Defining fibronectin's cell adhesion synergy site by site-directed mutagenesis. J. Cell Biol. *149*, 521–527.

Rohou, A., and Grigorieff, N. (2015). CTFFIND4: Fast and accurate defocus estimation

from electron micrographs. J. Struct. Biol. *192*, 216–221.

Schaffner, F., Ray, A.M., and Dontenwill, M. (2013). Integrin α5β1, the Fibronectin Receptor, as a Pertinent Therapeutic Target in Solid Tumors. Cancers (Basel) *5*, 27–47.

Sechler, J.L., Corbett, S.A., and Schwarzbauer, J.E. (1997). Modulatory roles for integrin activation and the synergy site of fibronectin during matrix assembly. Mol. Biol. Cell *8*, 2563–2573.

Springer, T.A., Zhu, J., and Xiao, T. (2008). Structural basis for distinctive recognition of fibrinogen gammaC peptide by the platelet integrin alphaIIbbeta3. J. Cell Biol. *182*, 791–800.

Su, Y., Xia, W., Li, J., Walz, T., Humphries, M.J., Vestweber, D., Cabañas, C., Lu, C., and Springer, T.A. (2016). Relating conformation to function in integrin α5β1. Proc. Natl. Acad. Sci. U.S.a. *113*, E3872–E3881.

Takada, Y., and Puzon, W. (1993). Identification of a regulatory region of integrin beta 1 subunit using activating and inhibiting antibodies. J. Biol. Chem. *268*, 17597–17601.

Takagi, J., Petre, B.M., Walz, T., and Springer, T.A. (2002). Global conformational rearrangements in integrin extracellular domains in outside-in and inside-out signaling. Cell *110*, 599–511.

Takagi, J., Strokovich, K., Springer, T.A., and Walz, T. (2003). Structure of integrin alpha5beta1 in complex with fibronectin. Embo J. *22*, 4607–4615.

Webb, B., and Sali, A. (2014). Comparative Protein Structure Modeling Using MODELLER. Curr Protoc Bioinformatics *47*, 5.6.1–.6.32.

Wierzbicka-Patynowski, I., and Schwarzbauer, J.E. (2003). The ins and outs of fibronectin matrix assembly. J. Cell. Sci. *116*, 3269–3276.

Winograd-Katz, S.E., Fässler, R., Geiger, B., and Legate, K.R. (2014). The integrin adhesome: from genes and proteins to human disease. Nat. Rev. Mol. Cell Biol. *15*, 273–288.

Xia, W., and Springer, T.A. (2014). Metal ion and ligand binding of integrin α5β1. Proc. Natl. Acad. Sci. U.S.a. *111*, 17863–17868.

Xiao, T., Takagi, J., Coller, B.S., Wang, J.-H., and Springer, T.A. (2004). Structural basis for allostery in integrins and binding to fibrinogen-mimetic therapeutics. Nature *432*, 59–67.

Xie, C., Zhu, J., Chen, X., Mi, L., Nishida, N., and Springer, T.A. (2010). Structure of an integrin with an alphaI domain, complement receptor type 4. Embo J. *29*, 666–679.

Xiong, J.P., Stehle, T., Diefenbach, B., Zhang, R., Dunker, R., Scott, D.L., Joachimiak, A., Goodman, S.L., and Arnaout, M.A. (2001). Crystal structure of the extracellular segment of integrin alpha Vbeta3. Science *294*, 339–345.

Xiong, J.-P., Mahalingham, B., Alonso, J.L., Borrelli, L.A., Rui, X., Anand, S., Hyman, B.T., Rysiok, T., Müller-Pompalla, D., Goodman, S.L., et al. (2009). Crystal structure of the complete integrin alphaVbeta3 ectodomain plus an alpha/beta transmembrane fragment. J. Cell Biol. *186*, 589–600.

Xiong, J.-P., Stehle, T., Zhang, R., Joachimiak, A., Frech, M., Goodman, S.L., and Arnaout, M.A. (2002). Crystal structure of the extracellular segment of integrin alpha Vbeta3 in complex with an Arg-Gly-Asp ligand. Science *296*, 151–155.

Zaidel-Bar, R., Itzkovitz, S., Ma'ayan, A., Iyengar, R., and Geiger, B. (2007). Functional atlas of the integrin adhesome. Nat. Cell Biol. *9*, 858–867.

Zhang, K. (2016). Gctf: Real-time CTF determination and correction. J. Struct. Biol. *193*, 1–12.

Zheng, M., Fang, H., and Hakomori, S. (1994). Functional role of N-glycosylation in alpha 5 beta 1 integrin receptor. De-N-glycosylation induces dissociation or altered association of alpha 5 and beta 1 subunits and concomitant loss of fibronectin binding activity. J. Biol. Chem. *269*, 12325–12331.

Zheng, S.Q., Palovcak, E., Armache, J.-P., Verba, K.A., Cheng, Y., and Agard, D.A. (2017). MotionCor2: anisotropic correction of beam-induced motion for improved cryo-electron microscopy. Nat. Methods *14*, 331–332.

Zhu, J., Luo, B.-H., Xiao, T., Zhang, C., Nishida, N., and Springer, T.A. (2008). Structure of a complete integrin ectodomain in a physiologic resting state and activation and deactivation by applied forces. Mol. Cell *32*, 849–861.

Zhu, J., Zhu, J., and Springer, T.A. (2013). Complete integrin headpiece opening in eight steps. J. Cell Biol. *201*, 1053–1068.

Zivanov, J., Nakane, T., Forsberg, B.O., Kimanius, D., Hagen, W.J., Lindahl, E., and Scheres, S.H. (2018). New tools for automated high-resolution cryo-EM structure determination in RELION-3. Elife *7*, 163.

3.2 The architecture of talin1 reveals an autoinhibition mechanism

Authors:
Dirk Dedden, **Stephanie Schumacher**, Charlotte F. Kelley, Martin Zacharias, Christian Biertümpfel, Reinhard Fässler, Naoko Mizuno

Published in: Cell (2019), 179, 120-131

During my PhD, I was able to contribute to a biochemical and structural study of the key adhesion protein and integrin activator talin 1. In this study, we solved the structure of full-length talin 1 in its autoinhibited state by cryo-EM. The arrangement of the molecule revealed how integrin-, membrane- and actin-binding sites within talin are shielded in the compact structure, which was confirmed by further biochemical experiments.

The study was performed under the supervision of Naoko Mizuno at the Max Planck Institute of Biochemistry in Martinsried, Germany, and conducted by the first author Dirk Dedden. I contributed to the biochemical characterization of talin 1. The detailed author contributions are listed in the manuscript.

Article

Cell

The Architecture of Talin1 Reveals an Autoinhibition Mechanism

Graphical Abstract

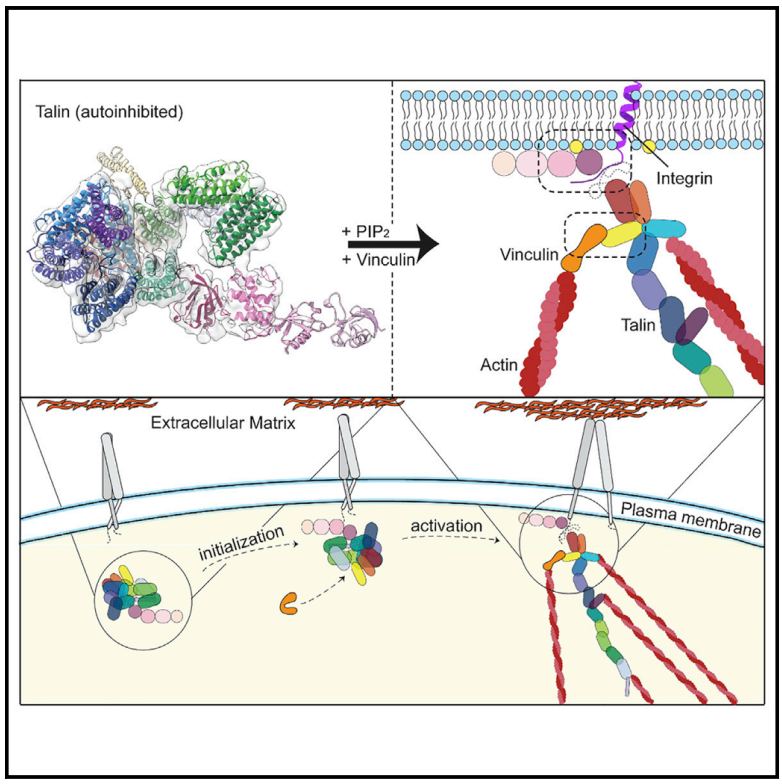

Authors

Dirk Dedden, Stephanie Schumacher, Charlotte F. Kelley, Martin Zacharias, Christian Biertümpfel, Reinhard Fässler, Naoko Mizuno

Correspondence

mizuno@biochem.mpg.de

In Brief

Structural characterization of talin shows how autoinhibition regulates interactions crucial for cell-cell contact and tension sensing.

Highlights

- The structure of the autoinhibited human full-length talin1 was analyzed by cryo-EM
- Talin1 reversibly changes between a 15-nm closed and a ~60-nm open conformation
- Rod R9/R12 and FERM domains synchronously shield membrane and cytoskeleton binding
- F-Actin and vinculin binding to talin is regulated by the opening of talin

Dedden et al., 2019, Cell *179*, 120–131
September 19, 2019
https://doi.org/10.1016/j.cell.2019.08.034

CellPress

Cell

Article

The Architecture of Talin1 Reveals an Autoinhibition Mechanism

Dirk Dedden,[1] Stephanie Schumacher,[1] Charlotte F. Kelley,[1] Martin Zacharias,[2] Christian Biertümpfel,[1] Reinhard Fässler,[3] and Naoko Mizuno[1,4,*]

[1]Department of Structural Cell Biology, Max Planck Institute of Biochemistry, Am Klopferspitz 18, 82152 Martinsried, Germany
[2]Physics Department (T38), Technical University Munich, James-Franck-Str. 1, 85748 Garching, Germany
[3]Department of Molecular Medicine, Max Planck Institute of Biochemistry, Am Klopferspitz 18, 82152 Martinsried, Germany
[4]Lead Contact
*Correspondence: mizuno@biochem.mpg.de
https://doi.org/10.1016/j.cell.2019.08.034

SUMMARY

Focal adhesions (FAs) are protein machineries essential for cell adhesion, migration, and differentiation. Talin is an integrin-activating and tension-sensing FA component directly connecting integrins in the plasma membrane with the actomyosin cytoskeleton. To understand how talin function is regulated, we determined a cryoelectron microscopy (cryo-EM) structure of full-length talin1 revealing a two-way mode of autoinhibition. The actin-binding rod domains fold into a 15-nm globular arrangement that is interlocked by the integrin-binding FERM head. In turn, the rod domains R9 and R12 shield access of the FERM domain to integrin and the phospholipid PIP_2 at the membrane. This mechanism likely ensures synchronous inhibition of integrin, membrane, and cytoskeleton binding. We also demonstrate that compacted talin1 reversibly unfolds to an ~60-nm string-like conformation, revealing interaction sites for vinculin and actin. Our data explain how fast switching between active and inactive conformations of talin could regulate FA turnover, a process critical for cell adhesion and signaling.

INTRODUCTION

Focal adhesions (FAs) are intracellular protein assemblies that serve as tension-sensing anchoring points to link cells to the extracellular environment (Geiger et al., 2009; Parsons et al., 2010). FAs not only tether cells to the extracellular matrix (ECM), but also facilitate intracellular reorganization, resulting in dynamic changes in cell functions and cell morphologies (Geiger et al., 2009; Legate et al., 2009; Parsons et al., 2010). FAs consist of hundreds of proteins in a layered arrangement that closely regulate each other (Kanchanawong et al., 2010). The first layer consists of integrin-signaling components at the plasma membrane, the second of force-transduction components, the third of actin-regulatory factors, and the fourth layer is made up of actin fibers. Several key proteins act to coordinate the individual functions of each layer, mediate crosstalk between layers, and to connect these layers with integrin receptor, the master-controller that links cytoplasmic FA complexes to the ECM (Bachir et al., 2014).

FA-mediated cellular processes are facilitated by alternating states of active and inactive integrins. In migrating cells, integrin activation initiates vast FA formation, allowing cells to attach to the extracellular environment, whereas integrin inactivation, followed by disassembly of FAs, detaches cells. This cycling of on/off states allows cells to continuously change anchoring points, facilitating cellular movement. Talin is a key component in FAs, responsible for activating integrins and mediating both inside-out and outside-in signaling (Tadokoro et al., 2003; Harburger and Calderwood, 2009; Nieswandt et al., 2007). Talin activates integrin by associating with the cytosolic tail of integrin beta-subunits. Once engaged, talin can assume an elongated conformation up to 100 nm in length (Liu et al., 2015), directly linking the beta-integrin subunit in the first layer of the FA to actin bundles in the fourth layer (Kanchanawong et al., 2010). By spanning all four layers of the FA, talin is in a unique position to act as a structural scaffold, greatly contributing to the overall composition and organization of FA complexes (Calderwood et al., 2013). In addition to its role as an integrin activator, talin also acts as a mechanosensor; it stretches like a spring and transmits tension between the ECM and the actomyosin machinery within the FA (Austen et al., 2015; Kumar et al., 2016), a process which is essential for regulating FA maturation and stability. As such, the transition between active and inactive talin likely plays a key regulatory role in FA dynamics, similar to the activation and inactivation of integrins.

Talin is a large, 270 kDa protein with 18 domains comprising an ~50 kDa globular head, a long rod made of 62 helices forming 13 helical bundle (rod) domains (R1–R13) (Calderwood et al., 2013; Goult et al., 2013), and a dimerization (DD) motif at the C terminus (Gingras et al., 2008). A unique conformational change of talin facilitates its spring-like behavior, through which talin can unfold into a linearly elongated 60–100 nm rod-like shape (Liu et al., 2015; Molony et al., 1987; Winkler et al., 1997). This allows it to bind to at least 11 different FA components including vinculin and actin (Goult et al., 2018). The talin head contains a 4.1-ezrin-radixin-moesin (FERM) domain with four subdomains (F0–F3), which is a common structural feature of several integrin tail-binding proteins (Elliott et al., 2010; Garcia-Alvarez et al., 2003; Goult et al., 2010; Rees et al., 1990). The FERM domain contains the integrin-binding site IBS1 (Tanentzapf and Brown, 2006; Wegener et al., 2007) and phosphatidylinositol-4,5-bisphosphate (PIP_2)

recognition site, allowing talin to attach to the membrane surface in a regulated way. The force-mediated stretching of talin is thought to follow (Atherton et al., 2015; Margadant et al., 2011), resulting in the exposure of up to 11 cryptic binding sites for vinculin (Fillingham et al., 2005; Gingras et al., 2005; Izard et al., 2004; Papagrigoriou et al., 2004). The binding of vinculin to talin is proposed to reinforce FA strength, as vinculin facilitates binding to actin, resulting in a cable-like configuration of F-actin (Case et al., 2015; Kanchanawong et al., 2010; Liu et al., 2015; Carisey et al., 2013; Humphries et al., 2007) and triggering the maturation of the FA (Zaidel-Bar et al., 2003).

While the active form of talin is well-characterized, the critical state of the inhibited form of talin is scarcely understood. The importance of talin inhibition is highlighted by the fact that disruption of proper talin inhibition leads to morphogenetic defects during fly development (Ellis et al., 2013) and it has been implicated in the migration of metastatic cancer cells (Desiniotis and Kyprianou, 2011; Fang et al., 2016; Haining et al., 2016). In its autoinhibited state, talin has a compact conformation (Goldmann et al., 1994; Goult et al., 2013; Winkler et al., 1997), with domains folded into each other, to occlude the interaction sites for binding partners such as integrin, membrane, vinculin, and F-actin. Although individual, truncated fragments of talin have been well-characterized, the regulation of full-length talin and the interplay among its domains are largely unknown on a molecular level. For example, a truncated fragment of the FERM domain (F3) was shown to interact with the R9 rod domain (Song et al., 2012); however, the overall mechanism is unclear because of the lack of information about the full-length architecture of talin.

Here, we report a cryoelectron microscopy (cryo-EM) structure of the autoinhibited form of recombinantly produced full-length talin1. The structure reveals charge-based interactions among the 13 rod domains of the talin1 monomer that entangle the protein into a compact 15 nm globular architecture, which is further secured by respective interactions between the F2 and F3 FERM subdomains and the R12 and R9 rod domains. Interestingly, the PIP_2-binding surface of the FERM domain is completely covered by the rod domain R12 to occlude access to the plasma membrane. The integrin-binding site is located at the deepest part of the autoinhibition pocket. The closure of the rod domains impedes binding to vinculin and to actin via the actin-binding site 2 (ABS2), although it does not occlude the other actin-binding site, ABS3. By mimicking talin activation, we facilitated talin1 binding to F-actin and vinculin. On the basis of these results, we propose a molecular model that explains how talin activation is controlled at a PIP_2-enriched membrane surface and how the protein transitions from a 15 nm globular structure to a 100 nm extended structure. Our results have wide-ranging implications for the mechanistic understanding of FAs and protein activation.

RESULTS

The Full-Length, Autoinhibited Talin1 Structure Shows Molecular Closure of the Rod Domains by the FERM Domain

Talin is thought to adopt open and closed conformational states (Figure 1A). While open talin is amenable to further stretching by its interacting partners, the globular state is likely to take on an autoinhibited conformation that hinders access to many of talin's binding sites, restricting interactions with other FA proteins. The autoinhibited form is thought to be the cytosolic state of talin that does not engage in FA assembly. It has been a challenge, however, to obtain a molecular view of the autoinhibited conformation. We successfully purified recombinantly expressed talin1 and pursued a full structural and biochemical characterization.

The cryo-EM analysis of full-length talin1 (talin-FL) in the autoinhibited conformation (Figures 1B, S1, and S2; Table S1) revealed an intertwined architecture. Although the intrinsic flexibility of talin limited the resolution of the structural reconstruction to a global resolution of 6.2 Å (Figures S2A–S2C; Table S1), the clear connectivity of the rod domains within the density map facilitated robust fitting of available structures of the 13 individual rod domains and the F2 and F3 subdomains of the FERM domain (Figures 1C and S3). We performed further refinement using a flexible fitting scheme by restraint molecular dynamics (Salomon-Ferrer et al., 2013). Our results show that the rod domains are entangled with each other, resulting in a compact organization, and the FERM domain closes the assembly via two anchoring points on rod domains R9 and R12, respectively, acting as a lid to secure the closure of the talin architecture (Figure 1D). At the first anchoring point, located in the deepest groove of the autoinhibition pocket (Figure 1E), the interacting surface between R9 and F3 agrees well with a previously reported crystal structure of isolated F3 and R9 fragments (Song et al., 2012) (Figure S4), which are necessary for talin inhibition in cells. At the second anchoring point (Figure 1E), located at the critical connecting point for the closure of talin1, K272 and K274 in F2 contact E2288 and D2297 at the C terminus of R12, respectively (Figure 1D).

While the F2 and F3 FERM subdomains revealed interactions necessary for talin1 autoinhibition, the densities corresponding to the F0 and F1 FERM subdomains were not visualized in our structure (Figure 1E). F0 serves as an interaction surface for the small GTPase Rap1 (Zhu et al., 2017), which acts as a recruiting factor to promote talin engagement with the plasma membrane (Goult et al., 2010; Plak et al., 2016) (Figure 1F). While these subdomains are missing from our structure, the corresponding fragments were identified by mass spectrometry (Figure S3B). This indicates that the F0-F1 subdomains are flexibly attached to the talin core structure, presumably by a long, 30 amino-acid linker between F1 and F2 (Figure 1E). Hence, F0 and F1 are likely not part of the inhibited structure, which suggests that talin can be recruited to the membrane surface via Rap1 without requiring disentanglement of the rod domains or disruption of the FERM domain interaction with R9 and R12 (Figures 1E and 1F).

The Closed Talin Configuration Occludes the Integrin-Binding Site and the Membrane-Binding Surface on the FERM Domain

The talin FERM domain was shown to interact with PIP_2 (Chinthalapudi et al., 2018; Orłowski et al., 2015; Song et al., 2012). Specific residues responsible for this interaction were recently identified including K272 of F2 and K316, K324, E342, and K343 of F3 (Chinthalapudi et al., 2018). We mapped their

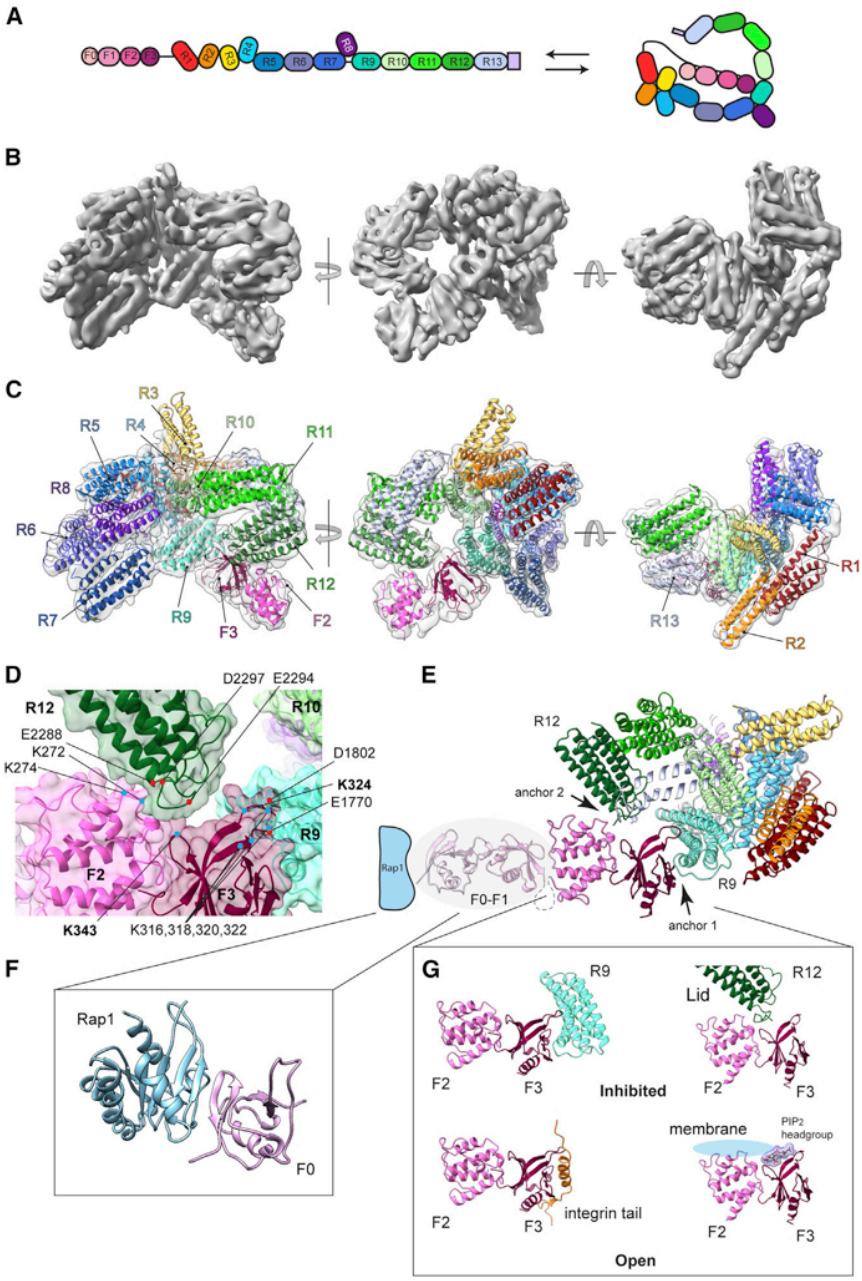

Figure 1. Structure of Full-Length Talin

(A) Schematic of the domain organization of talin in the open form (left) and the closed, autoinhibited form (right).

(B) Three views of the structure of full-length talin.

(C) Molecular fitting of talin fragments (PDB: 3IVF, 1SJ8, 2L7A, 2LQG, 2L7N, 2L10, 5IC1, 2KVP, 3DYJ, and 2JSW) to the EM density map.

(D) The molecular closure of talin achieved by F2-R12 and F3-R9 interactions and the charged amino acids surrounding the interaction interface. Bold highlighted numbers match previously published PIP_2-recognition residues.

(E) Superimposition of the F0-F1 subdomains of the talin FERM domain structure (overlaid with grey shadow, PDB: 3IVF) onto our cryo-EM talin model. The F0 and F1 subdomains were not visualized in our structural analysis due to the flexibility of the F1-F2 linker. The small GTP Rap1-binding site on F0 is mapped in blue and labelled "Rap1."

(F) The NMR structure of F0-Rap1 (PDB: 6BA6).

(G) Comparison of the F3-R9 and F2-R12 autoinhibition sites in the closed structure with the F3-integrin tail (PDB: 2H7D) and F2-F3-PIP_2 (PDB: 6MFS) as well as with the membrane-interaction sites of the FERM domain (Anthis et al., 2009), highlighting the mechanism of the autoinhibition of talin. In the inhibited form R12 forms a "lid" covering the PIP_2-binding site on F2-F3.

See also Figures S1, S2, S3, S4, and S5 and Table S1.

locations to understand the geometrical relationships among them in full-length talin (Figure 1D). In the autoinhibited talin structure, the PIP_2-binding surface was mostly covered by the rod domains, particularly by a region at the C terminus of R12, ensuring that the binding site was inaccessible to PIP_2 (Figures 1D and 1G). This region, containing the negatively charged amino acids E2288, E2294, and D2297 (Figure 1D), provides an acidic interface to complement the basic PIP_2-binding surface. Furthermore, to understand the arrangement of integrin and the plasma membrane with respect to talin in the open and closed configurations, we superimposed the available structure of the integrin cytosolic tail in complex with F3 (Anthis et al., 2009; Wegener et al., 2007) (Figure 1G). The integrin tail was shown to bind on the surface of the truncated F3 (Song et al., 2012), where R9 also binds in our autoinhibited structure, showing that the integrin-F3 interaction and the F3-R9 autoinhibitory interaction are mutually exclusive. Moreover, the integrin transmembrane helix directly precedes the integrin tail, indicating that F2 and R12 would have to separate to enable F2 and F3 to bind the inner face of the plasma membrane (Figure 1G). We also noted that the interaction surface of F3 for R9 has been reported to be a key interface for talin-binding partners, such as RIAM (Yang et al., 2014) and layilin (Wegener et al., 2008), which are likely involved in talin activation (Figure S4).

The Talin1 Folding Unit Is a Monomer in the Autoinhibited Form

The last 50 amino acids at the C terminus of talin1 have been crystalized as a coiled-coil in a dimeric structure (Gingras et al., 2008) (termed DD domain), suggesting the possibility that talin is capable of dimer formation. Furthermore, talin has been separately observed as a dumbbell-shaped dimer (Goldmann et al., 1994) when interacting with actin and as entwined dimers forming a globular assembly (Goult et al., 2013), keeping

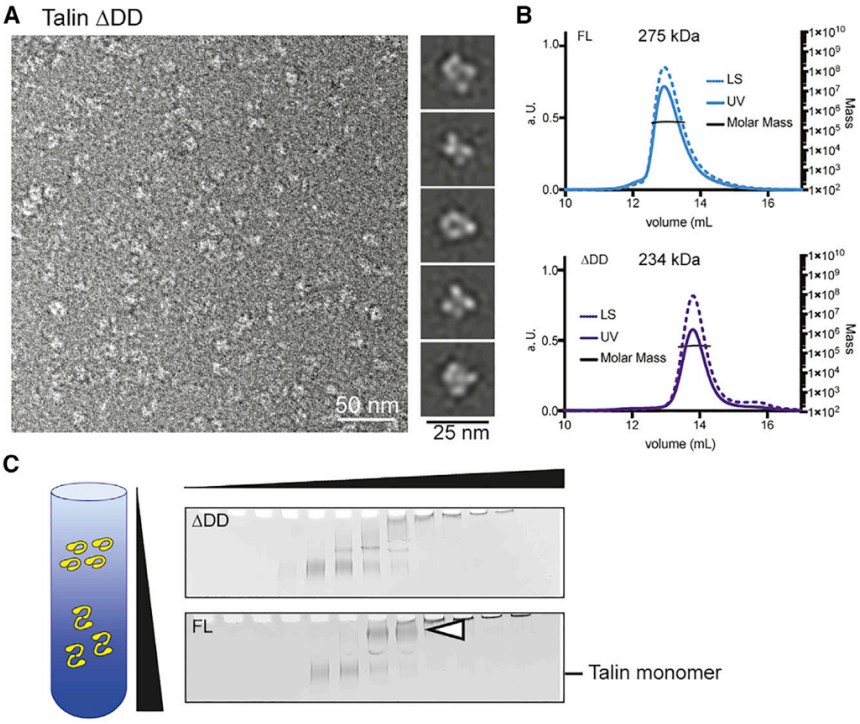

Figure 2. The Dimerization Domain Is Not Necessary for the Closure of Talin

(A) Negative-stain EM image of talin-ΔDD lacking the dimerization domain at 75 mM KCl, and 2D averages of the particles (right), showing a morphology similar to that of talin-FL.

(B) Size-exclusion chromatography coupled with multi-angle light-scattering profile of talin-FL and talin-ΔDD at 75 mM KCl, showing molecular weights corresponding to monomers. LS, light scattering, normalized; UV, absorbance.

(C) Centrifugation profiles of talin-ΔDD and talin-FL using the GraFix method. Talin-FL has an extra band in the fraction at higher sucrose density (open arrowhead). Black triangles depict the gradient of sucrose and glutaraldehyde concentrations.

the question open as to whether or not talin dimerization is necessary for its autoinhibition. Our cryo-EM structure clearly showed that talin1 monomers are capable of achieving an autoinhibited architecture.

The DD domain, which follows R13, was not clearly visible in our structure because of its flexibility, which in turn indicates that it is not engaged in the autoinhibited conformation. Indeed, a truncated talin construct that lacked the DD domain (talin-ΔDD) (Figure S3A) was still capable of assuming the autoinhibited conformation (Figure 2A), and analysis by size-exclusion chromatography coupled with multi-angle light scattering (SEC-MALS; Figure 2B) showed that both talin-FL and talin-ΔDD behave as monomers. Therefore, the DD domain appears to be inactive or not strong enough to hold talin-FL dimers together when talin is in the autoinhibited state. We further tested if we could find talin dimers as a minor component in the molecular population. Sucrose-gradient centrifugation of talin-FL in the presence of a concomitant gradient of the cross-linker glutaraldehyde (GraFix) (Stark, 2010) showed a minor population of talin that migrated differently in solution as well as on SDS-PAGE (Figure 2C), suggesting the presence of a talin-FL dimer, in agreement with the previous report (Goldmann et al., 1994). In contrast, talin-ΔDD did not display the corresponding minor band and showed only a single monomeric population, indicating that DD is the only domain in talin that is capable of facilitating dimerization.

Weak Interactions among Rod Domains Maintain the Compaction of Talin

To explore how the molecular opening of talin is regulated, we varied the ionic environment and tested if and how the conformation was changing. When we raised the ionic environment to 500 mM salt (NaCl or KCl), the conformation of full-length talin changed from the globular, closed architecture to the open, strand-like conformation (Figures 3A and 3B) with a length of 560 Å (SD = 170 Å) (Figure 3C), which fits well to the reported length of talin in a cell (Kanchanawong et al., 2010; Margadant et al., 2011). We looked for evidence of the conformational change as a function of the salt concentration using dynamic light-scattering (DLS) (Figure 3D), and the results fit well with a two-state model of protein folding-unfolding. At an ionic strength of 234 mM salt, the two states were equally populated and at a physiological salt concentration of 150 mM, 81% of talin had a compact conformation. We also found that this conformational change was reversible across fluctuating salt concentrations (Figure 3E).

Furthermore, we tested the importance of the inter-domain interactions for autoinhibition by creating point mutations as well as truncated talin constructs lacking the key domains for the interaction of F2-R12. We created a C-terminal truncation N-R11 lacking R12 and the C-terminus (Figure S3A), one of the two contact points necessary for the FERM-rod interactions, as well as N-R12 (Figure S3A). The DLS experiments showed the conformational changes of both constructs in response to the increase of salt concentration (Figure 3F). Point mutants of talin-FL altering the charge at the key interacting points on R12 (talin-FL-5K: E2288K/E2294K/D2297K/E2299K/D2300K and talin-FL-2K: E2288K/E2294K, Figure 1D) revealed a compact conformation at 75 mM salt and underwent a conformational change similar to wild type talin-FL upon change of the salt concentration (Figure 3G). These experiments led us to hypothesize that the rod domains themselves interact with each other to maintain a compact formation.

The rod domains contain several binding sites for critical FA components. Those sites include the F-actin-binding sites ABS2 and ABS3 on R4-R8 and R13-DD, respectively (Hemmings et al., 1996). We observed additional contacts among rod domains, as shown by the mapping of neighboring domains (Figure 4A). Particularly, R4 is placed at the "core" of the globular

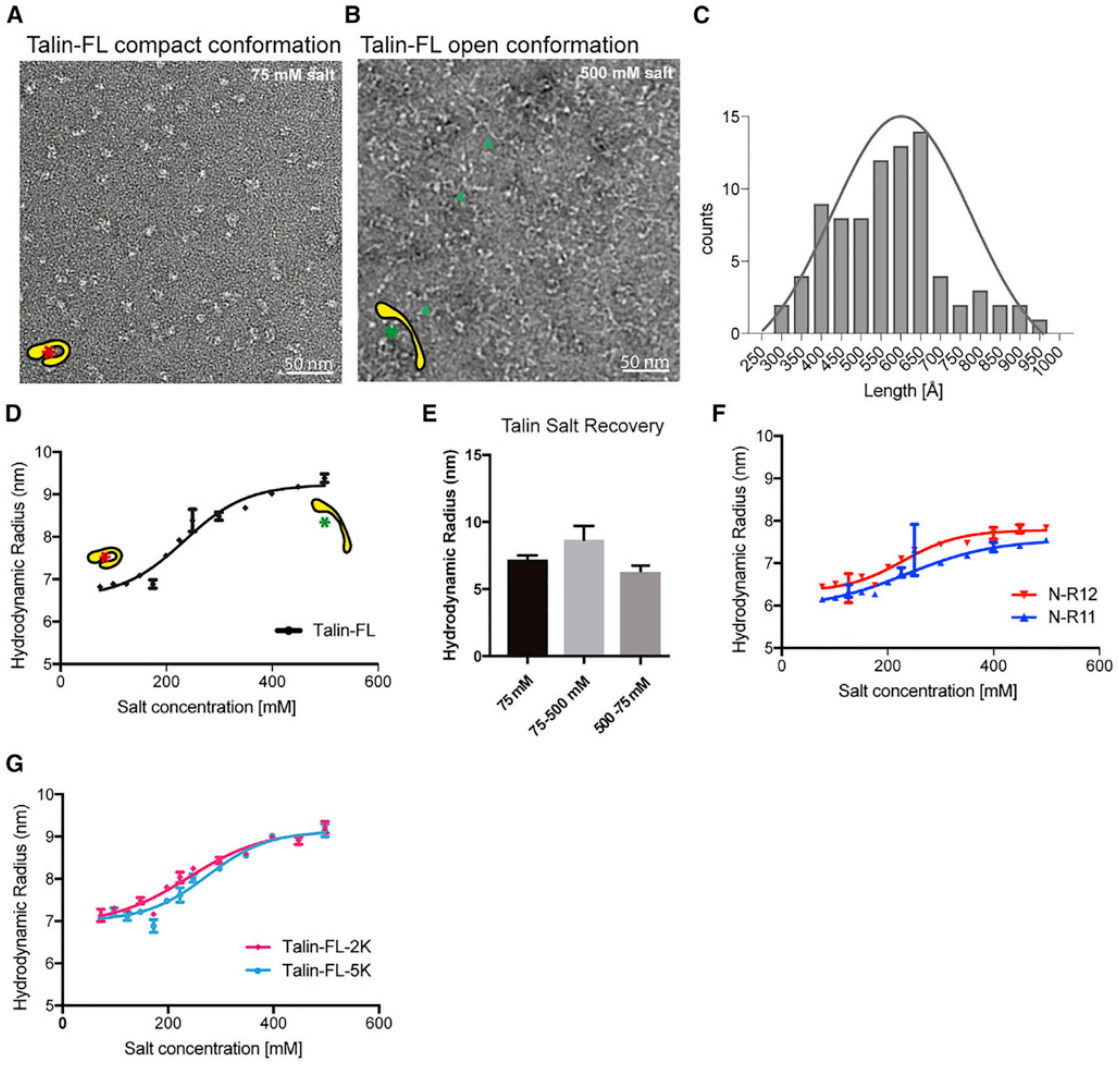

Figure 3. Two-State Conformational Ensemble of Talin

(A) Negative-stain EM image of talin-FL in the compact conformation at 75 mM KCl.

(B) Talin-FL in the open conformation in the presence of 500 mM KCl. Green arrowheads indicate examples of open talin.

(C) Distribution of the lengths of the open talin molecules from B (560 ± 170 Å, mean ± SD, N = 89).

(D) Dynamic light-scattering (DLS) measurements of the hydrodynamic radius of talin-FL under various salt concentrations, showing the conformational change of talin as a function of salt concentration. The fitted curve indicates that talin adopts both conformations at an equal ratio at a salt concentration of 234 mM. At a physiological salt concentration of 150 mM, 81% of talin employs the compact formation.

(E) Reversible conformational change of talin depending on the salt concentration as determined by DLS. Left: talin employs a closed conformation at an ionic strength of 75 mM. Center: talin opens and increases its size when the ionic strength is increased to 500 mM. Right: talin closes again when the ionic strength is lowered back to 75 mM, showing that the shape change of talin is reversible.

(F) DLS measurements of the hydrodynamic radius of N-R11 and N-R12 under various salt concentrations, showing a conformational change comparable to talin-FL with a lower amplitude. The data point at 250 mM was removed as the measurement was outside of the dynamic range of the detector.

(G) DLS measurements of point mutants of talin-FL-2K and talin-FL-5K, also showing conformational changes dependent on salt concentration. Error bars show standard deviations.

architecture and shielded by several rod domains (Figure 4B). We therefore tested the overall interactions among the rod domains by using a truncation construct that lacks the FERM domain (R1-C). DLS showed the change of the conformation in response to salt concentration (Figure 4C). To visualize the nature of the interaction, we calculated the electrostatic surface potential of each of the individual rod domains surrounding R4 and estimated the interaction energies of those domains to R4 (Figures 4A and S5). The calculated energy landscape for the domain-domain interactions indicated that the binding is rather weak (Figure S5B), resulting in an overall marginal stability. The rod domains may not rigidly bind to one another without cooperative, multi-module packing, as induced by the overall arrangement of the full-length protein. This explains the observation

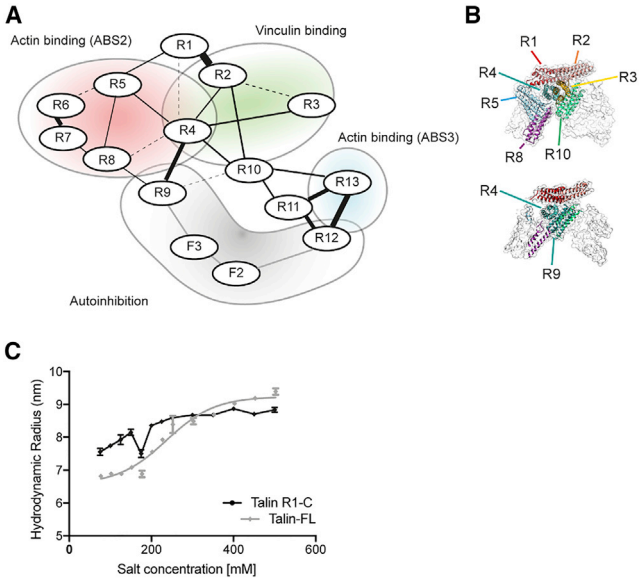

Figure 4. Interdomain Interactions of Talin

(A) Map of talin interdomain interactions derived from the EM structure. Binding domains relevant to this study are colored in red (actin-binding site ABS2), blue (actin-binding site ABS3), and green (vinculin-binding site). Dotted lines indicate positive (i.e., interactions are not favorable), while solid lines depict negative interaction energies (i.e., domains are interactive) as determined by MD simulations (see STAR Methods). The thickness of the lines is proportional to the calculated energies detailed in Figure S5.

(B) Spatial arrangement of the rod domains surrounding the R4 core in two vertical slices through the structure.

(C) DLS measurements of the hydrodynamic radius of R1-C under various salt concentrations in comparison to talin-FL (grey). The size distribution could not be fit to a two-state model. Error bars show standard deviations.

See also Figure S5.

that the talin architecture is highly sensitive and how its conformation can rapidly change in response to salt.

The Closed Conformation of Talin Prevents Vinculin Binding, whereas the Open Conformation Binds Vinculin with 1:1 Stoichiometry

Vinculin is a major talin-binding partner that facilitates crosstalk between talin and actin through its talin-binding head domain (V-head) and its actin-binding tail domain (V-tail) (Borgon et al., 2004; Johnson and Craig, 1994). Sequence-based analysis identified 11 potential vinculin-binding sites (VBSs) in talin (Gingras et al., 2005). Experiments using combinations of talin rod fragments indicated that R3, containing two VBSs, is a potent binding site for vinculin. It has been proposed that the unfolding of the helical bundle in R3 exposes the otherwise hidden binding domain to vinculin (Izard et al., 2004; Yao et al., 2014). Our truncation experiments supported that notion, as the talin fragments R1–R8 and R1–R3 formed complexes with V-head, whereas R4–R8 did not (Figure S6). It was unclear, however, how those observations would be reflected in the context of full-length talin.

To test the binding of vinculin to talin-FL, we performed reconstitution assays using size-exclusion chromatography (SEC, Figure 5A) at 75 mM KCl, where talin shows a compact architecture. While various truncations of talin including R3 readily bound to vinculin (Figure S6), the majority of talin-FL did not form complexes with full-length vinculin, V-head, or the vinculin mutant (V-mut, N773A/E775A) (Cohen et al., 2005), which exposes the talin interaction site by weakening the autoinhibition of vinculin (Figure 5A, first row). These findings suggest that the opening of the R3 helical bundle is hindered by steric constraints in the autoinhibited form of talin. The root of R3 is connected to R4, which is buried in the core of autoinhibited talin. Therefore, we attempted to reconstitute the talin-vinculin complex with talin at 500 mM KCl, where talin shows an open conformation. SEC revealed that talin and vinculin formed stable complexes with the V-mut (Figure 5A, second row). Talin formed a complex with V-head as well (Figures 5A and 5B). SEC-MALS showed that the corresponding chromatographic peaks were monodisperse with a molecular mass of 339 kDa, corresponding to a complex comprising one talin-FL and one vinculin molecule (Figure 5C). Interestingly, the talin-FL-2K and talin-FL-5K mutants, which were designed to weaken the interactions between F2 and R12 domains, were able to form a complex with V-head at 75 mM KCl (Figures 5D and 5E) significantly more than wild type talin-FL. This indicates that the disruption of F2-R12 leads to a partial access of vinculin, while these mutants employ compact conformations under this condition (Figure 3G).

The Compact Talin Can Retain Vinculin Head as a Complex but Induces the Dissociation of Full-Length Vinculin

To test the conformational change of talin in complex with vinculin, we exposed the reconstituted talin-V-head complex to low ionic strength conditions. We found that the retention volume of the SEC peak of the complex shifted from 1.27 mL (500 mM salt) to 1.31 mL (75 mM salt) (Figures 5A, S7A, and S7E), suggesting a possible compaction of the complex. DLS experiments of the preformed talin-FL-V-head complex indeed showed a conformational change upon variation in salt concentration, similar to talin-FL alone (Figures S7B–S7D). We also observed the conformational change of the complex of V-head with talin-FL-2K as well as talin-FL-5K, altogether pointing to the ability of talin to change its conformation in complex with vinculin head (Figures S7B and S7C).

The closed talin-V-head complex displayed a globular assembly that was similar to the closed morphology of talin alone (Figure S7F), although the talin-V-head complex had a slightly larger size (100 Å × 230 Å) than talin alone (~100 Å × 150 Å). Two-dimensional class averages of the talin-vinculin complex revealed a 60 Å protrusion from the ~100 Å globular head (Figure S7F, top panel). By combining available crystal structures of the talin VBS3 peptide bound to the vinculin N-terminal rods (N-terminal part of the vinculin head) (Izard et al., 2004), a full-length vinculin (Borgon et al., 2004), and our cryo-EM full-length talin in the autoinhibited form, we assembled a structural model of V-head binding to talin at the R3 domain with the talin helical bundle unfolded (Izard et al., 2004; Yao et al., 2014) (Figure S7G). This model matched well with the shape of the averaged talin-V-head complex (Figure S7F), indicating that the 60 Å protrusion on

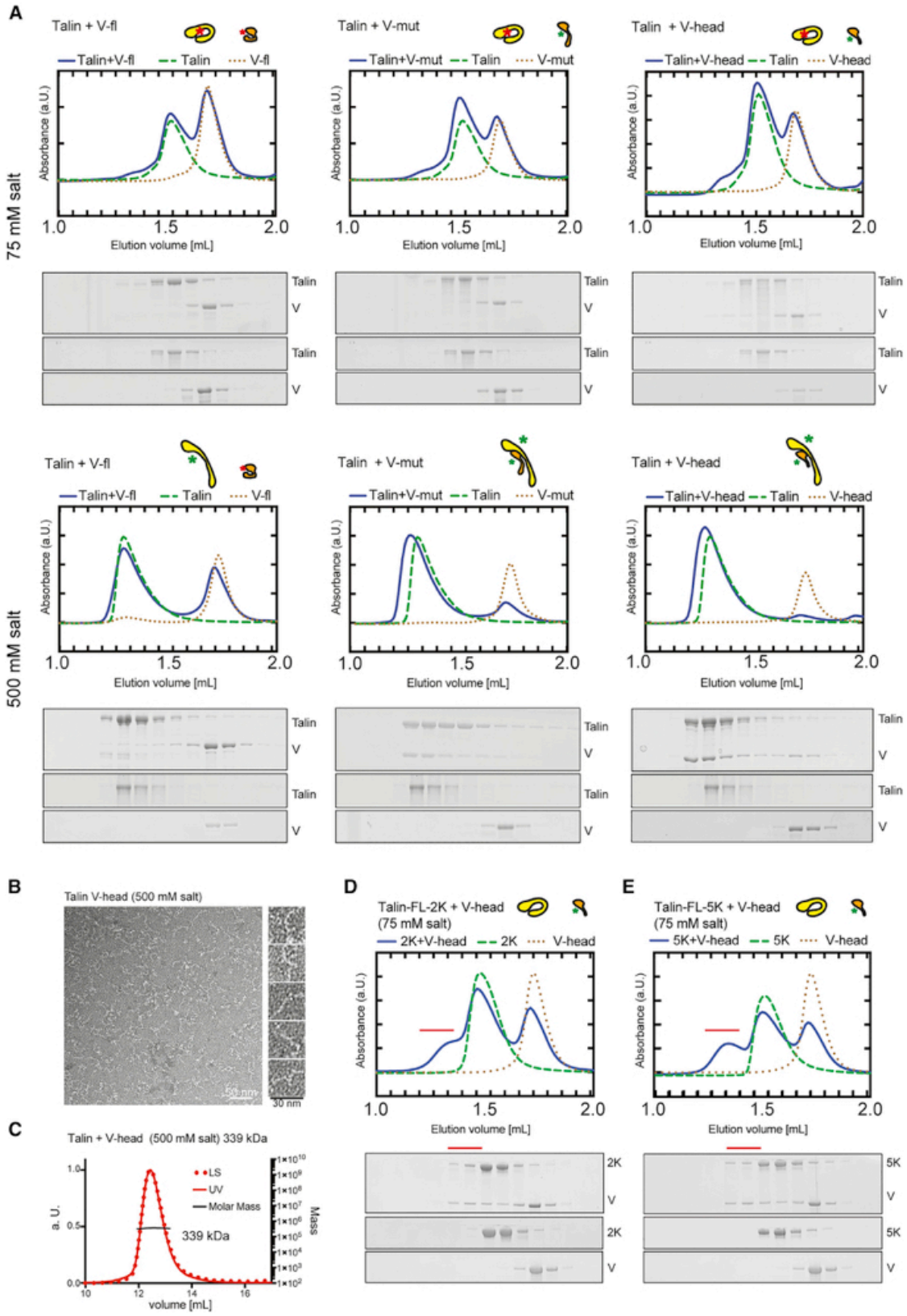

(legend on next page)

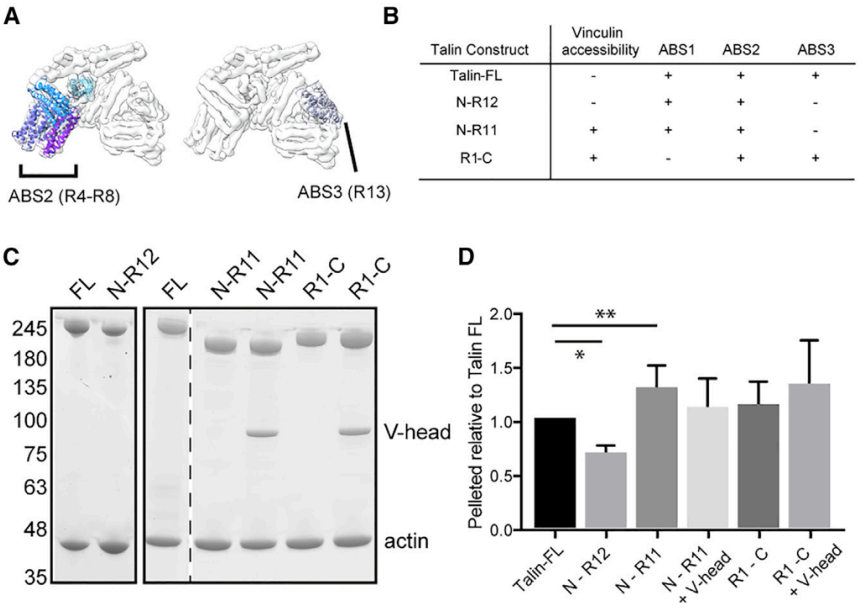

Figure 6. Talin-F-Actin Binding Assay

(A) Scheme of actin-binding domains ABS2 and ABS3 in the context of the autoinhibited talin structure.

(B) Table summarizing tested constructs for F-actin binding and vinculin accessibility of talin in compact conformation (75 mM KCl).

(C) Representative SDS-PAGE analysis of the F-actin co-sedimentation assay with various talin constructs at 75 mM salt. The dotted line indicates the elimination of an irrelevant lane from the gel.

(D) Quantification of the co-sedimented talin fragments. Data are represented as mean ± SD. N-R12, 0.68 ± 0.08; N-R11, 1.3 ± 0.2; N-R11 + V-head, 1.1 ± 0.3; R1-C, 1.1 ± 0.2; and R1-C + V-head, 1.3 ± 0.4. Differences between talin-FL and N-R12 as well as N-R11 are statistically significant (marked with *).

See also Figure S7.

the talin-vinculin complex likely corresponds to vinculin binding to R3. However, when we attempted to re-close talin in complex with the V-mut including the vinculin tail, vinculin was induced to be displaced from the complex (Figure S7A). This observation suggests that the vinculin tail competes with the talin R3 domain for binding to the vinculin head.

F-Actin Binding Is Enhanced by the Opening of Talin

Another major binding partner of talin is F-actin, which is located in the fourth layer of the FA. Acting as tension-generating machinery, actomyosin is thought to ensure the opening of talin by binding to two sites located at R4–R8 (ABS2) and R13 (ABS3; Figure 6A). Cell-based experiments with talin rod mutations suggested that ABS3 plays a role in recruiting talin to actin at the FA to activate talin, while ABS2 is critical for the maturation or growth of the FA (Atherton et al., 2015). Combining our structural findings, we hypothesized that the opening of talin is correlated with the engagement of talin to actin and tested the binding of various truncated talin variants to F-actin by co-sedimentation assays.

First, the truncated construct N-R12 was tested for binding to F-actin. In the tested condition at 75 mM KCl, N-R12, like talin-FL, employed an autoinhibited compact form (Figure 3F) that did not form a complex with vinculin (Figures 6B and S7H). Reflecting the fact that N-R12 lacks ABS3, the binding of F-actin to N-R12 was reduced compared to talin-FL (Figures 6C and 6D). Next, we tested the C-terminal truncation construct N-R11, which lacks the R12 domain. Without R12, talin N-R11 compaction is weak enough for vinculin to associate (Figures 6B and S7I). In contrast to N-R12, N-R11 bound F-actin with even higher amounts than talin-FL (Figures 6C and 6D), despite the fact that it lacks ABS3. Those results indicate that loosening the autoinhibitory lid (R12) of talin directly correlates with the activation of the F-actin binding of ABS2 as well as with vinculin binding. We also tested the truncation of the N-terminal FERM domain (R1-C) in the same way. R1-C showed binding similar to that of N-R11, although the described F-actin-binding activity of ABS1 at the FERM domain was missing from the fragment. R1-C was also capable of binding to the vinculin head (Figures 6B and S7J); however, it displayed no significant enhancement of F-actin binding.

Figure 5. Interaction Assays of Talin-FL and Vinculin under Various Conditions

(A) Talin-FL and vinculin reconstitution assays using size-exclusion chromatography (SEC). An ionic strength of 75 mM was used for the reconstitution assays shown in the upper panel and 500 mM in the lower panel. SDS-PAGE profiles (talin-vinculin mixture, talin control, vinculin control) of the peaks are shown below the SEC profiles. In order to achieve complex formation, it is necessary that both talin and vinculin employ open conformations (bottom-center and bottom-right). V-fl, vinculin full-length; V-mut, vinculin (N773A/E775A) mutant; V-head, vinculin head. Minor shoulders at the left side of talin peaks correspond to degraded talin without FERM domain. The control runs for talin come from the same experiment and the corresponding profile and SDS-PAGE are shown multiple times for comparison. The y-scaling has been adjusted for the different amplitudes of the chromatograms.

(B) Negative-stain EM image of vinculin head bound to open talin at 500 mM KCl.

(C) SEC-multi-angle light-scattering profile of V-head bound to open talin with a calculated molecular weight of 339 kDa, indicating that the complex is made with 1:1 stoichiometry. LS, light scattering, normalized; UV, absorbance.

(D) SEC reconstitution assay of talin-FL-2K mutant and vinculin head at 75 mM salt.

(E) SEC reconstitution assay of talin-FL-5K and vinculin head. The purified proteins have never been exposed to 500 mM salt, which facilitates the opening of talin. The complex formation of these mutants and V-head is observed (indicated by red lines). The control runs for V-head in (D) and (E) come from the same experiment and the corresponding profile and SDS-PAGE are shown twice for comparison.

See also Figures S6 and S7.

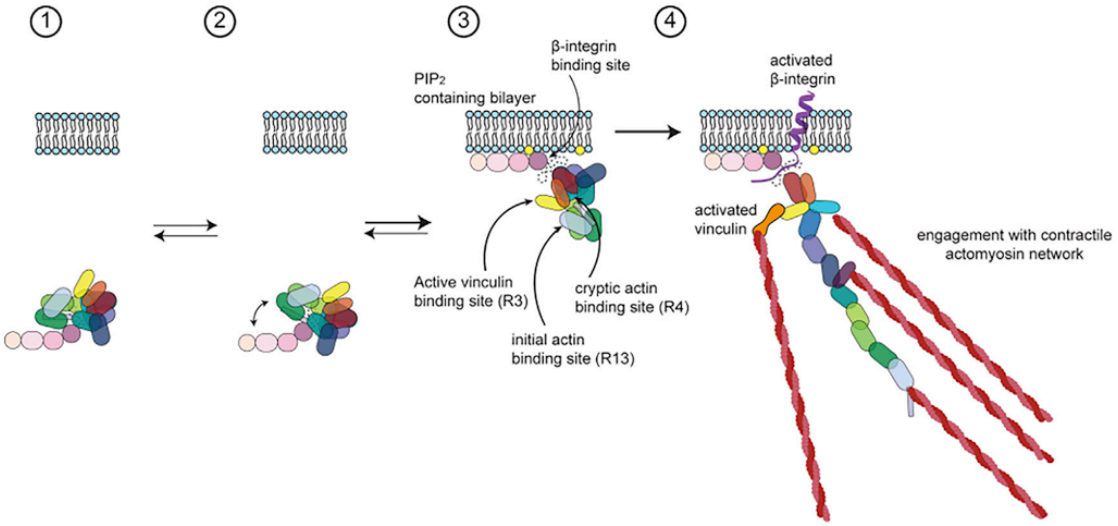

Figure 7. Model of Talin Activation

(1) Our structure of talin in the closed form reveals how inactivation is achieved through occlusion of functional sites. Rap1-mediated recruitment of talin to membranes can occur without breaking the closed formation of talin as the F0 and F1 subdomains are accessible.

(2) Our structural analysis also indicated that the closed form of talin is in equilibrium with a semi-opened state due to the instable FERM-lid connection (see Figure S1).

(3) Upon binding to the PIP_2-embedded membrane surface, the R12-F2 and R9-F3 interfaces are broken because of competitive interactions with PIP_2 and integrin, respectively (shown in Figure 1). The binding to the integrin tail hinders the F3-rod interaction (Wegener et al., 2007) and releases the rod domains from the FERM head as well as from the plasma membrane.

(4) The further opening of the rod domains may require the mechanical aid of actomyosin pulling via the ABS3 and ABS2 actin-binding sites. Vinculin may also take an active role in reinforcing the binding of talin to actin (Humphries et al., 2007).

DISCUSSION

Mechanism of Talin Regulation

In cellular environments, the concentration of talin can be as high as 50 μM (Zeiler et al., 2014; Zhu et al., 2017), making talin one of the most abundant components in cells. The activation of talin within FAs is essential; however, it is also critical that the adhesion components can be properly switched off to control cell attachment and migration. Therefore, the autoinhibited state of talin is essential (Ellis et al., 2013). Information is available about interactions among individual talin fragments (Goult et al., 2013; Song et al., 2012); however, the molecular architecture and the mechanism of talin's autoinhibition have been unknown in the regulatory context of full-length talin. We uncovered how talin can be folded to ensure its autoinhibition. A network of polar interactions keeps the 13 rod domains tangled into a compact globular architecture with the R4 domain buried in the core, thus shielding R4 and the actin-binding site ABS2 against actin binding. The compact architecture was further locked down by contacts between the F2 and F3 subdomains of the FERM head and the R12 and R9 rod domains, respectively. The PIP_2 binding FERM domain was masked by the R12 domain inhibiting the interaction of talin to the inner leaflet of the plasma membrane. The densities of R11–R13 are not well defined and show flexibility in the 3D classification (Figure S1C). This suggests that the connection between R12 and FERM domain F2 is loose. The interruption of this interaction may be sufficient to grant access to binding partners such as vinculin, whose binding cannot open the molecule completely. The conformational change of talin can be seen as an ensemble of open and closed states, which can be reversibly shifted by the change of salt concentration *in vitro*. The open conformation of talin likely mimics the activated talin stabilized by the actomyosin machinery during FA initiation.

Talin-Vinculin Complex Formation during Autoinhibition

We observed that one vinculin-binding site is readily available when full-length talin is released from the autoinhibited state without the application of any active force. Intriguingly, talin is able to reverse back to the closed conformation while vinculin-head is still bound to R3, but only in the absence of the vinculin tail. We speculate that this may hint at a mechanism to release vinculin when talin is inactivated and no longer engaged in the FA assembly. The closure of talin and concomitant folding of R3 may weaken the interaction of vinculin head to R3. In turn, the competition of vinculin tail for the head domain becomes more effective, resulting in the inactivation of vinculin and release from the complex in the autoinhibited form. It will be interesting to structurally map the interaction surface and find out which of the talin-binding partners can bind to the autoinhibited form of talin. Such an analysis will shed light on the functional role of talin in the cytosol and help to determine if there are preformed complexes that act as precursors of FA-related complexes. Along the same line, it is possible that talin dimerization might also occur upon talin activation and elongation. Binding to actin further expands the footprint of talin and exposes the C-terminal dimerization domain, as suggested previously (Goldmann et al., 1994), while dimerization appears

dispensable when talin is autoinhibited. Talin dimerization offers an additional layer of regulation and the possibility for larger complexes to be assembled from preformed FA subcomplexes. Further structural analysis of full-length talin in its active, elongated form in comparison with its autoinhibited form will provide a comprehensive view of talin function during FA initiation and maturation.

The Topological Positioning of Talin Is a Key Step in FA Activation

Our talin structure showed that the globular rod domains occlude the membrane-binding plane of the FERM domain. On the other hand, the N-terminal FERM F0-F1 subdomains and the C-terminal DD domain were not involved in maintaining the structural organization of the autoinhibited form of talin, indicating that those domains are freely accessible and not inhibited when talin is closed. In particular, F0 has been shown to be a key binding domain for Rap1, which has been suggested as the first step in the recruitment of talin to the cell-membrane surface (Zhu et al., 2017).

In addition, talin has a 30 amino-acid flexible linker between the F1 and F2 subdomains that separates F0-F1 from the globular autoinhibited structure (F2-DD). This separation may allow F0-F1 to "search" for cofactors. Our findings, together with previous results, suggest a model of how talin is recruited and correctly positioned at the membrane surface (Figure 7, model). Autoinhibited talin is recruited to the membrane via its freely accessible F0 subdomain in a Rap1-assisted manner. Thus, the FERM domain orchestrates the binding of Rap1 on the one hand (Zhu et al., 2017), while on the other it accesses the exposed, negatively charged plasma membrane via the flexible loop inserted in the F1 subdomain (Goult et al., 2010). This recruitment process increases the local concentration of PIP_2, due to the recruitment of PIPK1γ90 by the F3 subdomain (Di Paolo et al., 2002; Ling et al., 2002). PIP_2 may bind to talin, opening the R12 lid, thus shifting the conformational ensemble toward open structures. The F3-R9 interaction may then be abrogated (Figure 7, step 3), allowing the integrin tail to interact with F3.

This rearrangement releases the rod domains from the head domain (Figure 7, step 3), activating the interaction sites for various talin-binding proteins. The rod domains themselves can be readily approached by vinculin and actin (as shown in Figure 6), which could lead to the initiation of FA formation (Figure 7, step 4). Our actin co-sedimentation assays with truncated talin revealed that ABS2 is inhibited while talin is closed. This shows that the initial pulling of talin ABS3 by the actomyosin machinery aids the opening of talin to enable the accessibility of ABS2 as well as vinculin, as also shown in a previous report (Atherton et al., 2015). Finally, actin binding would enable actin retrograde force to exert tensile force on talin, enabling mechanical force to further stabilize talin opening (Sun et al., 2019). Our structure provides a mechanistic basis to understand the inhibition and activation of talin. Although our model is coherent, further testing is needed to validate key events. Furthermore, other yet-unknown activating factors may be involved to tightly regulate the inhibition and activation of talin or to modulate individual functions of talin.

STAR★METHODS

Detailed methods are provided in the online version of this paper and include the following:

- KEY RESOURCES TABLE
- LEAD CONTACT AND MATERIALS AVAILABILITY
- EXPERIMENTAL MODEL AND SUBJECT DETAILS
- METHOD DETAILS
  - Protein purification
  - Gradient Fixation (GraFix) of talin samples
  - Mass spectrometry
  - Negative-stain electron microscopy
  - Cryo-EM analysis of full-length talin
  - Molecular dynamics for flexible fitting
  - Estimation of interaction energies
  - F-Actin co-sedimentation assay
  - Analytical size-exclusion chromatography
  - Dynamic Light-Scattering (DLS)
  - Size-Exclusion Chromatography Coupled with Multi-Angle Light-Scattering (SEC-MALS)
- QUANTIFICATION AND STATISTICAL ANALYSIS
- DATA AND CODE AVAILABILITY

SUPPLEMENTAL INFORMATION

Supplemental Information can be found online at https://doi.org/10.1016/j.cell.2019.08.034.

ACKNOWLEDGEMENTS

We thank Carsten Grashoff and Giovanni Cardone for assistance at various stages of the project, Elena Conti, Wolfgang Baumeister, and the biochemistry- and cryo-EM core facilities for resources and infrastructure (Max Planck Institute of Biochemistry). N.M. acknowledges the Max Planck Society, Germany, Boehringer Ingelheim Foundation Plus 3 Program, Germany, and the European Research Council (ERC-CoG, 724209), European Union, for funding. N.M. is a recipient of the EMBO Young Investigator award. C.F.K. is supported by an EMBO long-term fellowship (EMBO ALTF 450-2017) and an Alexander von Humboldt (Germany) research fellowship for postdoctoral researchers.

AUTHOR CONTRIBUTIONS

Conceptualization, N.M.; Methodology, D.D., M.Z., C.B., and N.M.; Investigation, D.D., S.S., C.F.K., M.Z., and C.B.; Writing, N.M. and D.D.; Resources, N.M. and R.F.; Funding Acquisition, N.M.; Supervision, N.M.

DECLARATION OF INTERESTS

The authors declare no competing interests.

Received: January 2, 2019
Revised: April 4, 2019
Accepted: August 16, 2019
Published: September 19, 2019

REFERENCES

Afonine, P.V., Poon, B.K., Read, R.J., Sobolev, O.V., Terwilliger, T.C., Urzhumtsev, A., and Adams, P.D. (2018). Real-space refinement in PHENIX for cryo-EM and crystallography. Acta Crystallogr. D Struct. Biol. *74*, 531–544.

Anthis, N.J., Wegener, K.L., Ye, F., Kim, C., Goult, B.T., Lowe, E.D., Vakonakis, I., Bate, N., Critchley, D.R., Ginsberg, M.H., et al. (2009). The structure of an

integrin/talin complex reveals the basis of inside-out signal transduction. EMBO J. *28*, 3623–3632.

Atherton, P., Stutchbury, B., Wang, D.-Y., Jethwa, D., Tsang, R., Meiler-Rodriguez, E., Wang, P., Bate, N., Zent, R., Barsukov, I.L., et al. (2015). Vinculin controls talin engagement with the actomyosin machinery. Nat. Commun. *6*, 10038.

Austen, K., Ringer, P., Mehlich, A., Chrostek-Grashoff, A., Kluger, C., Klingner, C., Sabass, B., Zent, R., Rief, M., and Grashoff, C. (2015). Extracellular rigidity sensing by talin isoform-specific mechanical linkages. Nat. Cell Biol. *17*, 1597–1606.

Bachir, A.I., Zareno, J., Moissoglu, K., Plow, E.F., Gratton, E., and Horwitz, A.R. (2014). Integrin-associated complexes form hierarchically with variable stoichiometry in nascent adhesions. Curr. Biol. *24*, 1845–1853.

Bai, X.-C., Rajendra, E., Yang, G., Shi, Y., and Scheres, S.H.W. (2015). Sampling the conformational space of the catalytic subunit of human γ-secretase. eLife *4*, e11182.

Borgon, R.A., Vonrhein, C., Bricogne, G., Bois, P.R.J., and Izard, T. (2004). Crystal structure of human vinculin. Structure *12*, 1189–1197.

Calderwood, D.A., Campbell, I.D., and Critchley, D.R. (2013). Talins and kindlins: partners in integrin-mediated adhesion. Nat. Rev. Mol. Cell Biol. *14*, 503–517.

Carisey, A., Tsang, R., Greiner, A.M., Nijenhuis, N., Heath, N., Nazgiewicz, A., Kemkemer, R., Derby, B., Spatz, J., and Ballestrem, C. (2013). Vinculin regulates the recruitment and release of core focal adhesion proteins in a force-dependent manner. Curr. Biol. *23*, 271–281.

Case, L.B., Baird, M.A., Shtengel, G., Campbell, S.L., Hess, H.F., Davidson, M.W., and Waterman, C.M. (2015). Molecular mechanism of vinculin activation and nanoscale spatial organization in focal adhesions. Nat. Cell Biol. *17*, 880–892.

Chacón, P., and Wriggers, W. (2002). Multi-resolution contour-based fitting of macromolecular structures. J. Mol. Biol. *317*, 375–384.

Chinthalapudi, K., Rangarajan, E.S., and Izard, T. (2018). The interaction of talin with the cell membrane is essential for integrin activation and focal adhesion formation. Proc. Natl. Acad. Sci. USA *115*, 10339–10344.

Cohen, D.M., Chen, H., Johnson, R.P., Choudhury, B., and Craig, S.W. (2005). Two distinct head-tail interfaces cooperate to suppress activation of vinculin by talin. J. Biol. Chem. *280*, 17109–17117.

Cox, J., and Mann, M. (2008). MaxQuant enables high peptide identification rates, individualized p.p.b.-range mass accuracies and proteome-wide protein quantification. Nat. Biotechnol. *26*, 1367–1372.

Desiniotis, A., and Kyprianou, N. (2011). Significance of talin in cancer progression and metastasis. Int. Rev. Cell Mol. Biol. *289*, 117–147.

Di Paolo, G., Pellegrini, L., Letinic, K., Cestra, G., Zoncu, R., Voronov, S., Chang, S., Guo, J., Wenk, M.R., and De Camilli, P. (2002). Recruitment and regulation of phosphatidylinositol phosphate kinase type 1 gamma by the FERM domain of talin. Nature *420*, 85–89.

Elliott, P.R., Goult, B.T., Kopp, P.M., Bate, N., Grossmann, J.G., Roberts, G.C.K., Critchley, D.R., and Barsukov, I.L. (2010). The Structure of the talin head reveals a novel extended conformation of the FERM domain. Structure *18*, 1289–1299.

Ellis, S.J., Goult, B.T., Fairchild, M.J., Harris, N.J., Long, J., Lobo, P., Czerniecki, S., Van Petegem, F., Schöck, F., Peifer, M., et al. (2013). Talin autoinhibition is required for morphogenesis. Curr. Biol. *23*, 1825–1833.

Emsley, P., Lohkamp, B., Scott, W.G., and Cowtan, K. (2010). Features and development of Coot. Acta Crystallogr. D Biol. Crystallogr. *66*, 486–501.

Fang, K.-P., Dai, W., Ren, Y.-H., Xu, Y.-C., Zhang, S.-M., and Qian, Y.-B. (2016). Both Talin-1 and Talin-2 correlate with malignancy potential of the human hepatocellular carcinoma MHCC-97 L cell. BMC Cancer *16*, 45.

Fillingham, I., Gingras, A.R., Papagrigoriou, E., Patel, B., Emsley, J., Critchley, D.R., Roberts, G.C.K., and Barsukov, I.L. (2005). A vinculin binding domain from the talin rod unfolds to form a complex with the vinculin head. Structure *13*, 65–74.

Garcia-Alvarez, B., de Pereda, J.M., Calderwood, D.A., Ulmer, T.S., Critchley, D., Campbell, I.D., Ginsberg, M.H., and Liddington, R.C. (2003). Structural determinants of integrin recognition by talin. Mol. Cell *11*, 49–58.

Geiger, B., Spatz, J.P., and Bershadsky, A.D. (2009). Environmental sensing through focal adhesions. Nat. Rev. Mol. Cell Biol. *10*, 21–33.

Gingras, A.R., Ziegler, W.H., Frank, R., Barsukov, I.L., Roberts, G.C.K., Critchley, D.R., and Emsley, J. (2005). Mapping and consensus sequence identification for multiple vinculin binding sites within the talin rod. J. Biol. Chem. *280*, 37217–37224.

Gingras, A.R., Bate, N., Goult, B.T., Hazelwood, L., Canestrelli, I., Grossmann, J.G., Liu, H., Putz, N.S.M., Roberts, G.C.K., Volkmann, N., et al. (2008). The structure of the C-terminal actin-binding domain of talin. EMBO J. *27*, 458–469.

Goldmann, W.H., Bremer, A., Häner, M., Aebi, U., and Isenberg, G. (1994). Native talin is a dumbbell-shaped homodimer when it interacts with actin. J. Struct. Biol. *112*, 3–10.

Goult, B.T., Bouaouina, M., Elliott, P.R., Bate, N., Patel, B., Gingras, A.R., Grossmann, J.G., Roberts, G.C.K., Calderwood, D.A., Critchley, D.R., et al. (2010). Structure of a double ubiquitin-like domain in the talin head: a role in integrin activation. EMBO J. *29*, 1069–1080.

Goult, B.T., Xu, X.-P., Gingras, A.R., Swift, M., Patel, B., Bate, N., Kopp, P.M., Barsukov, I.L., Critchley, D.R., Volkmann, N., et al. (2013). Structural studies on full-length talin1 reveal a compact auto-inhibited dimer: implications for talin activation. J. Struct. Biol. *184*, 21–32.

Goult, B.T., Yan, J., and Schwartz, M.A. (2018). Talin as a mechanosensitive signaling hub. J. Cell Biol. *217*, 3776–3784.

Haining, A.W.M., Lieberthal, T.J., and Del Río Hernández, A. (2016). Talin: a mechanosensitive molecule in health and disease. FASEB J. *30*, 2073–2085.

Harburger, D.S., and Calderwood, D.A. (2009). Integrin signalling at a glance. J. Cell Sci. *122*, 159–163.

Hemmings, L., Rees, D.J., Ohanian, V., Bolton, S.J., Gilmore, A.P., Patel, B., Priddle, H., Trevithick, J.E., Hynes, R.O., and Critchley, D.R. (1996). Talin contains three actin-binding sites each of which is adjacent to a vinculin-binding site. J. Cell Sci. *109*, 2715–2726.

Heymann, J.B., and Belnap, D.M. (2007). Bsoft: image processing and molecular modeling for electron microscopy. J. Struct. Biol. *157*, 3–18.

Humphries, J.D., Wang, P., Streuli, C., Geiger, B., Humphries, M.J., and Ballestrem, C. (2007). Vinculin controls focal adhesion formation by direct interactions with talin and actin. J. Cell Biol. *179*, 1043–1057.

Izard, T., Evans, G., Borgon, R.A., Rush, C.L., Bricogne, G., and Bois, P.R.J. (2004). Vinculin activation by talin through helical bundle conversion. Nature *427*, 171–175.

Johnson, R.P., and Craig, S.W. (1994). An intramolecular association between the head and tail domains of vinculin modulates talin binding. J. Biol. Chem. *269*, 12611–12619.

Kanchanawong, P., Shtengel, G., Pasapera, A.M., Ramko, E.B., Davidson, M.W., Hess, H.F., and Waterman, C.M. (2010). Nanoscale architecture of integrin-based cell adhesions. Nature *468*, 580–584.

Kumar, A., Ouyang, M., Van den Dries, K., McGhee, E.J., Tanaka, K., Anderson, M.D., Groisman, A., Goult, B.T., Anderson, K.I., and Schwartz, M.A. (2016). Talin tension sensor reveals novel features of focal adhesion force transmission and mechanosensitivity. J. Cell Biol. *213*, 371–383.

Legate, K.R., Wickström, S.A., and Fässler, R. (2009). Genetic and cell biological analysis of integrin outside-in signaling. Genes Dev. *23*, 397–418.

Ling, K., Doughman, R.L., Firestone, A.J., Bunce, M.W., and Anderson, R.A. (2002). Type I gamma phosphatidylinositol phosphate kinase targets and regulates focal adhesions. Nature *420*, 89–93.

Liu, J., Wang, Y., Goh, W.I., Goh, H., Baird, M.A., Ruehland, S., Teo, S., Bate, N., Critchley, D.R., Davidson, M.W., et al. (2015). Talin determines the nanoscale architecture of focal adhesions. Proc. Natl. Acad. Sci. USA *112*, E4864–E4873.

Maier, J.A., Martinez, C., Kasavajhala, K., Wickstrom, L., Hauser, K.E., and Simmerling, C. (2015). ff14SB: Improving the Accuracy of Protein Side Chain and Backbone Parameters from ff99SB. J. Chem. Theory Comput. *11*, 3696–3713.

Margadant, F., Chew, L.L., Hu, X., Yu, H., Bate, N., Zhang, X., and Sheetz, M. (2011). Mechanotransduction in vivo by repeated talin stretch-relaxation events depends upon vinculin. PLoS Biol. *9*, e1001223.

Mastronarde, D.N. (2005). Automated electron microscope tomography using robust prediction of specimen movements. J. Struct Biol. *152*, 36–51.

Molony, L., McCaslin, D., Abernethy, J., Paschal, B., and Burridge, K. (1987). Properties of talin from chicken gizzard smooth muscle. J. Biol. Chem. *262*, 7790–7795.

Nieswandt, B., Moser, M., Pleines, I., Varga-Szabo, D., Monkley, S., Critchley, D., and Fässler, R. (2007). Loss of talin1 in platelets abrogates integrin activation, platelet aggregation, and thrombus formation in vitro and in vivo. J. Exp. Med. *204*, 3113–3118.

Onufriev, A., Bashford, D., and Case, D.A. (2000). Modification of the generalized Born model suitable for macromolecules. J. Phys. Chem. B *104*, 3712–3720.

Orłowski, A., Kukkurainen, S., Pöyry, A., Rissanen, S., Vattulainen, I., Hytönen, V.P., and Róg, T. (2015). PIP_2 and Talin Join Forces to Activate Integrin. J. Phys. Chem. B *119*, 12381–12389.

Papagrigoriou, E., Gingras, A.R., Barsukov, I.L., Bate, N., Fillingham, I.J., Patel, B., Frank, R., Ziegler, W.H., Roberts, G.C.K., Critchley, D.R., et al. (2004). Activation of a vinculin-binding site in the talin rod involves rearrangement of a five-helix bundle. EMBO J. *23*, 2942–2951.

Parsons, J.T., Horwitz, A.R., and Schwartz, M.A. (2010). Cell adhesion: integrating cytoskeletal dynamics and cellular tension. Nat. Rev. Mol. Cell Biol. *11*, 633–643.

Pettersen, E.F., Goddard, T.D., Huang, C.C., Couch, G.S., Greenblatt, D.M., Meng, E.C., and Ferrin, T.E. (2004). UCSF Chimera--a visualization system for exploratory research and analysis. J. Comput. Chem. *25*, 1605–1612.

Plak, K., Pots, H., Van Haastert, P.J.M., and Kortholt, A. (2016). Direct Interaction between TalinB and Rap1 is necessary for adhesion of Dictyostelium cells. BMC Cell Biol. *17*, 1.

Punjani, A., Rubinstein, J.L., Fleet, D.J., and Brubaker, M.A. (2017). cryoSPARC: algorithms for rapid unsupervised cryo-EM structure determination. Nat. Methods *14*, 290–296.

Rees, D.J., Ades, S.E., Singer, S.J., and Hynes, R.O. (1990). Sequence and domain structure of talin. Nature *347*, 685–689.

Salomon-Ferrer, R., Case, D.A., and Walker, R.C. (2013). An overview of the Amber biomolecular simulation package. Wiley Interdiscip. Rev. Comput. Mol. Sci. *3*, 198–210.

Schindelin, J., Arganda-Carreras, I., Frise, E., Kaynig, V., Longair, M., Pietzsch, T., Preibisch, S., Rueden, C., Saalfeld, S., Schmid, B., et al. (2012). Fiji: an open-source platform for biological-image analysis. Nat. Methods *9*, 676–682.

Song, X., Yang, J., Hirbawi, J., Ye, S., Perera, H.D., Goksoy, E., Dwivedi, P., Plow, E.F., Zhang, R., and Qin, J. (2012). A novel membrane-dependent on/off switch mechanism of talin FERM domain at sites of cell adhesion. Cell Res. *22*, 1533–1545.

Stark, H. (2010). GraFix: stabilization of fragile macromolecular complexes for single particle cryo-EM. Methods Enzymol. *481*, 109–126.

Sun, Z., Costell, M., and Fässler, R. (2019). Integrin activation by talin, kindlin and mechanical forces. Nat. Cell Biol. *21*, 25–31.

Tadokoro, S., Shattil, S.J., Eto, K., Tai, V., Liddington, R.C., de Pereda, J.M., Ginsberg, M.H., and Calderwood, D.A. (2003). Talin binding to integrin beta tails: a final common step in integrin activation. Science *302*, 103–106.

Tanentzapf, G., and Brown, N.H. (2006). An interaction between integrin and the talin FERM domain mediates integrin activation but not linkage to the cytoskeleton. Nat. Cell Biol. *8*, 601–606.

Wegener, K.L., Partridge, A.W., Han, J., Pickford, A.R., Liddington, R.C., Ginsberg, M.H., and Campbell, I.D. (2007). Structural basis of integrin activation by talin. Cell *128*, 171–182.

Wegener, K.L., Basran, J., Bagshaw, C.R., Campbell, I.D., Roberts, G.C.K., Critchley, D.R., and Barsukov, I.L. (2008). Structural basis for the interaction between the cytoplasmic domain of the hyaluronate receptor layilin and the talin F3 subdomain. J. Mol. Biol. *382*, 112–126.

Winkler, J., Lünsdorf, H., and Jockusch, B.M. (1997). Energy-filtered electron microscopy reveals that talin is a highly flexible protein composed of a series of globular domains. Eur. J. Biochem. *243*, 430–436.

Yang, J., Zhu, L., Zhang, H., Hirbawi, J., Fukuda, K., Dwivedi, P., Liu, J., Byzova, T., Plow, E.F., Wu, J., et al. (2014). Conformational activation of talin by RIAM triggers integrin-mediated cell adhesion. Nat. Commun. *5*, 5880.

Yao, M., Goult, B.T., Chen, H., Cong, P., Sheetz, M.P., and Yan, J. (2014). Mechanical activation of vinculin binding to talin locks talin in an unfolded conformation. Sci. Rep. *4*, 4610.

Zaidel-Bar, R., Ballestrem, C., Kam, Z., and Geiger, B. (2003). Early molecular events in the assembly of matrix adhesions at the leading edge of migrating cells. J. Cell Sci. *116*, 4605–4613.

Zeiler, M., Moser, M., and Mann, M. (2014). Copy number analysis of the murine platelet proteome spanning the complete abundance range. Mol. Cell. Proteomics *13*, 3435–3445.

Zhang, K. (2016). Gctf: Real-time CTF determination and correction. J. Struct. Biol. *193*, 1–12.

Zheng, S.Q., Palovcak, E., Armache, J.-P., Verba, K.A., Cheng, Y., and Agard, D.A. (2017). MotionCor2: anisotropic correction of beam-induced motion for improved cryo-electron microscopy. Nat. Methods *14*, 331–332.

Zhu, L., Yang, J., Bromberger, T., Holly, A., Lu, F., Liu, H., Sun, K., Klapproth, S., Hirbawi, J., Byzova, T.V., et al. (2017). Structure of Rap1b bound to talin reveals a pathway for triggering integrin activation. Nat. Commun. *8*, 1744.

Zivanov, J., Nakane, T., Forsberg, B.O., Kimanius, D., Hagen, W.J., Lindahl, E., and Scheres, S.H. (2018). New tools for automated high-resolution cryo-EM structure determination in RELION-3. eLife *7*, e42166.

STAR★METHODS

KEY RESOURCES TABLE

REAGENT or RESOURCE	SOURCE	IDENTIFIER
Bacterial and Virus Strains		
Escherichia coli, BL21-Gold (DE3)	Agilent	Cat# 230132
Escherichia coli, XL1-Blue	Agilent	Cat# 200249
Chemicals, Peptides, and Recombinant Proteins		
N-2-Hydroxyethylpiperazine-N'-2-ethanesulfonic acid (HEPES)	Roth	Cat# 9105.3
Potassium Chloride	Roth	Cat# 6781.1
Sodium Chloride	Merck	Cat# 1.06404
Ethylenediaminetetraacetic acid (EDTA)	VWR	Cat# 1.08418.0250
Dithiothreitol (DTT)	AppliChem	Cat# A1101
2-Mercaptoethanol	AppliChem	Cat# 4338.0100
D(+)-Saccharose	Roth	Cat# 4621.1
Glutharaldehyde	Sigma	Cat# 340855
Octyl β-D-glucopyranoside	Sigma	Cat# O8001-500MG
Uranyl acetate 2%	Science Services	Cat# E22400-2
Tris(hydroxymethyl)aminomethane (Tris/Trizma Base)	Sigma	Cat# T1503
4-Morpholineethanesulfonic acid (MES)	Sigma	Cat# M8250-250G
Imidazol	Merck	Cat# 1.04716.1000
Actin (rabbit skeletal muscle alpha actin)	Hypermol	Cat# 8101-03
L-Glutathione (reduced)	VWR	Cat# 0399-50G
Glyercol 99.5%	Roth	Cat# 3783.1
cOmplete EDTA-free, 3 x 20 Tablets	Roche	Cat# 5056489001
Magnesium chloride	Roth	Cat# 2189.2
Calcium chloride	Roth	Cat# 5239.2
Adenosine 5'-triphosphate disodium salt hydrate	Sigma	Cat# A2383-10G
Protein Marker VI (10 - 245) pre-stained	AppliChem	Cat# A8889.0500
Critical Commercial Assays		
NucleoSpin Plasmid EasyPure	Macherey Nagel	Cat# 740727.250
Roche cOmplete His-Tag purification column	Roche Diagnostics	Cat# 06781535001
HiTrap Q HP column	GE Healthcare	Cat# 17-1154-01
16/600 Superdex 200 GL	GE Healthcare	Cat# 28-9893-35
3.2/300 Superdex 200 increase	GE Healthcare	Cat# 28-9909-46
3.2/300 Superose 6 increase	GE Healthcare	Cat# 29-0915-98
GSTrap FF, HiTrap GSH/GST	GE Healthcare	Cat# 17-5131-01
Deposited Data		
Cryo-EM map of talin-FL	This study	EMD-4772
Atomic model of talin-FL	This study	PDB 6R9T
Experimental Models: Organisms/Strains		
Escherichia coli, BL21-Gold (DE3)	Agilent	Cat# 230132
Escherichia coli, XL1-Blue	Agilent	Cat# 200249
Oligonucleotides		
DNA Primers, see Table S2	This study	N/A
Recombinant DNA		
Plasmid DNAs, see Table S2	This study	N/A

(*Continued on next page*)

Continued

REAGENT or RESOURCE	SOURCE	IDENTIFIER
Software and Algorithms		
Serial EM	Mastronarde, 2005	http://bio3d.colorado.edu/SerialEM
Gctf	Zhang, 2016	https://en.wikibooks.org/w/index.php?title=Software_Tools_For_Molecular_Microscopy&stable=0#Gctf
Gautomatch	Andrew Carter lab, unpublished	https://www.mrc-lmb.cam.ac.uk/kzhang/
MotionCor2	Zheng et al., 2017	https://msg.ucsf.edu/software
RELION	Zivanov et al., 2018	http://www3.mrc-lmb.cam.ac.uk/relion
cryoSPARC	Punjani et al., 2017	https://cryosparc.com/
UCSF Chimera	Pettersen et al., 2004	http://www.cgl.ucsf.edu/chimera/
Bsoft	Heymann and Belnap, 2007	https://lsbr.niams.nih.gov/bsoft/
Coot	Emsley et al., 2010	http://www2.mrc-lmb.cam.ac.uk/Personal/pemsley/coot/
PHENIX	Afonine et al. 2018	https://www.phenix-online.org/
UNICORN	GE Healthcare	https://www.gelifesciences.com
OmniSEC	Malvern	https://www.malvernpanalytical.com
PRISM	Graphpad	https://www.graphpad.com/scientific-software/prism/
Amber 16/18	Salomon-Ferrer et al., 2013	http://ambermd.org/AmberTools.php
MaxQuant	Cox and Mann, 2008	https://www.maxquant.org/maxquant/
Other		
Carbon-coated copper grids	Home-made	N/A
Quantifoil Cu 200 mesh R1.2/1.3 grids	QUANTIFOIL	N/A

LEAD CONTACT AND MATERIALS AVAILABILITY

Further information and requests for resources and reagents should be directed to and will be fulfilled by the Lead Contact, Naoko Mizuno (mizuno@biochem.mpg.de). Materials and plasmids generated in this study (see Table S2) are available upon request.

EXPERIMENTAL MODEL AND SUBJECT DETAILS

E. coli XL1-blue was cultured at 37°C in LB medium supplemented with 100 μg/ml ampicillin for plasmid DNA extraction. *E. coli* BL21(DE3) gold was cultured at 37°C in ZY auto-induction medium supplemented with 100 μg/ml ampicillin until reaching an OD_{600} >2. The temperature was then switched to 16°C for protein expression overnight. Plasmids used for protein production are listed in Table S2.

METHOD DETAILS

Protein purification

Expression constructs of full-length talin1 (talin-FL) were prepared using human talin1 DNA (a gift from Christophe Le Clainche). DNA of talin-FL was amplified using PCR and subcloned into a pCB homemade expression vector with a His tag at the C-terminus for bacterial or mammalian cells. Talin1 was expressed in *E. coli* BL21 (DE3) gold using ZY auto-induction medium. Cells were lysed by sonication in 50 mM Tris-HCl pH 7.8, 500 mM NaCl, 10 mM imidazole, 1 mM DTT, 5 mM EDTA, purified by nickel-affinity chromatography (complete His-Tag purification column, Roche) and anion exchange (HiTrap Q HP, GE Healthcare). The His-tag was removed using 3C protease and proteins were further purified by size-exclusion chromatography using a Superdex 200 16/600 column (GE Healthcare) in 20 mM HEPES pH 7.8, 75 mM KCl, 0.5 mM β-Mercaptoethanol and 0.5 mM EDTA and 10% glycerol.

Talin truncation and mutation variants were obtained using mouse talin FL (pLPCXmod-Talin1-Ypet; a gift from Carsten Grashoff) as a template and cloned into homemade expression vectors (pCB and pEC vectors). Mouse talin constructs used in this study were 1-2482 (talin -ΔDD), 482-2541 (R1-C) 1-2294 (N-R12), 1-2141 (N-R11), 482-1655 (R1-R8), 482-913 (R1-R3), 913-1655 (R4-R8), talin mutant E2288K/E2294K/D2297K/E2299K/D2300K (talin-FL-5K) as well as talin mutant E2288K/E2294K (talin-FL-2K) (see Table S2).

The DNA fragments were amplified using PCR and subcloned into a pCB vector containing a cleavable N-terminal Venus-His8-Sumo tag or His tag. Proteins were expressed in *E. coli* BL21 (DE3) gold in ZY auto-induction medium. Talin truncation variants were purified using the same procedure as talin-FL. Tags were removed using 3C or Senp2 protease and proteins were further purified by size-exclusion chromatography using a Superdex 200 16/600 column (GE Healthcare) with 20 mM HEPES pH 7.5, 75 mM NaCl, 0.5 mM EDTA and 0.5 mM β-Mercaptoethanol.

Vinculin constructs were designed based on a previous report (Cohen et al., 2005) and cloned into homemade pEC vectors containing N-terminal GST-His tag and a 3C-cleavage site. V-head contains a.a. 1-851. Proteins were purified using His-affinity purification methods and eluted with 500 mM imidazole. Protein fragments were cleaved with 3C protease and dialyzed over night against 20 mM HEPES at pH 7.8, 100 mM KCl, 0.5 mM β-Mercaptoethanol, concentrated and subsequently applied to size-exclusion chromatography (Superdex 200 16/600, GE Healthcare). All purified proteins were stored at −80°C. Analytical size-exclusion chromatography experiments using talin were performed in 20 mM HEPES at pH 7.8, 0.5 mM β-Mercaptoethanol, 0.5 mM EDTA either with 75 or 500 mM KCl to test the influence of salt on the conformational change observed under negative-stain EM.

Gradient Fixation (GraFix) of talin samples

To stabilize weak protein-protein interactions, the GraFix crosslinking protocol was used (Stark, 2010). Talin samples were subjected to a sucrose and glutaraldehyde gradient of 10-30% and 0-0.2%, respectively, in a buffer containing 20 mM HEPES (pH 7.5), 75 mM KCl, 0.5 mM β-Mercaptoethanol and 0.5 mM EDTA. Gradients were prepared in 2.2 ml ultracentrifuge tubes (open-top polyclear tubes, Seton) using a Gradient Station machine (model ip, Biocomp). 50 μl of talin samples at a concentration of 5 mg/ml (approximately 18.5 μM) were placed on top of the gradients and centrifuged in a TLS55 rotor (Beckman Coulter) at 50 000 rpm, for 6 h at 4°C, using an Optima Max-XP ultracentrifuge (Beckman Coulter). 100 μl-Fractions were collected manually from top to bottom and quenched with 100 mM Tris (pH 7.5). Fractions containing the monomeric or dimeric talin, as determined by SDS-PAGE were pooled, concentrated, and buffer-exchanged to 20 mM HEPES (pH 7.5), 75 mM KCl, 0.5 mM β-Mercaptoethanol and 0.5 mM EDTA to remove excess sucrose using Amicon Ultra centrifugal filters (0.5 ml, 50 MWCO).

Mass spectrometry

For validating the full-length coverage of the protein sequence, the talin-FL sample was subjected to peptide mass fingerprinting analysis. The sample was diluted in equal volume of buffer containing 2% sodium deoxycholate (SDC), 20 mM TCEP and 80 mM chloroacetamide in 25 mM Tris at pH 8.5 and incubated at 37°C for 20 min. The sample was then further diluted with LC-MS grade water to reduce the SDC concentration to less than 0.5% and directly digested with 1 μg of trypsin (Promega) overnight. The peptides were then acidified and purified via SDB-SCX StageTips and analysed in a Q Exactive HF mass spectrometer using a 75 min gradient. Raw data were processed using the MaxQuant platform and all identifications were filtered at 1% false discovery rate (FDR).

Negative-stain electron microscopy

For negative-stain EM, homemade carbon-coated grids were prepared and glow discharged before use. 5 μl of sample was applied and incubated for 1 min, blotted, washed twice in two drops of water and stained in 2% uranyl acetate for 1 min. The prepared specimens were visualized with a FEI CM200 with an operating voltage of 160 kV equipped with an Eagle CCD camera with a pixel size of 2.16 Å/pix or with a FEI Tecnai F20 at 200 kV with an Eagle CCD camera with a pixel size of 2.21 Å/pix. For 2D classifications, particles were manually or automatically picked using RELION (Zivanov et al., 2018) and extracted in 276 Å boxes. For shape assessment, 1102 (talin-ΔDD) and 5678 (talin-FL V-head complex, treated with GraFix method for stabilization) particles were selected for reference-free 2D classification using RELION, resulting in 2D class averages. The lengths of open talin were measured using bshow in BSOFT (Heymann and Belnap, 2007). Five images of negatively stained talin were filtered using median filter (n=6) as well as Gaussian filter (sigma=4) to enhance the contrast of the protein densities. Particles showing clear boundaries were manually selected and their contour length was measured using the 'filament' option in BSOFT, facilitating the tracing of elongated, string-like particles. The histogram was created from a population size of N = 89, and the distribution was fit to normal distribution (average 560 Å, S.D. 170 Å).

Cryo-EM analysis of full-length talin

Samples for cryo-EM were applied to glow-discharged R1.2/1.3 Cu 200 mesh holey carbon grids at a concentration of 0.3 mg/mL in 20 mM HEPES at pH 7.8, 75 mM KCl, 0.5 mM β-Mercaptoethanol, 0.5 mM EDTA to ensure the compact formation of talin based on the DLS experiment shown in Figure 3D. Under salt concentrations of 200 mM KCl and higher, the compact formation of talin molecule was compromised in the cryo-EM environment, yielding poor 2D averages (Figure S2D). The grids were blotted at ~95% humidity at 4°C for 4 s and plunged into liquid ethane-propane using a Vitrobot Mark IV (FEI). 11007 micrographs were collected on a Titan Krios (FEI) at 300 kV equipped with a K2 Summit direct electron detector and a quantum energy filter (20 e-V)(Gatan). Micrographs were exposed for 10 s at 7.68 e-/Å2/s (total dose 76.8 e-/Å2) and 40 frames were collected in counting mode (pixel size 1.06 Å/pixel). Defocus was varied between -1 and -3 μm in steps of 0.3 μm. Movies were aligned, gain-normalized and dose-weighted using MotionCor2 (Zheng et al., 2017). Defocus values were determined using GCTF (Zhang, 2016). Particles were automatically picked with Gautomatch using the template-free mode (Gaussian blob with 220 Å diameter), imported to RELION-3 (Zivanov et al., 2018) and extracted in 224 pixel-sized boxes. Extracted particles were applied to 2D classification routine in RELION-3 to remove contaminations. 1,873,975 particles were selected and after removing low quality classes, initial 3D reconstruction was performed

using cryoSPARC (Punjani et al., 2017). Using the initial model, 5 batches of 3D classification were performed, yielding several models of a closed talin structure with different completeness of densities. Particles of the most complete model were combined, further aligned and classified. 30,438 particles were selected for the final 3D refinement, yielding a final map with a global resolution of 6.2 Å with up to 5.5 Å resolution in the core of talin using the RELION post-processing routine, using the gold-standard Fourier shell correction (FCS) = 0.143 criterion. In the final map, the R3 domain was only partially resolved. To visualize the R3 domain, flexible densities were computationally subtracted from individual particles using available scheme from RELION-3, and as previously described (Bai et al., 2015), facilitating the focused 3D classification of the core density R1-R10. The particle information and the alignment parameters of the 3D class with the most prominent density of R3 were applied to the original particles that contain the flexible densities (FERM domain and R11-C) and the final map with the R3 domain was obtained. This map was used for the assignment of the R3 domain. Finally, to assess the flexibility of the autoinhibition area in the talin structure, 3D classification was performed to the 750,432 particles obtained from the initial stage of the 3D classification. It was observed that the parts corresponding to R11-R13 exhibited a weaker density compared to the core part (R1-R10) of the structure, detecting high levels of flexibility. Overall, the analysis indicated that the packing of talin-FL is sensitive to its environment, which agrees well with its conformational change observed in our biochemical analysis as well as its cellular function. The graphical summary is depicted in Figure S1.

Molecular dynamics for flexible fitting

For each of the rod fragments (R1-R13) and the FERM domains, crystal and NMR structures are available. The corresponding PDB entries are 3ivf (FERM domain), 1sj8 (rod domains R1 and R2), 2l7a (R3), 2lqg (R4), 2l10 (R6), 2l7n (R5) 5ic1 (R7, R8, R9), 2kvp (R10), 3dyj (R11, R12), 2jsw (R13). Initially, the structures containing multiple domains (PDB: 3ivf, 1sj8 and 5ic1) were computationally divided into individual domains. These individual domain structures served as building blocks to build a model of the entire autoinhibited structure of talin (Figure S3).

The R1 rod domain has an asymmetric shape and only one unique well-fitted placement and orientation of this structure in the density could be identified by rigid-body fitting. The C-terminus of the fitted R1 model reaches into a neighboring helical bundle density in the cryo-EM map, which fitted well with the R2 model. The available structure of R1-R2 complex (PDB: 1SJ8) was independently fitted using the colores program of the Situs package (Chacón and Wriggers, 2002) showing that they matched to each other. This fitting served as a first anchor segment. The resolution of the density was sufficient to clearly distinguish between 4-helix and 5-helix bundle segments in the density. R7 and R8 were readily identified due to the inter-winded helical bundle feature of R7 within R8. Together with the constraint on the maximum linker length to covalently connect consecutive rod-domains it was possible to define placements and also orientations of the subsequent rod domains (R3-R13) in order to fit to the density and at the same time, to allow covalent connection to the previous and subsequent rod-domains. Placements that sterically did not allow connection of consecutive fragments to form a fully connected talin chain were eliminated. Finally, remaining densities, which did not represent a helical bundle arrangement, were assessed. These remaining densities consisted of two globular entities that were identified as F2 and F3 domains due to their secondary structures features. Overall, the fitting was performed independent of any available structural models showing the inter-domain connections. However, our placements brought the F3 segment in close binding vicinity to the R9 rod-domain. The placement coincided with the crystal structure of F2-F3 in complex with R9 (PDB 4f7g) (within a root-mean square deviation (RMSD) < 0.8 Å).

The resolution of the cyro-EM reconstruction of 6.2 Å together with the sterical constraints to covalently connect domains with smaller linker segments readily allowed the identification of the unique topology for the full chain. However, no cryo-EM densities for the FERM F0 and F1 domains and the DD domain were identified and these parts were not included during model building. Finally, a full covalently connected chain was formed by connecting N- and C-termini of consecutive rod fragments using the Leap module of the Amber16 package (Salomon-Ferrer et al., 2013) in combination with the ff14SB force field (Maier et al., 2015). The disordered connection between FERM F3 and R1 was not included and the F2 and F3 domains were treated as separate proteins not covalently connected to the rod fragments.

The emap/sander module of the Amber16 package was used to perform a flexible fitting and sterical force field optimization (based on the ff14SB force field). In order to keep the structure of each individual template structure (R1-R13 and F2 and F3) close to the corresponding experimental crystal structure distance restraints between backbone atoms within each fragment were included. These restraints kept the secondary structure and the arrangement of secondary structures in each domain to within RMSD < 1 Å from the corresponding experimental domain reference structures. Connecting loops and side chains were nevertheless fully mobile during flexible fitting. The full start structure was first energy minimized (5000 steps) followed by a Molecular Dynamics (MD) simulation at 300 K (0.5 ns) until no further shift of the mean structure was observed followed by another round of energy minimization. The model was then subjected to manual building and correction in COOT (Emsley et al., 2010) and real-space refinement in PHENIX (Afonine et al., 2018). The final structure fitted well to the cryo-EM density with a correlation coefficient around the model (CC_{mask}) of 0.81 without outliers in the Ramachandran plot (Table S1).

Estimation of interaction energies

The interaction energy between selected pairs of talin fragments (enthalpy) was calculated using the MMPBSA (Molecular Mechanics Poisson Boltzmann Surface Area) approach as implemented in the Amber18 package (Onufriev et al., 2000; Salomon-Ferrer et al., 2013). Pairs of talin subdomains were extracted from the compact talin autoinhibited structure in the same arrangement as observed

in the full structure. For each case an ensemble of 250 conformations was generated using short MD simulation (0.1 ns, 300 K) keeping the backbone strongly restraint to the starting placement (allowing shifts < 0.1 Å). The mean domain-domain interaction energy was calculated using the MMPBSA method. It accounts for changes in electrostatic Coulomb interactions, changes in electrostatic solvation (reaction field with the aqueous environment), changes in mean van-der-Waals interactions and nonpolar (hydrophobic) contributions that depend on the buried surface area upon complex formation. In the MMPBSA approach, the change in electrostatic reaction field contributions is calculated by solving the finite-difference Poisson-Boltzmann equation for each structure. The energy of interaction was estimated by subtracting the contributions of each partner from the result of the domain-domain complex for each case. Calculations were performed at a monovalent salt concentration of 0.15 M. We note that the calculated interaction energies represent enthalpic contributions and do not include the entropic penalties of restricting the large ensemble of open and flexible conformations of talin to a small ensemble of compact conformations seen in the autoinhibited state.

F-Actin co-sedimentation assay

Actin was purchased from Hypermol, Germany. Actin was polymerized in 10 mM Tris pH 7.5, 50 mM KCl, 2 mM $MgCl_2$, 0.2 mM $CaCl_2$, 0.2 mM ATP, 0.5 mM DTT for 20 min at RT. Buffer exchange of the samples was performed using Zeba Spin desalting columns (Thermo Scientific). The buffer for all constructs was 20 mM Tris pH 7.5, 75 mM KCl. 2.5 μM talin fragments were incubated with 2.5 μM F-actin for 15 min at RT. The mixture was then ultra-centrifuged at 175 000 x g (TL-100 Ultracentrifuge, Beckmann) for 20 minutes at RT. Pellets were re-suspended to comparable volumes as supernatants with 1x SDS buffer. 6x SDS buffer was added to the supernatant and 10 μl of samples were run on SDS-page and quantified using FIJI (Schindelin et al., 2012).

Analytical size-exclusion chromatography

For analytical size-exclusion chromatography, the buffer exchange of the sample was performed using Zeba Spin desalting columns (Thermo Scientific) to 20 mM HEPES pH 7.5, 75 or 500 mM KCl, and 10 μM of samples were injected to either an analytical Superdex 200i 3.2/300 (for the reconstitutions of R1-C, R1-R3, R4-R8 and R4-R8 and V-head) or Superose 6i 3.2/300 (all other constructs) on an ÄKTAmicro system (GE Healthcare). Fractions were collected, mixed with 6x SDS sample buffer and 10 μl were run on SDS-PAGE.

Dynamic Light-Scattering (DLS)

For measurements of hydrodynamic radius changes, talin-FL, talin N-R11 and talin N-R12 were initially prepared in 20 mM HEPES pH 7.5, 75 mM KCl, 0.5 mM EDTA, 0.5 mM β-Mercaptoethanol. Further, the samples were diluted to a final concentration of 0.3 mg/ml and final KCl concentrations of 75 – 500 mM (75/100/125/150/175/200/225/250/300/350/400/450/500 mM KCl) in the same buffer in 30 μl wells in a 384-well plate. DLS measurements were performed with a Dynapro Platereader-II Dynamic Light Scattering instrument (Wyatt Technology Corporation) at 20°C. Samples were independently prepared in triplicates and 20 measurement points per well were taken. The data was analyzed in Dynamic 7.8.1.3 (Wyatt Technology Corporation) and plotted with PRISM (GraphPad). The fitting of the curve was performed using a nonlinear regression fit with a sigmoidal curve.

Size-Exclusion Chromatography Coupled with Multi-Angle Light-Scattering (SEC-MALS)

To test the molecular weight of the protein complexes, talin-FL and talin truncations as well as the mixtures of talin and vinculin (1:1 ratio) were prepared in buffer containing 20 mM HEPES, pH 7.5, 75 or 500 mM KCl, 0.5 mM EDTA at 3 mg/ml concentration and 20 μl were run on a Superdex 200 5/150 GL column on an ÄKTAmicro system (GE Healthcare) coupled to a Viscotek TDA302 detector (Malvern, Herrenberg, Germany) in the same buffer. Bovine serum albumin was used as a standard and the refractive index increment (dn/dc) was set to 0.180 ml/g for calculations. Data was analyzed using the OmniSEC 4.5 software (Malvern) and plotted with PRISM (GraphPad).

QUANTIFICATION AND STATISTICAL ANALYSIS

Quantification and statistical analysis related to EM data are integral parts of algorithms and software used.

For DLS analysis, the experiments were performed 3 times independently. The results were averaged and the error bars represent the standard deviations. For the fitting, nonlinear regression fit, sigmoidal curve fitting was applied using the software PRISM (GraphPad).

For F-actin analysis shown in Figure 6, the experiments were performed at least 3 times independently. The talin-FL band was run on the same SDS-PAGE gel as an internal control to standardize the variability of the contrast caused by staining conditions of each SDS-PAGE gels. Therefore, relative quantified values compared to the talin-FL band were used for the analysis. These values were averaged and standard deviations were obtained. Unpaired t-test was used to assess statistical significance.

DATA AND CODE AVAILABILITY

The cryo-EM map of human talin1 was deposited in the EMDB database with accession code EMD-4772. The flexibly fitted atomic model was deposited in the PDB with accession code 6R9T.

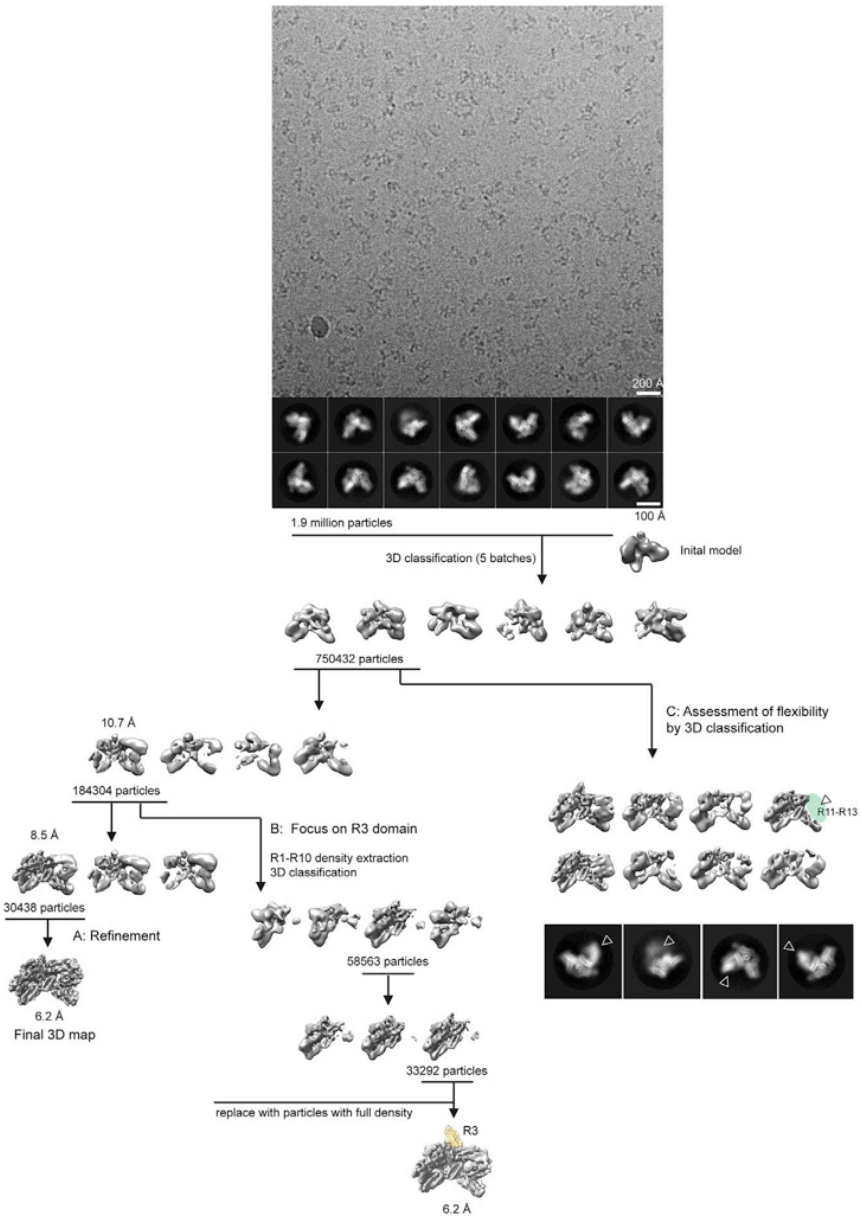

Figure S1. Summary of Cryo-EM Data Processing, Related to Figure 1

Top: Representative cryo-EM image of talin-FL at 75 mM salt with representative 2D averages. Bottom: Graphical scheme of image processing. 1.9 million particles were selected out of 2D classifications. Further 3D classifications and refinement facilitated the final map generation (A – left). To visualize the R3 domain, the core density (R1-R10) was computationally extracted and focused 3D classification of the core density was performed. At the final step of the processing, the alignment parameters were applied to the original particles to visualize the full density (B – center). Yellow density fitted with an available structural model of R3. To assess the flexibility of the autoinhibition pocket consisting of the interface between FERM domain F2-F3 and R12-R13 (lid), extensive 3D classifications were performed, yielding a visualization of the flexible densities of R11-R13 (C – right).

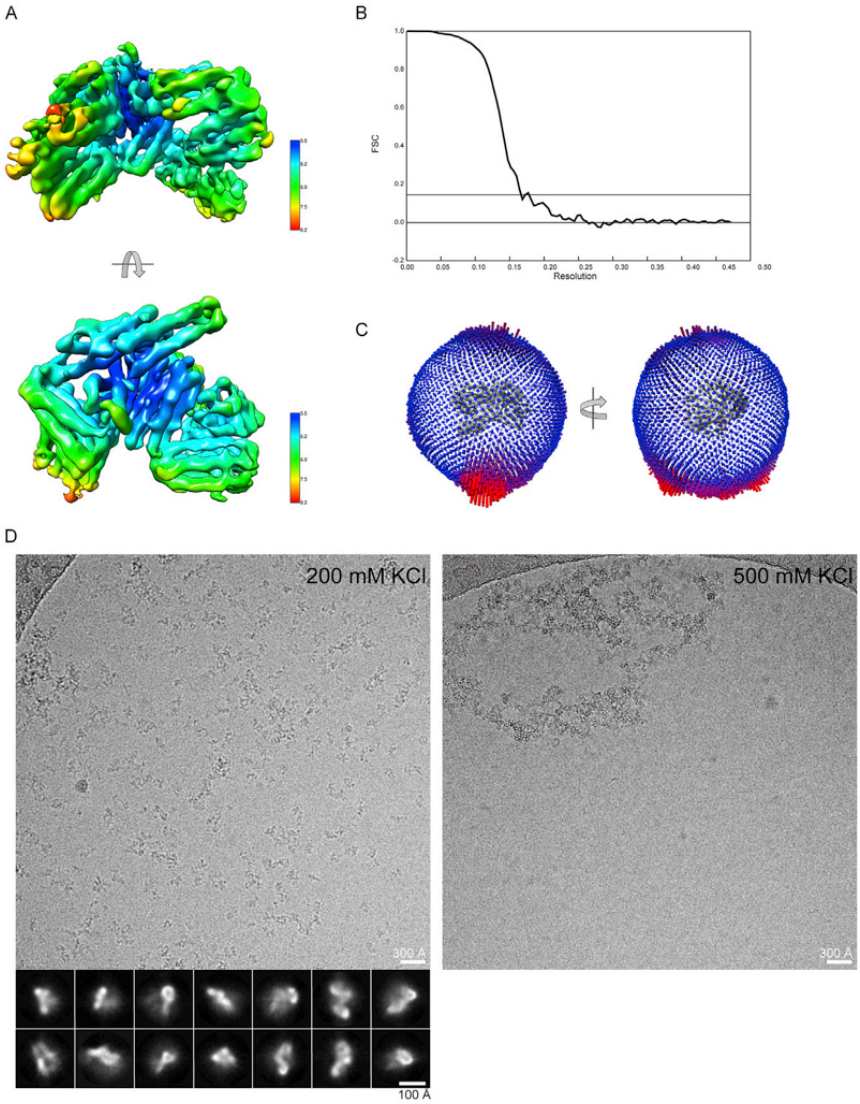

Figure S2. Quality Control of Cryo-EM Data Processing, Related to Figure 1

A: Local resolution map of the talin-FL structure, showing a resolution range between 5.5 Å and 7.9 Å. B: The Fourier shell correlation (FSC) curve of the talin-FL structure showing a global resolution of 6.2 Å. The additional line indicates a FSC of 0.143 C: Angular distributions of the particle orientations that were incorporated into the final 3D reconstruction. D: Cryo-EM images of talin-FL in the presence of 200 mM KCl and 500 mM KCl, showing aggregations presumably due to the talin opening at 500 mM KCl. 2D classifications of talin-FL at 200 mM KCl reveal less robust averages indicating higher structural heterogeneity.

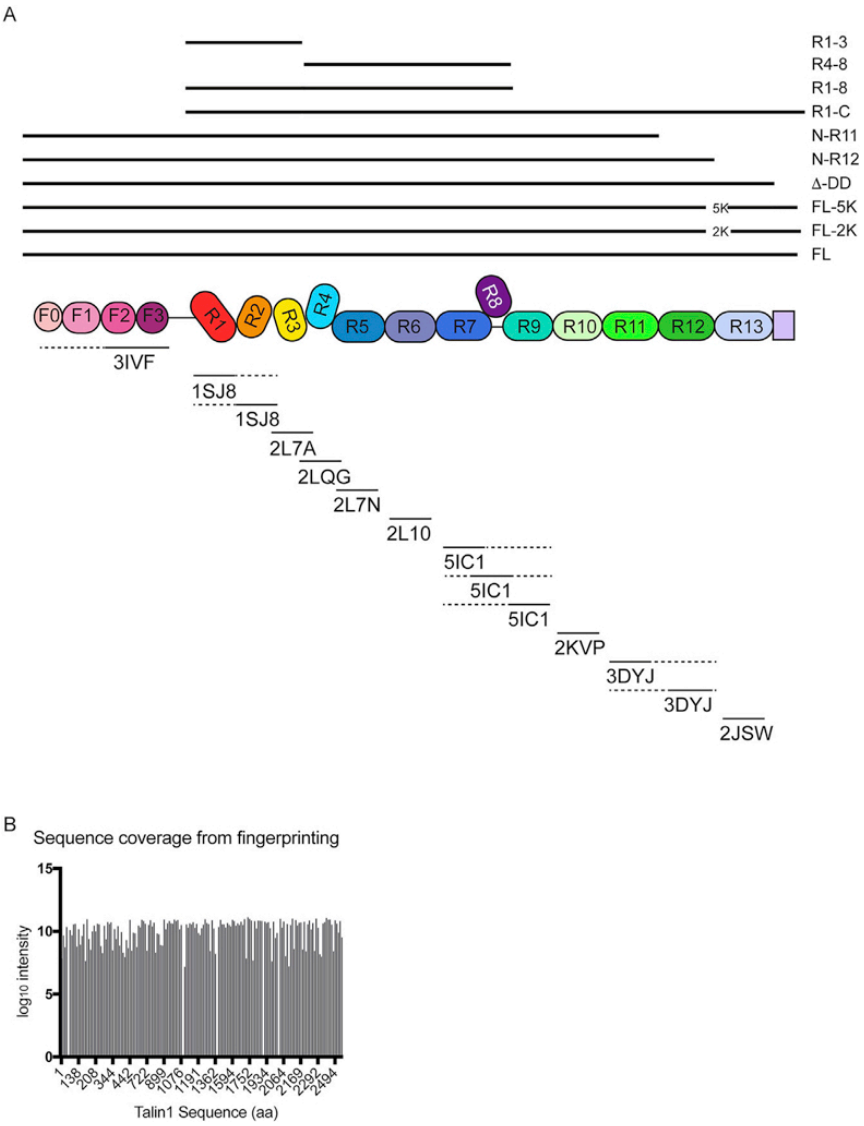

Figure S3. Talin Fragments Used in This Study and Sequencing Information of Talin-FL, Related to Figure 1

A: Scheme of talin fragments used in this study (top) and the structures (PDB codes) that were used as building blocks for the fitting and molecular modelling. For PDBs 3IVF, 1SJ8, 5IC1 and 3DYJ, individual domains are computationally extracted and used independently (see also STAR methods). 2K denotes charge-reversal double mutation E2288K, E2294K and 5K denotes mutations E2288K, E2294K, D2297K, E2299K, D2300K). B: Peptide detection of talin-FL by mass spectrometry. The entire sequence of talin (1-2541) is covered, showing no indication of spontaneous cleavage.

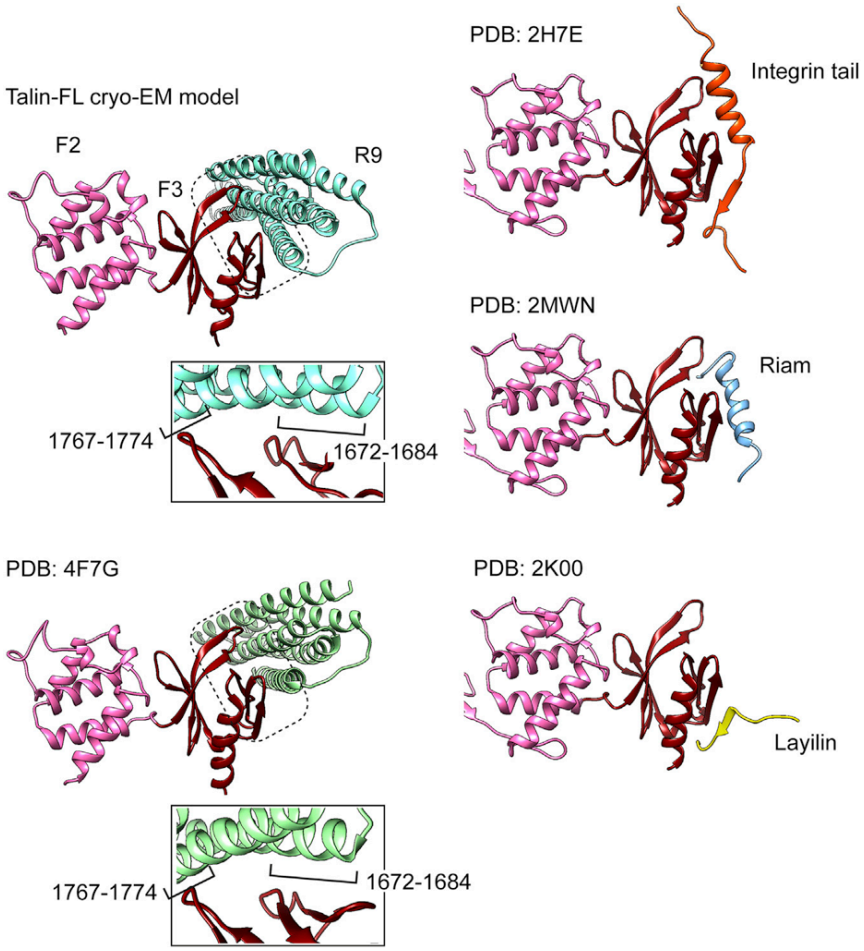

Figure S4. Talin F3-Rod Binding Surfaces Obtained from Our Cryo-EM Map in Comparison to Available Structures, Related to Figure 1
Top-left: Our cryo-EM model of the F3-rod binding surface. Bottom-left: crystal structure (PDB: 4F7G) of truncated F2-F3 and R9. Right: Examples of structures that bind to the talin F3-rod binding surface. From top to bottom: PDB: 4F7G superimposed to 2H7E (Integrin tail), 2MWN (RIAM), and 2K00 (Layilin).

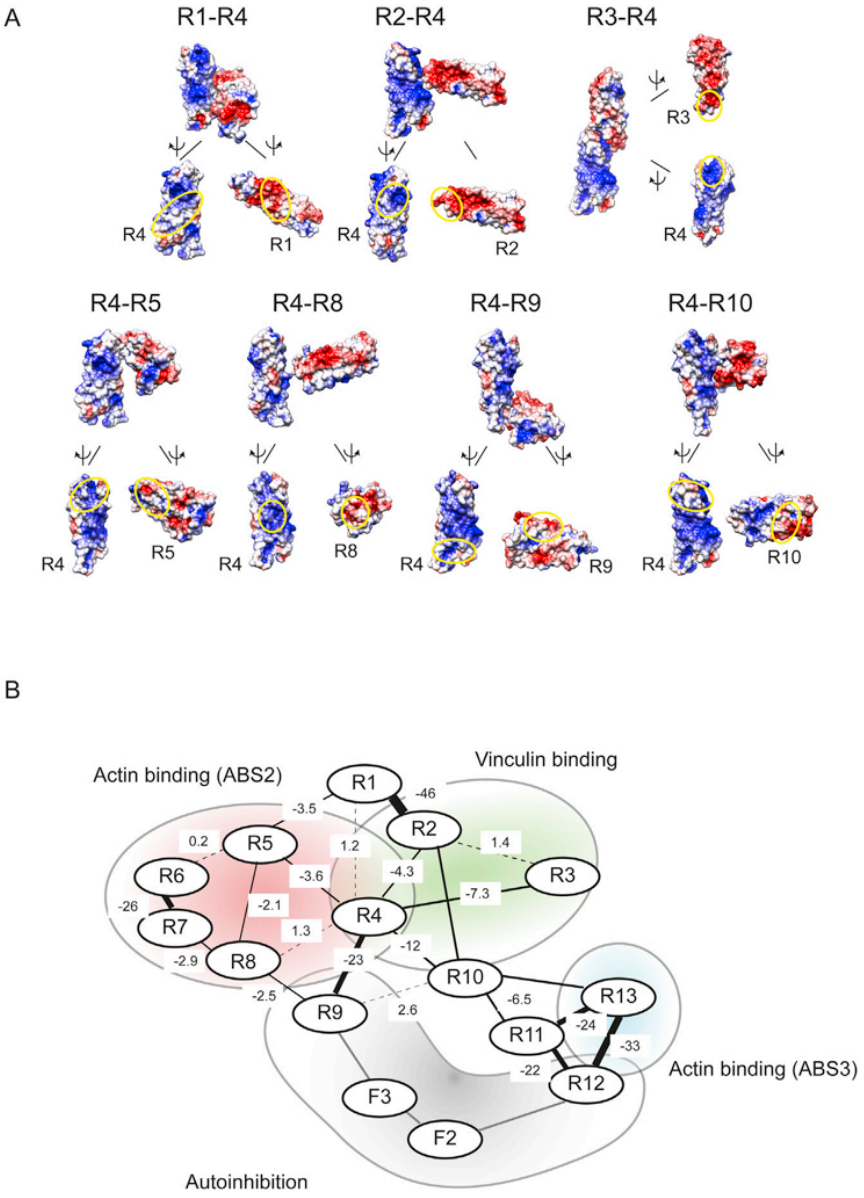

Figure S5. Talin Inter-Domain Interactions, Related to Figures 1 and 4

A: Electrostatic surface potential of individual rod domains surrounding R4 and forming the autoinhibition core. Sites contacting each other are indicated with yellow circles. B: Interaction energies calculated by restraint molecular dynamics simulations for major interaction surfaces in the presence of 150 mM salt. Units: kCal/mol. We note that the calculated interaction energies represent enthalpic contributions and do not include the entropic penalties of restricting the large ensemble of open and flexible conformations of talin to a small ensemble of compact conformations seen in the autoinhibited state.

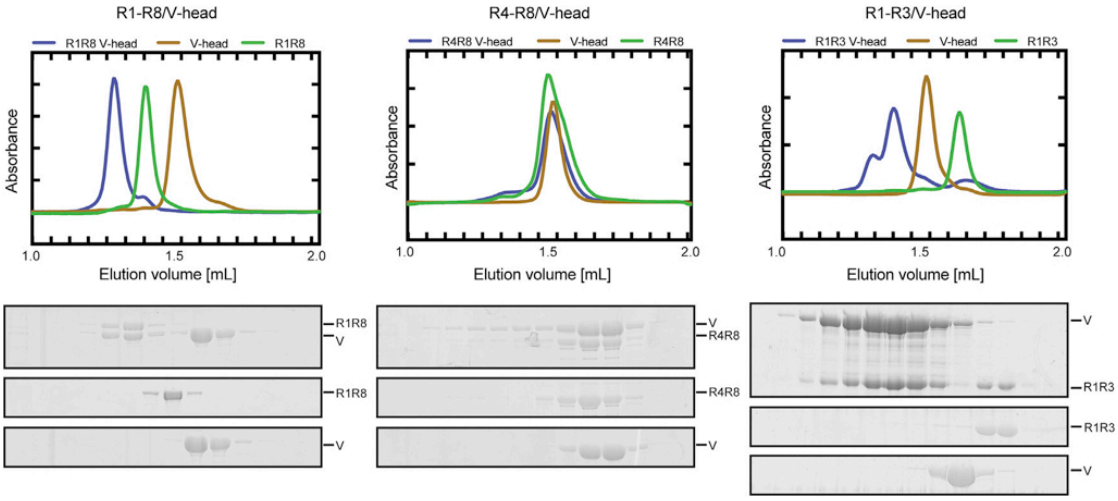

Figure S6. SEC Reconstitution Assay of Various Talin Rod Domains and the Vinculin Head (V-Head) at 75 mM Salt, Related to Figure 5

The SDS-PAGE analysis corresponds to the profile of the protein mixtures (top), talin control constructs (center), and vinculin head control (bottom), respectively.

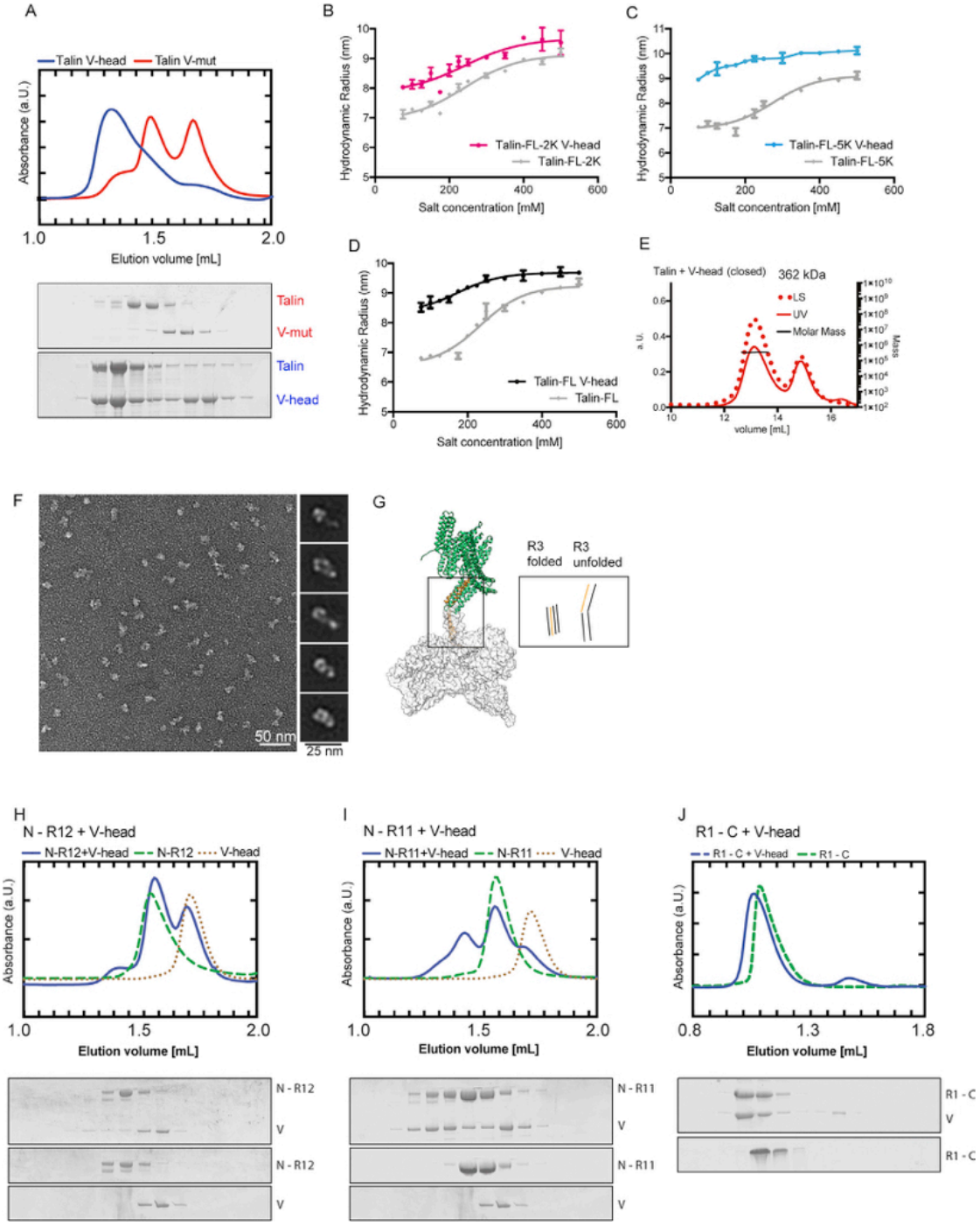

Figure S7. Conformational Change of Talin in Complex with V-Head, Related to Figures 5 and 6

A: Size-exclusion chromatography (SEC) profile of talin and vinculin constructs. Reconstitution assays of talin (open conformation) and V-head as well as V-mut were performed at 500 mM salt, and then the complex was assessed by changing the salt concentration to 75 mM. V-head stays in complex with talin (blue), while V-mut dissociates from talin (red). B-D: DLS measurements of the hydrodynamic radius of the reconstituted talin constructs (talin-FL, talin-FL-2K and talin-FL-5K) in complex with V-head under various salt concentrations. In comparison to talin-FL constructs alone (shown in grey), the increased size of the sample is observed showing complex formation. A conformational change of talin-V-head complex upon the change of salt concentration is also observed. For the case of talin-FL-5K in complex with V-head, the profile did not fit to a two-state model. E: SEC-multi-angle light-scattering profile of the talin (75mM salt, closed) -V-head complex showed a molecular weight of 362 kDa, indicating a 1:1 stoichiometry. LS: light scattering, normalized, UV: absorbance F: Negative-stain EM image of the talin-vinculin head complex in closed talin and two-dimensional averages (right), showing a long protrusion from the main globular density. G: Molecular modeling of our talin structure (white) with R3 unfolded (yellow) to accommodate the vinculin head density (green). The model was created by combining our cryo-EM talin-FL

(legend continued on next page)

structure (white) with available structures of a part of the V-head (a.a. 1–258) complexed with talin peptide (a.a. 1944–1969) (PDB: 1RKC, yellow) and the vinculin head (a.a. 259–843) extracted from full-length vinculin (PDB: 1TR2, green). H-J: SEC profiles of various talin truncation constructs with V-head at 75 mM salt, showing that the complex formation of talin and V-head occurs only with N-R11 (I) and R1-C (J). N-R12 containing the R12 (lid) did not form a complex with V-head (H). In the reconstitution assay of R1-C + V-head, a Superdex S200 column was used while a Superose 6 was used for the other assays. The control runs for V-head come from the same experiment and the corresponding profile and SDS-PAGE are shown twice for comparison. Error bars show standard deviations.

4. Discussion

Integrins are the key receptors of FAs and involved in basic cellular processes such as adhesion and migration. Aberrant integrin function can have detrimental effects for the body and lead to diseases such as cancer.

Despite its importance for cellular and tissue function, how integrin α5β1 functions and binds its ligand FN on a molecular level has not been fully understood so far.

Our study revealed molecular insights into the integrin α5β1-FN interaction, which showed that the interface is comprised of several modules. For the first time, next to binding of the well-known RGD motif, the interaction between the synergy site on FN and the α5 subunit was directly observed. Moreover, an additional binding interface between FN and ADMIDAS in integrin β1 could be determined. Our physiological integrin α5β1 sample, purified from human placenta, also revealed that N-glycans contribute to the ligand binding. The inactive state of α5β1 was analyzed as well and showed that the ectodomain is arranged in a novel semi-bent conformation. The same bent organization was also observed in presence of ligand-mimetic Mn^{2+} and only changed to the open conformation when the full FN ligand was additionally present. Together, the results obtained in our study show that the activation mode of integrin α5β1 differs from other isoforms of the integrin family.

Integrin α5β1 is the major FN receptor in the human body. It is ubiquitously expressed and has been shown to play a direct role in angiogenesis (Schaffner et al., 2013). On a cellular level, it contributes to adhesion by anchoring the cell to the ECM. Vice versa, α5β1 is actively involved in ECM network formation. Fibronectin is expressed as a soluble dimer, which assembles into fibrillary networks upon binding to cells, in particular cells expressing α5β1 (Schwarzbauer and Sechler, 1999). The binding of FN to α5β1 then induces fibrillary assembly. How this occurs exactly, is still under investigation. Most likely, the interaction and accompanying force exertion induces conformational changes in the FN molecule which enable the access of certain polymerization sites.

Integrin α5β1 was reported to be overexpressed in several aggressive cancer types, such as breast, ovarian, colon and lung cancer, where it contributes to tumoral neoangiogenesis (Schaffner et al., 2013). As its overexpression strongly correlates with

poor long-term survival of patients, it could be used as a diagnostic marker and is a promising therapeutical target. Thus, drugs such as the antibody Volociximab and ATN-161, a small molecule mimicking the synergy site, have been developed and showed initial promise in cancer therapy approaches (Schaffner et al., 2013). However, as of 2017, only seven integrin-specific drugs entered the pharmaceutical market, none of which are targeting a5β1, whereas the rest of the 480 registered drugs did not make it past clinical phase trials (Raab-Westphal et al., 2017). There are several explanations for this lack of suitable integrin-targeting drugs. The main reason probably lies in the complexity of integrin biology. We still do not understand how integrins are distributed throughout tissues in health and disease. Moreover, integrin activation leads to complex signaling cascades which first have to be elucidated further to get a complete picture of integrin function. Lastly, how integrins interplay with their environment and with other isoforms has to be clarified to reduce off-target effects and to fine-tune integrin targeting (Raab-Westphal et al., 2017). This complexity further underlines the importance of integrin research.

Our study directly validated several predicted interaction sites between integrin α5β1 and FN. Next to the well-known RGD motif in FN10 binding to both α and β subunits, the synergy site in FN 9, comprising residues 1373-1380 (DRVPHSRN), contributes to a stable interaction. Although mutational studies and MD simulations have been conducted to analyze the effect of the synergy site on α5β1-FN binding, we, for the first time, could directly show the interaction on a structural level since we used a bigger part of FN instead of single RGD peptides. Two residues R1374 and R1379 have been denoted as key residues for the synergy site interaction and catch-bond formation (Friedland et al., 2009; Redick et al., 2000). The interaction between D154 (α5) and R1379 (FN9), which has been observed before by MD and biochemical assays (Nagae et al., 2012), was confirmed in our structure. Moreover, several hydrophobic residues surrounding these residues contribute to the synergy site interaction. However, we did not observe any interaction between R1374, the second key residue in the synergy site, and integrin α5. In our experimental setup, no force was applied to the molecules. Thus, it is possible that the reported binding between R1374 and α5 plays a more important role in the context of the catch-bond formation between FN and α5β1 (Friedland et al., 2009; Kong et al., 2009; Redick et al., 2000). Upon force transduction, FN and integrin might be stretched in a way

that alters their orientation slightly towards each other and thus may lead to further engagement between R1374 and integrin α5.

Importantly, we unveiled novel FN residues next to RGD and synergy site, engaging in interaction with integrin, in particular, residues surrounding ADMIDAS in the β1 subunit. The importance of ADMIDAS for the activation and headpiece opening of integrins has been underlined by many studies over the recent years, which show that ADMIDAS mutations abrogate conformational changes of integrins (Zhang and Chen, 2012). Along the same line, it has been shown recently that integrin αvβ8, the only integrin which does not contain an ADMIDAS, functions entirely in its extended-closed state and does not undergo any conformational changes (Campbell et al., 2020; Cormier et al., 2018). The ADMIDAS is connected to the α1 helix in the βI domain, which, together with α7 helix, has been reported as crucial for headpiece opening and integrin extension (Luo et al., 2007). By pulling on the ADMIDAS cation, the translocation of the α1 helix and subsequent headpiece opening might be stabilized. Our structural analysis suggested that additional residues on FN10, such as Y1446, could potentially support the headpiece opening by interaction with the ADMIDAS cation. This might help to explain why in past studies, RGD peptide alone has opened integrin headpieces to a lesser degree than the bigger ligand (Takagi et al., 2003) (and our own unpublished results).

Our integrin sample was purified from human placenta and thus contained α5β1 with its physiological N-glycosylations. So far, the role of N-glycosylation for integrin α5β1 has been studied extensively; however, mostly by using recombinant sample preparations (Isaji et al., 2009; Isaji et al., 2006). It has been shown that upon de-glycosylation or mutations of N-glycosylation sites, integrin α5β1 function is severely impaired since heterodimer formation and ligand binding are reduced (Guo et al., 2002; Isaji et al., 2009; Isaji et al., 2006; Zheng et al., 1994). Our study, for the first time, revealed how exactly glycosylations could be involved in FN binding on a molecular level. The glycan at position N275 is of particular importance, as it extends to the interface of FN9-10 and seems to contribute to the docking of FN by charged interactions.

Taken together, our study revealed that the interface between integrin α5β1 and FN is more extensive than initially thought and that all interaction sites, i.e. RGD, synergy site, ADMIDAS and glycans, contribute together to a stable binding.

Integrin equilibrium and fine-tuning of conformational changes

Integrins are thought to exist in an equilibrium of conformational states, i.e. to continuously fluctuate between bent and extended-open states (Luo et al., 2007). Whenever another factor, such as ligand or intracellular protein, is added to or removed from the system, the dynamic equilibrium might be shifted further to one side. In that way, by using negative-stain EM analysis, we were able to observe that all integrin α5β1 conformations are present in all conditions. However, the percentage of integrins in extended-open conformation increased drastically when Mn^{2+}, stabilizing antibody TS2/16 and ligand FN were added. None of the components induced such a significant increase in open conformations by themselves.

Another negative-stain EM study reported that the distribution of conformational states varies strongly between different integrin isoforms (Miyazaki et al., 2018). This suggests that all integrins have adapted and fine-tuned their activation mechanism and equilibrium depending on their cellular function. Therefore, integrins that contain β2 and β3 subunits, which are mainly expressed on circulating cells (such as platelets and leucocytes), seem to mainly adopt the bent conformation when no activating factors are present. In the case of α5β1, however, a stable portion of extended integrins was also present under resting conditions. This observed 'uncoupling' of affinity and conformational state in the case of β1 integrins could be due to their different expression patterns: since β1 is mainly expressed on adherent cells, it might be beneficial to have a 'fail-safe' mechanism where a portion of integrins is always extended and engaged in ECM binding, independent of stimuli. In the case of β2 and β3 integrins, the presence of extended integrins on cells that should be inactive could have detrimental effects, such as platelet aggregation or inflammation caused by overactive leucocytes. Thus, the affinity for ligand binding and conformational change seem to be more tightly coupled for β2 and β3 integrins than for β1.

Furthermore, we observed that the extent of bending seems to differ for integrin α5β1 in comparison to the well-studied β3 integrins. In its resting state, α5β1 exhibits a semi-bent conformation (~90˚ between head and legs), whereas integrins αIIbβ3 and αvβ3 show a more acutely bent conformation (~45˚ between head and legs) (Xiong et al., 2001; Zhu et al., 2008). This observation is in agreement with the uncoupling of affinity and conformational state. Most likely, it represents another layer of regulation designed

to keep integrins on circulating cells (β2, β3) inactive, whereas integrins on adhering cells (β1) do not need to be switched off so severely.

In regard to these observations, it has often been discussed how inside-out activation of integrins by intracellular factors, such as talin and kindlin, is achieved. It has been hypothesized that activation of integrin by talin might be mainly crucial for hematopoietic cells but not for cells within whole tissues (Klapholz and Brown, 2017). Calculations by Springer and colleagues have predicted that forces around 1-3 pN are already sufficient for the opening of the integrin headpiece (Li and Springer, 2017), which furthermore raises the question whether inside-out activation is required for all integrins or if outside-in activation is more significant. It could be possible that talin and kindlin only maintain the open-extended conformation in some cell types but are not actively causing it (Sun et al., 2019).

Overall, the fine-tuned integrin equilibrium of conformational states is an exciting concept that helps to explain the different behavior of integrin isoforms. It suggests that integrins have adapted to their intercellular context and specific role in the body and thus have different layers of regulation.

Limitations of the study

Although we were able learn a lot using the approach of purified placental integrin with a bigger FN ligand fragment 7-10, and cryo-EM single-particle analysis, our study has some limitations.

We successfully inserted purified integrin α5β1 into a nanodisc system, consisting of a membrane scaffold protein and lipids (Bayburt and Sligar, 2003; Denisov et al., 2004), which was confirmed by size-exclusion chromatography, SDS-PAGE as well as negative-stain EM. However, we did not observe any membrane density under cryo-EM conditions. Most likely, due to the harsh air-water interface, integrin got 'pulled-out' of the nanodisc and the TM and CT domains were too flexible to be averaged and did not appear as density in our maps. As a result, only the stable parts of the ectodomain were visualized in our 2D and 3D reconstructions for both conformational states.

Furthermore, since we focused on studying the detailed molecular interaction between integrin and FN, we worked with a simplified system, using only the mentioned components, i.e. integrin α5β1, FN7-10, Mn^{2+} and the stabilizing antibody TS2/16. This allows us to get a clear and detailed picture of their interactions; however, it also limits

the conclusions we are able to draw for integrin activation in a bigger, cellular context. There are still many open questions regarding integrin function. How other factors, such as mechanical force as well as intracellular activators like talin, which have been shown to be important for proper integrin activation in cells, affect integrin function is still unclear. The *in vitro* setup presented in our work does not cover these additional factors of integrin activation and their interplay.

Despite these limitations, our study provides novel insights into integrin α5β1 function and reveals an extensive regulatory mechanism comprised by several modules on the FN-integrin interface, N-glycans as well as by a semi-bent arrangement of the resting integrin α5β1. Getting a full overview on how integrins work is relevant, as they are interesting therapeutic targets for diseases such as cancer. The findings and experimental approaches presented in this work could be used as a basis for future investigations and adapted to address further questions regarding integrin biology.

5. Outlook

Integrins have been studied extensively for years and the activation mechanism derived from these studies has been thought to apply to most isoforms. Our findings highlight that different integrin isoforms might employ different activation mechanisms and need additional regulatory components present on both their ligands and on integrins themselves. Earlier studies that suggested that integrins function in different modes might have been neglected and explained by experimental errors (Arnaout et al., 2005; Luo et al., 2007; Luo and Springer, 2006). However, recent studies regarding αvβ8 (Campbell et al., 2020; Cormier et al., 2018) as well as our study of α5β1 presented in this work give a clear indication that integrins indeed might not all be sharing the exact same activation mechanism. In contrast to other integrins, neither αvβ8 nor α5β1 seem to adopt the acutely bent, inactive conformation which has been postulated based on β3 and β2 integrins (Xie et al., 2010; Xiong et al., 2001; Zhu et al., 2008). αvβ8 appears to function entirely in an extended-closed conformation (without headpiece opening), while α5β1 seems to be incompletely bent and activation-mimetic Mn^{2+} does not induce a change in conformation. These observations underline the need to study every integrin individually on a structural basis; and more comparative studies for other integrin isoforms will yield vast insights into their behavior. Especially the recent advances in the field of cryo-EM will be of substantial help as they allow to study integrins in a more native, 'in-solution' environment, and circumvent the need for crystallization that could introduce artefacts. It will be interesting to dissect how other integrins managed to fine-tune their working mechanisms in order to adapt to their individual roles in the body.

Furthermore, although we used full-length integrin for our study, our cryo-EM analysis only visualized the ectodomains of α5β1 in molecular detail. It will be of great interest to see the activation mechanism of full-length integrin in context of their physiological membrane. For many membrane proteins, it has been hypothesized that the membrane surrounding is crucial for proper functioning. For this, approaches to keep membrane proteins soluble, such as the nanodisc system, saposin-lipoprotein (Salipro) or styrene maleic-acid lipid particles (SMALP), could be utilized and optimized since they are compatible with the cryo-EM approach (Sgro and Costa, 2018). The membrane composition might also affect integrin behavior and could be studied via these systems. In this way, it would be interesting to see what effect PIP_2, which has been denoted as key

regulatory lipid component of FAs, by binding to FA proteins such as vinculin and talin (Chinthalapudi et al., 2018; Chinthalapudi et al., 2014; Janmey et al., 2018; Song et al., 2012), has on integrin.

Moreover, it would be intriguing to add and study more layers of integrin regulation on a molecular level. By adding the integrin activators kindlin, talin and other intracellular components, early NA complexes could be reconstituted *in vitro*. Building a reconstituted complex from top-to-bottom would lead to a deeper understanding of how adhesions are initially assembled and function in general. By studying larger parts of the ligand FN or complex FN fibers, insights in integrin activation, and possibly clustering, could be gained as well.

In addition, exploring the role of mechanical forces on both integrin-ligand interactions and structural conformations is of particular interest. The effect of force on integrin-ligand bonds has been studied using a variety of biophysical methods, such as atomic force microscopy (Kong et al., 2009), molecular FRET-based tension sensors (Nordenfelt et al., 2016) and spinning-disc devices (Friedland et al., 2009). Deciphering what occurs on the atomic level during force transduction could offer a direct explanation for many of these observed effects. In this regard, it would be interesting to visualize by cryo-EM the binding of the second synergy site residue R1374 to integrin, which was not engaged in the interaction in our structure. To obtain more information, the integrin-ligand interaction would have to be subjected to force on the cryo-EM grid, which might be achieved by combining EM with a single-molecule approach using myosin II and molecular motors.

Advances in cryo-electron tomography enable studies on proteins in near-native context in sub-nanometer resolution. This field is rapidly expanding and new technical breakthroughs allow for the visualization of proteins within the cell (Beck and Baumeister, 2016). Via focused ion beam (FIB) milling, thin slices of vitrified cell samples can be generated that enable studying protein complexes *in situ*. The resolutions do not yet reach the range of single-particle cryo-EM, however, will certainly continue to improve within the next couple of years. Studying integrins and FA complexes via cryo-electron tomography would circumvent many limitations and possible artefacts of *in vitro* biochemical setups and give a clear picture of how integrins function in their physiological environment.

The invaluable information gained from structural studies on integrins is not only of theoretical interest but could benefit clinical research and the development of new therapeutic approaches. By discovering more specific molecular targets on integrin as well as differences in their conformational states, more specific antibodies or small molecules can be designed for several integrin-related diseases, such as cancer (Zheng and Leftheris, 2020).

In summary, although a vast amount of knowledge has been acquired in the field of integrins in the last decades, many critical open questions remain, which can be addressed using the new technological advances, especially in the field of electron microscopy.

6. References

Adair, B.D., Xiong, J.P., Maddock, C., Goodman, S.L., Arnaout, M.A., and Yeager, M. (2005). Three-dimensional EM structure of the ectodomain of integrin {alpha}V{beta}3 in a complex with fibronectin. J Cell Biol *168*, 1109-1118.

Adair, B.D., and Yeager, M. (2002). Three-dimensional model of the human platelet integrin alpha IIbbeta 3 based on electron cryomicroscopy and x-ray crystallography. Proc Natl Acad Sci U S A *99*, 14059-14064.

Akiyama, S.K., Yamada, S.S., and Yamada, K.M. (1989). Analysis of the role of glycosylation of the human fibronectin receptor. J Biol Chem *264*, 18011-18018.

Alon, R., and Dustin, M.L. (2007). Force as a facilitator of integrin conformational changes during leukocyte arrest on blood vessels and antigen-presenting cells. Immunity *26*, 17-27.

Anthis, N.J., Wegener, K.L., Critchley, D.R., and Campbell, I.D. (2010). Structural diversity in integrin/talin interactions. Structure *18*, 1654-1666.

Anthis, N.J., Wegener, K.L., Ye, F., Kim, C., Goult, B.T., Lowe, E.D., Vakonakis, I., Bate, N., Critchley, D.R., Ginsberg, M.H.*, et al.* (2009). The structure of an integrin/talin complex reveals the basis of inside-out signal transduction. EMBO J *28*, 3623-3632.

Aota, S., Nagai, T., and Yamada, K.M. (1991). Characterization of regions of fibronectin besides the arginine-glycine-aspartic acid sequence required for adhesive function of the cell-binding domain using site-directed mutagenesis. J Biol Chem *266*, 15938-15943.

Armulik, A., Nilsson, I., von Heijne, G., and Johansson, S. (1999). Determination of the border between the transmembrane and cytoplasmic domains of human integrin subunits. J Biol Chem *274*, 37030-37034.

Arnaout, M.A., Mahalingam, B., and Xiong, J.P. (2005). Integrin structure, allostery, and bidirectional signaling. Annu Rev Cell Dev Biol *21*, 381-410.

Askari, J.A., Tynan, C.J., Webb, S.E., Martin-Fernandez, M.L., Ballestrem, C., and Humphries, M.J. (2010). Focal adhesions are sites of integrin extension. J Cell Biol *188*, 891-903.

Astrof, N.S., Salas, A., Shimaoka, M., Chen, J., and Springer, T.A. (2006). Importance of force linkage in mechanochemistry of adhesion receptors. Biochemistry *45*, 15020-15028.

Atherton, P., Stutchbury, B., Wang, D.Y., Jethwa, D., Tsang, R., Meiler-Rodriguez, E., Wang, P., Bate, N., Zent, R., Barsukov, I.L.*, et al.* (2015). Vinculin controls talin engagement with the actomyosin machinery. Nat Commun *6*, 10038.

Austen, K., Ringer, P., Mehlich, A., Chrostek-Grashoff, A., Kluger, C., Klingner, C., Sabass, B., Zent, R., Rief, M., and Grashoff, C. (2015). Extracellular rigidity sensing by talin isoform-specific mechanical linkages. Nat Cell Biol *17*, 1597-1606.

Bachir, A.I., Zareno, J., Moissoglu, K., Plow, E.F., Gratton, E., and Horwitz, A.R. (2014). Integrin-associated complexes form hierarchically with variable stoichiometry in nascent adhesions. Curr Biol *24*, 1845-1853.

Barczyk, M., Carracedo, S., and Gullberg, D. (2010). Integrins. Cell Tissue Res *339*, 269-280.

Bate, N., Gingras, A.R., Bachir, A., Horwitz, R., Ye, F., Patel, B., Goult, B.T., and Critchley, D.R. (2012). Talin contains a C-terminal calpain2 cleavage site important in focal adhesion dynamics. PLoS One *7*, e34461.

Bayburt, T.H., and Sligar, S.G. (2003). Self-assembly of single integral membrane proteins into soluble nanoscale phospholipid bilayers. Protein Sci *12*, 2476-2481.

Beck, M., and Baumeister, W. (2016). Cryo-Electron Tomography: Can it Reveal the Molecular Sociology of Cells in Atomic Detail? Trends Cell Biol *26*, 825-837.

Benito-Jardon, M., Klapproth, S., Gimeno, L.I., Petzold, T., Bharadwaj, M., Muller, D.J., Zuchtriegel, G., Reichel, C.A., and Costell, M. (2017). The fibronectin synergy site re-enforces cell adhesion and mediates a crosstalk between integrin classes. Elife *6*.

Bledzka, K., Liu, J., Xu, Z., Perera, H.D., Yadav, S.P., Bialkowska, K., Qin, J., Ma, Y.Q., and Plow, E.F. (2012). Spatial coordination of kindlin-2 with talin head domain in interaction with integrin beta cytoplasmic tails. J Biol Chem *287*, 24585-24594.

Bottcher, R.T., Veelders, M., Rombaut, P., Faix, J., Theodosiou, M., Stradal, T.E., Rottner, K., Zent, R., Herzog, F., and Fassler, R. (2017). Kindlin-2 recruits paxillin and Arp2/3 to promote membrane protrusions during initial cell spreading. J Cell Biol *216*, 3785-3798.

Bouaouina, M., Lad, Y., and Calderwood, D.A. (2008). The N-terminal domains of talin cooperate with the phosphotyrosine binding-like domain to activate beta1 and beta3 integrins. J Biol Chem *283*, 6118-6125.

Byron, A., Humphries, J.D., Askari, J.A., Craig, S.E., Mould, A.P., and Humphries, M.J. (2009). Anti-integrin monoclonal antibodies. J Cell Sci *122*, 4009-4011.

Calderwood, D.A., Campbell, I.D., and Critchley, D.R. (2013). Talins and kindlins: partners in integrin-mediated adhesion. Nat Rev Mol Cell Biol *14*, 503-517.

Calderwood, D.A., Fujioka, Y., de Pereda, J.M., Garcia-Alvarez, B., Nakamoto, T., Margolis, B., McGlade, C.J., Liddington, R.C., and Ginsberg, M.H. (2003). Integrin beta cytoplasmic domain interactions with phosphotyrosine-binding domains: a structural prototype for diversity in integrin signaling. Proc Natl Acad Sci U S A *100*, 2272-2277.

Calderwood, D.A., Huttenlocher, A., Kiosses, W.B., Rose, D.M., Woodside, D.G., Schwartz, M.A., and Ginsberg, M.H. (2001). Increased filamin binding to beta-integrin cytoplasmic domains inhibits cell migration. Nat Cell Biol *3*, 1060-1068.

Calderwood, D.A., Yan, B., de Pereda, J.M., Alvarez, B.G., Fujioka, Y., Liddington, R.C., and Ginsberg, M.H. (2002). The phosphotyrosine binding-like domain of talin activates integrins. J Biol Chem *277*, 21749-21758.

Calderwood, D.A., Zent, R., Grant, R., Rees, D.J., Hynes, R.O., and Ginsberg, M.H. (1999). The Talin head domain binds to integrin beta subunit cytoplasmic tails and regulates integrin activation. J Biol Chem *274*, 28071-28074.

Campbell, I.D., and Humphries, M.J. (2011). Integrin structure, activation, and interactions. Cold Spring Harb Perspect Biol *3*.

Campbell, M.G., Cormier, A., Ito, S., Seed, R.I., Bondesson, A.J., Lou, J., Marks, J.D., Baron, J.L., Cheng, Y., and Nishimura, S.L. (2020). Cryo-EM Reveals Integrin-Mediated TGF-beta Activation without Release from Latent TGF-beta. Cell *180*, 490-501 e416.

Case, L.B., Baird, M.A., Shtengel, G., Campbell, S.L., Hess, H.F., Davidson, M.W., and Waterman, C.M. (2015). Molecular mechanism of vinculin activation and nanoscale spatial organization in focal adhesions. Nat Cell Biol *17*, 880-892.

Chan, C.E., and Odde, D.J. (2008). Traction dynamics of filopodia on compliant substrates. Science *322*, 1687-1691.

Chang, A.C., Mekhdjian, A.H., Morimatsu, M., Denisin, A.K., Pruitt, B.L., and Dunn, A.R. (2016). Single Molecule Force Measurements in Living Cells Reveal a Minimally Tensioned Integrin State. ACS Nano *10*, 10745-10752.

Chang, D.D., Hoang, B.Q., Liu, J., and Springer, T.A. (2002). Molecular basis for interaction between Icap1 alpha PTB domain and beta 1 integrin. J Biol Chem *277*, 8140-8145.

Chen, J., Salas, A., and Springer, T.A. (2003). Bistable regulation of integrin adhesiveness by a bipolar metal ion cluster. Nat Struct Biol *10*, 995-1001.

Chen, W., Lou, J., Evans, E.A., and Zhu, C. (2012). Observing force-regulated conformational changes and ligand dissociation from a single integrin on cells. J Cell Biol *199*, 497-512.

Chinthalapudi, K., Rangarajan, E.S., and Izard, T. (2018). The interaction of talin with the cell membrane is essential for integrin activation and focal adhesion formation. Proc Natl Acad Sci U S A *115*, 10339-10344.

Chinthalapudi, K., Rangarajan, E.S., Patil, D.N., George, E.M., Brown, D.T., and Izard, T. (2014). Lipid binding promotes oligomerization and focal adhesion activity of vinculin. J Cell Biol *207*, 643-656.

Choi, C.K., Vicente-Manzanares, M., Zareno, J., Whitmore, L.A., Mogilner, A., and Horwitz, A.R. (2008). Actin and alpha-actinin orchestrate the assembly and maturation of nascent adhesions in a myosin II motor-independent manner. Nat Cell Biol *10*, 1039-1050.

Choi, W.S., Rice, W.J., Stokes, D.L., and Coller, B.S. (2013). Three-dimensional reconstruction of intact human integrin alphaIIbbeta3: new implications for activation-dependent ligand binding. Blood *122*, 4165-4171.

Cormier, A., Campbell, M.G., Ito, S., Wu, S., Lou, J., Marks, J., Baron, J.L., Nishimura, S.L., and Cheng, Y. (2018). Cryo-EM structure of the alphavbeta8 integrin reveals a mechanism for stabilizing integrin extension. Nat Struct Mol Biol *25*, 698-704.

Czuchra, A., Meyer, H., Legate, K.R., Brakebusch, C., and Fassler, R. (2006). Genetic analysis of beta1 integrin "activation motifs" in mice. J Cell Biol *174*, 889-899.

Dai, A., Ye, F., Taylor, D.W., Hu, G., Ginsberg, M.H., and Taylor, K.A. (2015). The Structure of a Full-length Membrane-embedded Integrin Bound to a Physiological Ligand. J Biol Chem *290*, 27168-27175.

Debrand, E., Conti, F.J., Bate, N., Spence, L., Mazzeo, D., Pritchard, C.A., Monkley, S.J., and Critchley, D.R. (2012). Mice carrying a complete deletion of the talin2 coding sequence are viable and fertile. Biochem Biophys Res Commun *426*, 190-195.

Dedden, D., Schumacher, S., Kelley, C.F., Zacharias, M., Biertumpfel, C., Fassler, R., and Mizuno, N. (2019). The Architecture of Talin1 Reveals an Autoinhibition Mechanism. Cell *179*, 120-131 e113.

del Rio, A., Perez-Jimenez, R., Liu, R., Roca-Cusachs, P., Fernandez, J.M., and Sheetz, M.P. (2009). Stretching single talin rod molecules activates vinculin binding. Science *323*, 638-641.

Denisov, I.G., Grinkova, Y.V., Lazarides, A.A., and Sligar, S.G. (2004). Directed self-assembly of monodisperse phospholipid bilayer Nanodiscs with controlled size. J Am Chem Soc *126*, 3477-3487.

Di Paolo, G., Pellegrini, L., Letinic, K., Cestra, G., Zoncu, R., Voronov, S., Chang, S., Guo, J., Wenk, M.R., and De Camilli, P. (2002). Recruitment and regulation of phosphatidylinositol phosphate kinase type 1 gamma by the FERM domain of talin. Nature *420*, 85-89.

Elliott, P.R., Goult, B.T., Kopp, P.M., Bate, N., Grossmann, J.G., Roberts, G.C., Critchley, D.R., and Barsukov, I.L. (2010). The Structure of the talin head reveals a novel extended conformation of the FERM domain. Structure *18*, 1289-1299.

Ellis, S.J., Lostchuck, E., Goult, B.T., Bouaouina, M., Fairchild, M.J., Lopez-Ceballos, P., Calderwood, D.A., and Tanentzapf, G. (2014). The talin head domain reinforces integrin-mediated adhesion by promoting adhesion complex stability and clustering. PLoS Genet *10*, e1004756.

Elosegui-Artola, A., Trepat, X., and Roca-Cusachs, P. (2018). Control of Mechanotransduction by Molecular Clutch Dynamics. Trends Cell Biol *28*, 356-367.

Eng, E.T., Smagghe, B.J., Walz, T., and Springer, T.A. (2011). Intact alphaIIbbeta3 integrin is extended after activation as measured by solution X-ray scattering and electron microscopy. J Biol Chem *286*, 35218-35226.

Engel, J., Odermatt, E., Engel, A., Madri, J.A., Furthmayr, H., Rohde, H., and Timpl, R. (1981). Shapes, domain organizations and flexibility of laminin and fibronectin, two multifunctional proteins of the extracellular matrix. J Mol Biol *150*, 97-120.

Engler, A.J., Sen, S., Sweeney, H.L., and Discher, D.E. (2006). Matrix elasticity directs stem cell lineage specification. Cell *126*, 677-689.

Erickson, H.P., Carrell, N., and McDonagh, J. (1981). Fibronectin molecule visualized in electron microscopy: a long, thin, flexible strand. J Cell Biol *91*, 673-678.

Evans, E.A., and Calderwood, D.A. (2007). Forces and bond dynamics in cell adhesion. Science *316*, 1148-1153.

Franco, S.J., Rodgers, M.A., Perrin, B.J., Han, J., Bennin, D.A., Critchley, D.R., and Huttenlocher, A. (2004). Calpain-mediated proteolysis of talin regulates adhesion dynamics. Nat Cell Biol *6*, 977-983.

Friedland, J.C., Lee, M.H., and Boettiger, D. (2009). Mechanically activated integrin switch controls alpha5beta1 function. Science *323*, 642-644.

Fukuda, K., Bledzka, K., Yang, J., Perera, H.D., Plow, E.F., and Qin, J. (2014). Molecular basis of kindlin-2 binding to integrin-linked kinase pseudokinase for regulating cell adhesion. J Biol Chem *289*, 28363-28375.

Garcia-Alvarez, B., de Pereda, J.M., Calderwood, D.A., Ulmer, T.S., Critchley, D., Campbell, I.D., Ginsberg, M.H., and Liddington, R.C. (2003). Structural determinants of integrin recognition by talin. Mol Cell *11*, 49-58.

Geiger, B., Bershadsky, A., Pankov, R., and Yamada, K.M. (2001). Transmembrane crosstalk between the extracellular matrix--cytoskeleton crosstalk. Nat Rev Mol Cell Biol *2*, 793-805.

Geiger, B., and Yamada, K.M. (2011). Molecular architecture and function of matrix adhesions. Cold Spring Harb Perspect Biol *3*.

Gingras, A.R., Bate, N., Goult, B.T., Hazelwood, L., Canestrelli, I., Grossmann, J.G., Liu, H., Putz, N.S., Roberts, G.C., Volkmann, N.*, et al.* (2008). The structure of the C-terminal actin-binding domain of talin. EMBO J *27*, 458-469.

Gingras, A.R., Ziegler, W.H., Frank, R., Barsukov, I.L., Roberts, G.C., Critchley, D.R., and Emsley, J. (2005). Mapping and consensus sequence identification for multiple vinculin binding sites within the talin rod. J Biol Chem *280*, 37217-37224.

Goh, K.L., Yang, J.T., and Hynes, R.O. (1997). Mesodermal defects and cranial neural crest apoptosis in alpha5 integrin-null embryos. Development *124*, 4309-4319.

Goksoy, E., Ma, Y.Q., Wang, X., Kong, X., Perera, D., Plow, E.F., and Qin, J. (2008). Structural basis for the autoinhibition of talin in regulating integrin activation. Mol Cell *31*, 124-133.

Gough, R.E., and Goult, B.T. (2018). The tale of two talins - two isoforms to fine-tune integrin signalling. FEBS Lett *592*, 2108-2125.

Goult, B.T., Bate, N., Anthis, N.J., Wegener, K.L., Gingras, A.R., Patel, B., Barsukov, I.L., Campbell, I.D., Roberts, G.C., and Critchley, D.R. (2009). The structure of an interdomain complex that regulates talin activity. J Biol Chem *284*, 15097-15106.

Goult, B.T., Xu, X.P., Gingras, A.R., Swift, M., Patel, B., Bate, N., Kopp, P.M., Barsukov, I.L., Critchley, D.R., Volkmann, N.*, et al.* (2013). Structural studies on full-length talin1 reveal a compact auto-inhibited dimer: implications for talin activation. J Struct Biol *184*, 21-32.

Grzesiak, J.J., and Pierschbacher, M.D. (1995). Changes in the concentrations of extracellular Mg++ and Ca++ down-regulate E-cadherin and up-regulate alpha 2 beta 1 integrin function, activating keratinocyte migration on type I collagen. J Invest Dermatol *104*, 768-774.

Gu, J., and Taniguchi, N. (2004). Regulation of integrin functions by N-glycans. Glycoconj J *21*, 9-15.

Guo, H.B., Lee, I., Kamar, M., Akiyama, S.K., and Pierce, M. (2002). Aberrant N-glycosylation of beta1 integrin causes reduced alpha5beta1 integrin clustering and stimulates cell migration. Cancer Res *62*, 6837-6845.

Huang, R., and Rofstad, E.K. (2018). Integrins as therapeutic targets in the organ-specific metastasis of human malignant melanoma. J Exp Clin Cancer Res *37*, 92.

Hughes, P.E., Diaz-Gonzalez, F., Leong, L., Wu, C., McDonald, J.A., Shattil, S.J., and Ginsberg, M.H. (1996). Breaking the integrin hinge. A defined structural constraint regulates integrin signaling. J Biol Chem *271*, 6571-6574.

Humphries, J.D., Byron, A., and Humphries, M.J. (2006). Integrin ligands at a glance. J Cell Sci *119*, 3901-3903.

Humphries, M.J. (1990). The molecular basis and specificity of integrin-ligand interactions. J Cell Sci *97 (Pt 4)*, 585-592.

Huveneers, S., and Danen, E.H. (2009). Adhesion signaling - crosstalk between integrins, Src and Rho. J Cell Sci *122*, 1059-1069.

Hynes, R.O. (2002). Integrins: bidirectional, allosteric signaling machines. Cell *110*, 673-687.

Isaji, T., Sato, Y., Fukuda, T., and Gu, J. (2009). N-glycosylation of the I-like domain of beta1 integrin is essential for beta1 integrin expression and biological function: identification of the minimal N-glycosylation requirement for alpha5beta1. J Biol Chem *284*, 12207-12216.

Isaji, T., Sato, Y., Zhao, Y., Miyoshi, E., Wada, Y., Taniguchi, N., and Gu, J. (2006). N-glycosylation of the beta-propeller domain of the integrin alpha5 subunit is essential for alpha5beta1 heterodimerization, expression on the cell surface, and its biological function. J Biol Chem *281*, 33258-33267.

Iwamoto, D.V., and Calderwood, D.A. (2015). Regulation of integrin-mediated adhesions. Curr Opin Cell Biol *36*, 41-47.

Iwasaki, K., Mitsuoka, K., Fujiyoshi, Y., Fujisawa, Y., Kikuchi, M., Sekiguchi, K., and Yamada, T. (2005). Electron tomography reveals diverse conformations of integrin alphaIIbbeta3 in the active state. J Struct Biol *150*, 259-267.

Janmey, P.A., Bucki, R., and Radhakrishnan, R. (2018). Regulation of actin assembly by PI(4,5)P2 and other inositol phospholipids: An update on possible mechanisms. Biochem Biophys Res Commun *506*, 307-314.

Johansson, S., Svineng, G., Wennerberg, K., Armulik, A., and Lohikangas, L. (1997). Fibronectin-integrin interactions. Front Biosci *2*, d126-146.

Kanchanawong, P., Shtengel, G., Pasapera, A.M., Ramko, E.B., Davidson, M.W., Hess, H.F., and Waterman, C.M. (2010). Nanoscale architecture of integrin-based cell adhesions. Nature *468*, 580-584.

Kato, A. (1997). The biologic and clinical spectrum of Glanzmann's thrombasthenia: implications of integrin alpha IIb beta 3 for its pathogenesis. Crit Rev Oncol Hematol *26*, 1-23.

Katsumi, A., Naoe, T., Matsushita, T., Kaibuchi, K., and Schwartz, M.A. (2005). Integrin activation and matrix binding mediate cellular responses to mechanical stretch. J Biol Chem *280*, 16546-16549.

Kim, C., Schmidt, T., Cho, E.G., Ye, F., Ulmer, T.S., and Ginsberg, M.H. (2011). Basic amino-acid side chains regulate transmembrane integrin signalling. Nature *481*, 209-213.

Kim, C., Ye, F., Hu, X., and Ginsberg, M.H. (2012). Talin activates integrins by altering the topology of the beta transmembrane domain. J Cell Biol *197*, 605-611.

Kim, M., Carman, C.V., and Springer, T.A. (2003). Bidirectional transmembrane signaling by cytoplasmic domain separation in integrins. Science *301*, 1720-1725.

Klapholz, B., and Brown, N.H. (2017). Talin - the master of integrin adhesions. J Cell Sci *130*, 2435-2446.

Kong, F., Garcia, A.J., Mould, A.P., Humphries, M.J., and Zhu, C. (2009). Demonstration of catch bonds between an integrin and its ligand. J Cell Biol *185*, 1275-1284.

Kuhlbrandt, W. (2014). Biochemistry. The resolution revolution. Science *343*, 1443-1444.

Kuo, J.C., Han, X., Hsiao, C.T., Yates, J.R., 3rd, and Waterman, C.M. (2011). Analysis of the myosin-II-responsive focal adhesion proteome reveals a role for beta-Pix in negative regulation of focal adhesion maturation. Nat Cell Biol *13*, 383-393.

Lau, T.L., Dua, V., and Ulmer, T.S. (2008a). Structure of the integrin alphaIIb transmembrane segment. J Biol Chem *283*, 16162-16168.

Lau, T.L., Kim, C., Ginsberg, M.H., and Ulmer, T.S. (2009). The structure of the integrin alphaIIbbeta3 transmembrane complex explains integrin transmembrane signalling. EMBO J *28*, 1351-1361.

Lau, T.L., Partridge, A.W., Ginsberg, M.H., and Ulmer, T.S. (2008b). Structure of the integrin beta3 transmembrane segment in phospholipid bicelles and detergent micelles. Biochemistry *47*, 4008-4016.

Lavelin, I., Wolfenson, H., Patla, I., Henis, Y.I., Medalia, O., Volberg, T., Livne, A., Kam, Z., and Geiger, B. (2013). Differential effect of actomyosin relaxation on the dynamic properties of focal adhesion proteins. PLoS One *8*, e73549.

Leahy, D.J., Aukhil, I., and Erickson, H.P. (1996). 2.0 A crystal structure of a four-domain segment of human fibronectin encompassing the RGD loop and synergy region. Cell *84*, 155-164.

Lee, H.S., Anekal, P., Lim, C.J., Liu, C.C., and Ginsberg, M.H. (2013). Two modes of integrin activation form a binary molecular switch in adhesion maturation. Mol Biol Cell *24*, 1354-1362.

Legate, K.R., and Fassler, R. (2009). Mechanisms that regulate adaptor binding to beta-integrin cytoplasmic tails. J Cell Sci *122*, 187-198.

Legate, K.R., Wickstrom, S.A., and Fassler, R. (2009). Genetic and cell biological analysis of integrin outside-in signaling. Genes Dev *23*, 397-418.

Lele, T.P., Thodeti, C.K., Pendse, J., and Ingber, D.E. (2008). Investigating complexity of protein-protein interactions in focal adhesions. Biochem Biophys Res Commun *369*, 929-934.

Li, H., Deng, Y., Sun, K., Yang, H., Liu, J., Wang, M., Zhang, Z., Lin, J., Wu, C., Wei, Z., *et al.* (2017a). Structural basis of kindlin-mediated integrin recognition and activation. Proc Natl Acad Sci U S A *114*, 9349-9354.

Li, J., and Springer, T.A. (2017). Integrin extension enables ultrasensitive regulation by cytoskeletal force. Proc Natl Acad Sci U S A *114*, 4685-4690.

Li, J., Su, Y., Xia, W., Qin, Y., Humphries, M.J., Vestweber, D., Cabanas, C., Lu, C., and Springer, T.A. (2017b). Conformational equilibria and intrinsic affinities define integrin activation. EMBO J *36*, 629-645.

Li, R., Babu, C.R., Lear, J.D., Wand, A.J., Bennett, J.S., and DeGrado, W.F. (2001). Oligomerization of the integrin alphaIIbbeta3: roles of the transmembrane and cytoplasmic domains. Proc Natl Acad Sci U S A *98*, 12462-12467.

Lin, C.H., Espreafico, E.M., Mooseker, M.S., and Forscher, P. (1997). Myosin drives retrograde F-actin flow in neuronal growth cones. Biol Bull *192*, 183-185.

Ling, K., Doughman, R.L., Firestone, A.J., Bunce, M.W., and Anderson, R.A. (2002). Type I gamma phosphatidylinositol phosphate kinase targets and regulates focal adhesions. Nature *420*, 89-93.

Liu, J., Wang, Y., Goh, W.I., Goh, H., Baird, M.A., Ruehland, S., Teo, S., Bate, N., Critchley, D.R., Davidson, M.W.*, et al.* (2015). Talin determines the nanoscale architecture of focal adhesions. Proc Natl Acad Sci U S A *112*, E4864-4873.

Liu, S., Thomas, S.M., Woodside, D.G., Rose, D.M., Kiosses, W.B., Pfaff, M., and Ginsberg, M.H. (1999). Binding of paxillin to alpha4 integrins modifies integrin-dependent biological responses. Nature *402*, 676-681.

Lu, Z., Mathew, S., Chen, J., Hadziselimovic, A., Palamuttam, R., Hudson, B.G., Fassler, R., Pozzi, A., Sanders, C.R., and Zent, R. (2016). Implications of the differing roles of the beta1 and beta3 transmembrane and cytoplasmic domains for integrin function. Elife *5*.

Luo, B.H., Carman, C.V., and Springer, T.A. (2007). Structural basis of integrin regulation and signaling. Annu Rev Immunol *25*, 619-647.

Luo, B.H., and Springer, T.A. (2006). Integrin structures and conformational signaling. Curr Opin Cell Biol *18*, 579-586.

Luo, B.H., Springer, T.A., and Takagi, J. (2004). A specific interface between integrin transmembrane helices and affinity for ligand. PLoS Biol *2*, e153.

Ma, Y.Q., Qin, J., Wu, C., and Plow, E.F. (2008). Kindlin-2 (Mig-2): a co-activator of beta3 integrins. J Cell Biol *181*, 439-446.

Mackinnon, A.C., Qadota, H., Norman, K.R., Moerman, D.G., and Williams, B.D. (2002). C. elegans PAT-4/ILK functions as an adaptor protein within integrin adhesion complexes. Curr Biol *12*, 787-797.

Main, A.L., Harvey, T.S., Baron, M., Boyd, J., and Campbell, I.D. (1992). The three-dimensional structure of the tenth type III module of fibronectin: an insight into RGD-mediated interactions. Cell *71*, 671-678.

Mao, Y., and Schwarzbauer, J.E. (2005). Fibronectin fibrillogenesis, a cell-mediated matrix assembly process. Matrix Biol *24*, 389-399.

Margadant, F., Chew, L.L., Hu, X., Yu, H., Bate, N., Zhang, X., and Sheetz, M. (2011). Mechanotransduction in vivo by repeated talin stretch-relaxation events depends upon vinculin. PLoS Biol *9*, e1001223.

Mezzenga, R., and Mitsi, M. (2019). The Molecular Dance of Fibronectin: Conformational Flexibility Leads to Functional Versatility. Biomacromolecules *20*, 55-72.

Mitchison, T., and Kirschner, M. (1988). Cytoskeletal dynamics and nerve growth. Neuron *1*, 761-772.

Miyazaki, N., Iwasaki, K., and Takagi, J. (2018). A systematic survey of conformational states in beta1 and beta4 integrins using negative-stain electron microscopy. J Cell Sci *131*.

Molony, L., McCaslin, D., Abernethy, J., Paschal, B., and Burridge, K. (1987). Properties of talin from chicken gizzard smooth muscle. J Biol Chem *262*, 7790-7795.

Monkley, S.J., Zhou, X.H., Kinston, S.J., Giblett, S.M., Hemmings, L., Priddle, H., Brown, J.E., Pritchard, C.A., Critchley, D.R., and Fassler, R. (2000). Disruption of the talin gene arrests mouse development at the gastrulation stage. Dev Dyn *219*, 560-574.

Montanez, E., Ussar, S., Schifferer, M., Bosl, M., Zent, R., Moser, M., and Fassler, R. (2008). Kindlin-2 controls bidirectional signaling of integrins. Genes Dev *22*, 1325-1330.

Moore, S.W., Roca-Cusachs, P., and Sheetz, M.P. (2010). Stretchy proteins on stretchy substrates: the important elements of integrin-mediated rigidity sensing. Dev Cell *19*, 194-206.

Moser, M., Bauer, M., Schmid, S., Ruppert, R., Schmidt, S., Sixt, M., Wang, H.V., Sperandio, M., and Fassler, R. (2009a). Kindlin-3 is required for beta2 integrin-mediated leukocyte adhesion to endothelial cells. Nat Med *15*, 300-305.

Moser, M., Legate, K.R., Zent, R., and Fassler, R. (2009b). The tail of integrins, talin, and kindlins. Science *324*, 895-899.

Moser, M., Nieswandt, B., Ussar, S., Pozgajova, M., and Fassler, R. (2008). Kindlin-3 is essential for integrin activation and platelet aggregation. Nat Med *14*, 325-330.

Mould, A.P., Askari, J.A., Aota, S., Yamada, K.M., Irie, A., Takada, Y., Mardon, H.J., and Humphries, M.J. (1997). Defining the topology of integrin alpha5beta1-fibronectin interactions using inhibitory anti-alpha5 and anti-beta1 monoclonal antibodies. Evidence that the synergy sequence of fibronectin is recognized by the amino-terminal repeats of the alpha5 subunit. J Biol Chem *272*, 17283-17292.

Mould, A.P., Barton, S.J., Askari, J.A., Craig, S.E., and Humphries, M.J. (2003). Role of ADMIDAS cation-binding site in ligand recognition by integrin alpha 5 beta 1. J Biol Chem *278*, 51622-51629.

Nagae, M., Kizuka, Y., Mihara, E., Kitago, Y., Hanashima, S., Ito, Y., Takagi, J., Taniguchi, N., and Yamaguchi, Y. (2018). Structure and mechanism of cancer-associated N-acetylglucosaminyltransferase-V. Nat Commun *9*, 3380.

Nagae, M., Re, S., Mihara, E., Nogi, T., Sugita, Y., and Takagi, J. (2012). Crystal structure of alpha5beta1 integrin ectodomain: atomic details of the fibronectin receptor. J Cell Biol *197*, 131-140.

Nakagawa, H., Zheng, M., Hakomori, S., Tsukamoto, Y., Kawamura, Y., and Takahashi, N. (1996). Detailed oligosaccharide structures of human integrin alpha 5 beta 1 analyzed by a three-dimensional mapping technique. Eur J Biochem *237*, 76-85.

Nieswandt, B., Moser, M., Pleines, I., Varga-Szabo, D., Monkley, S., Critchley, D., and Fassler, R. (2007). Loss of talin1 in platelets abrogates integrin activation, platelet aggregation, and thrombus formation in vitro and in vivo. J Exp Med *204*, 3113-3118.

Nishida, N., Xie, C., Shimaoka, M., Cheng, Y., Walz, T., and Springer, T.A. (2006). Activation of leukocyte beta2 integrins by conversion from bent to extended conformations. Immunity *25*, 583-594.

Nordenfelt, P., Elliott, H.L., and Springer, T.A. (2016). Coordinated integrin activation by actin-dependent force during T-cell migration. Nat Commun *7*, 13119.

Nordenfelt, P., Moore, T.I., Mehta, S.B., Kalappurakkal, J.M., Swaminathan, V., Koga, N., Lambert, T.J., Baker, D., Waters, J.C., Oldenbourg, R.*, et al.* (2017). Direction of actin flow dictates integrin LFA-1 orientation during leukocyte migration. Nat Commun *8*, 2047.

O'Toole, T.E., Katagiri, Y., Faull, R.J., Peter, K., Tamura, R., Quaranta, V., Loftus, J.C., Shattil, S.J., and Ginsberg, M.H. (1994). Integrin cytoplasmic domains mediate inside-out signal transduction. J Cell Biol *124*, 1047-1059.

O'Toole, T.E., Mandelman, D., Forsyth, J., Shattil, S.J., Plow, E.F., and Ginsberg, M.H. (1991). Modulation of the affinity of integrin alpha IIb beta 3 (GPIIb-IIIa) by the cytoplasmic domain of alpha IIb. Science *254*, 845-847.

Obara, M., Kang, M.S., and Yamada, K.M. (1988). Site-directed mutagenesis of the cell-binding domain of human fibronectin: separable, synergistic sites mediate adhesive function. Cell *53*, 649-657.

Oria, R., Wiegand, T., Escribano, J., Elosegui-Artola, A., Uriarte, J.J., Moreno-Pulido, C., Platzman, I., Delcanale, P., Albertazzi, L., Navajas, D.*, et al.* (2017). Force loading explains spatial sensing of ligands by cells. Nature *552*, 219-224.

Oxley, C.L., Anthis, N.J., Lowe, E.D., Vakonakis, I., Campbell, I.D., and Wegener, K.L. (2008). An integrin phosphorylation switch: the effect of beta3 integrin tail phosphorylation on Dok1 and talin binding. J Biol Chem *283*, 5420-5426.

Pankov, R., and Yamada, K.M. (2002). Fibronectin at a glance. Journal of Cell Science *115*, 3861-3863.

Partridge, A.W., Liu, S., Kim, S., Bowie, J.U., and Ginsberg, M.H. (2005). Transmembrane domain helix packing stabilizes integrin alphaIIbbeta3 in the low affinity state. J Biol Chem *280*, 7294-7300.

Paszek, M.J., Boettiger, D., Weaver, V.M., and Hammer, D.A. (2009). Integrin clustering is driven by mechanical resistance from the glycocalyx and the substrate. PLoS Comput Biol *5*, e1000604.

Paszek, M.J., DuFort, C.C., Rossier, O., Bainer, R., Mouw, J.K., Godula, K., Hudak, J.E., Lakins, J.N., Wijekoon, A.C., Cassereau, L.*, et al.* (2014). The cancer glycocalyx mechanically primes integrin-mediated growth and survival. Nature *511*, 319-325.

Paszek, M.J., DuFort, C.C., Rubashkin, M.G., Davidson, M.W., Thorn, K.S., Liphardt, J.T., and Weaver, V.M. (2012). Scanning angle interference microscopy reveals cell dynamics at the nanoscale. Nat Methods *9*, 825-827.

Patla, I., Volberg, T., Elad, N., Hirschfeld-Warneken, V., Grashoff, C., Fassler, R., Spatz, J.P., Geiger, B., and Medalia, O. (2010). Dissecting the molecular architecture of integrin adhesion sites by cryo-electron tomography. Nat Cell Biol *12*, 909-915.

Plow, E.F., Haas, T.A., Zhang, L., Loftus, J., and Smith, J.W. (2000). Ligand binding to integrins. J Biol Chem *275*, 21785-21788.

Pochec, E., Litynska, A., Amoresano, A., and Casbarra, A. (2003). Glycosylation profile of integrin alpha 3 beta 1 changes with melanoma progression. Biochim Biophys Acta *1643*, 113-123.

Ponti, A., Machacek, M., Gupton, S.L., Waterman-Storer, C.M., and Danuser, G. (2004). Two distinct actin networks drive the protrusion of migrating cells. Science *305*, 1782-1786.

Puklin-Faucher, E., Gao, M., Schulten, K., and Vogel, V. (2006). How the headpiece hinge angle is opened: New insights into the dynamics of integrin activation. J Cell Biol *175*, 349-360.

Qu, H., Tu, Y., Shi, X., Larjava, H., Saleem, M.A., Shattil, S.J., Fukuda, K., Qin, J., Kretzler, M., and Wu, C. (2011). Kindlin-2 regulates podocyte adhesion and fibronectin matrix deposition through interactions with phosphoinositides and integrins. J Cell Sci *124*, 879-891.

Raab-Westphal, S., Marshall, J.F., and Goodman, S.L. (2017). Integrins as Therapeutic Targets: Successes and Cancers. Cancers (Basel) *9*.

Reddy, K.B., Gascard, P., Price, M.G., Negrescu, E.V., and Fox, J.E. (1998). Identification of an interaction between the m-band protein skelemin and beta-integrin subunits. Colocalization of a skelemin-like protein with beta1- and beta3-integrins in non-muscle cells. J Biol Chem *273*, 35039-35047.

Redick, S.D., Settles, D.L., Briscoe, G., and Erickson, H.P. (2000). Defining fibronectin's cell adhesion synergy site by site-directed mutagenesis. J Cell Biol *149*, 521-527.

Roca-Cusachs, P., del Rio, A., Puklin-Faucher, E., Gauthier, N.C., Biais, N., and Sheetz, M.P. (2013). Integrin-dependent force transmission to the extracellular matrix by alpha-actinin triggers adhesion maturation. Proc Natl Acad Sci U S A *110*, E1361-1370.

Roca-Cusachs, P., Gauthier, N.C., Del Rio, A., and Sheetz, M.P. (2009). Clustering of alpha(5)beta(1) integrins determines adhesion strength whereas alpha(v)beta(3) and talin enable mechanotransduction. Proc Natl Acad Sci U S A *106*, 16245-16250.

Roca-Cusachs, P., Iskratsch, T., and Sheetz, M.P. (2012). Finding the weakest link: exploring integrin-mediated mechanical molecular pathways. J Cell Sci *125*, 3025-3038.

Rognoni, E., Ruppert, R., and Fassler, R. (2016). The kindlin family: functions, signaling properties and implications for human disease. J Cell Sci *129*, 17-27.

Rosenkranz, A.R., and Mayadas, T.N. (1999). Leukocyte-endothelial cell interactions - lessons from knockout mice. Exp Nephrol *7*, 125-136.

Ross, T.D., Coon, B.G., Yun, S., Baeyens, N., Tanaka, K., Ouyang, M., and Schwartz, M.A. (2013). Integrins in mechanotransduction. Curr Opin Cell Biol *25*, 613-618.

Schaffner, F., Ray, A.M., and Dontenwill, M. (2013). Integrin alpha5beta1, the Fibronectin Receptor, as a Pertinent Therapeutic Target in Solid Tumors. Cancers (Basel) *5*, 27-47.

Schaller, M.D., Otey, C.A., Hildebrand, J.D., and Parsons, J.T. (1995). Focal adhesion kinase and paxillin bind to peptides mimicking beta integrin cytoplasmic domains. J Cell Biol *130*, 1181-1187.

Schiller, H.B., and Fassler, R. (2013). Mechanosensitivity and compositional dynamics of cell-matrix adhesions. EMBO Rep *14*, 509-519.

Schoen, I., Pruitt, B.L., and Vogel, V. (2013). The Yin-Yang of Rigidity Sensing: How Forces and Mechanical Properties Regulate the Cellular Response to Materials. Annu Rev Mater Res *43*, 589-618.

Schwarzbauer, J.E., and Sechler, J.L. (1999). Fibronectin fibrillogenesis: a paradigm for extracellular matrix assembly. Curr Opin Cell Biol *11*, 622-627.

Sechler, J.L., Corbett, S.A., and Schwarzbauer, J.E. (1997). Modulatory roles for integrin activation and the synergy site of fibronectin during matrix assembly. Mol Biol Cell *8*, 2563-2573.

Sechler, J.L., Takada, Y., and Schwarzbauer, J.E. (1996). Altered rate of fibronectin matrix assembly by deletion of the first type III repeats. J Cell Biol *134*, 573-583.

Sgro, G.G., and Costa, T.R.D. (2018). Cryo-EM Grid Preparation of Membrane Protein Samples for Single Particle Analysis. Front Mol Biosci *5*, 74.

Shibata, A.C., Fujiwara, T.K., Chen, L., Suzuki, K.G., Ishikawa, Y., Nemoto, Y.L., Miwa, Y., Kalay, Z., Chadda, R., Naruse, K.*, et al.* (2012). Archipelago architecture of the focal adhesion: membrane molecules freely enter and exit from the focal adhesion zone. Cytoskeleton (Hoboken) *69*, 380-392.

Shimaoka, M., Takagi, J., and Springer, T.A. (2002). Conformational regulation of integrin structure and function. Annu Rev Biophys Biomol Struct *31*, 485-516.

Shroff, H., Galbraith, C.G., Galbraith, J.A., White, H., Gillette, J., Olenych, S., Davidson, M.W., and Betzig, E. (2007). Dual-color superresolution imaging of genetically expressed probes within individual adhesion complexes. Proc Natl Acad Sci U S A *104*, 20308-20313.

Singh, P., Carraher, C., and Schwarzbauer, J.E. (2010). Assembly of fibronectin extracellular matrix. Annu Rev Cell Dev Biol *26*, 397-419.

Smagghe, B.J., Huang, P.S., Ban, Y.E., Baker, D., and Springer, T.A. (2010). Modulation of integrin activation by an entropic spring in the {beta}-knee. J Biol Chem *285*, 32954-32966.

Song, X., Yang, J., Hirbawi, J., Ye, S., Perera, H.D., Goksoy, E., Dwivedi, P., Plow, E.F., Zhang, R., and Qin, J. (2012). A novel membrane-dependent on/off switch mechanism of talin FERM domain at sites of cell adhesion. Cell Res *22*, 1533-1545.

Spiess, M., Hernandez-Varas, P., Oddone, A., Olofsson, H., Blom, H., Waithe, D., Lock, J.G., Lakadamyali, M., and Stromblad, S. (2018). Active and inactive beta1 integrins segregate into distinct nanoclusters in focal adhesions. J Cell Biol *217*, 1929-1940.

Stefansson, A., Armulik, A., Nilsson, I., von Heijne, G., and Johansson, S. (2004). Determination of N- and C-terminal borders of the transmembrane domain of integrin subunits. J Biol Chem *279*, 21200-21205.

Su, Y., Xia, W., Li, J., Walz, T., Humphries, M.J., Vestweber, D., Cabanas, C., Lu, C., and Springer, T.A. (2016). Relating conformation to function in integrin alpha5beta1. Proc Natl Acad Sci U S A *113*, E3872-3881.

Sun, Z., Costell, M., and Fassler, R. (2019). Integrin activation by talin, kindlin and mechanical forces. Nat Cell Biol *21*, 25-31.

Sun, Z., Guo, S.S., and Fassler, R. (2016a). Integrin-mediated mechanotransduction. J Cell Biol *215*, 445-456.

Sun, Z., Lambacher, A., and Fassler, R. (2014). Nascent adhesions: from fluctuations to a hierarchical organization. Curr Biol *24*, R801-803.

Sun, Z., Tseng, H.Y., Tan, S., Senger, F., Kurzawa, L., Dedden, D., Mizuno, N., Wasik, A.A., Thery, M., Dunn, A.R.*, et al.* (2016b). Kank2 activates talin, reduces force transduction across integrins and induces central adhesion formation. Nat Cell Biol *18*, 941-953.

Tadokoro, S., Shattil, S.J., Eto, K., Tai, V., Liddington, R.C., de Pereda, J.M., Ginsberg, M.H., and Calderwood, D.A. (2003). Talin binding to integrin beta tails: a final common step in integrin activation. Science *302*, 103-106.

Takagi, J., Erickson, H.P., and Springer, T.A. (2001). C-terminal opening mimics 'inside-out' activation of integrin alpha5beta1. Nat Struct Biol *8*, 412-416.

Takagi, J., Petre, B.M., Walz, T., and Springer, T.A. (2002). Global conformational rearrangements in integrin extracellular domains in outside-in and inside-out signaling. Cell *110*, 599-511.

Takagi, J., Strokovich, K., Springer, T.A., and Walz, T. (2003). Structure of integrin alpha5beta1 in complex with fibronectin. EMBO J *22*, 4607-4615.

Taverna, D., Disatnik, M.H., Rayburn, H., Bronson, R.T., Yang, J., Rando, T.A., and Hynes, R.O. (1998). Dystrophic muscle in mice chimeric for expression of alpha5 integrin. J Cell Biol *143*, 849-859.

Theodosiou, M., Widmaier, M., Bottcher, R.T., Rognoni, E., Veelders, M., Bharadwaj, M., Lambacher, A., Austen, K., Muller, D.J., Zent, R.*, et al.* (2016). Kindlin-2 cooperates with talin to activate integrins and induces cell spreading by directly binding paxillin. Elife *5*.

Tu, Y., Wu, S., Shi, X., Chen, K., and Wu, C. (2003). Migfilin and Mig-2 link focal adhesions to filamin and the actin cytoskeleton and function in cell shape modulation. Cell *113*, 37-47.

Ulmer, T.S. (2010). Structural basis of transmembrane domain interactions in integrin signaling. Cell Adh Migr *4*, 243-248.

Ussar, S., Moser, M., Widmaier, M., Rognoni, E., Harrer, C., Genzel-Boroviczeny, O., and Fassler, R. (2008). Loss of Kindlin-1 causes skin atrophy and lethal neonatal intestinal epithelial dysfunction. PLoS Genet *4*, e1000289.

Valdramidou, D., Humphries, M.J., and Mould, A.P. (2008). Distinct roles of beta1 metal ion-dependent adhesion site (MIDAS), adjacent to MIDAS (ADMIDAS), and ligand-associated metal-binding site (LIMBS) cation-binding sites in ligand recognition by integrin alpha2beta1. J Biol Chem *283*, 32704-32714.

Vallar, L., Melchior, C., Plancon, S., Drobecq, H., Lippens, G., Regnault, V., and Kieffer, N. (1999). Divalent cations differentially regulate integrin alphaIIb cytoplasmic tail binding to beta3 and to calcium- and integrin-binding protein. J Biol Chem *274*, 17257-17266.

van der Flier, A., and Sonnenberg, A. (2001). Function and interactions of integrins. Cell Tissue Res *305*, 285-298.

Vinogradova, O., Velyvis, A., Velyviene, A., Hu, B., Haas, T., Plow, E., and Qin, J. (2002). A structural mechanism of integrin alpha(IIb)beta(3) "inside-out" activation as regulated by its cytoplasmic face. Cell *110*, 587-597.

Wegener, K.L., and Campbell, I.D. (2008). Transmembrane and cytoplasmic domains in integrin activation and protein-protein interactions (review). Mol Membr Biol *25*, 376-387.

Wegener, K.L., Partridge, A.W., Han, J., Pickford, A.R., Liddington, R.C., Ginsberg, M.H., and Campbell, I.D. (2007). Structural basis of integrin activation by talin. Cell *128*, 171-182.

Wehrle-Haller, B. (2012). Assembly and disassembly of cell matrix adhesions. Curr Opin Cell Biol *24*, 569-581.

Winkler, J., Lunsdorf, H., and Jockusch, B.M. (1997). Energy-filtered electron microscopy reveals that talin is a highly flexible protein composed of a series of globular domains. Eur J Biochem *243*, 430-436.

Winograd-Katz, S.E., Fassler, R., Geiger, B., and Legate, K.R. (2014). The integrin adhesome: from genes and proteins to human disease. Nat Rev Mol Cell Biol *15*, 273-288.

Wolfenson, H., Lubelski, A., Regev, T., Klafter, J., Henis, Y.I., and Geiger, B. (2009). A role for the juxtamembrane cytoplasm in the molecular dynamics of focal adhesions. PLoS One *4*, e4304.

Wozniak, M.A., Modzelewska, K., Kwong, L., and Keely, P.J. (2004). Focal adhesion regulation of cell behavior. Biochim Biophys Acta *1692*, 103-119.

Xia, W., and Springer, T.A. (2014). Metal ion and ligand binding of integrin alpha5beta1. Proc Natl Acad Sci U S A *111*, 17863-17868.

Xiao, T., Takagi, J., Coller, B.S., Wang, J.H., and Springer, T.A. (2004). Structural basis for allostery in integrins and binding to fibrinogen-mimetic therapeutics. Nature *432*, 59-67.

Xie, C., Zhu, J., Chen, X., Mi, L., Nishida, N., and Springer, T.A. (2010). Structure of an integrin with an alphaI domain, complement receptor type 4. EMBO J *29*, 666-679.

Xiong, J.P., Mahalingham, B., Alonso, J.L., Borrelli, L.A., Rui, X., Anand, S., Hyman, B.T., Rysiok, T., Muller-Pompalla, D., Goodman, S.L.*, et al.* (2009). Crystal structure of the complete integrin alphaVbeta3 ectodomain plus an alpha/beta transmembrane fragment. J Cell Biol *186*, 589-600.

Xiong, J.P., Stehle, T., Diefenbach, B., Zhang, R., Dunker, R., Scott, D.L., Joachimiak, A., Goodman, S.L., and Arnaout, M.A. (2001). Crystal structure of the extracellular segment of integrin alpha Vbeta3. Science *294*, 339-345.

Xiong, J.P., Stehle, T., Goodman, S.L., and Arnaout, M.A. (2003). New insights into the structural basis of integrin activation. Blood *102*, 1155-1159.

Xiong, J.P., Stehle, T., Zhang, R., Joachimiak, A., Frech, M., Goodman, S.L., and Arnaout, M.A. (2002). Crystal structure of the extracellular segment of integrin alpha Vbeta3 in complex with an Arg-Gly-Asp ligand. Science *296*, 151-155.

Xu, X.P., Kim, E., Swift, M., Smith, J.W., Volkmann, N., and Hanein, D. (2016). Three-Dimensional Structures of Full-Length, Membrane-Embedded Human alpha(IIb)beta(3) Integrin Complexes. Biophys J *110*, 798-809.

Yamanashi, Y., and Baltimore, D. (1997). Identification of the Abl- and rasGAP-associated 62 kDa protein as a docking protein, Dok. Cell *88*, 205-211.

Yang, J.T., Rayburn, H., and Hynes, R.O. (1993). Embryonic mesodermal defects in alpha 5 integrin-deficient mice. Development *119*, 1093-1105.

Ye, F., Hu, G., Taylor, D., Ratnikov, B., Bobkov, A.A., McLean, M.A., Sligar, S.G., Taylor, K.A., and Ginsberg, M.H. (2010). Recreation of the terminal events in physiological integrin activation. J Cell Biol *188*, 157-173.

Ye, F., Petrich, B.G., Anekal, P., Lefort, C.T., Kasirer-Friede, A., Shattil, S.J., Ruppert, R., Moser, M., Fassler, R., and Ginsberg, M.H. (2013). The mechanism of kindlin-mediated activation of integrin alphaIIbbeta3. Curr Biol *23*, 2288-2295.

Zaidel-Bar, R., Ballestrem, C., Kam, Z., and Geiger, B. (2003). Early molecular events in the assembly of matrix adhesions at the leading edge of migrating cells. J Cell Sci *116*, 4605-4613.

Zaidel-Bar, R., and Geiger, B. (2010). The switchable integrin adhesome. J Cell Sci *123*, 1385-1388.

Zaidel-Bar, R., Itzkovitz, S., Ma'ayan, A., Iyengar, R., and Geiger, B. (2007). Functional atlas of the integrin adhesome. Nat Cell Biol *9*, 858-867.

Zhang, K., and Chen, J. (2012). The regulation of integrin function by divalent cations. Cell Adh Migr *6*, 20-29.

Zhang, X., Jiang, G., Cai, Y., Monkley, S.J., Critchley, D.R., and Sheetz, M.P. (2008). Talin depletion reveals independence of initial cell spreading from integrin activation and traction. Nat Cell Biol *10*, 1062-1068.

Zheng, M., Fang, H., and Hakomori, S. (1994). Functional role of N-glycosylation in alpha 5 beta 1 integrin receptor. De-N-glycosylation induces dissociation or altered association of alpha 5 and beta 1 subunits and concomitant loss of fibronectin binding activity. J Biol Chem *269*, 12325-12331.

Zheng, Y., and Leftheris, K. (2020). Insights into Protein-Ligand Interactions in Integrin Complexes: Advances in Structure Determinations. J Med Chem.

Zhu, J., Luo, B.H., Barth, P., Schonbrun, J., Baker, D., and Springer, T.A. (2009). The structure of a receptor with two associating transmembrane domains on the cell surface: integrin alphaIIbbeta3. Mol Cell *34*, 234-249.

Zhu, J., Luo, B.H., Xiao, T., Zhang, C., Nishida, N., and Springer, T.A. (2008). Structure of a complete integrin ectodomain in a physiologic resting state and activation and deactivation by applied forces. Mol Cell *32*, 849-861.

Zhu, J., Zhu, J., and Springer, T.A. (2013). Complete integrin headpiece opening in eight steps. J Cell Biol *201*, 1053-1068.

Acknowledgements

This work would not have been possible without the help and support of many people.

First, I would like to sincerely thank my supervisor Naoko Mizuno for giving me the opportunity to do my PhD in her group at the MPI in a fantastic working environment. I learned a lot during the past years and am immensely grateful for her scientific guidance, her constant trust in me and continuous support throughout my PhD.

Special thanks also go to Elena Conti, my doctoral mother and TAC member, for hosting and supporting me throughout my PhD, and for providing an excellent research environment.

During my PhD, I had the opportunity to visit the lab of Junichi Takagi in Osaka, Japan. Thanks to Junichi and his lab, especially Kyoko-san, I had a wonderful time in Osaka and learned a lot. My stay there was a game changer for my PhD project.

Furthermore, I would also like to thank my TAC members, Christine Ziegler and Carsten Grashoff for great scientific input and advice throughout the years.

I would also like to thank the MPI biochemistry core facility as well as the cryo-EM facility for excellent support – thank you, Daniel and Tilman for all your help and for being a shining light in even the darkest of (EM) bunkers. Many thanks also go to Wolfgang Baumeister and his department, for initial support and help with all EM-related issues, and especially Günter, Jürgen and Rado for support.

I also want to thank the International Max Planck Research School for Molecular Life Sciences (IMPRS-LS) for providing help with organizational issues, many opportunities to connect to fellow scientists and financial support.

Also, I would like to thank all the past and present members in the Mizuno and Biertümpfel groups: Dirk, Nirakar, Chris, Giulia, Shun, Sven, Carina, Iosune, Qianmin, Hana, Charlotte, Iuliia, Julia, Rebecca, Simon, Lorenzo, Alethia, WoFi and of course Christian Biertümpfel for immense scientific support. I am very grateful for many fruitful discussions and a nice atmosphere inside and also outside of the lab!

Many thanks also go the whole Conti department, for the friendly and encouraging atmosphere. Thank you, Peter, for rescuing our Aektas and columns more often than can be counted! My thanks also go to Jerome and the X-tal facility, Karina and Sabine. Fabien, Claire, Ariane, Judith, and the whole kitchen staff – thank you for all of your helpful suggestions in all these years and for keeping everything running smoothly. I would also

like to thank Petra and Ulrike for helping out with any administrative issues, and Rajan and Christian for providing a smooth computing environment. And thanks to all people from 3rd floor for many good times ('we should have a BBQ every weekend, guys!'), I cannot imagine my time here in Munich without you. This goes especially to Jana, Michi, Ksenia, Lukas, Achim, Felix, Alex, Mahesh, Christian, Yair, Ingmar, Steffen, Peter, and also extends to Nikki, Marc, Lisa, Jan, Sandra, Julian, Marcela and Piotr.

My thanks also extend to many countless people within the MPI that contributed to a friendly (and fun) environment – playing volleyball (Team Conti FTW!) and other games on campus, as well as going to 'Get-togethers' really let me enjoy my time at the MPI.

Last but not least, this work would have never been possible without the constant love and support of my family and friends.

Ich möchte vor allem meinen Eltern danken, für die jahrelange Unterstützung und Hilfe in wirklich jeder Lebenslage – ohne euch hätte ich das alles niemals geschafft! Auch meinem Bruder Walter und Neffen Liam: vielen Dank, dass es euch gibt! Ich habe euch alle sehr lieb. Ich möchte an dieser Stelle auch meinen Großeltern und meinem Onkel danken.

Auch an meine engsten Freunde, seit wahrscheinlich nun schon 20 Jahren, Yasmin, Kata, Jenny und Laura: danke, dass ihr immer für mich da seid und mich immer auf den Boden der Tatsachen zurückholt! Dank gebührt auch meinen Freunden aus München, ohne die meine Zeit hier mit Sicherheit nur halb so viel Spaß gemacht hätte –Jana (Schumalbrecht), Giulia (my favorite Rock band member), Chris, Nirakar, Shun und selbstverständlich Dirk -

Danke auch dir, für die wundervolle Zeit – ohne dich hätte ich das niemals durchgestanden.

Vielen Dank an euch alle!!
Thank you all!!